UNIVERSITY OF CALIFORNIA SAN DIEGO

Observations and Insights into Source Heterogeneity, Mixing, and Tectonic Evolution of the Mantle from Osmium Isotopes and Highly Siderophile Elements

A Dissertation submitted in partial satisfaction of the requirements
for the degree Doctor of Philosophy

in

Earth Sciences

by

Brian Oller

Committee in charge:

Professor James Day, Co-Chair
Professor Neal Driscoll, Co-Chair
Professor Falko Kuester
Professor Ross Parnell-Turner
Professor David Sandwell

2024

The Dissertation of Brian Oller is approved, and it is acceptable in quality and form for publication on microfilm and electronically.

University of California San Diego

2024

DEDICATION

To my friends who didn’t make it home, and those who did but never really came back.

TABLE OF CONTENTS

LIST OF FIGURES

LIST OF TABLES

LIST OF SUPPLEMENTAL FILES

Oller_Ch2_Data_Tables.xlsx

Oller_Ch3_Data_Tables.xlsx

Oller_Ch4_Data_Tables.xlsx

Oller_Ch5_Data_Tables.xlsx

ACKNOWLEDGEMENTS

First, I would like to recognize my advisors Neal Driscoll and James Day for seeing potential in me that few others saw. Most students are accepted to the program at a nice dinner. I was accepted with a handshake at a gas station parking lot during a field trip. I can't think of anything more fitting. James, thank you for taking me to my first first-world country. Most life changing experiences are unpleasant. The Canaries trip was categorically positive.

Thank you to the science parties, technicians, and crews of the R/V Sally Ride, R/V Thomas G. Thompson, R/V Marcus G. Langseth, and R/V Melville. We've done things I never could have imagined sitting in a classroom at South Plains College.

Finally, and perhaps most importantly I'd like to thank the U.S. taxpayer for the unwavering financial support I received through the Post 9-11 Montgomery GI Bill and various other VA funded educational programs, school supplies such as textbooks, computers, software, even parking tickets. Not to mention the publicly funded university and numerous grants of which I have directly or indirectly been a benefactor. I am fully aware that many of these people think this is a complete waste of money, maybe the parking tickets were, but I would like to think that most of it was not, and the future investment will be well spent. Perhaps I will be fortunate enough to show a handful of taxpayers that it was money well spent.

Chapter 2, in full, is a reprint of the material as it appears in Geochemistry Geophysics Geosystems 2022. Oller, Brian; Day, James M.D.; Driscoll, Neal W.; Lonsdale, Peter, F. The dissertation author was the primary investigator and author of this paper.

Chapters 3, 4, and 5, in part are currently being prepared for submission for publication of the material. Oller, Brian; Day, James M.D; Driscoll, Neal W. The dissertation author was the primary researcher and author of this material.

VITA

2000-2005 United States Marine Corps.

2015 Bachelor of Science in Earth Science, University of California San Diego

2016 Master of Science in Earth Science, University of California San Diego

2024 Doctor of Philosophy in Degree Earth Science, University of California San Diego

PUBLICATIONS

Oller, B., Day, J. M. D., Driscoll, N. W., & Lonsdale, P. F. (2022). Generation of Continental Lithospheric Mantle by Tectonic Isolation of Oceanic Plate. *Geochemistry, Geophysics, Geosystems*, *23*(11).

Day, J.M.D., Koppers, A.A.P., Mendenhall, B.C., Oller, B. (2019). The Scripps Dike and its implications for mid-Miocene volcanism and tectonics of the California Continental Borderland. In Marsaglia KM, Schwalbach J, Behl R (Editors). From the Mountains to the Abyss: The California Borderland as an Archive of Southern California Evolution, Special Publication 110: SEPM (Society for Sedimentary Geology), Broken Arrow, Oklahoma.

FIELD OF STUDY

Isotope Geochemistry
Marine Geology
Neotectonics

ABSTRACT OF THE DISSERTATION

Observations and Insights into Source Heterogeneity, Mixing, and Tectonic Evolution of the Mantle from Osmium Isotopes and Highly Siderophile Elements

by

Brian Oller

Doctor of Philosophy in Earth Sciences

University of California San Diego, 2024

Professor James Day, Co-Chair
Professor Neal Driscoll, Co-Chair

Ultramafic xenoliths and mafic lavas have been instrumental in understanding the composition of Earth's mantle and processes that influence its composition. These processes can be obscured by overprinting from eruption, emplacement and magma storage processes prior to the rocks coming to the surface. In this dissertation mantle processes are examined using melt depleted peridotite xenoliths and through the eruptive products of the mantle, ultramafic cumulate xenoliths, and ocean island basalts. Similarities between oceanic lithosphere and non-cratonic continental lithosphere (CLM) suggest these domains are linked. To begin, in chapter two, xenoliths from the Ferrel seamount are determined to sample a fragment of ancient Farallon Plate

lithosphere at the abandoned spreading ridge. Next, similarities between these xenoliths and non-cratonic CLM are used to develop a new model for the evolution of oceanic lithosphere to non-cratonic CLM. Chapter three explores the isotopically distinct Loa and Kea trends in Hawai'i through a novel approach of studying cumulate xenoliths. The Loa and Kea trends show disparities in long-lived radiogenic isotope systems, including Re-Os, that suggest these magmas are sourced from two distinct mantle reservoirs. This study evaluates the potential for mixing between these two trends considering recently published seismic evidence suggesting a shared magmatic system. Chapter four shows the Canary Islands are built atop lithosphere more similar to the Atlantic rather than the adjacent non-cratonic African lithosphere. Lavas erupted here show evidence of lithospheric contamination and likely sample two different mantle endmembers, yet lack the characteristic bilateral zoning observed in the Pacific Ocean islands. Finally, chapter five examines an emerging continental rift zone east of the Sierra Nevada mountains in California. Peridotite and pyroxenite cumulate xenoliths from the Papoose Canyon volcanic sequence in the Owens Valley have trace element and Os isotopic systematics which suggest crustal contamination has had a significant impact on their parental magmas. A model of Os isotopic composition and HSE fractionation suggests that only a small amount of crustal addition is required to replicate the observed compositions. Despite the apparent crustal contamination, absolute and relative HSE abundances preserve information on the parental melt.

CHAPTER 1 Introduction

The mantle accounts for ~65% of Earth's mass, ~80% of its volume, as well as the overwhelming majority of its silicate composition (Helffrich & Wood, 2001). The mantle extends from the top of the metallic core ~2900 km deep to the base of the crust, which is generally subdivided into two domains: the upper and lower mantle. The lower mantle, more specifically the asthenosphere, is the ductile, mechanically weak region that encompasses much of the total mantle from the core to base of the lithosphere. This is the convecting zone of the mantle responsible for heat transfer and mixing, although the degree and efficiency to which mixing occurs is debated (e.g., Morgan, 1971; Stracke, 2012). The upper mantle, defined as the section of mantle above the transition zone from ~ 660 km to 410 km deep, can be subdivided into asthenosphere and lithosphere. Differentiation of these two zones is defined by a thermal boundary layer at ~1600K as opposed to an absolute depth. The lithosphere is a thin veneer overlying the asthenosphere and is characterized by its ability to support stress and is the "rigid plate" of plate tectonics.

The lithospheric mantle can be classified into three different categories based on thickness age and principal composition. Cratonic lithosphere is considered the stable keel upon which continents are built and examples are found beneath all of Earth's major continental land masses. Seismic discontinuities suggest the lithosphere asthenosphere boundary is ~150 to 300 km deep (French & Romanowicz, 2015), making this the thickest lithospheric domain. Samples of cratonic material are limited to peridotite xenoliths encased in basaltic eruptions. Although limited these samples show cratonic lithosphere is highly melt depleted, with a mineral composition dominantly olivine having little accessory pyroxene content. Olivines typically show elevated Mg/Fe ratios,

often expressed as Mg-number {Mg-number = [Mg_{molar} / (Mg_{molar} + Fe_{molar}) * 100]} compared to olivine from other lithospheric domains and peridotite suites (Boyd, 1989; Herzberg & Rudnick, 2012). The elevated degree of melt depletion is indicative of inherent buoyancy thus longevity of theses lithospheric keels (Herzberg & Rudnick, 2012). Evidence of their long-term stability is provided by Re-Os isotope model ages that consistently suggest Proterozoic to Archean stabilization ages (Pearson et al., 2004).

Oceanic lithosphere and its complement mid-ocean ridge basalt (MORB) is formed at mid ocean spreading ridges from adiabatic decompression melting of upwelling asthenosphere (Hofmann, 1997). Up to ~20% partial melting of this material produces oceanic crust complex of gabbros, sheeted dikes, and pillow basalt and leaves behind a depleted residue. As the depleted lithosphere moves away from the ridge it cools and thickens over time before being recycled into the mantle through subduction. This process can be considered the dynamic representation of mantle convection. Oceanic lithosphere is sampled by xenoliths entrained in low degree basaltic melts, oceanic transform fracture zones, and terrestrially as ophiolites. These samples typically span a compositional range from harzburgite to lherzolite and higher Al and Ca, and lower Mg-numbers than their cratonic counterparts. Although the maximum observed age of oceanic crust is ~200 Ma, Re-Os model ages of abyssal peridotites routinely record melt depletion events >1 Ga (Day et al., 2017) which suggests some ancient oceanic lithosphere is preserved and provides one example of evidence for a heterogeneously mixed mantle (d'Errico et al., 2016; Day et al., 2017; Warren, 2016).

Non-cratonic continental lithospheric mantle (CLM) is often indistinguishable from oceanic lithosphere in terms of degree of melt depletion, Mg-numbers, and stabilization model ages which suggests a possible link between oceanic and non-cratonic CLM (Boyd, 1987; Pearson

et al., 2004; Oller et al., 2022). These similarities have led to several models of continental growth all involving the isolation of oceanic lithosphere from subduction and welding the oceanic fragment to a cratonic nuclei. Observed compositional differences between non-cratonic CLM xenolith suites and abyssal peridotites are likely due in large part to isolation from subduction and subsequent long-term exposure to metasomatizing fluids.

Understanding chemical, isotopic, and lithological variability with the lithospheric mantle has been archived through studies of spinel and garnet facies mantle xenoliths, tectonically exhumed outcrops such as massifs and ophiolites, and abyssal peridotites. These samples are advantageous because they can generally be considered direct representations of the upper mantle with relatively minimal post-emplacement alteration. Accessing the lower mantle is not as straight forward and studies of this mantle reservoir are achieved through examination of "hotspot" volcanics. Hotspots are observed in a wide range of environments, within continental and oceanic plates, along spreading ridges, passive oceanic-continental margins, and in close proximity to subduction zones. The origin of hotspots is uncertain, possibly derived from thermal anomalies, mantle plumes, or chemical heterogeneity in the lower mantle. The general theory regarding the origin of hotspots suggests that material upwells from the deep mantle and impinges at the base of the lithosphere resulting in volcanic eruptions at the surface (e.g., Morgan, 1971). The geochemically distinct lavas erupted from hotspots have reveled chemically distinct endmembers within the lower mantle (e.g., Day et al., 2010; Halliday et al., 1995; Hofmann, 1988; Ireland et al., 2009) that, along with mid-ocean ridges, show that Earth's mantle is demonstrably heterogeneous despite convection, and recycling of the lithosphere since the onset of plate tectonics.

This thesis investigates the oceanic lithosphere, non-cratonic CLM, and hotspots using fundamental geochemical tools, major and trace elements for bulk rock and minerals, as well as the "HSE Re-Os toolbox," with a primary focus on processes and evolution of oceanic, non-cratonic CLM, and hotspot volcanism. Highly siderophile elements (HSE: Re, Pd, Pt, Ru, Ir, Os) and the Re-Os isotope system have been shown to be an effective constraint for understanding mantle differentiation, partial melting, melt-refertilization, and crustal contamination processes in mafic and ultramafic systems (Day, 2013; Rehkamper et al., 1999). In contrast to lithophile element behavior, the HSE have a strong affinity for Fe and in systems lacking metallic phases, sulfides. Experiments have shown the metal/silicate bulk partition coefficients for HSE can vary from 10^3 to 10^7 at a broad range of pressures from ~1 to 18 GPa (Day, 2013; Mann et al., 2012; Mungall & Brenan, 2014; Peach et al., 1990; Peach et al., 1994). In addition to siderophile characteristics, the HSE display contrasting behavior during partial melting with Re + palladium platinum group elements (PPGE = Pd, Pt) showing moderately incompatible behavior and iridium platinum group elements (IPGE = Ru, Ir, Os) showing compatible behavior (e.g., Barnes et al., 1985; Luguet et al., 2007; Pearson et al., 2004). Unlike lithophile elements, the primary control on HSE distribution during partial melting is the presence of early crystalizing sulfide phases (Luguet et al., 2007). These phases tend to preserve primary partial melt signature and are generally resistant to low degree melt-rock reactions metasomatic processes that frequently occur during and after magma storage and eruption.

The Re-Os isotope system has shown utility in providing model age constraints for partial melting events and providing an indication of melt-rock contamination, particularly when complimented with HSE abundances. The parent isotope to ^{187}Os is ^{187}Re (^{187}Re – ^{187}Os + β-; λ = 1.6668×10^{-11}) with a half-life of ~42 Ga (Shirey & Walker, 1998). Throughout the following

chapters Os isotopes will be reported as a ratio normalized to ^{188}Os (e.g., $^{187}Os/^{188}Os$) or as a percent difference between a sample and the average chondritic composition, which is γ_{Os}, and is defined as: $\gamma_{Os} = ([^{187}Os/^{188}Os_{sample} / {}^{187}Os/^{188}Os_{chondrite}] - 1) \times 100$. Here, positive values are considered radiogenic and represent the addition of ^{187}Re and subsequent ingrowth of ^{187}Os, whereas negative values are non-radiogenic and represent the removal of ^{187}Re. Reported ratios of $^{187}Os/^{188}Os$ that exceed the average primitive mantle value of 0.1296 (Meisel et al., 2001) are also considered radiogenic and imply a similar interpretation. Osmium isotopic ratios can also be expressed as a Re depletion model age or T_{RD}, where T_{RD} is defined as: $T_{RD} = 1/\lambda \times \ln\{([^{187}Os/^{188}Os_{chondrite} - {}^{187}Os/^{188}Os_{sample}] / [^{187}Re/^{188}Os_{chondrite}]) + 1\}$. The Re depletion model age can be particularly useful for constraining the minimum time of a melt depletion event for mantle residues. A key assumption when interpreting T_{RD} model ages is no ingrowth from ^{187}Re since the most recent melt depletion event. Osmium concentration is often interpreted in conjunction with $^{187}Os/^{188}Os$. Previous studies have definitively shown that samples with low Os concentration, below 50 ng/g, are highly susceptible to crustal or lithospheric contamination (Day, 2013; Marcantonio et al., 1995; Simon et al., 2008; Widom et al., 1999). Given Os is highly compatible in the mantle compared to Re, there are significant differences in Re/Os between the primitive mantle, non-cratonic CLM, and continental and oceanic crust (Becker et al., 2006; Walker et al., 1989). Over long time scales this results in substantial $^{187}Os/^{188}Os$ variations in the crust ($^{187}Os/^{188}Os > 1$; Peucker-Ehrenbrink and Jahn (2001)) versus the mantle ($^{187}Os/^{188}Os < 0.13$; Day et al. (2017), Luguet and Reisberg (2016), Rudnick and Lee (2002)). Thus, samples with an initial low Os concentration are susceptible to overprinting from crustal reservoirs with elevated $^{187}Os/^{188}Os$. This effective tracer of contamination is used extensively in Chapters 3 through 5 (**Figure 1.1**). The following chapters will utilize the "HSE Re-Os isotope toolbox" to assess

processes of crust-mantle interaction, degree and extent of partial melting, crystal-liquid fractionation, and to model the composition of parent melts. These are fundamental factors for interpretation of mantle processes and determining the origin of mantle melts.

1.1 Outline

Chapter 2 examines the petrogenesis and evolution of spinel peridotite xenoliths dredged from the Ferrel Seamount off the west coast of Baja California, Mexico (**Figure 1.1**) and offers a new model for the formation of non-cratonic continental lithospheric mantle. Correlations between melt depletion indicators, $^{187}Os/^{188}Os$, and HSE show evidence that the xenoliths are ancient depleted oceanic lithosphere from the abandoned Pacific-Farallon ridge. Bulk-rock and clinopyroxene compositions show at least two episodes of melt-refertilization, one from melt rock reaction processes at the active spreading ridge and the later from alkali-basalt refertilization from the Ferrel Seamount itself. The low degree refertilization observed in these peridotite xenoliths is consistent with other non-cratonic peridotite xenoliths, particularly from localities in the western United States. The highly melt-depleted xenoliths with evidence of MORB-melt and alkali-melt refertilization suggest the oceanic lithosphere was rafted onto the Baja-Guadalupe continental margin through the process of a "ridge jump." Through this tectonic process and continual low degree melt refertilization these peridotites provide the frame work of a model for the evolution of non-cratonic continental lithospheric mantle from oceanic lithosphere. This manuscript was published in Geochemistry Geophysics and Geosystems in October of 2022.

Next, Chapter 3 investigates processes affecting the isotopically distinct Loa and Kea trends of the Hawaiian Archipelago lavas (**Figure 1.1**). The Loa and Kea trends are geographically

subparallel linear, isotopically distinct lavas that have been identified from Oahu to the Island of Hawai'i. These trends are best defined by the Rb-Sr, Sm-Nd, and U-Th-Pb isotopic systems with the southern Loa trend having more radiogenic values than the northern Kea trend. New HSE and Re-Os isotopic data presented in this chapter show that mafic and ultramafic cumulate xenoliths from the Loa trend have more radiogenic $^{187}Os/^{188}Os$ than Kea trend counterparts however, no distinction is observed in absolute or relative HSE abundances. This distinction implies the Loa trend has a long-lived enrichment in large ion lithophile elements and Re/Os relative to the Kea trend that, in order to produce the isotopic disparities, must be a unique characteristic of the Loa source. In spite of this implication, new geophysical research has revealed a potential plumbing system that links two volcanoes, Mauna Loa and Kilauea, from the opposing trends. This new insight into magma transit beneath Hawai'i suggests possible mixing between the two compositionally distinct trends. This chapter uses the new Os-isotopic data to test the Loa and Kea trend mixing hypothesis.

Chapter 4 shifts focus from the Pacific to the Atlantic lithosphere with a project focused on the Canary Islands. Here, mantle and cumulate xenolith samples from El Hierro, La Palma, and Tenerife, and basanite, basalt, and picrite samples from the former as well as Lanzarote and Gran Canaria (**Figure 1.1**) are analyzed for major and trace elements, HSE, and Os isotopes. Osmium isotopic compositions of the mantle xenoliths are consistent with an Atlantic lithosphere protolith. Relative trace element abundances for the lavas show distinct HIMU characteristics which suggests an ancient, recycled slab endmember in the source. However, the high variability of HSE composition in an estimated parent melt suggest multiple sources and/or mixing of parent magmas between islands. New $^{187}Os/^{188}Os$ data presented in this study are then used to further evaluate

potential mixing and contamination, showing possible addition of lithosphere ± lower crust and sediment.

Finally, Chapter 5 transitions from the oceanic lithosphere to the non-cratonic continental lithosphere east of the Sierra Nevada Mountains in the Owens Valley of California (**Figure 1.1**). This is a fault bounded valley with a right lateral to normal sense of shear which defines the westernmost basin of the Basin and Range geomorphic province. Within the Owens Valley is a series of monogenic vents known as the Big Pine Volcanic Field (BPVF). Among the numerous scoria cones and lava flows that comprise this volcanic field is the Papoose Canyon which is notable for an abundance of pyroxenitic and peridotic cumulate xenoliths. This chapter presents new major- and trace-element data for both whole-rock and mineral separates as well as whole-rock HSE and Os isotopic data from a suit of pyroxenite and peridotite xenoliths. These new data offer insights into the range of equilibration depth for clinopyroxenes and orthopyroxenes, the oxidation state of olivines, and the melting source of the BPVF. In addition, $^{187}Os/^{188}Os$ and HSE fractionation ratios provide some constraint on the degree of crustal contamination that has impacted the Papoose Canyon lava sequence.

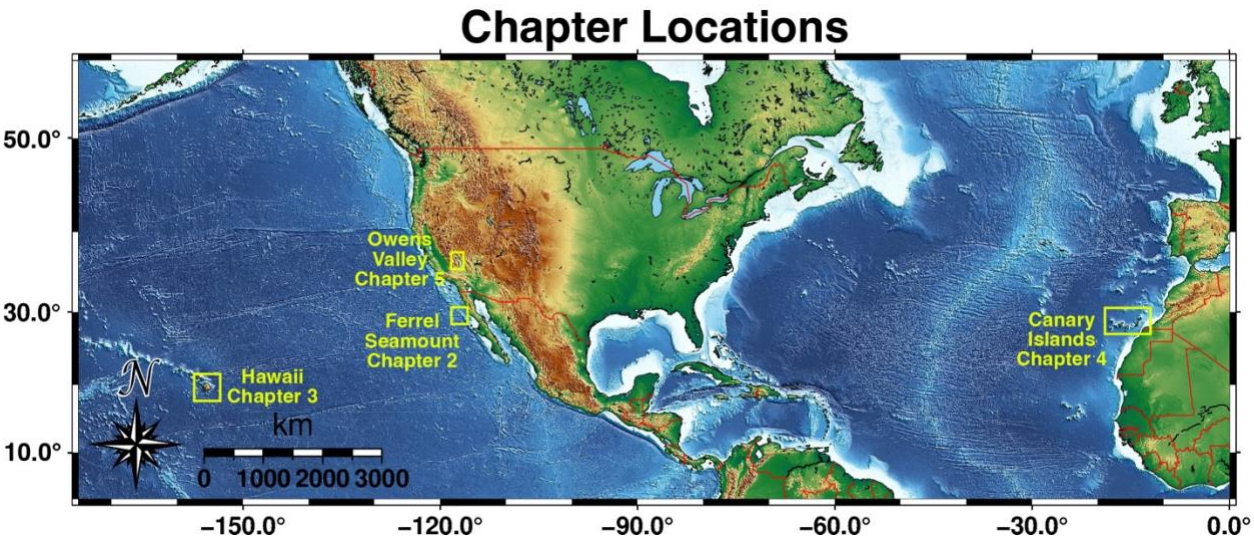

Figure 1.1 Study site locations for chapters 2 through 5.

CHAPTER 2 Generation of Continental Lithospheric Mantle by Tectonic Isolation of Oceanic Plate

2.1 Abstract

Continental formation models invoke subduction or plume-related processes to create the buoyant, refractory character of continental lithospheric mantle (CLM). From similarities in melt depletion, major element composition, modal clinopyroxene, and Os isotope systematics it has been proposed that oceanic mantle lithosphere is the likely protolith to non-cratonic CLM, however, a direct link between the two has been difficult to ascertain. Using dredged mantle peridotite xenoliths from the Ferrel Seamount, off the west coast of Baja California, Mexico, we show that tectonic isolation of an oceanic plate may lead to formation of non-cratonic CLM. Ferrel xenoliths are coarse-grained spinel lherzolite, or rare harzburgite. Bulk-rock and clinopyroxene trace element compositions reveal two-stages of melt refertilization following melt depletion, with infiltration by mid-ocean ridge basalt-type melts, followed by melt addition from host alkali basalt. Melt depletion correlations with $^{187}Os/^{188}Os$ and highly siderophile element abundances indicate preserved melt depletion and refertilization processes are ancient. From these observations, the Ferrel xenoliths represent lithosphere from the abandoned Pacific-Farallon ridge. The history of melt depletion, followed by MORB-melt refertilization is consistent with the peridotites representing oceanic mantle lithosphere that was subsequently incorporated into the Baja-Guadalupe microplate during 'ridge jump'. These peridotites demonstrate that isolation of oceanic lithosphere that is rafted onto a continental margin provides a viable means for producing non-cratonic CLM. We suggest that continuation of late-stage, low degree melt refertilization may

provide a link between oceanic lithosphere and non-cratonic CLM and propose a tectonic model to preserve and facilitate this continued evolution.

2.2 Introduction

The formation of thick, geologically stable non-cratonic continental lithospheric mantle is partially responsible for the oceanic-continental crustal dichotomy and is fundamental for the formation of continents beyond the cratons (Pearson & Wittig 2008, Pearson et al., 2021). Despite the relative importance of continental lithospheric mantle, the mechanisms of its formation remain poorly understood. Several hypotheses have been outlined, all involving substantial melt extraction of mantle residues either by deep plume melting (Boyd, 1989; Griffin et al., 1998), shallow melting and subduction (e.g. Schulze, 1986; Canil & Wei, 1992), or by lithospheric melt extraction prior to subduction stacking (Canil, 2004; Lee, 2006; Simon et al., 2008). Furthermore, the mechanisms by which continental lithosphere has formed may have changed with time, as mantle potential temperatures have decreased since the Archean (e.g., Nisbet et al., 1993), and progressive Wilson cycles have occurred (Shirey & Richardson, 2011).

Understanding of the nature of the non-cratonic continental lithospheric mantle (CLM) has been predominantly driven by studies of mantle xenolith suites, where peridotite nodules are entrained in alkali basalts, basanites and other low degree partial melts, during magma ascent to the surface (e.g., Nixon, 1987). In these cases, melt depletion trends can be well-preserved in peridotite xenolith suites (e.g., Frey & Green, 1974; Frey & Prinz, 1978; Jagoutz, 1988; Galer & O'Nions, 1989) in spite of metasomatic effects. Oceanic lithosphere shows melt depletion trends with variable degrees of refertilization, but the effects of most melt refertilization can be decoupled from primary melt depletion trends (Niu, 2004; Day et al., 2017). In contrast, the CLM has a

prolonged history of exposure to variable degrees of depletion and refertilization (Galer & O'Nions, 1989; Pearson et al., 1995). The different melt depletion/refertilization histories of CLM and oceanic mantle lithosphere can generally be attributed to the isolation of CLM from subduction, removing it from recycling and mixing processes in the mantle.

Abyssal peridotites are compositionally distinct from non-cratonic CLM peridotites, but broad overlap of the two mantle domains suggests a common link, with CLM formed from upper mantle materials over Earth history. For example, globally, CLM is often indistinguishable from oceanic lithosphere in terms of degree of melt extraction, bulk rock and mineral Mg/Fe ratios, and stabilization model ages (Pearson et al., 2004 and *Supplementary Information*). This is in strong contrast with on-craton mantle xenoliths that are highly depleted with Proterozoic or Archean model ages. These similarities have led some authors to postulate oceanic lithosphere as a potential protolith for the non-cratonic CLM (i.e., Peslier et al., 2000; Harvey et al., 2012). While similarities exist, differences in fundamental constituents such as major element composition, and modal clinopyroxene content require additional processes in their genesis. Abyssal peridotites are typically represented by spinel facies lherzolites and harzburgites that have experienced $\leq 20\%$ melt extraction, with long-term stability compared to oceanic lithosphere being a key feature of CLM (Pearson et al., 1995; Lassiter et al., 2014). The distinction in age also implies the older CLM has been exposed to refertilization from percolating melts for a longer period than for abyssal peridotites. If CLM can form from oceanic lithosphere in the present-day it must be tectonically isolated to a continental margin, as the clear majority of oceanic lithosphere is recycled within subduction zones (e.g., Stern, 2002).

Here, we consider the geochemical and tectonic implications of spinel peridotite xenoliths dredged from the Ferrel Seamount offshore Baja California for the formation of recent CLM. The

xenoliths come from an isolated microplate formed during the subduction to rift transition and southern migration of the Rivera triple junction, ~10 to ~14 Ma, along the Pacific and North American plate boundary (Lonsdale, 1991). New major and trace element abundance data are compared to bulk rock and mineral highly siderophile element concentrations (HSE; Os, Ir, Ru, Pt, Pd, Re) and $^{187}Os/^{188}Os$ data of non-cratonic CLM-derived xenoliths from the southwest USA (Dish Hill, CA and Kilbourne Hole, NM; Armytage et al., 2014; Harvey et al., 2012). Effects of refertilization on young, buoyant oceanic lithosphere are examined and compared to the known geochemistry of peridotites at CLM localities. The results of our study reveal the melt depletion and refertilization process on the abandoned Pacific-Farallon ridge, confirming the conclusions of previous studies of HSE abundance and $^{187}Os/^{188}Os$ systematics for abyssal peridotites (Day et al., 2017; Warren, 2016; Harvey et al., 2006; Brandon et al., 2000), and imply an oceanic lithosphere protolith. Comparison of Ferrel Seamount with western United States xenolith suites indicates that formation of some recent non-cratonic CLM may have begun when the oceanic fragment was 'welded' to the over-riding plate after ridge jump.

2.3 Geological Setting and Samples

The Ferrel Seamount (29° 33.90N, 117° 15.60W) is located off the west coast of Baja Mexico, between Guadalupe Island to the west and the San Quintin volcanic field to the east. The seamount was constructed from mafic to intermediate alkali lavas and intrusive units that were probably emplaced at an abandoned Pacific-Cocos spreading center (Lonsdale, 1991) (**Figure 2.1**). The Ferrel Seamount lies on the western boundary of a section of crust formed at the abandoned East Pacific Rise and the southern boundary of an associated transform fault, the Guadalupe Fracture Zone. The north-northwestern boundary abuts the southern extent of the Patton

Escarpment. Although tectonic deformation from the southern Continental Borderlands, as well as terrigenous sediment partially obscure the magnetic anomalies proximal to the Ferrel Seamount, resolution of Chron 5AC provides an estimated crustal age of ~10 to ~14 Ma (Müller et al., 2008). Samples investigated here were collected during the WOBA-3D dredge from the Ferrel Seamount in October 2012, aboard R/V Melville. The WOBA-3D dredge recovered >200 kg of material, including alkali basalt lavas containing fresh spinel peridotite xenoliths and at least one gabbro xenolith, at an average water depth of 800 m (**Figure 2.1**).

2.4 Analytical Methods

Fourteen spinel peridotite xenoliths, one gabbro xenolith, and three lava samples were selected from a larger sample suite. The xenoliths are roughly elliptical ranging in size from ~10 to 16 cm across the long axis and ~5 to 8 cm across the short axis with weights ranging from ~0.5 to ~10 kg. Major-element mineral chemistry was determined with a *Cameca SX-100* electron probe micro analyzer at the University of Tennessee. Modal abundances were determined through photo analysis of thin sections and cut slabs as well as quantitatively based on mineral major element compositions using the constrained least-squares method described in Albarède (1995). Trace-element abundances in minerals were obtained using a *New Wave Research UP213* (213 nm) laser-ablation system coupled to a *ThermoScientific* iCAPQ c ICP-MS at the *Scripps Isotope Geochemistry Laboratory (SIGL)* with standardization performed relative to standard reference material glasses NIST 610, BCR-2G and BHVO-2G for silicate minerals and MASS-1 sulfide and iron meteorite metals for sulfides (Jochum et al., 2005).

For whole-rock compositions, powders were measured for major element compositions by X-ray fluorescence (XRF) at Franklin and Marshall College using a *PW 2404 PANalytical* XRF

vacuum spectrometer. Trace-element abundances were determined at the *SIGL* using a *ThermoScientific* iCAPQ c ICP-MS. Reproducibility of the reference materials was generally better than 5% (RSD) for basaltic and peridotite standards. Osmium isotopes and HSE (Re, Pd, Pt, Ru, Ir, Os) abundances were determined using isotope dilution at the *SIGL*. Osmium was triply extracted using CCl_4, back-extracted into HBr and purified by micro-distillation. Rhenium and platinum group elements were recovered and purified from the residual solutions by anion exchange separation, and then analyzed on a *Thermo Scientific* iCAPQ c ICP-MS. Isotopic compositions of Os were measured in negative-ions using a *ThermoScientific* Triton thermal ionization mass spectrometer. Total procedural blanks typically represented <5% of total analyte with the exception of Re and Pd, which were <16% in the worst cases. Detailed analytical methods are provided in the *Supplementary Information* accompanying this article.

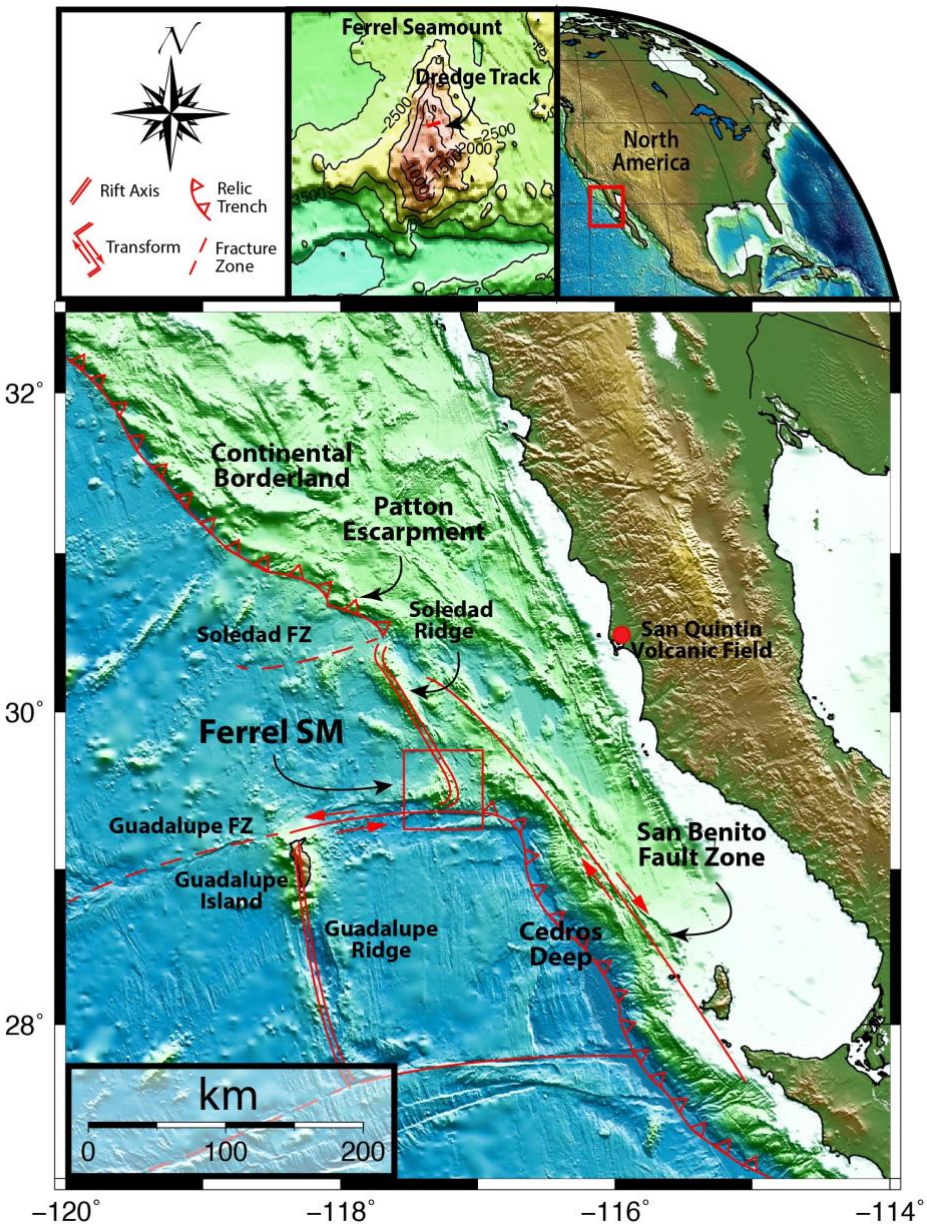

Figure 2.1 Regional bathymetry and elevation model map for offshore northern Baja California, Mexico. Highlighted is the Ferrel Seamount (topographic map, 500 m intervals) with the red box showing the location of the WOBA-3D dredge track. This locality sits atop an abandoned section of East Pacific/Farallon Rise, known as the Soledad Ridge (Lonsdale, 1991).

2.5 Results

2.5.1 Textures, modal mineralogy and mineral compositions

Peridotites from the Ferrel Seamount have coarse, equigranular textures and are dominantly spinel lherzolites (43.7 to 68.2 modal % olivine; 17.5 to 40.8 modal % orthopyroxene; 20.0 to 8.7 modal % clinopyroxene; 0.6 to 3.2 modal % spinel), with one spinel harzburgite, WOBA-3D-5 (68.8 modal % olivine; 24.3 modal % orthopyroxene; 3.2 modal % clinopyroxene; 3.8 modal % spinel). Using the constrained least-squares approach of Albarede (1995) yields tighter ranges of olivine and pyroxene modal mineralogy, and slightly overestimates spinel relative to the optical mode (60.8 to 64.3 modal % olivine; 21.3 to 26.7 modal % orthopyroxene; 9.3 to 11.2 modal % clinopyroxene; 1.6 to 3.5 modal % spinel). The disparity between the two methods is likely a result of disequilibrium between the pyroxene phases, where the quantitative model assumes equilibrium between the two. Both intra-granular Type 1 and interstitial Type 2 sulfide phases, as defined by Luguet & Pearson, 2019, are represented in the sample set. Interstitial Type 2 elongated skeletal grains are less than 10 microns across, while Type 1 have intra-granular rounded to sub-rounded sulfide grains, hosted primarily in orthopyroxene. The extent of melt glass infiltration is limited to the outer periphery of xenolith samples, where little evidence of melt reaction with adjacent minerals was observed. Olivine compositions from the xenoliths have Mg-numbers from 84.7 to 91.8. Orthopyroxene has enstatite composition ($En_{0.888\pm0.008}Wo_{0.017\pm0.003}Fs_{0.095\pm0.007}$), with Mg-numbers from 89.2 to 91.9. Clinopyroxene is homogeneous Cr-diopside ($En_{0.486\pm0.006}\,Wo_{0.467\pm0.009}\,Fs_{0.047\pm0.004}$), with Cr_2O_3 from 0.7 to 1.3 wt. %, and Mg-numbers between 91.2 and 89.9. Spinel Mg-numbers from 66.0 to 73.5 (70.6 ±2.3) and Cr-numbers from 18 to 40.3 (25.2 ±5.7), falling within the compositional field of abyssal

peridotites, (**Figure 2.2, Table S2.5**) and corresponding to between 7 and 15% melt depletion using the method of Hellebrand (2002), with an average of 10 ± 2%.

Orthopyroxene grains in the Ferrel Seamount samples typically have lower absolute abundances (<0.1 × PM) of the incompatible trace elements than depleted mid ocean ridge basalt mantle (DMM) estimates (Workman & Hart, 2005), but they have systematically higher La, Ba and Rb (**Figure 2.3a)**. Like DMM orthopyroxene compositions, and orthopyroxene grains measured from the Gakkel Ridge (D'Errico et al., 2016), Ferrel Seamount xenoliths contain orthopyroxene grains with large Zr and Hf enrichments relative to elements of similar incompatibility. Unlike DMM, however, the Ferrel Seamount samples do not have prominent Nb or Ta enrichments in orthopyroxene. Clinopyroxene grains generally have lower abundances of the incompatible trace elements (<1 × PM) than DMM (**Figure 2.3b**). The patterns for clinopyroxene exhibit a notable variation in the LREE, where La/Yb_{PM} and Sm/Yb_{PM} span a range of values from 0.06 to 1.6 and 0.06 to 1.7, respectively.

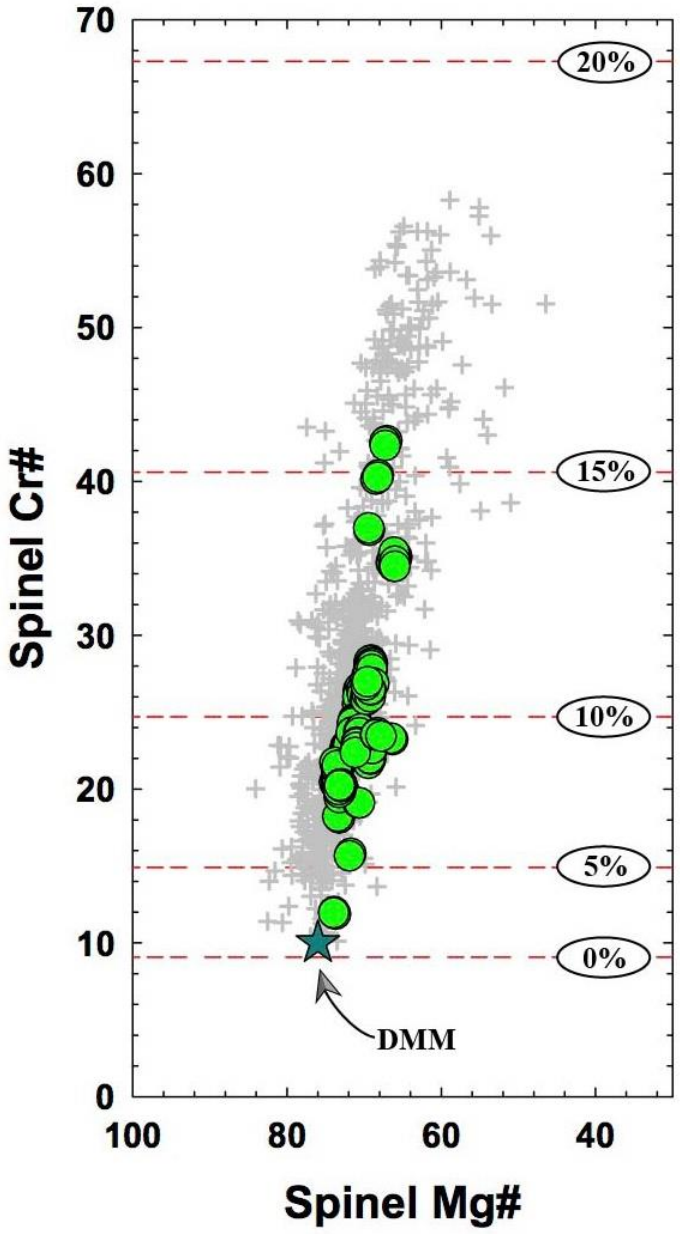

Figure 2.2 Spinel Cr# [(Cr/Cr + Al)) × 100] against Spinel Mg# [(Mg/Mg + Fe)) × 100] for Ferrel Seamount peridotites (green circles) versus a 'global field' of abyssal peridotites (grey crosses; from Warren, 2016 and references therein). Depleted MORB Mantle (blue star) from Workman & Hart (2005). Melt removal lines (red dashed lines) are from Hellebrand et al. (2001).

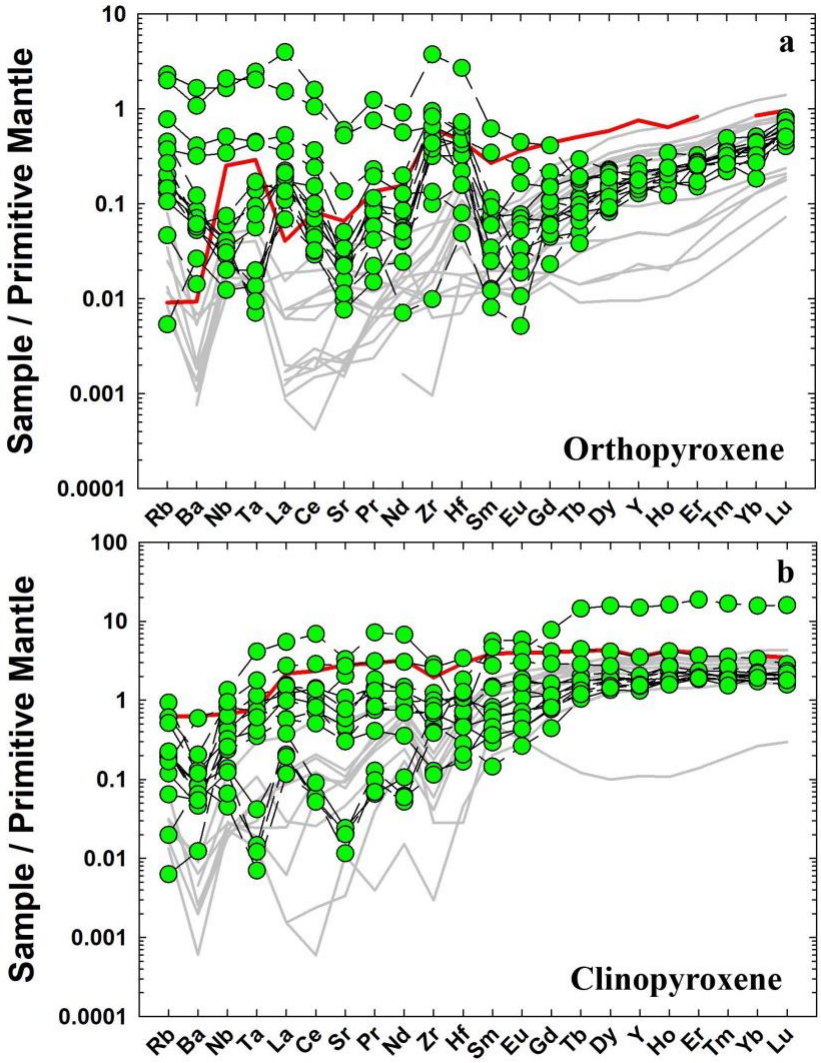

Figure 2.3 Primitive mantle normalized trace element patterns for (a) orthopyroxene and (b) clinopyroxene grains (green circles with dashed lines) from Ferrel Seamount peridotites. Depleted MORB Mantle (thick red line) (Workman & Hart, 2005), and (grey lines) Gakkel Ridge (a) orthopyroxene, and (b) clinopyroxene grains from D'Errico et al., 2016 are shown for comparison. Primitive mantle normalization is given in the Supplementary Information. Gakkel Ridge (D'Errico et al., 2016), Ferrel Seamount xenoliths contain orthopyroxene grains with large Zr and Hf enrichments relative to elements of similar incompatibility. Unlike DMM, however, the Ferrel Seamount samples do not have prominent Nb or Ta enrichments in orthopyroxene. Clinopyroxene grains generally have lower abundances of the incompatible trace elements (<1 × PM) than DMM (**Figure 2.3b**). The patterns for clinopyroxene exhibit a notable variation in the LREE, where La/Yb_{PM} and Sm/Yb_{PM} span a range of values from 0.06 to 1.6 and 0.06 to 1.7, respectively.

2.5.2 Bulk-rock major and trace element compositions

Ferrel Seamount xenoliths are generally extremely fresh peridotites characterized by low bulk-rock Al_2O_3 (1.06 to 2.59 wt. %) and CaO contents (0.75 to 3.03 wt. %). The MgO-Al_2O_3-SiO_2 systematics of the xenoliths indicate greater depletion than non-cratonic CLM xenolith suites, such as Dish Hill, or Kilbourne Hole (**Figure 2.4**), plotting between the mean composition of cratonic and non-cratonic peridotite xenoliths (Pearson et al., 2004). Magnesium-numbers for samples range between 88 and 90.7, within the off-craton range (Pearson et al., 2004). Ophiolitic terranes may have formed in supra-subduction settings, and so likely experienced modification from slab de-watering (i.e., Snortum & Day, 2020; Choi et al., 2008) thus, we limit the comparison to peridotite xenoliths. Using the two-pyroxene and calcium orthopyroxene thermobarometers of Brey and Kohler (1990), equilibration temperatures range from 887-1061°C and 932-1069°C respectively, at a reference pressure of 2 GPa, at the extent of spinel stability. Average log fO_2 Δ QFM was estimated in a range of +0.4 to +1.4 for the sample set, at the upper range of abyssal peridotites. The peridotite xenoliths have relatively homogeneous abundances of Cr (2500 ±300 ppm), Ni (2100 ±140 ppm), Ti (220 ±90 ppm), Li (1.0 ±0.2 ppm), Sc (11 ±3 ppm), V (52 ±12 ppm), Co (99 ±5 ppm), Cu (5 ±3 ppm), and Zn (33 ±4 ppm). The xenoliths show a wide range in both absolute (~0.06 to 1 × PM) and relative (La/Yb = 0.7 to 3.7) incompatible trace element abundances, with relative enrichments in Ba, U, Zr and Hf, and relative depletions in Pb and K (**Figure S2.1**). Samples WOBA-3D-10, and -17 both have prominent Zr and Hf enrichments relative to the sample suite; this is likely the effect of trace-element enriched infiltrated glass observed in the two samples (**Figure S2.1 and S2.3**).

The host lavas are alkali basalts with high MgO (12.3 ±1.2 wt.%) and are incompatible element enriched patterns (~4-100 × primitive mantle). A single gabbro xenolith has a composition similar to mid-oceanic ridge gabbros (Niu & O'Hara, 2003) with high Al_2O_3 and CaO and flat primitive mantle normalized incompatible trace element pattern (**Figure S2.2**, see *Supplementary Information* for detailed descriptions).

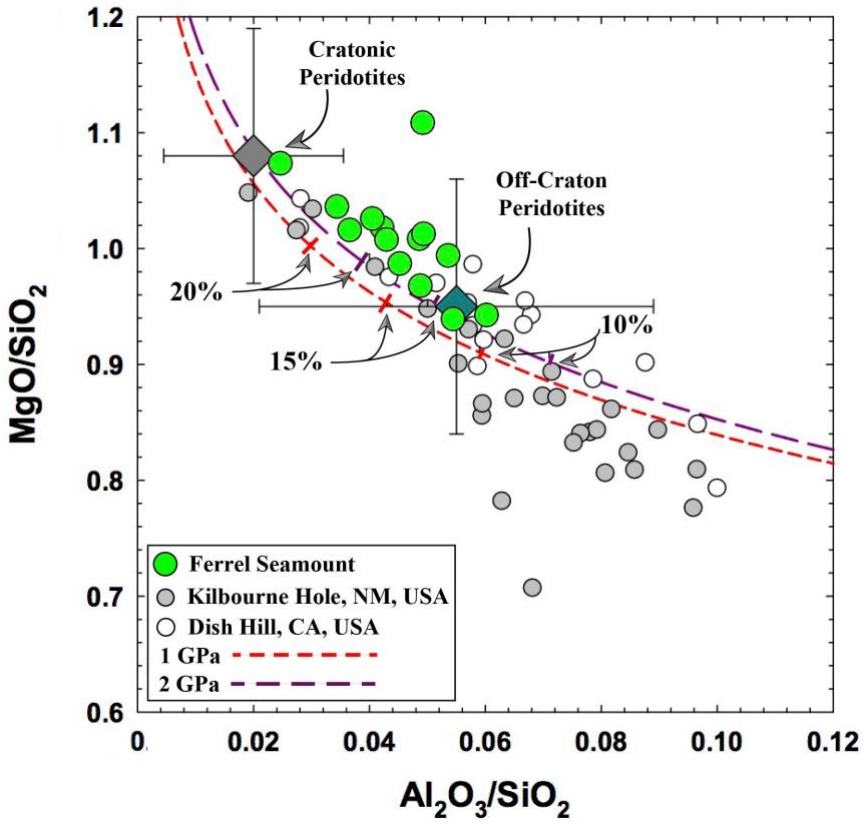

Figure 2.4 Terrestrial Si-Al-Mg array diagram from Jagoutz et al. (1979), with melting curves at 1 and 2 GPa from Herzberg (2004). Filled diamonds represent the average compositions of cratonic and non-cratonic peridotites (Pearson et al., 2004). Calculated melt depletion percentages (bold tick marks) are annotated on the figure.

2.5.3 Highly Siderophile Element abundances and $^{187}Os/^{188}Os$ ratios

Highly siderophile element abundances (HSE: Re, Pd, Pt, Ru, Ir, Os) for Ferrel Seamount peridotites are similar to those of East Pacific Rise abyssal peridotites (Rehkamper et al., 1999; Paquet et al., 2022), with variable depletions in Re and Pd relative to Pt, Ru, Ir, and Os (**Table 2.1**). Absolute and relative abundances of Os, Ir, and Ru (Os/Ir = 0.86 ±0.19; Ru/Ir = 2.15 ±0.29) from the Ferrel Seamount are consistently depleted relative to Primitive Mantle (PM) estimates (Day et al., 2017). In contrast, Pd and Pt abundances exhibit considerable dispersion (Pd/Ir = 1.42 ±0.68; Pt/Ir = 2.01 ±0.64), with absolute Pd abundances that range from ~0.04 – 1.2 × PM. Absolute abundances of Re span a wider range of depleted values (0.04 – 0.9 × PM) and produce a broad variation or 'fanning' pattern (Re/Ir = 0.03 ±0.02) (**Figure 2.5**). The HSE are poorly correlated with bulk rock melt depletion indicators (i.e., MgO, Al_2O_3), except for Re, which approximately co-varies with MgO ($r^2 = 0.55$).

The $^{187}Os/^{188}Os$ ratios measured in the bulk-rock peridotite xenoliths range from 0.1170 to 0.1326, consistent with the range in $^{187}Os/^{188}Os$ for off-craton xenoliths from the western United States (Meisel et al., 2001; Harvey et al., 2012; Armytage et al., 2014), and corresponds to averages for abyssal peridotites proposed by Lassiter et al. (2014) (0.1263 ±0.0099, 2 SD) and Day et al. (2017) (0.1275 ±0.0153, 2 SD). Applying the Os isotope ratios of Ferrel Seamount peridotites to model ages of Re depletion gives an average age of 0.73 ±0.49 Ga, with individual T_{RD} ages up to 1.8 Ga. These model ages correspond with the distribution of Nd model ages for abyssal peridotites proposed by Mallick et al. (2014) (<2.4 Ga). The sample suite shows a rough correlation in $^{187}Re/^{188}Os$-$^{187}Os/^{188}Os$ space but does not define an isochronous relationship, whereas $^{187}Re/^{188}Os$ and $^{187}Os/^{188}Os$ ratios correlate negatively with bulk rock MgO ($r^2 = 0.64$; 0.51), and positively with bulk rock Al_2O_3 ($r^2 = 0.62$; 0.48) (**Figure S2.6**).

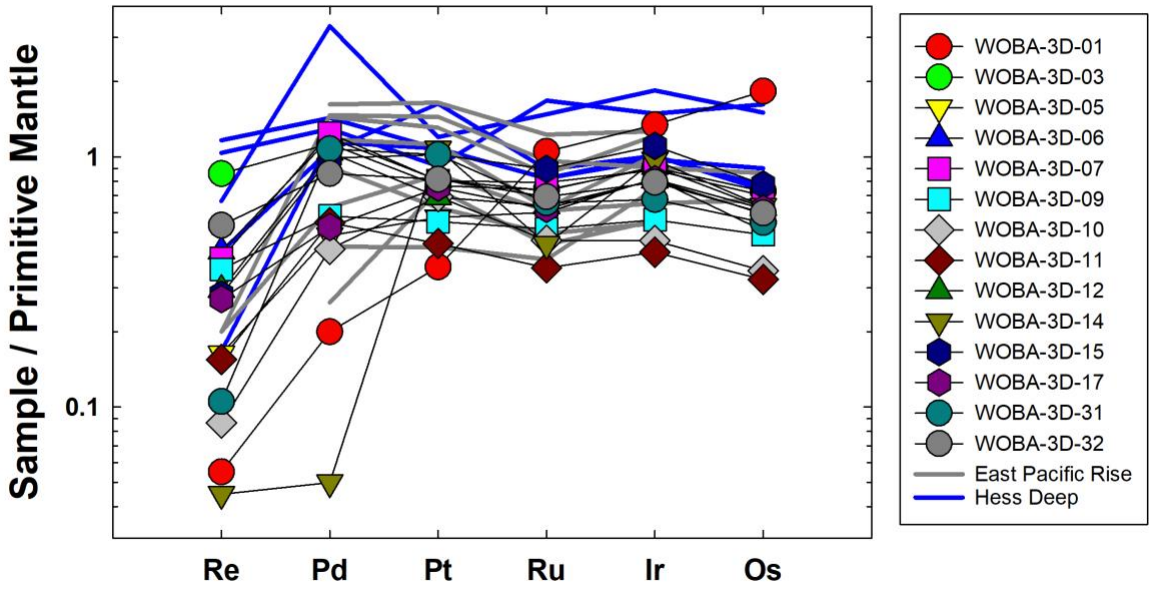

Figure 2.5 Primitive Mantle normalized highly siderophile element patterns for Ferrel Seamount peridotites, and published data from the East Pacific Rise (heavy grey lines) (Rehkamper et al., 1999; Snow & Schmidt, 1998) and Hess Deep (heavy blue lines) (Paquet et al., 2022). Primitive mantle composition is from Day et al. (2017).

Table 2.1 Whole-rock Re-Os isotope and highly siderophile element (ng g^{-1}) abundances and selected bulk rock and olivine data for Ferrel Seamount peridotites.

	MgO (wt.%)	Al_2O_3 (wt.%)	Olivine (Fo)	2s	*F* Spinel	Re
WOBA 3D-1	46.2	1.1	91.6	0.1	15	0.017
WOBA 3D-3	41.1	2.4	89.8	0.04	8	0.257
WOBA 3D-5	43.0	1.8	89.1	0.1	7	0.049
WOBA 3D-6	42.6	2.0	90.2	0.1	11	0.126
WOBA 3D-7	42.5	2.3	89.8	0.1	8	0.118
WOBA 3D-9	42.7	1.8	90.0	0.1	9	0.107
WOBA 3D-10	45.3	2.0	89.0	4.2	10	0.026
WOBA 3D-11	42.1	2.1	89.9	0.1	9	0.046
WOBA 3D-12	44.0	1.5	90.1	0.1	11	0.088
WOBA 3D-14	43.6	1.6	89.4	0.1	14	0.013
WOBA 3D-15	42.8	2.1	90.2	0.1	11	0.085
WOBA 3D-17	42.9	2.1	90.1	0.1	11	0.081
WOBA 3D-31	43.6	1.7	90.1	0.1	8	0.032
WOBA 3D-32	40.5	2.6	89.7	0.1	9	0.160
MUH-1 RED						0.221
n = 2, 2σ						0.001
OKUM RED						0.538
n = 2, 2σ						0.008

	Pd	Pt	Ru	Ir	Os	Pd/Ir	Ru/Ir
WOBA 3D-1	1.06	2.73	8.31	4.84	7.15	0.56	1.16
WOBA 3D-3	5.99	5.76	5.84	3.26	2.84	1.77	2.06
WOBA 3D-5	2.57	4.30	4.75	2.95	1.98	1.45	2.40
WOBA 3D-6	6.31	6.06	5.80	3.29	2.44	1.84	2.38
WOBA 3D-7	6.60	6.03	6.25	3.19	2.73	1.89	2.29
WOBA 3D-9	3.08	4.14	4.08	2.02	1.91	2.05	2.14
WOBA 3D-10	2.27	5.20	3.67	1.67	1.37	3.12	2.68
WOBA 3D-11	2.89	3.38	2.85	1.50	1.26	2.26	2.26
WOBA 3D-12	5.54	5.19	5.04	2.91	2.31	1.78	2.18
WOBA 3D-14	0.26	8.07	3.53	3.50	2.48	2.30	1.43
WOBA 3D-15	5.25	7.66	7.07	3.99	3.02	1.92	2.34
WOBA 3D-17	2.78	5.66	4.90	2.93	2.42	1.93	2.02
WOBA 3D-31	5.71	7.66	5.18	2.43	2.13	3.15	2.43
WOBA 3D-32	4.55	6.11	5.48	2.85	2.33	2.14	2.35

Table 2.1 Whole-rock Re-Os isotope and highly siderophile element (ng g^{-1}) abundances and selected bulk rock and olivine data for Ferrel Seamount peridotites. (Continued)

	Pd	Pt	Ru	Ir	Os	Pd/Ir	Ru/Ir
MUH-1 RED	10.3	10.1	7.93	4.05	5.17		
n = 2, 2σ	0.266	2.144	0.593	0.669	1.069		
OKUM RED	12.5	11.0	4.66	0.98	0.71		
n = 2, 2σ	0.003	0.044	0.010	0.061	0.034		

	$^{187}Re/^{188}Os$	2σ	$^{187}Os/^{188}Os$	2σ	T_{RD} (Ma)
WOBA 3D-1	0.0111	0.0002	0.11700	0.00006	1757
WOBA 3D-3	0.4366	0.0065	0.13056	0.00006	-
WOBA 3D-5	0.1192	0.0018	0.12208	0.00015	1054
WOBA 3D-6	0.2492	0.0037	0.13261	0.00011	-
WOBA 3D-7	0.2085	0.0031	0.12899	0.00011	86
WOBA 3D-9	0.2695	0.0040	0.12590	0.00010	522
WOBA 3D-10	0.0912	0.0014	0.12252	0.00070	993
WOBA 3D-11	0.1773	0.0027	0.12981	0.00010	-
WOBA 3D-12	0.1848	0.0028	0.12732	0.00015	321
WOBA 3D-14	0.0262	0.0004	0.12256	0.00014	987
WOBA 3D-15	0.1348	0.0020	0.12398	0.00008	790
WOBA 3D-17	0.1615	0.0024	0.12599	0.00015	508
WOBA 3D-31	0.0713	0.0011	0.12750	0.00008	297
WOBA 3D-32	0.3310	0.0050	0.13071	0.00010	-
MUH-1 RED			0.12644	0.00003	
n = 2, 2σ					
OKUM RED			0.2919	0.0066	
n = 2, 2σ					

TRD = Time of rhenium depletion age, calculated as: $1/\lambda$ x ln{([$^{187}Os/^{188}Os_{chondrite}$ – $^{187}Os/^{188}Os_{sample}$]/[$^{187}Re/^{188}Os_{chondrite}$])+1}

Note: TRD ages are generally relevant only to strongly melt-depleted, refractory harzburgites and are included here solely as points of comparison.

2.6 Discussion

The new data for Ferrel Seamount peridotites and their similarity to oceanic abyssal peridotites, along with the tectonic framework in which the xenoliths occur, after ridge jump and plate isolation, suggest a possible link between oceanic and continental lithospheric mantle. In the following discussion, we consider the possible effects of tectonic isolation, metasomatism, melt refertilization and melt depletion, ultimately establishing hypotheses for non-cratonic CLM formation.

2.6.1 Metasomatic processes affecting Ferrel Seamount peridotites

Metasomatism by melts of variable compositions is a common characteristic of abyssal peridotites (e.g., Warren, 2016; D'Errico et al., 2016). Notable geochemical evidence in the Ferrel Seamount peridotites are the elevated relative abundances of incompatible trace elements within whole-rock samples that are not reflected in clinopyroxene, the main carrier of the LREE in peridotites (**Figure S2.1, 2.6a, b**). Eight of the 14 peridotite samples have whole-rock $(La/Yb)_N > 1$ (WOBA-3D-1, -3, -5, -6, -10, -12, -17, -31) indicating that the LREE were added by interaction with migrating melts (e.g., Johnson et al., 1990). The remainder of the samples (WOBA-3D-7, -9, -11, -14. -15, -32) have U-shaped REE patterns with $(La/Yb)_N$ near unity, suggesting depletion of LREE–MREE followed by cryptic metasomatic addition, resulting in the enrichment of light REE relative to primitive mantle in the bulk rock.

LREE enrichments relative to the HREE in peridotites can only be achieved through reaction with small melt volumes (Hellebrand et al., 2002; D'Errico et al., 2016). To test this hypothesis on Ferrel Seamount peridotites samples we used a closed system equilibrium model starting with the most REE depleted Ferrel peridotite sample, WOBA-3D-14 and incrementally

added the alkali host rock composition ($(La/Yb)_N = 12.9 \pm 1$) (**Figure 2.7**). The results demonstrate that ~0.1% to 1.5% addition of this melt can approximate the REE range of the Ferrel Seamount peridotites. The LREE in whole-rock peridotites are therefore sensitive tracers of melt modification that are otherwise unrecognized from mineralogical or textural attributes in samples. Such cryptic metasomatism likely results from re-equilibration at mantle temperatures, consistent with both our results and those of previous studies (e.g., Harvey et al., 2012; Hellebrand et al., 2002; D'Errico et al., 2016).

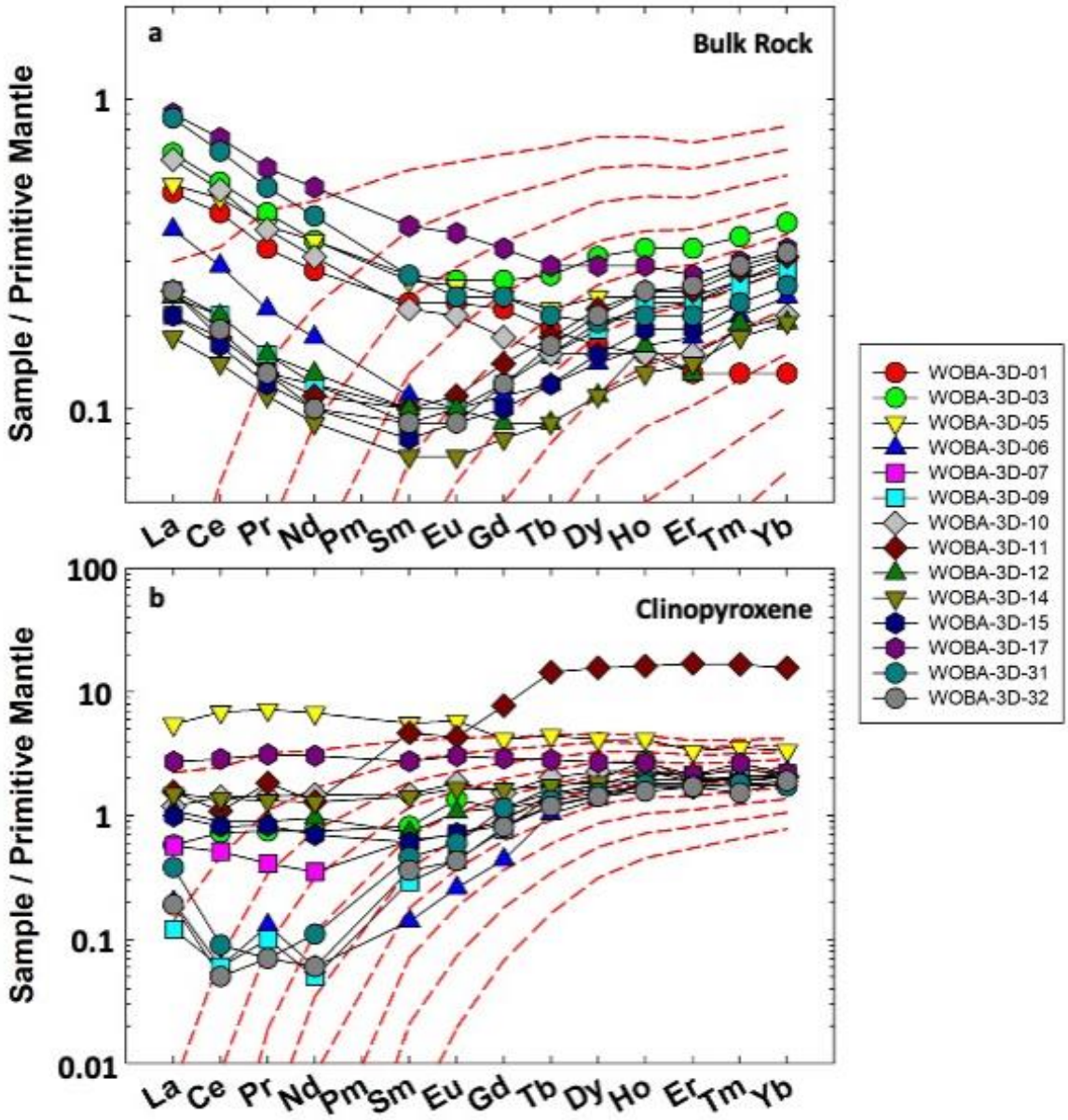

Figure 2.6 Primitive mantle normalized rare earth element patterns for Ferrel peridotites, (a) bulk rock, (b) average clinopyroxene. Red dashed lines indicate 2% melt increments (0% - 18%) for non-modal fractional melt model. Model parameters from Warren (2016). Primitive mantle normalization from McDonough & Sun (1995).

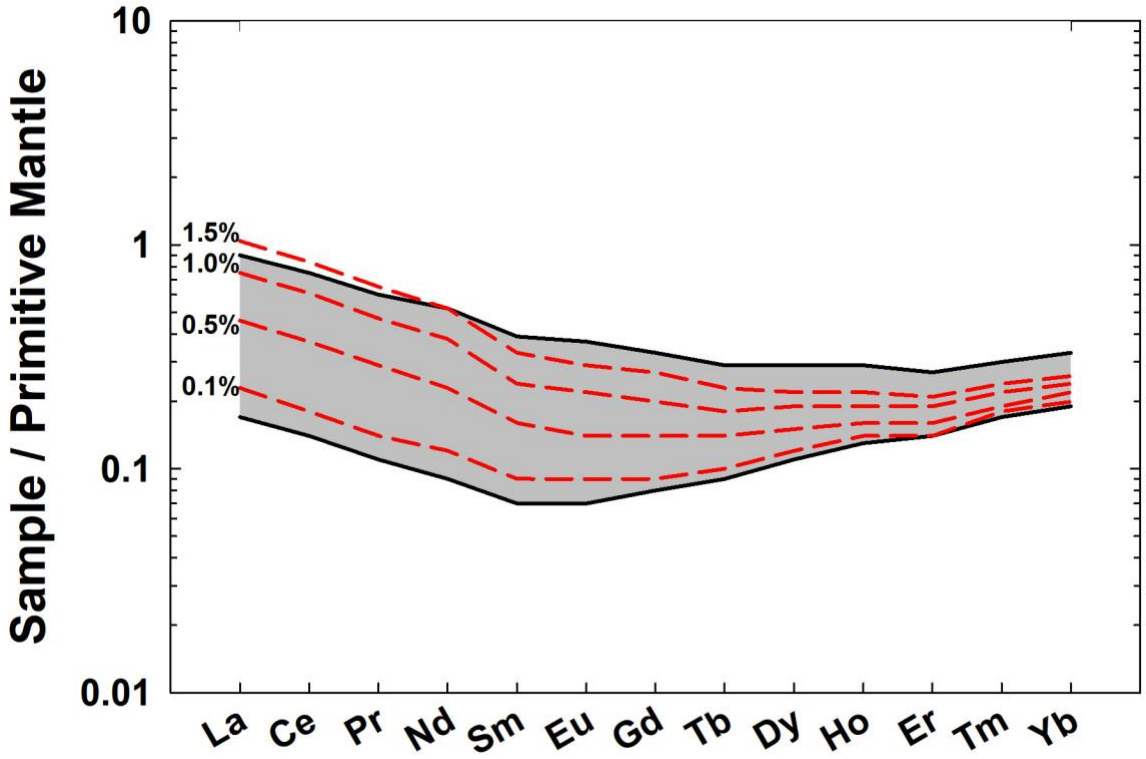

Figure 2.7 Closed system equilibrium model showing the effect of melt addition on LREE abundances. The initial composition is WOBA-3D-14. The grey field shows the Ferrel seamount peridotite samples from this study. The red dashed lines show the effect of ~0.1%, 0.5%, 1.0%, & 1.5% addition of the host alkali basalt on depleted peridotite.

Melt refertilization processes are also evident from clinopyroxene grains in Ferrel Seamount peridotites. Clinopyroxene grains have 120° triple junctions, exsolution lamellae of clinopyroxene from orthopyroxene, and vermicular spinel, possibly consistent with garnet breakdown textures, implying long-term equilibration at high temperature (**Figure S2.3**). The clinopyroxene grains have elevated incompatible trace element and LREE relative abundances (**Figure 2.6a, b**). Our results support previous suggestions that clinopyroxene grains hosted in spinel peridotites are not a primary phase, but resulted from melt refertilization, or were exsolved from orthopyroxene and/or garnet (e.g., Niu, 2004; Johnson et al., 1990).

The LREE enrichment apparent in the whole-rock REE patterns in conjunction with the exsolution textures and incompatible REE enrichments of clinopyroxene suggest at least two episodes of melt refertilization. First, from a tholeiitic MORB-like melt during interaction of Ferrel Seamount peridotites at a mid-ocean ridge. This is likely responsible for the textural observations in clinopyroxene grains. Second, low degree, alkali basalt melt refertilization evidenced by elevated whole-rock LREE's imparted as cryptic metasomatism. Melt refertilization episodes have also likely affected the main HSE host sulfide populations in the peridotites. Ferrel Seamount peridotites can be broken into two groups based on the sulfide population classifications of Luguet & Pearson (2019), those with rounded intra-granular sulfides hosted primarily in orthopyroxene (Type 1), and those predominantly hosting interstitial sulfides (Type 2). Twelve sulfide grains were analyzed from five samples, WOBA-3D-05, -10, -12, -17, and -31. Of those sulfides, five are classified as Type 1, and seven as Type 2 (*Supplemental Information*, **Figure S2.4** & **Figure S2.5**). Harvey et al. (2006) have demonstrated that interstitial sulfides in the abyssal peridotites that they studied were a metasomatic product precipitated from sulfide-rich melts. Because sulfides exist at grain boundaries, they are susceptible to open system behavior by precipitation of Re and Pd from low degree sulfide rich melts (Luguet et al., 2003). Ferrel Seamount peridotites exhibit highly variable Re and Pd contents, but inter-element HSE ratios of the Ferrel peridotites are approximately chondritic, indicative of minor refertilization following melt depletion (Rehkamper et al., 1999). Therefore, despite evidence for formation of interstitial sulfides during refertilization (e.g., Luguet & Reisberg, 2016), the overall tenor of HSE compositions in the Ferrel Seamount peridotites appears to have been largely unaffected by these processes, and instead indicates progressive decrease in Pd/Ir with increasing degrees of partial melt loss (**Figure 2.8**).

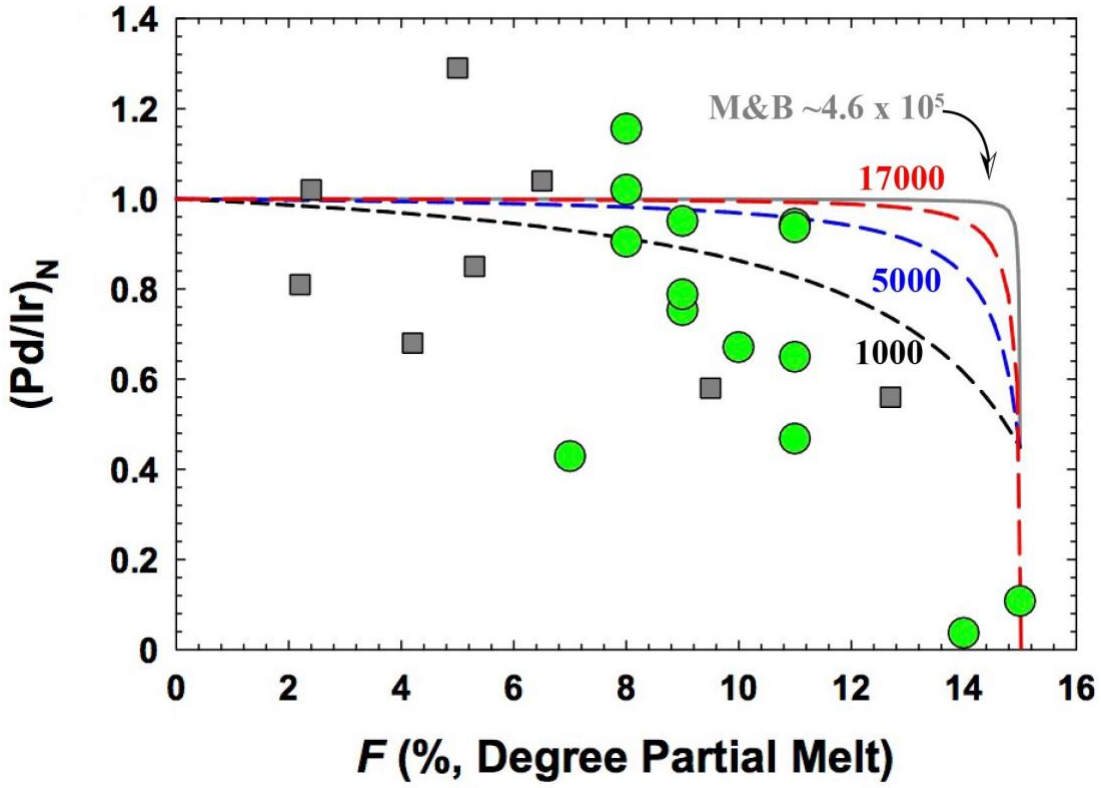

Figure 2.8 Primitive mantle normalized Pd/Ir melt model where F is obtained from Cr-spinel compositions (Hellebrand et al., 2001). Green circles are samples from this study; grey squares are SWIR (Day et al., 2017). This model predicts depletion of Pd/Ir from ~6 to 15% F; it is not intended to predict the trajectory of depletion. The initial Pd/Ir composition used is that of the primitive mantle. Curves represent Pd sulfide-silicate partition coefficients of 17,000, 5000, and 1000. The grey solid curve is the experimentally derived Kd ($4.6 \pm 6.9 \times 10^5$) from Mungall & Brenan, 2014. A constant sulfide-silicate partition coefficient of 26,000 was used for Ir (Fleet et al., 1999). Initial conditions were set at 150 ppm S in a depleted mantle reservoir with a dissolved S of 1000 ppm in melt. Under these conditions available sulfides in the residue are exhausted at F = 15% (Luguet et al., 2003).

2.6.2 HFSE fractionation in pyroxene grains

Fractionation patterns of the high field strength elements (HFSE: Nb, Ta, Zr, and Hf) in Ferrel Seamount peridotite pyroxene grains show considerable variability relative to the whole-rock, suggesting a complex history of depletion and re-fertilization typical of spinel facies mantle peridotites (e.g., Pfänder et al., 2007; Niu, 2004; Weyer et al., 2003; Rudnick et al., 1993). The elemental pairs Nb-Ta and Zr-Hf have the same charge (5+ and 4+ respectively), similar ionic

radii, and peridotite-melt distribution coefficients (~0.5), therefore the initial ratios of Nb/Ta and Zr/Hf should remain relatively constant during a single melting event (Pearce & Parkinson, 1993). However, the HFSE ratios from orthopyroxene and clinopyroxene show variable fractionation patterns that have no correspondence between the two phases, which rules out sub-solidus re-equilibration (Matusiak-Malek et al., 2017). In addition, the lack of agreement between HFSE ratios of pyroxene phases and bulk rock melt depletion indicators imply either inherited source heterogeneity or melting followed by refertilization (Weyer et al., 2003; Niu, 2004). In contrast, bulk peridotite HFSE ratios are uniformly fractionated (Avg. Nb/Ta = 15.9 ±0.8; Avg. Zr/Hf = 43.6 ±1.4), with absolute abundances of these elements being slightly depleted relative to primitive mantle. The clinopyroxene HFSE ratios are variable relative to the bulk peridotite or the gabbro. The variability within the clinopyroxenes and lack of correspondence with melt depletion suggest that interaction with low degree metasomatic melt and varying, partial re-equilibration occurred. Fractionation of the HFSE has been observed in other studies of abyssal peridotites and can be attributed to low degree partial melts from the asthenosphere (Niu, 2004).

2.6.3 The extent and timing of melt-depletion

A common characteristic of abyssal peridotites worldwide is broad range of partial melt depletion that commonly exceeds 5% (*F*; Day et al., 2017; Warren, 2016; Lassiter et al., 2014; Harvey et al., 2006; Paquet et al., 2022). For example, abyssal peridotite suites from the Gakkel Ridge (4-16%) (D'Errico et al., 2016), Mid-Atlantic (10-14%) (Harvey et al., 2006), Southwest (2-9%) and Central Indian (2-12%) Ridges (Day et al., 2017) extend to >10% melt depletion, with the exception of the Southwest Indian Ridge. Two independent estimates of melt depletion using spinel compositions (Hellebrand et al., 2001) and HREE contents in whole-rock samples (e.g.,

Johnson et al., 1990; Warren, 2016) yield between 7 to 15% and 6 to 18% melt removal, respectively, indicating a similar degree of melt depletion in Ferrel peridotites relative to abyssal peridotites (**Figure 2.6a)**.

Clinopyroxene is the primary reservoir of the REE in abyssal and continental peridotites, and as such the REE composition has been widely employed as a melt depletion indicator (Johnson et al., 1990). Nevertheless, we have demonstrated that the Ferrel peridotite clinopyroxene formed during melt refertilization during mid-ocean ridge processes and prior to the cryptic metasomatism affecting bulk rocks due to interaction with the host melt. Melt depletion calculations for the clinopyroxene indicate 4 to 12% melt removal, agreeing well with the whole rock and spinel estimates. Despite the lack of correspondence between HFSE's and melt depletion, these results suggest Ferrel peridotites are both residues after melt removal and have been refertilized with melts from similarly depleted sources.

The HSE are hosted in sulfide phases as opposed to silicate phases used for typical melt depletion indicators. Given the high abundance of the HSE in peridotite relative to melts, bulk rock HSE abundances in peridotites preserve melt depletion signatures relatively robustly (Paquet al., 2022; Day et al., 2017; Luguet et al., 2001; Brandon et al., 2000). To examine this for Ferrel peridotites, a non-modal batch melt model that tracks F as a function of $(Pd/Ir)_N$ was used with parameters from Day et al. (2017), Luguet et al. (2003), and Liu et al. (2009) (**Figure 2.8**). This model assumes HSE control by sulfide-melt, which is exhausted at $F \geq 15\%$. The intent is to predict the degree of melt depletion where Pd/Ir ratios will be affected, not the specific ratio of Pd/Ir as this model does not account for pre-existing heterogeneity. As such, an exact fit to the model curves is not expected. The model agrees well with silicate melt-depletion models, showing sulfide removal in the range of 7-15% F.

2.6.4 Origin of Ferrel Seamount Peridotites from an oceanic lithosphere protolith

Ferrel Seamount peridotites have physical, chemical, and isotopic characteristics suggesting that they are essentially identical to abyssal peridotites, with the exception that they have experienced recent cryptic metasomatism by alkali basalt partial melts and are generally fresher rocks. Otherwise, enrichments in whole rock LREE and other incompatible elements are characteristic features indicative of melt refertilization (Niu et al., 2004; Warren et al., 2016; Day et al., 2017), and Os isotopes, along with relative and absolute abundances of the HSE point to at least one ancient (hundreds of million years ago) melt depletion event with between 6% to 15% melt-loss, with strong similarities to East Pacific Rise abyssal peridotites.

Seamounts and volcanic islands within the Baja California margin have been interpreted as edifices emplaced atop of abandoned spreading centers (Castillo et al., 2010; Batiza, 1977). For example, geochemical studies of basalts dredged from the Davidson seamount have shown temporally variable fractionation, consistent with a shallow DMM source (Castillo et al., 2010; Davis et al., 2007). Seamounts along the California margin and California Borderlands (Guide, Pioneer, and Gumdrop seamounts), share similar characteristics to the Davidson seamount and those of the Baja California margin (Castillo et al., 2010; Davis et al., 2007). Perhaps most notable of these edifices is nearby Isla Guadalupe, for which Batiza (1977) drew a similar conclusion (**Figure 2.1**). Based on this evidence, we conclude that the Ferrel Seamount is a younger edifice emplaced atop an abandoned spreading section of the Pacific-Farallon ridge. In a detailed geomorphological, magnetic and seismic survey of the region, Lonsdale (1991) suggested that the Ferrel Seamount, and the Soledad rise to the north, defines the northern and southern features of a mid-ocean ridge segment, referred to as the Soledad Ridge. The location of the peridotite xenoliths,

and their compositions, are consistent with them being oceanic mantle lithosphere incorporated into the northwest boundary of the captured Guadalupe microplate.

2.6.5 An 'isolation' hypothesis for the formation of non-cratonic CLM

The continental lithospheric mantle (CLM) is distinct in its thickness, and long-term stability compared to oceanic mantle lithosphere, as well as rigidity with regard to young lithosphere. Three models, outlined in the introduction, have previously been proposed to explain this distinction, all of which invoke substantial partial melting to render a buoyant, refractory residue that is difficult to subduct and recycle (**Figure 2.9**). The two models considered to occur after reduction in mantle potential temperatures in the Archaean propose that buoyant slabs, of hotspot or volcanic arc origin, are accreted laterally or under-plated to the continental margin in subduction zones.

Here, we propose an alternative and complementary model that may be relevant to modern plate tectonics whereby subduction stalling, followed by ridge jump preserves a refractory oceanic slab, which can then be transposed and accreted to the margin by transpressive tectonic regimes, similar to processes that formed the Canadian Cordillera (Samson & Patchett, 1991). Geophysical surveys, along with xenolith studies, indicate the non-cratonic continental margin of the western United States and Canada is ~100 – 150 km thick (Artemieva, 2009). Therefore, if fragments of oceanic lithosphere can evolve to non-cratonic CLM (especially relatively young, non-subducting lithosphere) the fragments must be thickened either through shortening from under thrusting, folding, or stacking. We envisage that a variety of other tectonically driven isolation processes (for example, rifting to isolate the plate) may also lead to formation of new CLM. Van den Broek & Gaina (2020) suggested that extension and rifting play an important role in the formation of

microcontinents, and proposed southern Baja California to be a "proto-microcontinent". Here, we provide evidence for such a process on the Baja California margin. The Baja California margin approached its present-day state at ~15 to 10 Ma, when subduction ended, followed by the capture of the remaining Farallon micro-plates by the Pacific plate, and rifting inboard of the abandoned trench, which opened the Gulf of California (e.g., Lonsdale, 1991; Atwater, 1970). The result of this tectonic reorganization is a diffuse Pacific-North American plate boundary that incorporates many of the abandoned Pacific-Farallon spreading ridges, including the Soledad Ridge and associated Ferrel Seamount. The significance of ridge jump is that nascent oceanic lithosphere was isolated from subduction for at least 10 Ma. The Ferrel Seamount peridotites reveal that the lithosphere beneath is refractory material incorporated into the diffuse Pacific-North American plate boundary.

A modern analog for this sequence of events is the Colima basin southeast of the mouth of the Gulf of California proximal to the Rivera triple junction (**Figure 2.10**). Here, another Farallon remnant, the Rivera microplate is subducting beneath the northern most extent of the Middle America Trench at a decreasing rate over the last 2 Ma (Nixon, 1982). Detailed mapping, geochronology, and geochemical analysis by Luhr et al. (1985) suggests the Colima basin is an active rift inboard a waning subduction zone. These results imply subduction of the Rivera microplate will stall, inland rifting of the continental margin will continue, and the Rivera microplate along with a fragment of the North American plate will be captured and translated northward by the Pacific plate, preserving the underlying oceanic mantle lithosphere. In both cases of the Ferrel Seamount and Colima basin, oceanic lithosphere is incorporated into the Pacific plate along with marginal non-cratonic CLM and eventually accreted to the margin, in contrast to previous models, which suggest buoyant oceanic lithosphere is directly accreted to a continental

margin. The geochemical consequence of this process is that nascent CLM will have characteristics more akin to oceanic mantle lithosphere than to lithosphere involved in subduction processes, as in previous models for CLM formation. For example, comparing the Ferrel xenolith suite to other mantle xenolith suites from the Pacific (Snortum et al., 2019) shows the Ferrel Seamount shares the same range of $^{187}Os/^{188}Os$ and Os concentration, consistent with a Pacific oceanic lithosphere origin (**Figure 2.11**).

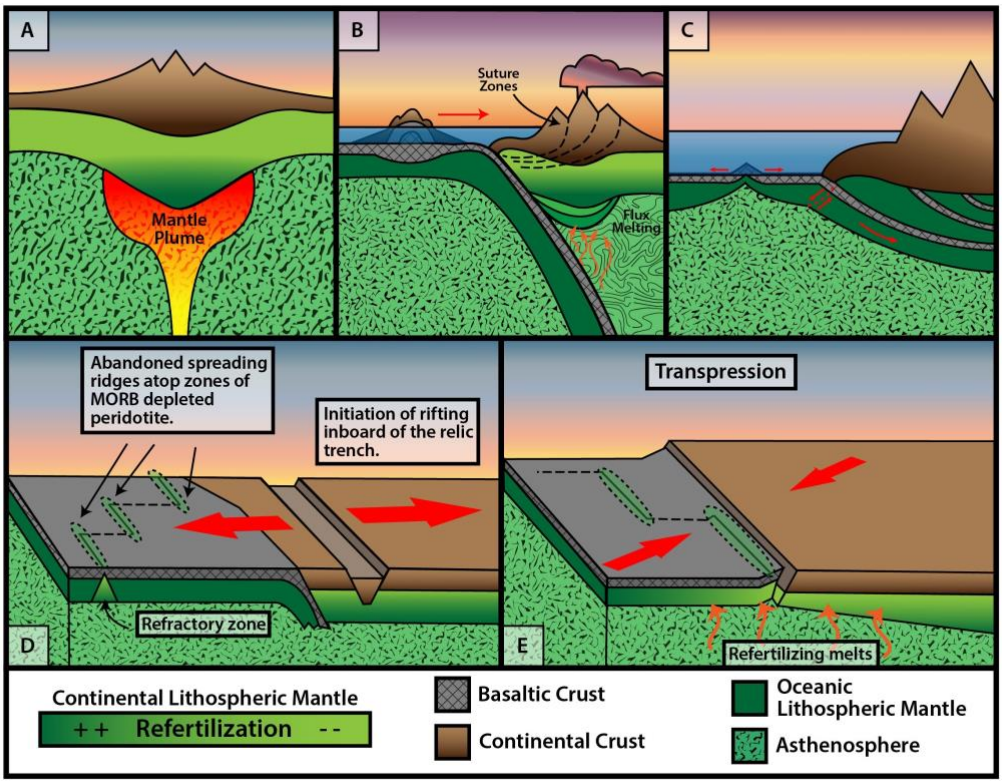

Figure 2.9 Schematic diagrams of mechanisms for formation of continental lithospheric mantle (A-C) and isolation of oceanic lithosphere and formation of nascent continental lithospheric mantle (D-E). A) The plume model showing lithospheric thickening from prolonged melt depletion by a mantle plume (i.e. Griffin et al., 1998). B) Exotic terrain accretion and lithospheric thickening from flux melting of the asthenosphere (Canil & Wei, 1992). C) Imbrication of oceanic lithosphere from low angle subduction ('Subduction zone stacking; i.e., Simon et al., 2008). D) Model showing the isolation of refractory lithosphere by ridge jump, followed by E) translation and accretion of the micro plate in a transpressive environment (this study).

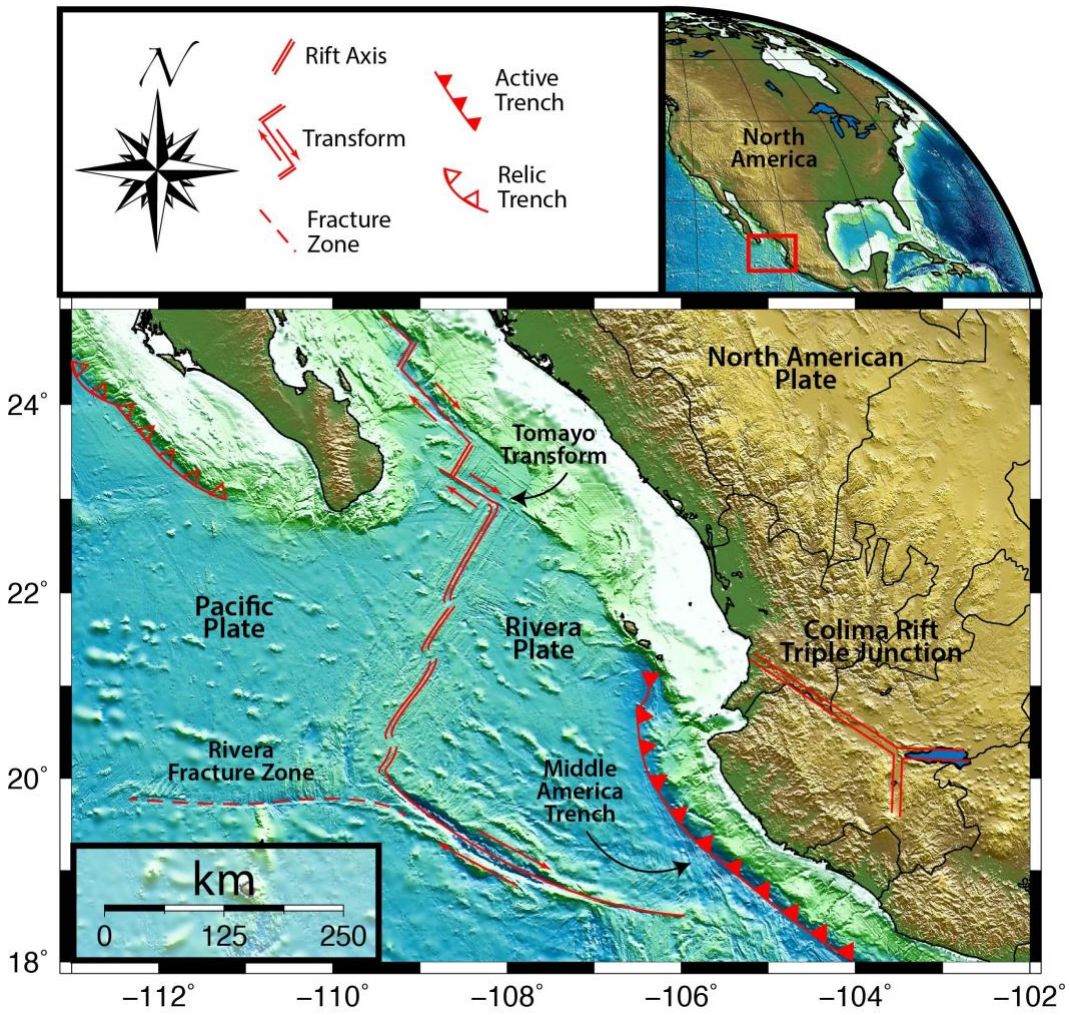

Figure 2.10 Elevation and bathymetry map of the Colima Rift in western Mexico near the southern point of Baja California. The Colima rift forms a triple junction structure where active spreading is advancing inland as subduction comes to a stop and spreading on the East Pacific Rise slows. This likely represents the transition of the North American-Pacific plate boundary and subsequent isolation of the Rivera section of the EPR.

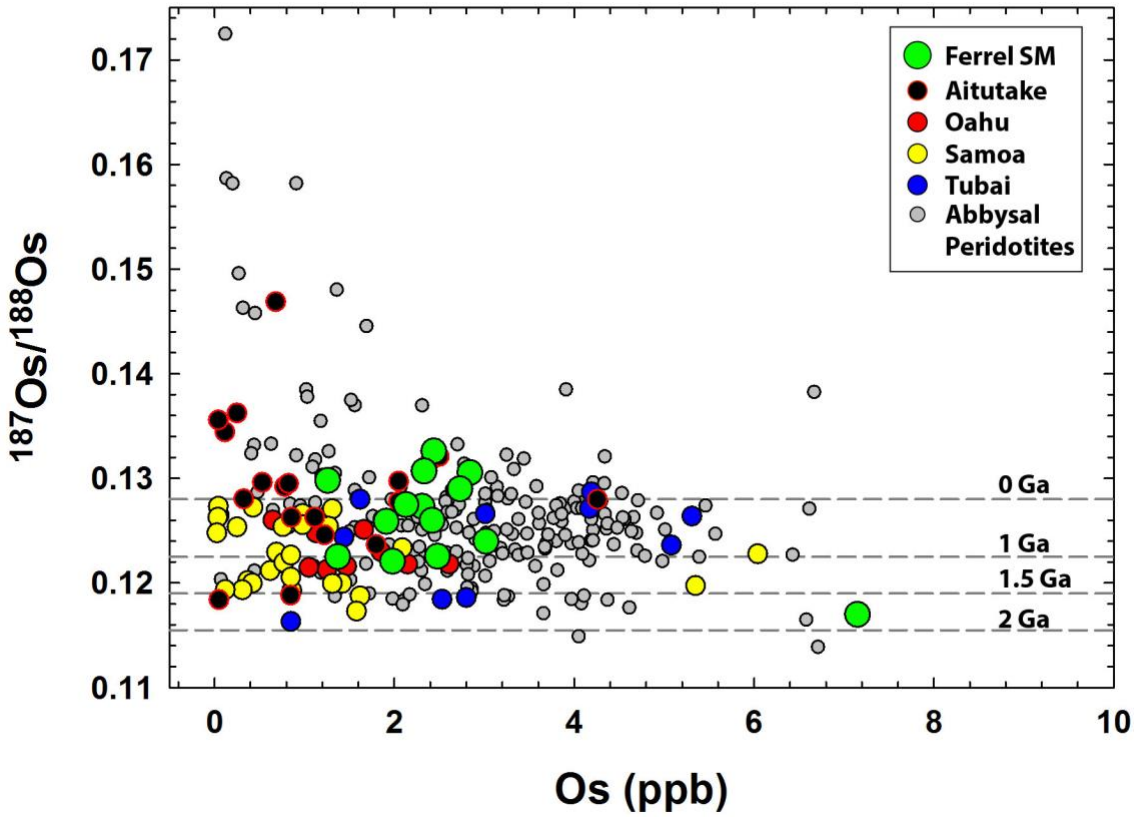

Figure 2.11 $^{187}Os/^{188}Os$ versus Os concentration for Ferrel Seamount xenoliths compared to Pacific Island xenoliths representing ~75 to 100 ma lithosphere and abyssal peridotites from around the globe. (Aitutake: Snortum et al., 2019; Oahu, Hawai'i: Bizimis et al., (2007); Samoa & Tubai: Jackson et al., (2016); abyssal peridotites: Day et al., (2017)).

2.6.6 Examining the oceanic to continental lithospheric mantle model

The model of tectonic isolation to form CLM presented here suggests that refractory oceanic mantle lithosphere beneath the abandoned Pacific-Farallon spreading ridge has a higher probability of forming non-cratonic CLM due to chemical properties imparted by ridge processes coupled with tectonic reorganization through ridge jump. Therefore, an important question is whether CLM formation by isolation is a widespread process given the vast linear extent of subduction zones and mid ocean ridges worldwide. Although ridge subduction was initially

thought to explain post Miocene volcanism along the North American margin, geophysical modeling and direct observation of abandoned ridge segments have cast doubt on this scenario (Michaud et al., 2006). Instead, as the hot, depleted ridge approaches the trench the angle of the subducting slab flattens and ultimately stalls prompting tectonic reorganization in the form of plate capture. These observations imply that oceanic lithosphere is not completely recycled, and rather that a limited fraction of the slab can be welded onto the plate. From this vantage point, the preserved lithosphere is accreted to the margin and oceanic lithosphere is imbricated against it (i.e. Luffi et al., 2009). This may be a major form of non-cratonic continental lithosphere formation.

Another question regards the role melt refertilization plays in the modification of oceanic lithosphere to CLM. Localities where non-cratonic CLM peridotites can be sampled in the western United States include Dish Hill and Kilbourne Hole, and these peridotite suites show evidence of more prolonged metasomatism than the Ferrel Seamount. Modal clinopyroxene for these CLM domains fall within the range of the Ferrel Seamount (3-20%) but unlike peridotites from this study, the range of bulk rock Al_2O_3 for Dish Hill and Kilbourne Hole overlap fertile mantle values indicative of low degree metasomatism (**Figure 2.12**), implying the CLM becomes less stable with time due the addition of melt (i.e., Fe; Lee et al., 2011). Armytage et al. (2014) has suggested that the addition of refractory peridotite by under plating or partial melting shields the metasomatized lithosphere from further modification thus prolonging gravitational stability. This suggests a positive correlation between increasing degrees of melt depletion and depth. Where this theory implies vertical stacking of upper mantle domains as a result of subduction, our new model suggests isolated lithosphere can be added laterally in a strike-slip regime, broadly similar to the exotic terrain accretion model, in this case lacking the subduction component. Such a hypothesis

works well with the ridge jump model proposed here in that continual tectonic processes gradually build CLM by lateral addition of refractory material along a diffuse transpressive boundary.

A comparison of $^{187}Os/^{188}Os$ and melt depletion indicators for Ferrel Seamount peridotites versus western United States xenolith suites indicates similar melt depletion processes consistent with previous studies that have suggested an oceanic mantle lithosphere origin for Dish Hill (Luffi et al., 2009) and Rio Grande Rift xenoliths (Byerly & Lassiter, 2012). However, conclusive evidence linking abyssal peridotites to off-craton xenoliths is difficult due to post melt depletion modification by metasomatizing melts. This is illustrated in ^{187}Re-^{187}Os ratios for Dish Hill and Kilbourne Hole samples that suggest elevated melt removal, similar to the Ferrel Seamount, but Al_2O_3 compositions that encompass the fertile mantle value (**Figure 2.12**).

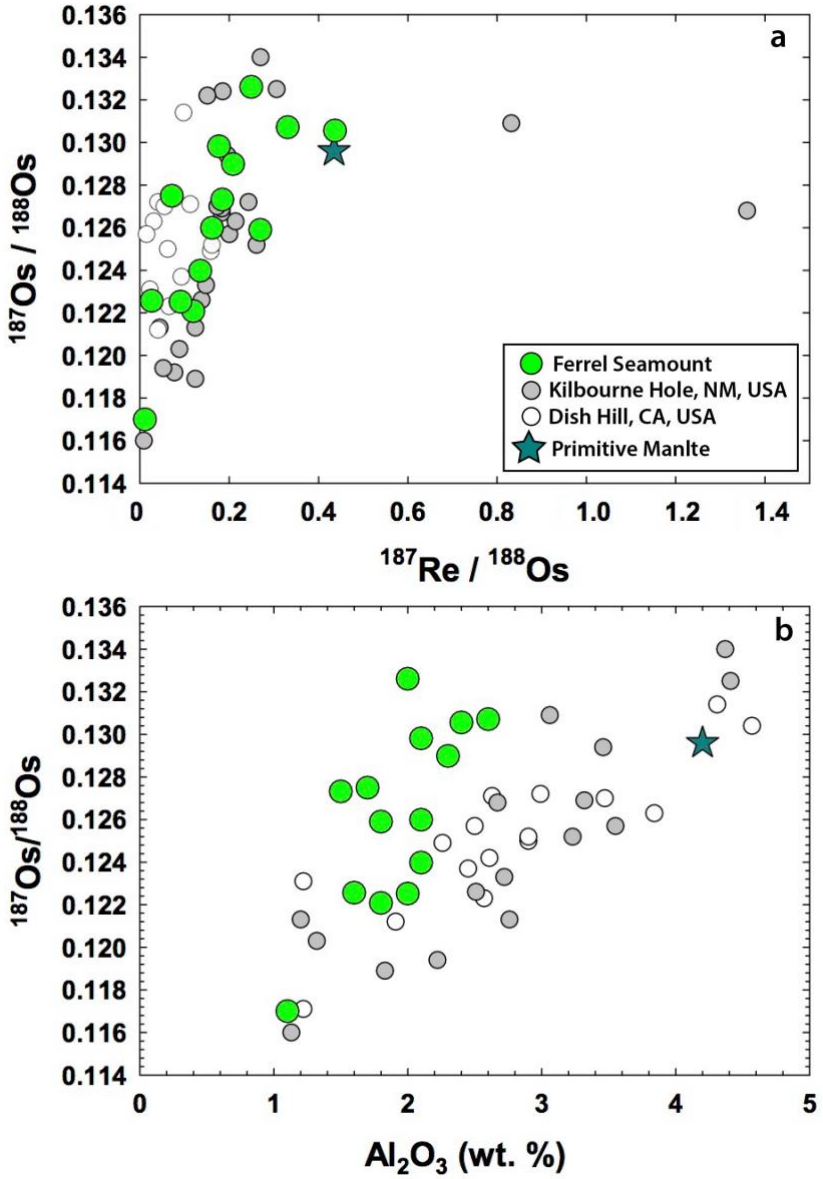

Figure 2.12 Plots of (A) $^{187}Re/^{188}Os$-$^{187}Os/^{188}Os$ for samples from the Ferrel Seamount, and Dish Hill, and Kilbourne Hole; (B) $^{187}Os/^{188}Os$ versus melt depletion indices, Al_2O_3. The CLM samples show a more fertile character, implying refertilization even in strongly melt-depleted samples. Primitive mantle value (PM - star) from Meisel et al. (2001).

2.7 Conclusions

Results for spinel peridotites dredged from the Ferrel Seamount indicate strong chemical, mineralogical, isotopic, and textural similarities to oceanic peridotites. The regional context of seafloor morphology indicates that the Ferrel Seamount is a post active spreading edifice situated

atop an abandoned segment of the Pacific-Cocos Ridge system that likely samples preserved Pacific-Farallon lithosphere. Three independent melt models suggest the Ferrel samples experienced 8 to 15% melt removal. Osmium isotopes indicate that most of this melt extraction occurred hundreds of millions of years before formation of this piece of oceanic lithosphere. At least one episode of refertilization is identified in the peridotite, preserved in clinopyroxene, occurring at the mid ocean ridge. This was followed by exposure of the peridotite xenoliths to low degree metasomatism, which imparted elevated LREE concentrations. Decoupling of melt depletion indicators and HFSE ratios of clinopyroxene versus bulk rock compositions support this conclusion. A model that tracks HSE behavior during partial melting support the results of Day et al., (2017) showing that HSE and Os isotopic systematics are not strongly leveraged by the effects of low degree melt rock reaction. These data lead to the framework of a new model for the formation of CLM represented by non-cratonic xenoliths. We propose that tectonic reconfiguration, known as ridge jump, can isolate refractory and buoyant sections of lithosphere that may have experienced relatively recent melting. Hot and depleted in dense elements, lacking the force of slab pull, these sections of lithosphere are free to accrete to continental margins. During this time, they may be exposed to prolonged addition and modification from highly variable degrees and compositions of refertilizing melt. Therefore, it seems necessary that further addition of refractory material to the base of the modified oceanic lithosphere is required to maintain gravitational stability over the 2 Ga time scales commonly reported for non-cratonic CLM xenolith suites.

2.8 Acknowledgments

Chapter 2, in full, is a reprint of the material as it appears in Geochemistry Geophysics Geosystems 2022. Oller, Brian; Day, James M.D.; Driscoll, Neal W.; Lonsdale, Peter, F. The dissertation author was the primary investigator and author of this paper.

The work would not have been possible without the support of our colleague, L.A. Taylor (1938-2017). We are grateful to L. Reisberg, A. Stracke and an anonymous reviewer for constructive journal review comments. D. van Acken and L. Ackerman are also thanked for comments on a previous version of the manuscript. Financial support from the National Science Foundation (Grants EAR 1447130 and EAR 1918322) is gratefully acknowledged. We thank the WOBA cruise participants, but especially B. Peters for selection and initial preparation of samples.

2.9 Supplemental Material

2.9.1 Petrography and mineral chemistry

Fourteen spinel lherzolite xenoliths, one gabbro xenolith, and three lava samples were selected for study from a larger available suite. Petrography and modal analysis were done at the *Scripps Isotope Geochemistry Laboratory (SIGL)*. Samples were sawn, buffed with corundum paper to remove any signs of physical alteration or saw marks and washed, before being crushed and powdered using an alumina jaw-crusher and an alumina shatterbox, respectively. Modal abundances were determined by photographic analysis of large (>3 cm × 3 cm) polished rock slabs using *ImageJ* processing software. Polished thick section slides (~50 μm thick) and one inch (2.5 cm) polished mounts were prepared for petrology and mineral chemistry.

Major element abundances of mineral phases were measured for 162 olivine, 53 orthopyroxene, 108 clinopyroxene, and 179 spinel grains using polished thick sections and grain mounts from the xenoliths with a *Cameca SX-100* electron probe micro analyzer at the University of Tennessee. All analyses were made with an accelerating potential of 15 kV, a beam size of 1 μm, and a current of 30 nA. Both natural and synthetic standards were used for calibration and standards were measured throughout analytical sessions to ensure data quality. Background and peak counting times used were 20-30 s and standard PAP (ZAF) correction procedures were used. Detection limits were <0.03 wt. % for SiO_2, TiO_2, Al_2O_3, MgO, CaO, and Na_2O, <0.04 wt. % for V_2O_3 and Cr_2O_3, <0.05 wt. % for MnO, FeO, and NiO. These procedures were identical to those reported previously in Peters et al. (2016).

Laser ablation inductively coupled plasma mass spectrometry (LA-ICP-MS) analyses of silicate mineral phases were performed using a *New Wave Research UP213* (213 nm) laser-ablation system coupled to a *ThermoScientific* iCAPq ICP-MS at the *SIGL*. Analyses were done using ~0.5 mm long rasters with a 100 μm beam diameter, a laser repetition rate of 5 Hz, and a photon fluence of ~3 to 3.5 J/cm^2. Ablation analysis took place in a 3 cm^3 ablation cell. The cell was flushed with a He-gas flow to enhance production and transport of fine aerosols and was mixed with an Ar carrier-gas flow of ~1 L/min before reaching the torch. Each analysis consisted of ~60 s of data collection. Backgrounds on the sample gas were collected for ~20 s, followed by ~40 s of laser ablation. Washout time between analyses was >120 s. Data were collected in time-resolved mode so effects of inclusions, mineral zoning, and possible penetration of the laser beam to underlying phases could be evaluated. Plots of counts per second versus time were examined for each analysis, and integration intervals for the gas background and the sample analysis were

selected. Standardization was performed using the standard reference material glasses NIST 610, BCR-2g and BHVO-2g.

Sulfide mineral elemental abundances were determined using a *Thermo Scientific* iCAP Qc ICP-MS coupled to a *New Wave Research* UP213 Laser Ablation System. Ablation took place in a 3 cm^3 ablation cell flushed with a He-gas flow and mixed with an Ar carrier at ~1 L min^{-1}. Signals were acquired in time resolved acquisition for spots, with a 20 s background and 40 s sample measurement. Wash time between analyses was 120 s. The laser was fired using an energy density of ~3.5 J.cm^{-2} at a frequency of 5 Hz and a constant 60 µm beam size. Normalization of the HSE and other siderophile element abundances was done using Fe contents, assuming 62.3 wt.% Fe in the sulfide. Standardization was performed using iron meteorites as reference materials, using preferred values. Standards used included the USGS MRM sulfide mix MASS-1 (156,000 ppm Fe) and iron meteorites Hoba (844,000 ppm Fe), North Chile (referred to as 'Filomena'; 942,000 ppm Fe) and Coahuila (944,000 ppm Fe) using values from Day et al. (2018). Calibration curves were made using these standards for each analytical session, with the curves dominated by MASS-1 for Zn and Cu, and by the iron meteorites, especially Hoba, for Co, Ni and the HSE. Complete standard data are reported in **Table S2.8**.

2.9.2 Whole-rock major- and trace-element abundance determination

Major element compositions were measured by X-ray fluorescence (XRF) at Franklin and Marshall College using a *PW 2404 PANalytical* XRF vacuum spectrometer following the procedures outlined in Boyd & Mertzman, 1987. Major element analyses by XRF involved standard lithium tetraborate fusion techniques using 3.6:0.4 g $LiBO_4$:sample powder. Ferrous iron concentrations were determined by titration with potassium dichromate. Precision and accuracy

are estimated using repeat analyses of standards, and the long-term precision and reproducibility are reported in Day et al., 2017.

Trace-element abundances were determined at the *SIGL* using methods described in Day et al., 2014. One hundred milligram aliquots of sample powder were precisely weighed and digested in a 1:4 mixture of Teflon-distilled HNO_3:HF for >72 hours at 150˚C on a hotplate. Rock standards (BHVO-2, BIR-1, BCR-2, AGV-2) and total procedural blanks were prepared along with the samples. After drying down and sequential HNO_3 dry-down steps to break-down fluorides, clear sample solutions were diluted by a factor of 5000 in 2% HNO3 and doped with a 1 ppb In solution to monitor instrumental drift. Solutions were measured using a *Thermo Scientific* iCAPq c quadrupole ICP-MS in standard mode. Reproducibility of the reference materials was generally better than 5% (RSD) for basaltic and peridotite standards, and element abundances were generally within error of recommended values (**Table S2.1**).

2.9.3 Osmium isotope and highly siderophile element abundance measurements

Osmium isotope and HSE (Re, Pd, Pt, Ru, Ir, Os) abundance analyses were performed at the *SIGL* according to methods described in Day et al., 2016. Between 0.99 and 1.06g of homogenized powder was precisely weighed and digested in sealed borosilicate Carius tubes with 'spikes' and 10 mL of a 2:3 mixture of multiply Teflon-distilled HCl and Teflon-distilled HNO_3 that had been purged of Os. Powders were equilibrated with isotopically enriched multi-element HSE spikes (^{99}Ru, ^{106}Pd, ^{185}Re, ^{190}Os, ^{191}Ir, ^{194}Pt). Samples were digested at 240°C in an oven for 72 hours. Osmium was then triply extracted from the acid using CCl_4, back-extracted into HBr and purified by micro-distillation (Birck et al., 1997). Rhenium and platinum group elements were

recovered and purified from the residual solutions by anion exchange separation, and then analyzed on a *Thermo Scientific* iCAPq-c ICPMS in standard mode. Isotopic compositions of Os were measured in negative-ions by peak-jumping on the *Thermo Scientific* Triton thermal ionization mass spectrometer (Creaser et al., 1991; Volkening et al., 1991) and were oxide and fractionation corrected using $^{192}Os/^{188}Os = 3.08271$. Concentrations of Os were determined from the same data using a ^{190}Os spike deconvolution and were appropriately blank-corrected. Measurements of 36 and 72 pg UMCP Johnson-Matthey standards were used to monitor precision of the Os-isotopic measurements, and averaged 0.11407 ±0.00008 (2σ, n = 30). Total procedural blanks for Os analyses (n = 3) had an average corrected $^{187}Os/^{188}Os$ of 0.106 and [Os] of 2.2 ±2.3 pg. Measured Re, Ir, Pt, Pd and Ru isotopic ratios for sample solutions were corrected for mass fractionation using the deviation of the standard average run on the day over the natural ratio for the element, and all reported values are blank corrected. HSE abundances of these blanks (n = 3) were (in pg, with the value underlined used for correction): 4.3-9.0 for Ir, 14-158 for Ru, 9-11 for Pt, 37-42 for Pd and 5-6.1 for Re. These blanks represented <1% of total analyte for Os, Ir and Pt, <4% for Pd (apart from WOBA 3D-14 at 16%) and <5% for Ru and <3.5% for Re (apart from WOBA 3D-31 at 15%).

2.9.4 Textures and modal mineralogy

Peridotites from the Ferrel Seamount have coarse, equigranular textures and are dominantly spinel lherzolites (43.7-68.2 modal% olivine; 17.5-40.8 modal% orthopyroxene; 20.0-8.7 modal % clinopyroxene; 0.6-3.2 modal % spinel), with one spinel harzburgite, WOBA-3D-5 (68.8 modal % olivine; 24.3 modal % orthopyroxene; 3.2 modal% clinopyroxene; 3.8 modal% spinel) (**Table S2.7**). The xenolith suite shows no visible signs of serpentinization or seafloor

weathering. Olivine and orthopyroxene grains average ~3 to 8 mm in size while clinopyroxene grains average ~0.25 to 0.75 mm, and spinel grains are typically a micron to tens of microns in size. Equigranular silicate grains have well defined ~120° triple junctions whereas spinel grains are dominantly vermicular in texture, with a few anhedral grains (**Figure 2.6**). The vermicular spinel grains are typically accompanied by interstitial clinopyroxene and/or orthopyroxene, indicative of re-equilibration of spinel from the breakdown of exhumed garnet (Hellebrand et al., 2002). Larger orthopyroxene grains can show exsolution lamellae of clinopyroxene, and in some cases, these exsolved grains exhibit a sheared fabric (**Figure 2.6**).

Sulfide grains were observed in polished sections of ten of the fourteen peridotite samples (WOBA-3D-03, -05, -06, -07, -09, -10, -12, -15, -17, -31). These sulfides are categorized into two populations based on the classification of Luguet & Pearson, 2019. Type 1 sulfides are intra-granular, round to sub-round (<100 microns) hosted primarily in orthopyroxene (WOBA-3D-05, -06, 10, -15). The remainder are Type 2. These are interstitial with skeletal textures, elongated <200 microns along the long axis (**Figure S4**). With the exception of two samples (WOBA-3D-10 and -17) no melt veins or evidence of melt-infiltration were noted. For the cases mentioned, the effect of melt infiltration is isolated based on the lack of reaction rims or zoning in pyroxene phases, consistent with the rest of the peridotite suite. The extent of glass infiltration is limited to the outer periphery of the samples, where little evidence of melt reaction with adjacent minerals was observed. Host lavas are highly-vesiculated, fine-grained rocks with minor plagioclase and large (2 – 10 mm) olivine grains. The outside of the host lavas has limited manganese coating, consistent with the relatively shallow collection depth, < 800 m, as indicated from dredge logs.

2.9.5 Mineral major-element compositions

Major-element abundances for olivine, orthopyroxene, clinopyroxene, and spinel are given in **Tables S2.3-S2.7**. The olivine phase grains measured from 14 Ferrel Seamount xenoliths average 39.9 ±0.7 wt.% SiO_2, 49.2 ±0.6 wt.% MgO, 0.07 ±0.02 wt.% CaO, 0.14±0.01 wt.% MnO, 9.8 ±0.8 wt.% FeO and 0.41 ±0.02 wt.% NiO (1 St. Dev. Error) with a range of forsterite contents from 84.7 to 91.8. The highest Fo contents were measured in WOBA 3D-1 (91.6-91.8) and the lowest from WOBA 3D-10 (84.7-84.8). Orthopyroxene is enstatite composition ($En_{0.888\pm0.008}Wo_{0.017\pm0.003}Fs_{0.095\pm0.007}$), with Mg-numbers ranging from of 89.2-91.9. Sample WOBA 3D-1 has the highest orthopyroxene Mg-number (91.9), broadly in equilibrium with olivine in the sample. Clinopyroxene is homogeneous Cr-diopside ($En_{0.486\pm0.006}Wo_{0.467\pm0.009}Fs_{0.047\pm0.004}$), with Cr_2O_3 from 0.7-1.3 wt. %, and Mg-numbers between 91.2-89.9.

Spinel Mg-numbers range from 66.0 to 73.5 (70.6 ±2.3) and Cr-numbers range from 18 to 40.3 (25.2 ±5.7). WOBA 3D–1 and WOBA 3D-14 both have significantly higher Cr-numbers (~40) than other samples. The Cr-numbers of spinel and clinopyroxene fall on a well-correlated trend (r^2 = 0.88) and the spinel grains fall within the compositional field of abyssal peridotites, defined by Zhou et al., 1996 (**Figure 2.2**). The majority of the WOBA samples plot close to - but are somewhat more depleted than - the DMM composition estimated by Workman & Hart, 2005. According to the modified spinel melt depletion calculation of Hellebrand et al., 2002, the compositions of the spinel indicate between 7 and 15% melt depletion, with an average of 10 ±2% melt depletion for the entire suite of samples.

2.9.6 LA-ICP-MS trace-element compositions of orthopyroxene clinopyroxene and sulfide

Trace-element abundances were measured using LA-ICP-MS for orthopyroxene in all fourteen peridotite samples, and for clinopyroxene in all samples apart from WOBA 3D-1 (**Table S2.2**). Orthopyroxene grains in the Ferrel Seamount samples typically have lower absolute abundances (~<0.1 × PM) of the incompatible trace elements than DMM orthopyroxene, but they have systematically higher La, Ba and Rb (**Figure 2.3a**). Some samples (WOBA 3D–6, -7, -15) have relative and absolute enrichments in the most incompatible elements (Rb to Eu). Most of the samples cluster around a restricted range of La/Yb_{PM} and Sm/Yb_{PM} values (~0.56 and ~0.13, respectively), but the inclusion of the incompatible element-enriched samples extends the total range of these values (0.33 to 14.7 and 0.03 to 3.4, respectively). Like DMM orthopyroxene, and orthopyroxene grains measured from the Gakkel Ridge (D'Errico et al., 2016), Ferrel Seamount xenoliths contain orthopyroxene grains with significant Zr and Hf enrichments relative to elements of similar incompatibility. Unlike DMM, however, the Ferrel Seamount samples do not have prominent Nb or Ta enrichments.

Clinopyroxene grains generally have lower abundances of the incompatible trace elements (<1 × PM) than DMM clinopyroxene (**Figure 2.3b**), except for WOBA 3D–11, which has elevated heavy REE abundances (>10 × PM). The patterns for clinopyroxene exhibit a notable 'fanning', where La/Yb_{PM} and Sm/Yb_{PM} span a range of values from 0.06 to 1.6 and 0.06 to 1.7, respectively. For the most incompatible trace element-depleted clinopyroxene grains in samples (WOBA 3D–6, -9, -31, -32), there are relative depletions in Nb, Sr and Nd. Orthopyroxene, shows four contrasting $(Nb/Ta)_N$ fractionation patterns: First, depleted relative to DMM with $(Nb/Ta)_N > 1$; Second, depleted relative to DMM with $(Nb/Ta)_N < 1$; Third, enriched relative to DMM with $(Nb/Ta)_N > 1$; Fourth, enriched relative to DMM with $(Nb/Ta)_N < 1$ (**Figure 2.3a**). Clinopyroxene

has more uniform $(Nb/Ta)_N$ ratios having only four samples with $(Nb/Ta)_N > 1$ which are also strongly depleted relative to DMM and one highly enriched sample with $(Nb/Ta)_N < 1$. The same four depleted clinopyroxene samples also have variable ratios of $(Zr/Hf)_N$ (**Figure 2.3b**).

Five sulfide bearing samples were selected for measurement based on size (WOBA-3D-05, -10, -12, -17, -31). The intra-granular (Type 1) sulfides have higher absolute abundances of Ni and Cu than the interstitial (Type 2) sulfides and generally lower abundances of Ru, Pd, Pt. Type 2 sulfides have generally elevated, but highly variable abundances of the HSE.

2.9.7 Whole-rock major- and trace-element compositions of host lavas and gabbro xenoliths

To assess likely interaction with alkali basalt and the peridotite xenoliths that were studied, bulk-rock major and trace element compositions were measured for three of the associated lavas, as well as a single gabbro xenolith (**Table S2.1**). The alkali basalts have variable loss on ignition (0.06-2.8 wt.%) but are otherwise quite homogeneous with 46.5 ±0.4 wt.% SiO_2, 5.5 ±0.2 wt.% total alkalis ($Na_2O + K_2O$), 12.3 ±1.2 wt.% MgO and ~2.3 wt. TiO_2. The gabbro xenolith that we measured is broadly similar to mid-oceanic ridge gabbros (Niu & O'Hara, 2003) with high Al_2O_3 and CaO, 0.3 wt.% TiO_2, 9.9 wt.% MgO and a broadly tholeiitic composition, consistent with oceanic crust. Primitive mantle normalized, incompatible trace element patterns are plotted for the lavas and gabbro xenolith in **Figure S2.1**. The lavas are incompatible trace element enriched (~4-100 × PM) compared with the gabbro (~0.5-8 × PM) and have negative Pb and Ti anomalies and relative enrichment of the light REE relative to the heavy REE, and for the most incompatible trace elements (e.g., Ba, Rb). The gabbro xenolith has a flatter primitive mantle normalized pattern, with relative enrichments in Pb and Sr and depletions in Th, Nb and Ta, consistent with a MORB-like protolith to which cumulate plagioclase has been added.

The gabbro xenolith analyzed in this study (WOBA-3D-22) supports an origin of the Ferrel Seamount xenolith suite partly through mid-ocean ridge petrogenesis. The REE and major element composition of the gabbro are consistent with tholeiitic basalts and gabbros commonly associated with spreading centers (Niu & O'Hara, 2003). Tholeiites are generated by relatively high degrees of partial melt, which is consistent with the Ferrel Seamount melt models indicating 6-15% partial melt to explain clinopyroxene compositions.

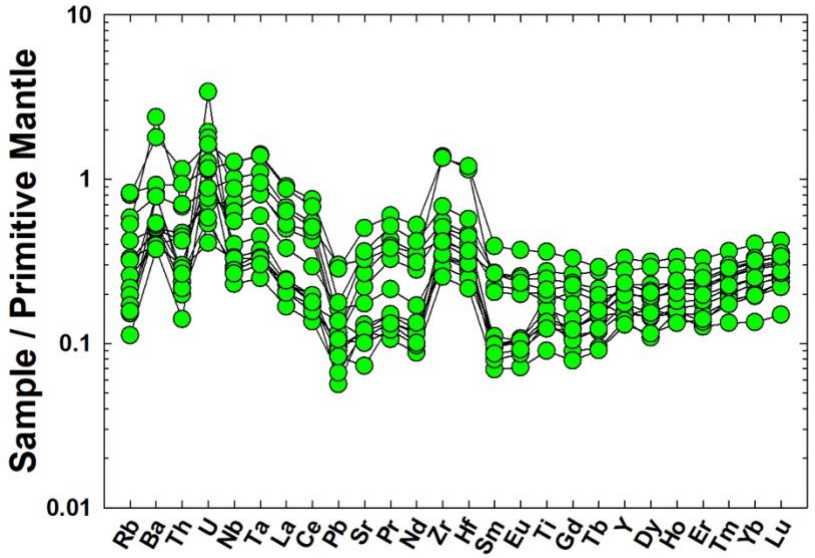

Figure S2.1 Primitive mantle normalized bulk rock, incompatible trace element patterns for Ferrel Seamount peridotites. Primitive mantle normalization from McDonough & Sun (1995).

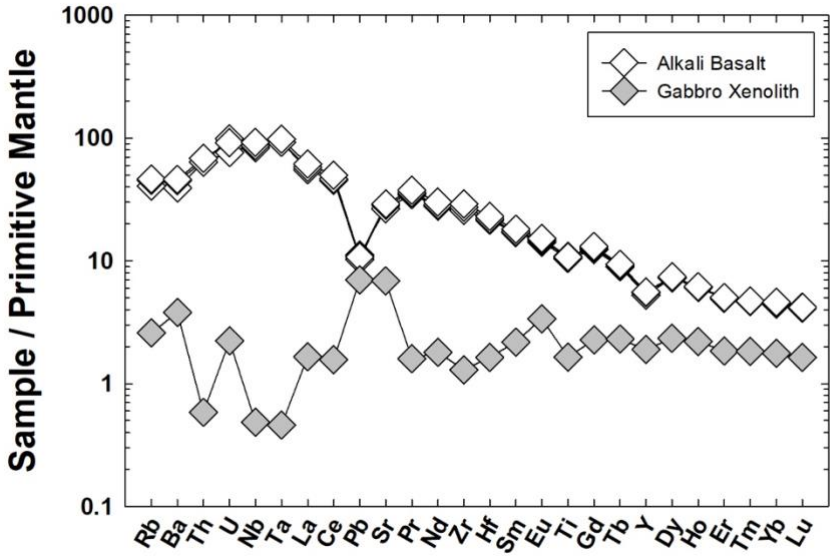

Figure S2.2 Primitive mantle normalized incompatible trace element patterns for alkali basalt host rocks, and a single gabbro xenolith from the Ferrel Seamount. Primitive mantle normalization from McDonough & Sun (1995).

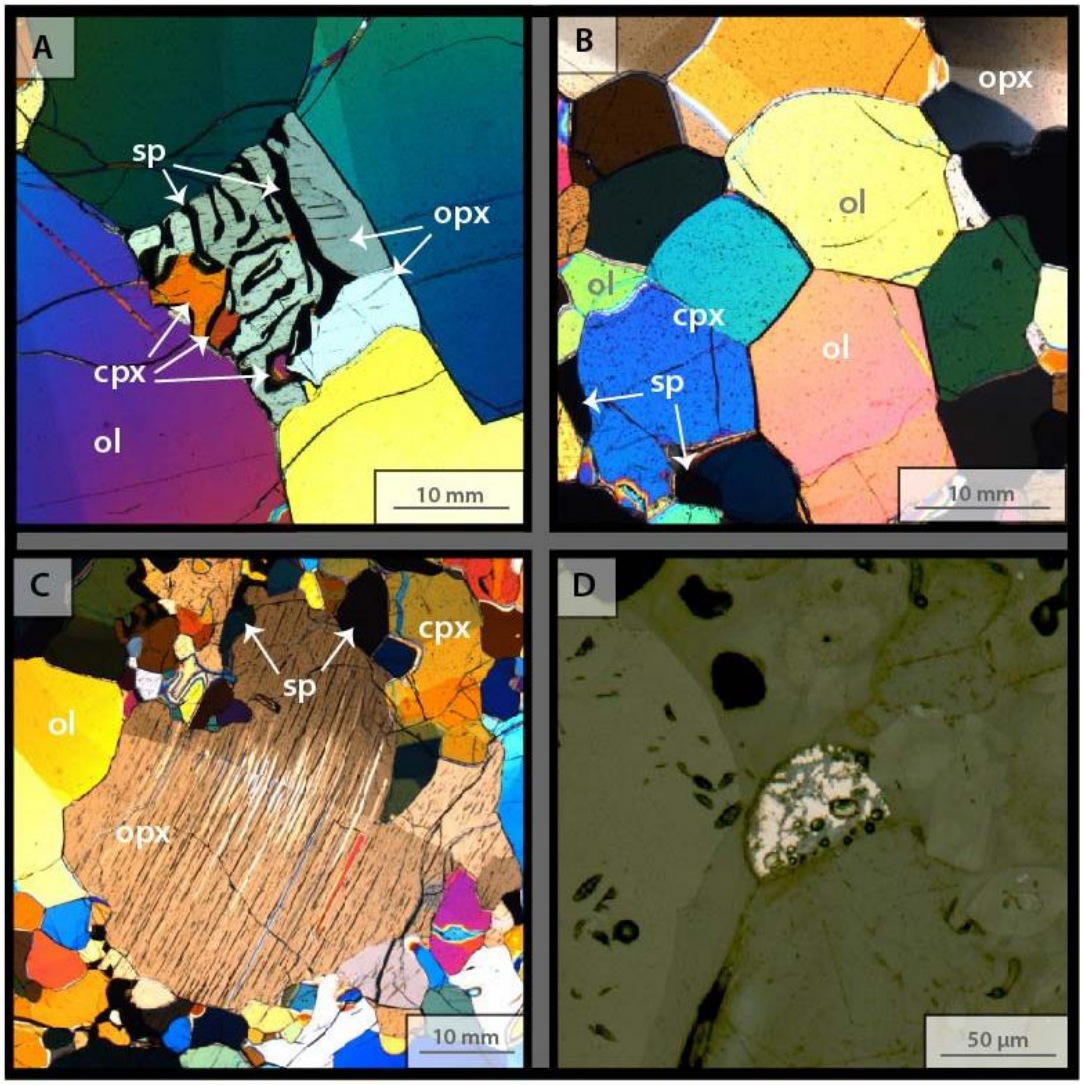

Figure S2.3 Examples of textures and mineralogical relationships in Ferrel Seamount peridotite 50 μm thick polished sections. (a) (WOBA-3D-11) cross-polarized light (XPL) image of vermicular spinel with interstitial opx and cpx. (b) (WOBA-3D-1) Olivine and cpx with ~120° trigonal symmetry. (c) (WOBA-3D-14) Orthopyroxene showing bent exsolution lamellae of clinopyroxene. (d) (WOBA-3D-31) Reflected light image of an interstitial sulfide grain with skeletal reaction texture.

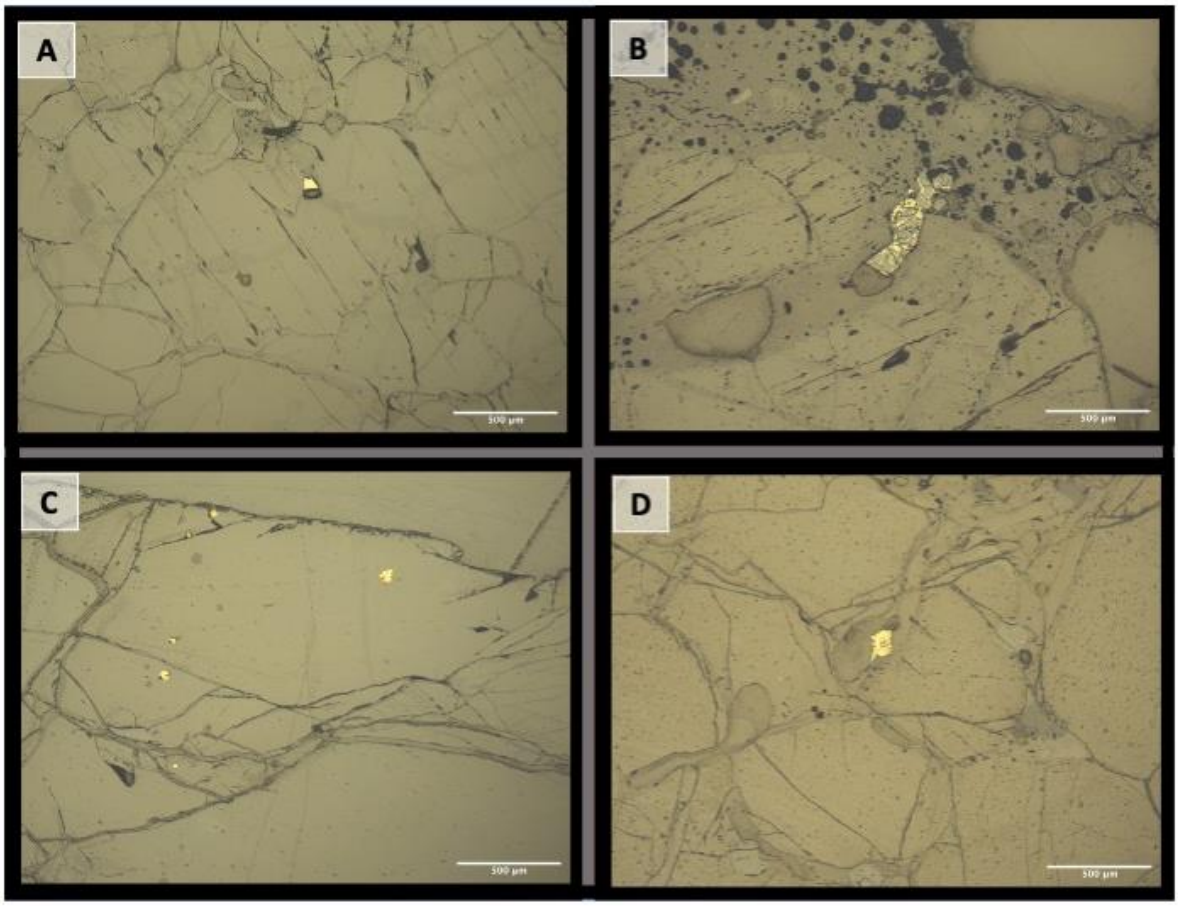

Figure S2.4 Examples of intra-granular (Type 1) and interstitial (Type 2) sulfides in the Ferrel Seamount peridotites. A) WOBA-3D-05, Type 1 intra-granular sulfide hosted orthopyroxene; B) WOBA-3D-12, Type 2 interstitial sulfide with a skeletal and partly altered texture, proximal to melt; C) WOBA-3D-10, Type 1 intra-granular sulfides hosted in orthopyroxene; D) WOBA-3D-17, Type 2 interstitial sulfide between clinopyroxene grains. Scale-bars are 0.5 mm.

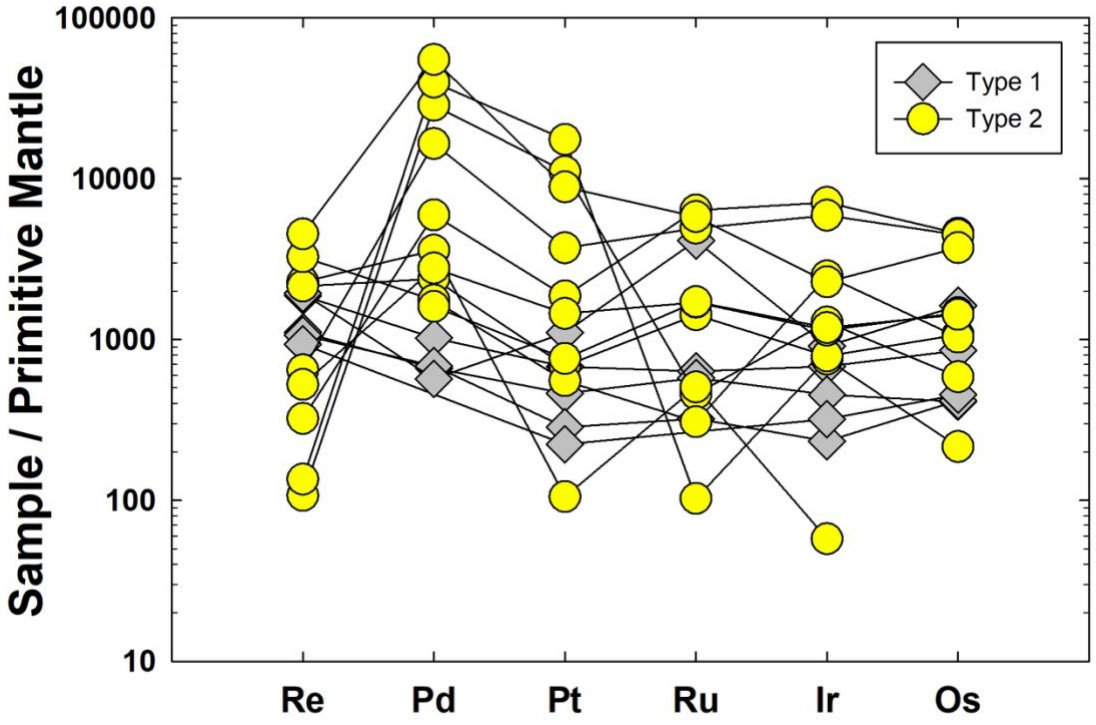

Figure S2.5 Primitive Mantle normalized highly siderophile element patterns for Ferrel Seamount peridotite sulfides. Primitive mantle composition is from Day et al. (2017).

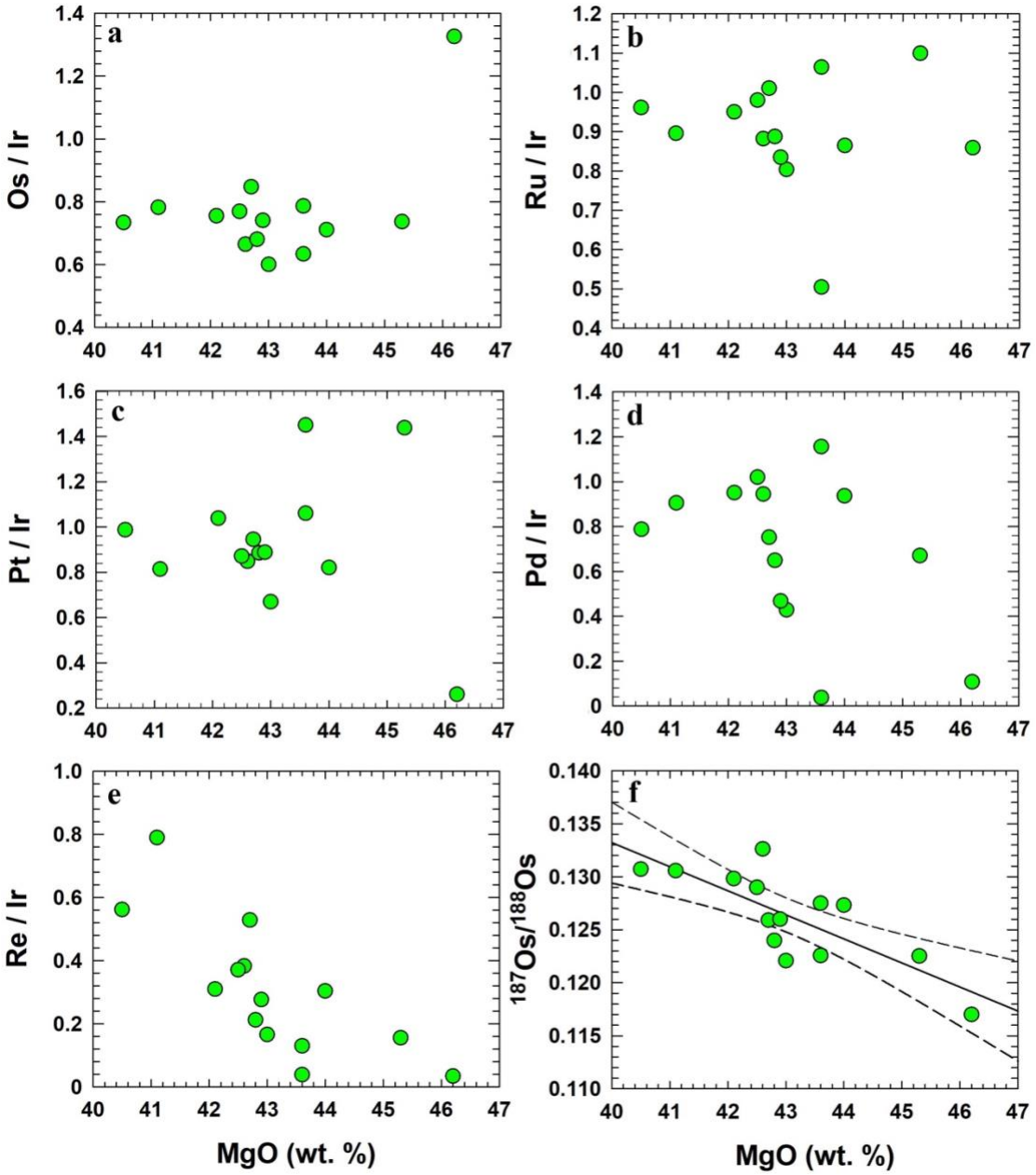

Figure S2.6 MgO variation diagrams for (a) Os/Ir, (b) Ru/Ir, (c) Pt/Ir, (d) Pd/Ir, (e) Re/Ir, and (f) $^{187}Os/^{188}Os$ with 95% confidence interval. Correspondence of $^{187}Os/^{188}Os$ and MgO in (f) juxtaposed with the lack of correspondence in (a)-(d) and weak correspondence in (e) suggests ancient melt depletion events are preserved by $^{187}Os/^{188}Os$ but are weakly preserved by inter-element ratios (Day et al., 2017).

CHAPTER 3 Highly Siderophile Elements and $^{187}Os/^{188}Os$ from Hawaiian Cumulate Xenoliths Show Potential Mixing Between the Loa and Kea Trends

3.1 Abstract

Cumulate xenoliths derived from primitive melts provide information on processes that occur during magma storage and modification in the crust. Major- and trace-element abundances, as well as highly siderophile element (HSE: Os, Ir, Ru, Pt, Pd, Re) abundances and $^{187}Os/^{188}Os$ are reported for 18 mafic and ultramafic xenoliths from Hualālai, Mauna Loa (Loa Trend) and Mauna Kea (Kea Trend). The Loa and Kea trends are two isotopically distinct endmembers that have been best defined by long-lived Rb-Sr, Sm-Nd and U-Th-Pb isotopes. The new samples provide the strongest constraints yet on $^{187}Os/^{188}Os$ for the Loa and Kea trend, defining more radiogenic compositions (0.1342 ±0.0043; all uncertainties are 2 St. Dev.) for the Loa trend than the Kea trend (0.1270 ±0.0062). There are no clear distinctions between absolute or relative HSE abundances between the two trends. These new results show that, in addition to lithophile radiogenic isotope systematics, there is clear distinction in long-term Re/Os between the mantle sources of the two trends. Several concepts have been presented to account for the distinction between the two trends, including addition of a recycled slab component in the mantle, or recycled lithosphere for the Loa trend, a depleted MORB mantle component for the Kea trend, and/or magma chamber wall rock assimilation. However, seismic and gravity studies suggest the presence of shared magma chamber and/or plumbing systems between volcanoes of Loa and Kea trend composition. These observations seem to contradict the available geochemical and isotopic data. In this chapter the

concepts regarding the Loa and Kea trend are evaluated and weighed against the new data and $^{187}Os/^{188}Os$ mixing models are uses to address the viability of different mixing scenarios.

3.2 Introduction

The Hawai'ian Islands are an oceanic hotspot situated on ~100 Ma Pacific lithosphere, with the Big Island of Hawai'i representing the largest and youngest island in the archipelago (Clague & Dalrymple, 1987). Hawai'i is made up of six volcanoes, five subaerial, Kohala, Hualālai, Mauna Kea, Mauna Loa, and Kilauea, and one submarine seamount, Kama'ehuakanaloa. In addition, Mauna Kea is the world's tallest volcano standing ~10,000 m from seafloor to summit, and Mauna Loa is the world's largest active volcano by volume at ~75,000 km^3 (Robinson & Eakins, 2006). The Hawaiian hotspot is among the largest, hottest and most productive hotspots (Hoggard et al., 2020; Sleep, 1990) with recent eruptions occurring in 2018, 2022 and 2023 at both Kilauea and Mauna Loa. Throughout their lifespans, each individual volcanic edifice has produced voluminous flows of high-MgO tholeiitic and picritic basalts, which have proven instrumental as windows into deep mantle processes (e.g., Norman & Garcia, 1999). Geochemical heterogeneities in the mantle beneath Hawai'i have been well documented and extend over broad spatial scales, but the causality is poorly constrained (e.g., Abouchami et al., 2005; Weis et al., 2011). Ocean island basalts (OIB) are thought to be a direct product of mantle melting with variable degrees of lithospheric and crustal contamination that can generally be constrained (e.g., Day, 2013; Stracke, 2012). The mantle plume which feeds the Hawaiian hotspot has geochemical and tomographic evidence suggesting it originates in the deep mantle, perhaps as deep as the core-mantle boundary (Brandon et al., 1998; French & Romanowicz, 2015; Montelli et al., 2006). This makes Hawai'i critically important from a geological perspective as it offers insight to the deep mantle, mantle mixing

processes, and crustal recycling, which contribute to the broader geochemical heterogeneity of Earth's mantle. Another unique feature of Hawaiian volcanism are the Loa and Kea trends. Although sub-parallel trends in OIB have been observed in volcanic chains across the Pacific basin (e.g.: Society Islands, Marquesas Islands, Foundation Seamount chain, Samoa Islands, and Galapagos Islands) (Chauvel et al., 2012; Harpp & Weis, 2020; Huang et al., 2011; Jackson et al., 2014; O'Connor et al., 2001; Payne et al., 2013), none are as distinct as the Loa and Kea trends of Hawai'i (Abouchami et al., 2005; Jackson et al., 2012; Weis et al., 2011). Additionally, no isotopically distinct parallel trends have been unequivocally identified in the Atlantic or Indian basins. This observation suggests geochemically distinct volcanic chain pairs may be tied to distinct physical properties of the Pacific mantle, such as being related to the vigor of the plume, spreading rate or changes in relative plate motion. However, processes responsible for the heterogeneity of sub-parallel trends within the lithosphere, crust, or magma transit system have not been completely ruled out.

The Loa and Kea trends are compositionally distinct in both major and trace element abundances (Hauri et al., 1996), radiogenic isotope ratios (e.g., Weis et al., 2011), and correspond to geographic tracks within the Hawaiian Archipelago, the Kea trend being the northern track line and Loa making the southern track (**Figure 3.1**). Kea trend basalts typically have lower SiO_2 when corrected for olivine fractionation than the Loa trend (Jackson et al., 2012). Incompatible element abundances are typically higher for the Kea trend than for Loa and have differing incompatible trace element ratios, such as Sr/Nb and Zr/Nb (Frey et al., 2016). Collectively these data have been interpreted to reflect different source melts. Conversely, similar incompatible major element ratios, such as K_2O/P_2O_5, observed in some Loa and Kea volcanoes, suggest a common source differentiated by processes within the plume and/or magma chambers (Frey et al., 2016; Jackson

et al., 2012). Both trends have distinct ranges in radiogenic isotope compositions which are most distinct in $^{206}Pb/^{204}Pb$ and $^{208}Pb/^{204}Pb$. This is better expressed in terms of $^{208}Pb^*/^{206}Pb^*$ which accounts for the ingrowth of radiogenic Pb over the course of Earth history (Abouchami et al., 2005). The Loa volcanoes are characterized by high $^{208}Pb^*/^{206}Pb^*$ versus their Kea counterparts (Abouchami et al., 2005). The Loa trend has high $^{87}Sr/^{88}Sr$ and low $^{143}Nd/^{144}Nd$ compared to the Kea trend with these systems showing poor correspondence with parent daughter ratio Rb/Sr and Sm/Nd for both trends. The geographical variations in these isotopes have been used to infer the lateral composition of the Hawaiian plume. Given the dispersion of Pb isotopes Abouchami et al. (2005) proposed an asymmetrically zoned plume while earlier models have argued for a concentrically zoned plume (Hauri et al., 1996; Lassiter & Hauri, 1998). In either case, differences in long-lived radiogenic isotopes require different initial compositions of the parent/daughter ratios which provides strong evidence for distinct mantle sources. The isotopic evidence is generally reflective of the broader Pacific mantle as a potential source for the Kea trend and the elevated $^{208}Pb^*/^{206}Pb^*$, $^{87}Sr/^{88}Sr$ in the Loa trend suggests an initial source enrichment in large ion lithophile elements (LILE) and U/Th (Tanaka et al., 2008). This initial enrichment in incompatible trace elements has been attributed to a recycled melt component possibly from the large low sheer velocity province (LLSVP) seismic anomaly observed at the core-mantle boundary in the South Pacific (Weis et al., 2011). Other theories accounting for the compositional heterogeneity suggests various forms of assimilation or contamination ranging from the shallow lithosphere and extending into the oceanic crust and volcanic edifices. Osmium isotopes and highly siderophile element (HSE) abundances have previously been employed to test these concepts. Because the HSE are chalcophile at typical mantle conditions and so hosted in sulfide phases (e.g., Carlson et al., 2005; Day, 2013; Mungall & Brenan, 2014), they are broadly independent of processes that affect

lithophile elements. The majority of Loa trend samples show supra-chondritic or radiogenic $^{187}Os/^{188}Os$ and the Kea trend is typically lower (Bizimis et al., 2007; Brandon et al., 1999; Hauri et al., 1996; Ireland et al., 2011; Ireland et al., 2009; Lassiter & Hauri, 1998), nearer chondritic values ($^{187}Os/^{188}Os_{chon}$ ~0.1296; Meisel et al. (2001)). This Os isotopic evidence has generally strengthened the case for source heterogeneity.

Recent petrological models (Gao et al., 2016; Gao et al., 2022; Lassiter et al., 2022; Yang et al., 2023), gravity models (Kauahikaua et al., 2000) and geophysical observations of micro earthquake loci (Wilding et al., 2023) suggest the possibility of common magma chambers and/or shared plumbing systems between specific Loa and Kea trend volcanoes, specifically Kilauea (Kea trend) and Mauna Loa (Loa trend). The micro seismicity observations suggest a common lithospheric magma reservoir and imply some degree of magma mixing may occur in the upper lithosphere prior to transiting through the crust. The petrologic models lead to a range of conclusions that suggest assimilation of lithospheric, crustal, or edifice material of older Hawaiian volcanoes. These observations are difficult to reconcile against the geochemical and isotopic heterogeneities. The isotopic disparities require long term fractionation of the parent/daughter isotopes and isolation in closed-system reservoirs. Open-system behavior between the two reservoirs has been shown to perturb radiogenic isotopic ratios, usually in the form of enrichment, but the open-system behavior must be reconciled with major and trace element data (Lassiter et al., 2022).

This study uses 18 mafic and ultramafic cumulate xenoliths collected from Hualālai, Mauna Loa and Mauna Kea and takes advantage of the compatible nature of HSE in mafic and ultramafic rocks reporting isotope dilution HSE abundances and Os isotope compositions. The mineral phases in these rocks concentrate the HSE allowing for a clearer assessment of Os isotopes

within the Loa and Kea trends. The xenoliths presented here are dunitic to gabbroic in composition and were likely sourced from a high-volume cumulate pile that precipitated from a primitive melt, preserving primary signatures. The HSE and Os isotope "toolbox" has proven valuable for elucidating mantle processes such as partial melting, slab recycling, refertilization, and metasomatism (Day, 2013; Day et al., 2017; Rehkamper et al., 1999). Using the HSE and $^{187}Os/^{188}Os$, this study evaluates various endmembers thought to contribute to the geochemical and isotopic distinctions between the Loa and Kea trend. Osmium isotope ratios are then used in mixing models to test the effect of magma mixing on observed $^{187}Os/^{188}Os$ compositions and evaluate geophysical models which suggest Hawaiian volcanos share complex magma storage and transport systems.

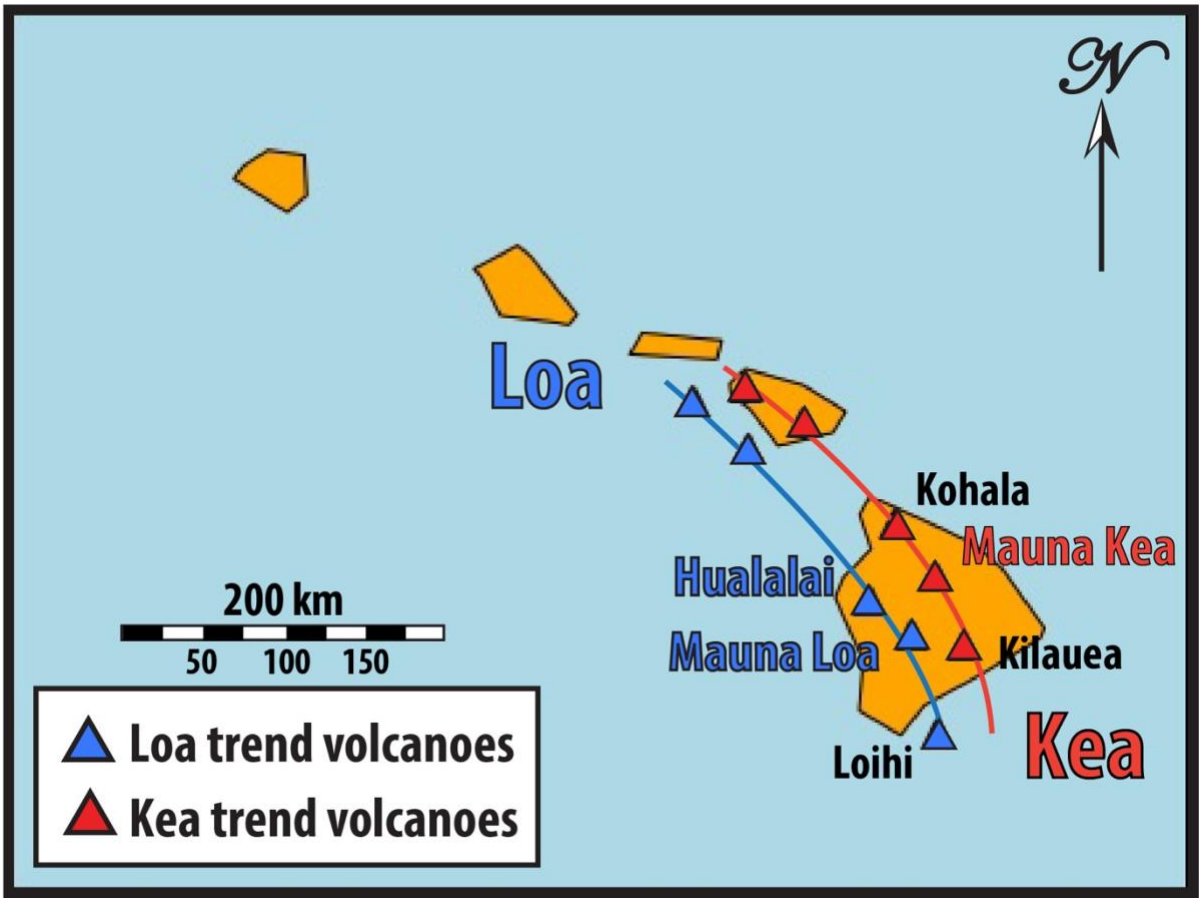

Figure 3.1 Simplified map of the Hawaiian Islands showing the Loa trend (blue) and Kea trend (red). Volcanoes sampled for this study are labeled in large font, color coordinated to their trends. The other Hawaiian volcanoes are labeled in smaller black font. Trends are based on Pb isotopes from Abouchami et al. (2005) and Weis et al. (2011).

3.3 Methods

Thirteen peridotite and five gabbro xenoliths were collected from Hualālai, Mauna Loa and Mauna Kea lava flows for analysis during field trips in 2015 and 2018. The Hualālai samples were extracted from the 1801 lava flow off Hawaii Route 200 and the Mauna Loa sample was collected from a flow downslope from the summit caldera. The Mauna Kea samples were collected from a debris field on the southern flank of Mauna Kea, upslope from Hawaii Route 200 (see **Table S3.2**

for coordinates). The xenoliths varied in size from ~5 cm to ~15 cm in diameter. Petrography was determined at the *Scripps Isotope Geochemistry Laboratory (SIGL)* using prepared sections ground to ~60 μm thick. The samples were sawn, buffed with corundum paper, and washed to remove saw marks, dust, and debris before being crushed in an alumina jaw crusher and powdered in an alumina shatterbox. All equipment was thoroughly cleaned between each sample to prevent cross-contamination.

Major element compositions, with the exception of samples MK1701, ML1702, and ML1703, were measured by X-ray fluorescence (XRF) at Franklin and Marshall College using a *PW 2404 PANalytical* XRF vacuum spectrometer following the procedures outlined in Boyd and Mertzman (1987). Major element analyses by XRF involved standard lithium tetraborate fusion techniques using 3.6:0.4 g $LiBO_4$:sample powder. Ferrous iron concentrations were determined by titration with potassium dichromate. Precision and accuracy are estimated using repeat analyses of standards, and the long-term precision and reproducibility are reported in Day et al. (2017).

Whole-rock trace element compositions, and major element compositions for samples ML1701, MK1702, and MK1703, were determined at SIGL using methods described in Day et al. (2014). One hundred milligram aliquots of sample powder were precisely weighed and digested in a 1:4 mixture of Teflon-distilled HNO_3:HF for >72 hours at 150˚C on a hotplate. Rock standards (BHVO-2, BCR-2, HARZ-01) and total procedural blanks were prepared along with the samples (**Table S3.2**). After drying down and sequential HNO_3 dry-down steps to break-down fluorides, clear sample solutions were diluted by a factor of 5000 in 2% HNO3 and spiked with a 1 ppb In solution to monitor instrumental drift. Solutions were measured using a *Thermo Scientific* iCAPq c quadrupole ICP-MS in standard mode. Reproducibility of the reference materials was better than 4.5% RSD, and elemental abundances were within error of the recommended ranges.

Osmium isotope and HSE (Re, Pd, Pt, Ru, Ir, Os) abundances were measured at *SIGL* using the methods described in Day et al. (2015). The sample powders were well homogenized, precisely weighed, then digested in sealed borosilicate Carius tubes with Os isotope and HSE "spikes" and 10 mL of a 2:3 mixture of Teflon-distilled HCl and Teflon-distilled HNO_3 that had been purged of Os. The samples were digested at 240°C for 72 hours. Osmium was then triply extracted from the acid using CCl_4, back-extracted into HBr and purified by micro-distillation. Rhenium and platinum group elements were separated from the solution with anion exchange columns, then measured on a *Thermo Scientific* iCAPq-c ICPMS in standard mode. Osmium isotope compositions were measured on a *Thermo Scientific* Triton thermal ionization mass spectrometer by peak-jumping in negative ion phase. The measurements were corrected for oxide and fractionation using a ratio $^{192}Os/^{188}Os = 3.08271$. Os concentrations were determined using ^{190}Os spike deconvolution and were blank-corrected. Loads of 70 pg UMCP Johnson-Matthey standards were used to monitor instrument precision. Measurements of the standards averaged 0.1138 ±0.0003 (2 St. Dev., n = 7). Procedural blanks for Os analyses (n = 2) had an average corrected $^{187}Os/^{188}Os$ of 0.1445 and [Os] of 4 pg. To determine HSE abundances by isotope dilution, isotopic ratios for individual elements were corrected for mass fractionation using the deviation of the standard average run on the day over the natural ratio for the element, and all reported values are blank corrected. HSE abundances of these blanks (n = 3) were: Re = 0.009 ppb, Pd = 0.098 ppb, Pt = 0.052 ppb, Ru = 0.096 ppb, Ir = 0.214 ppb.

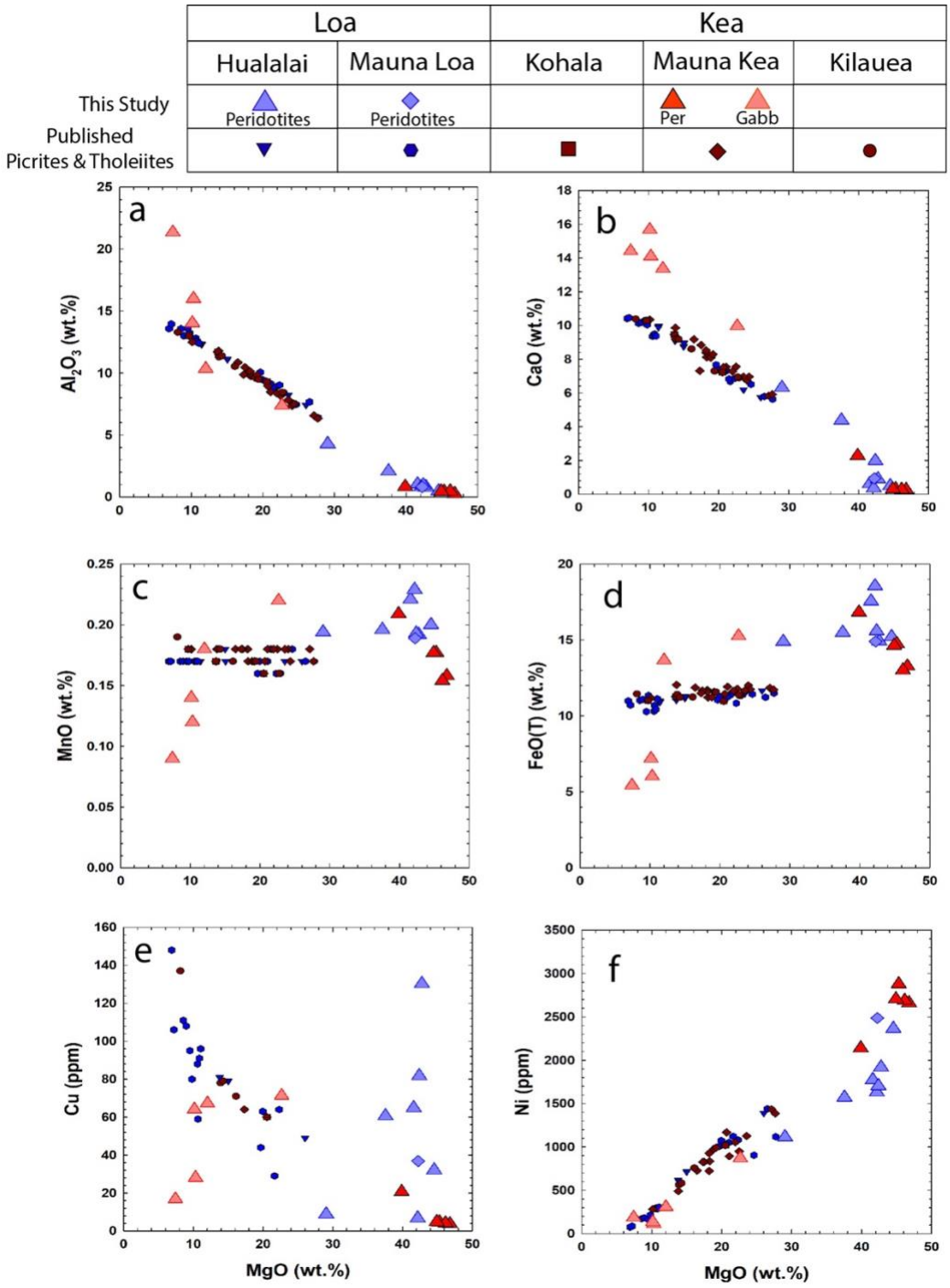

Figure 3.2 Major element versus MgO Harker diagrams for mafic and ultramafic xenoliths from this study and tholeiitic and picritic lavas from the literature. (Per = peridotite; Gabb = gabbro) Literature sources were selected from the compilation of Jackson et al. (2012). A comprehensive list of references is provided in the Data Availability Section.

3.3 Results

3.3.1 Bulk-Rock Major & Trace Element Abundance Compositions

Eight samples, seven from Hualālai and one from Mauna Loa, representative of the Loa trend, are ultramafic xenoliths, dominantly olivine and clinopyroxene with spinel ±orthopyroxene. Sample HI1503 from Hualālai is a spinel bearing feldspathic peridotite. Of the ten Mauna Kea samples representative of the Kea trend, five fit a similar description as ultramafic xenoliths, along with five gabbroic samples, HI1504E, -F, -G, -H, and I. The Loa samples range in MgO content from 29.1 to 44.6 wt.% and Mg-numbers from 79.4 to 85.3 wt. %. Alumina compositions for this set spans 0.46 to 4.28 wt.% and CaO from 0.35 to 6.31 wt.% and correlate negatively with MgO (**Figure 3.2**). The feldspathic peridotite, HI1503 defines the high end of this range. Ultramafic Mauna Kea samples are similar in MgO composition to ultramafic Loa trend rocks, with 39.9 to 46.8 wt.% with corresponding Mg-numbers 82.4 to 87.5 wt.%. The mafic Kea samples' MgO content varies from 7.4 to 22.7 with Mg-numbers from 63.5 to 74.6. CaO and Al_2O_3 compositions cover a range 10.0 to 15.7 wt.% and 7.4 to 21.4 wt.% respectively. CaO/Al_2O_3 for all three volcanoes define a narrow range averaging 1.2 ±0.6 wt.%. Average $Fe_2O_{3(T)}$ is 13.9 ±3.7 wt.% showing little variation with respect to MgO (**Figure 3.2**). Loss on ignition (LOI) is low throughout the entire sample set showing that the samples are fresh, averaging 0.53 wt.% with the highest value of 2.27 wt.% (HI10-01) with some negative values likely resulting from Fe^{2+} oxidation during the heating process for LOI measurements. Contents of MnO are low throughout all samples and defines a narrow range averaging 0.18 ±0.04 wt.%. Average Ni concentrations for the Loa ultramafic samples is 1821 ±441 ppm, and 2614 ±279 ppm for the Mauna Kea ultramafic samples, and 323 ±315 ppm for the Mauna Kea gabbros. Both sample sets show a strong positive

correlation with MgO (**Figure 3.2**). Copper concentrations are considerably more variable averaging 39 ±36 ppm for both sample sets.

Primitive mantle (PM) normalized incompatible trace element patterns for Hualālai and Mauna Loa are typically depleted with one exception, HI1503. This sample is ~10× primitive mantle values and has a strong negative Pb anomaly. Sample HI1502B is near parity with PM showing depletions Rb, Ba, Th, U, and Nb. The remainder are depleted relative to PM showing positive Ba, Ta, Pb, and Ti anomalies except for HI10-01 which has a negative Ba anomaly. HI1502A has positive Zr and Hf anomalies that are not observed in the other samples. Unlike Hualālai samples the Mauna Loa sample (ML1701) is depleted in Rb and Ba (**Figure 3.3a**). The mafic Mauna Kea samples show variable degrees of enrichment relative PM with strong Ba, Sr, and Eu anomalies attributable to the high plagioclase abundance. Notably, HI1504H has strong positive Ba, Nb, Ta, and Ti anomalies. Like the Loa samples the ultramafic Mauna Kea sample are variably depleted relative to PM. Like ML1701, HI1504D and MK1702 are strongly depleted in Rb and Ba, and HI1504D shows a prominent negative Sr anomaly (**Figure 3.3b**). OIB trace element ratios (Hofmann, 1997) Ce/Pb, Sr/Nd, and Nb/Zr for the Loa samples are typically lower than the Kea samples (Avg Loa Ce/Pb = 12.1 ±12.9; Avg Loa Sr/Nd = 12.5 ±4.7; Avg Loa Nb/Zr = 9.9 ±4.0; Avg Kea Ce/Pb = 52.8 ±43.7; Avg Kea Sr/Nd = 53.1 ±59.4; Avg Kea Nb/Zr = 11.7 ±2.7), whereas Th/U is lower in the Kea samples (Avg Loa Th/U = 2.5 ±0.5; Avg Kea Th/U = 1.9 ±0.7). Rare Earth element patterns (REE) for the Loa and ultramafic Kea samples are typically flat except for HI1503 which has an elevated La/Yb ratio. HI1502B, HI1502D, and HI1503 are REE enriched relative PM with HI1503 showing the strongest enrichment exceeding one order of magnitude in the LREE (**Figure 3.4a**). The mafic Kea samples and one ultramafic sample

(HI1504B) show a broad hump shaped pattern with the previously noted positive Eu anomaly (**Figure 3.4b**).

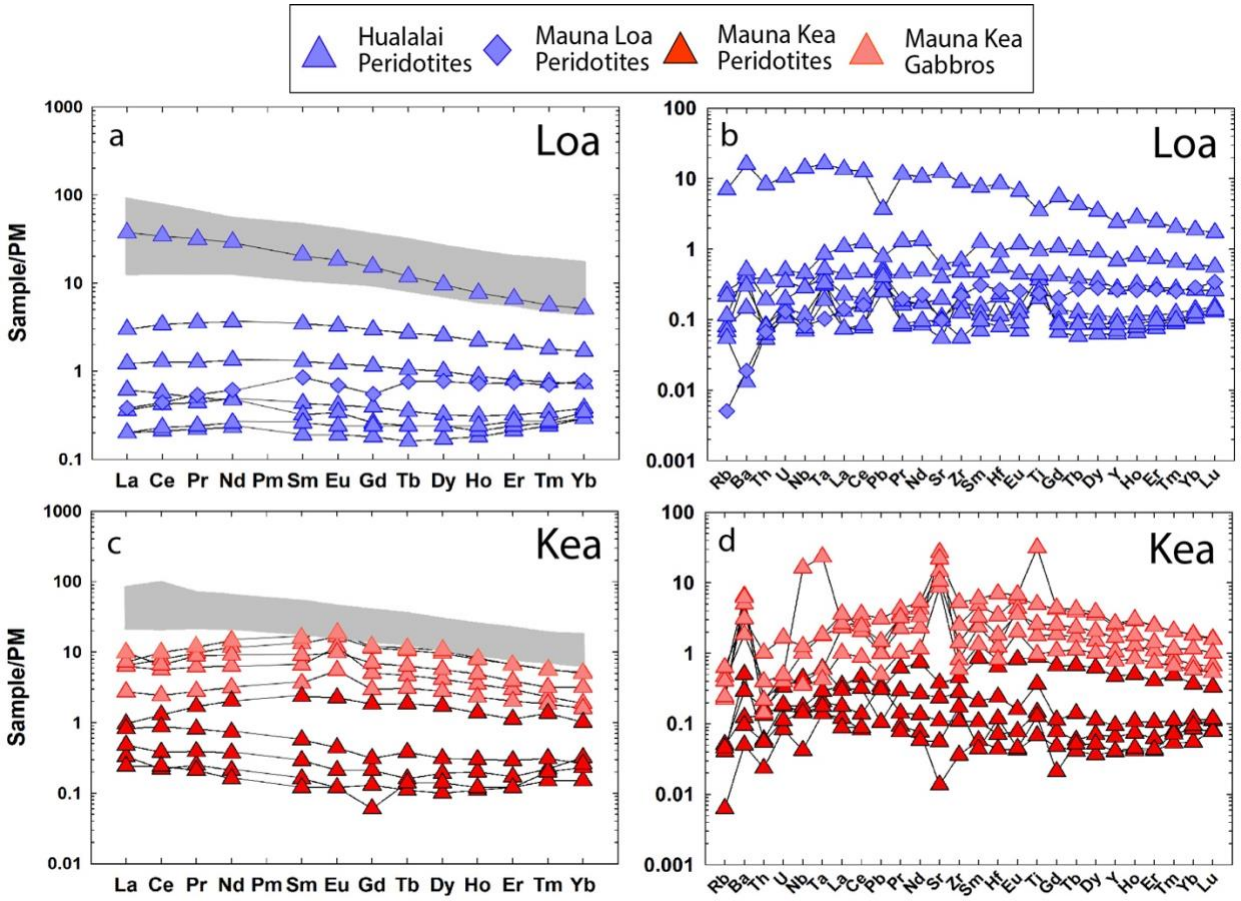

Figure 3.3 Primitive mantle normalized Rare Earth element (REE) and incompatible trace element (ITE) diagrams for Loa and Kea trend mafic and ultramafic xenoliths. (a & c) Loa and Kea trend REE with fields of published picritic and tholeiitic basalts. (b 7 d) Loa and Kea trend TE. Primitive mantle normalization from McDonough and Sun (1995). Literature sources were selected from the compilation of Jackson et al. (2012). A comprehensive list of references is provided in the Data Availability Section.

3.3.2 Osmium Isotopes & Highly Siderophile Element Abundances

All eighteen samples from Hualālai, Mauna Loa, and Mauna Kea were analyzed for HSE (HSE: Re, Pd, Pt, Ru, Ir, Os) abundances and Re-Os isotopes, these data are presented in **Table 3.1**. Platinum, Ru, Ir, and Os show positive covariations with MgO, consistent with compatible

element behavior. Mauna Kea samples show much better correlation than do those from Hualālai and Mauna Loa which display considerable scatter. In the case of Re and Pd, both sample sets show no statistical correlation with MgO, however demonstrably trend to lower Re and Pd with higher MgO. However, Pd/Ir and Pt/Ir from Mauna Kea have strong negative correlations with MgO and Mg-number, while the Loa trend samples show no variation. This suggests that in the case of Mauna Kea, olivine accumulation is a controlling factor in IPGE abundances. Additionally, Re and Pd correlate positively with Cu, and to a lesser degree Pt, suggesting PPGE abundances are controlled by interstitial, metasomatic Cu-sulfide phases. Primitive mantle normalized abundances of the HSE show similar but highly variable fractionation patterns between the three Hualālai, Mauna Loa, and Mauna Kea volcanoes, although not to the same degree as those reported by Pitcher et al. (2009). Samples HI1504A, -D, and -E from Mauna Kea are strongly depleted in Pd and Pt, as well as HI1502C from Hualālai. The Mauna Kea samples are all depleted relative to PM, as are Mauna Loa and the majority of Hualālai except for HI1502C and HI1503.

Osmium isotopic ratios for Mauna Kea average 0.1270 ±0.0062 (all uncertainties reported at 2 St. Dev.); close to the depleted mantle value (0.1296) from Meisel et al. (2001) and slightly less radiogenic than the average from previous studies of Kea trend picrites and tholeiitic basalts (Avg = 0.1312 ±0.0068) (Ireland et al., 2009; Jackson et al., 2012). Hualālai and Mauna Loa xenolith samples are distinctly more radiogenic with average Os isotopic ratios of 0.1342 ±0.0043, with one exception (HI1503, 0.12879 ±0.0003), consistent, in this case, with previous Loa trend studies from lavas (Avg = 0.1354 ±0.0027; (Ireland et al., 2009; Jackson et al., 2012). Osmium isotopes show little if any variation with respect to MgO content, Mg-number, or Os concentration, unlike, for example, Canary Island ultramafic xenoliths and lavas which become more radiogenic with decreasing Os concentration (Day et al., 2010; Day et al., 2022). Concentrations of Os

increase positively with MgO, particularly for the mafic Kea sample becoming more scattered for the ultramafic sample in both the Loa and Kea sets.

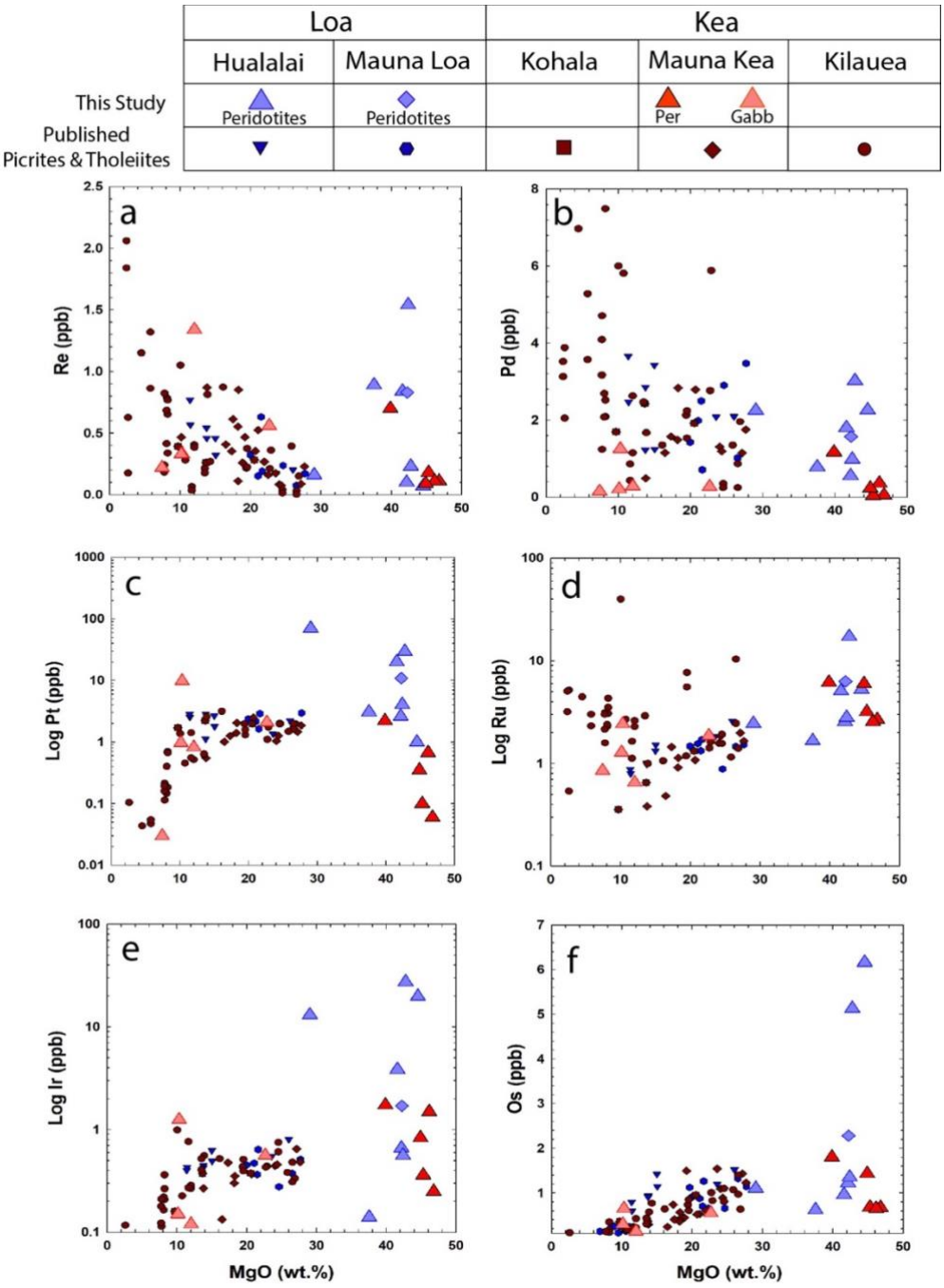

Figure 3.4 HSE versus MgO Harker diagrams for mafic and ultramafic xenoliths from this study and tholeiitic and picritic lavas from the literature. Literature sources were selected from the compilation of Jackson et al. (2012). A comprehensive list of references is provided in the Data Availability Section.

Table 3.1 Whole-rock Re-Os isotope and highly siderophile element abundances (ng g^{-1}) for Hawaiian cumulate xenoliths.

Sample	Location	MgO (wt%)	Re	Pd	Pt	Ru	Ir
HI1501	Hualālai	41.6	0.84	1.80	20.03	5.09	3.85
HI1501 duplicate			0.28	2.09	7.70	2.36	1.40
HI1502A	Hualālai	42.2	0.10	0.55	2.60	2.55	0.66
HI1502A duplicate			0.14	0.68	1.88	1.24	0.28
HI1502B	Hualālai	37.6	0.89	0.78	3.06	1.66	0.14
HI1502B duplicate			0.90	1.00	1.79	0.49	0.42
HI1502C	Hualālai	42.8		3.02	29.51	17.18	27.41
HI1502C (i) duplicate			0.23	0.18	0.10	5.01	0.08
HI1502C (ii) duplicate			1.30	7.80	19.38	10.67	21.60
HI1502D	Hualālai	42.4	1.54	0.98	4.06	2.80	0.56
HI1502D duplicate			1.05	1.33	2.62	1.19	0.05
HI1503	Hualālai	29.1	0.16	2.25	69.98	2.44	13.06
HI1503 duplicate			0.10	2.18	6.65	0.77	0.53
ML1701	Mauna Loa	42.3	0.83	1.57	10.87	6.30	1.70
HI10-01	Hualālai	44.6	0.07	2.26	0.99	5.27	19.76
HI1504A	Mauna Kea	45.3	0.18		0.10	3.18	0.36
HI1504A duplicate			0.07	0.04	0.04	1.79	0.22
HI1504B	Mauna Kea	39.9	0.70	1.17	2.21	6.16	1.73
HI1504B duplicate			0.14	1.57	1.26	1.78	0.76
HI1504D	Mauna Kea	46.8	0.11	0.05	0.06	2.67	0.25
HI1504D duplicate			0.06	0.04	0.05	1.65	0.22
HI1504E	Mauna Kea	7.4	0.22	0.15	0.03	0.85	
HI1504E duplicate			0.28	0.15	0.04	0.09	
HI1504G	Mauna Kea	10.1	0.33	0.21	0.97	1.28	0.15
HI1504G duplicate			0.20	0.27	0.74	0.41	0.13
HI1504F	Mauna Kea	10.3	0.33	1.25	9.82	2.42	1.25
HI1504F duplicate			0.33	1.82	6.15	1.07	0.83
HI1504H	Mauna Kea	12.0	1.34	0.28	0.82	0.65	0.12
HI1504H duplicate			1.40	0.26	0.51	0.24	0.07
HI1504I	Mauna Kea	22.7	0.56	0.27	2.08	1.86	0.56
Sample	Location	MgO (wt%)	Re	Pd	Pt	Ru	Ir
HI1504I duplicate			0.34	0.24	1.31	0.72	0.35
MK1702	Mauna Kea	46.2	0.11	0.36	0.67	2.54	1.49

Table 3.1 Whole-rock Re-Os isotope and highly siderophile element abundances (ng g^{-1}) for Hawaiian cumulate xenoliths. (Continued)

MK1703	Mauna Kea	44.9	0.09	0.23	0.35	5.98	0.83
Avg Loa Trend		40.30	0.59	1.90	11.51	4.28	6.26
2σ		9.9	1.0	3.8	37.4	9.2	19.5
Avg Kea Trend		28.56	0.39	0.52	1.60	1.92	0.60
2σ		34.9	0.8	1.2	5.2	3.6	1.1

Sample	Os	Pt/Ir	$^{187}Re/^{188}Os$	2σ	$^{187}Os/^{188}Os$	2σ	γOs
HI1501	0.958	5.2	4.1782	0.152	0.13671	0.00015	5.5
HI1501 duplicate	5.294	5.5	0.25511	0.008	0.13606	0.00012	5.0
HI1502A	1.225	4.0	0.37989	0.015	0.13381	0.00014	3.2
HI1502A duplicate	0.968	6.7	0.79473	0.024	0.12950	0.00017	-0.1
HI1502B	0.620	21.7	6.91755	0.245	0.13476	0.00015	4.0
HI1502B duplicate	0.676	4.3	7.41011	0.222	0.12914	0.00018	-0.4
HI1502C		1.1			0.13463	0.00003	3.9
HI1502C (i) duplicate	5.132	1.3	0.21683	0.007	0.13392	0.00027	3.3
HI1502C (ii) duplicate	8.047	0.9	0.78076	0.023	0.13632	0.00026	5.2
HI1502D	1.345	7.2	5.52654	0.095	0.13444	0.00008	3.7
HI1502D duplicate	0.702	47.6	7.17755	0.215	0.13163	0.00020	1.6
HI1503	1.099	5.4	0.70942	0.028	0.12879	0.00014	-0.6
HI1503 duplicate		12.5	0.63315	0.019			
ML1701	2.282	6.4	1.74587	0.066	0.13475	0.00013	4.0
HI10-01	6.160	0.1	0.05638	0.001	0.13474	0.00005	4.0
HI1504A	0.684	0.3	1.27014	0.025	0.12885	0.00013	-0.6
HI1504A duplicate	1.086	0.2	0.31121	0.009	0.12455	0.00011	-3.9
HI1504B	1.805	1.3	1.88061	0.035	0.12935	0.00015	-0.2
HI1504B duplicate	0.711	1.7	0.93806	0.028	0.12250	0.00011	-5.5
HI1504D		0.2					
HI1504D duplicate	0.666	0.2	0.42313	0.013	0.12263	0.00014	-5.4
HI1504E	0.086		12.50113	0.237	0.13063	0.00033	0.8
HI1504E duplicate	0.687		2.01670	0.061			
HI1504G	0.303	6.3	5.27864	0.199	0.12901	0.00017	-0.5
HI1504G duplicate	0.264	5.8	3.64303	0.109			
HI1504F	0.648	7.8	2.44331	0.047	0.12859	0.00016	-0.8
HI1504F duplicate	0.706	7.4	2.22475	0.067	0.12254	0.00018	-5.4
HI1504H	0.139	7.0	46.3209	0.696	0.13011	0.00023	0.4
HI1504H duplicate	0.615	7.3	10.9512	0.329	0.12351	0.00036	-4.7
Sample	Os	Pt/Ir	$^{187}Re/^{188}Os$	2σ	$^{187}Os/^{188}Os$	2σ	γOs

Table 3.1 Whole-rock Re-Os isotope and highly siderophile element abundances (ng g^{-1}) for Hawaiian cumulate xenoliths. (Continued)

HI1504I	0.553	3.7	4.83516	0.089	0.12969	0.00018	0.1
HI1504I duplicate	0.705	3.7	2.30702	0.104	0.12509	0.00030	-3.5
MK1702	0.648	0.4	0.82390	0.016	0.12925	0.00015	-0.3
MK1703	1.435	0.4	0.28722	0.006	0.12913	0.00014	-0.4
Avg Loa Trend	2.07	8.65	2.6273		0.13351		3.0
2σ	5.1	24.1	5.85		0.005		4.1
Avg Kea Trend	0.69	3.37	5.7915		0.12703		-2.0
2σ	0.9	6.2	22.04		0.006		4.8

3.4 Discussion

3.4.1 The use of ultramafic xenoliths for Os isotopes and HSE abundance studies

Ultramafic xenoliths are useful samples for HSE abundance and Os isotope studies. Under conditions of partial melting, the HSE (which include the platinum group elements, Os, Ir, Ru, Rh, Pt and Pd) experience substantial fractionation (Rehkamper et al., 1999). This is evident from the highly variable degrees of fractionation between MORB, OIB or komatiites, where komatiites are more HSE enriched than OIB or MORB (Day, 2013). Abundances of the HSE are largely controlled by sulfide phases as opposed to silicate phases. Furthermore, Platinum-PGE (PPGE: Pd and Pt) are usually hosted by Cu-sulfide phases which are commonly metasomatic grains precipitated interstitially between silicate crystals. Iridium-PGE (IPGE: Ru, Ir, and Os) are concentrated in primary sulfide phases, often included within olivine and to a lesser degree Cr-spinel (Luguet et al., 2007). Rhenium is not as strongly controlled by sulfide phases and instead is moderately incompatible in basaltic melts. Due to their varying degrees of compatible behavior Pd, Pt, Ru, Ir, and Os tend to concentrate in early formed oxide or silicate phases. This is

advantageous for working with olivine-bearing cumulates from basaltic melts because they will incorporate the sulfide-included olivine, whereas the basalts will typically have lower HSE concentrations. This is particularly important in the case of Os where studies have shown Os isotope ratios can be heavily leveraged in low Os concentrated samples. These samples with < 0.030 – 0.050 ng/g Os typically show highly radiogenic $^{187}Os/^{188}Os$, which has been attributed to various forms of crustal contamination (Day, 2013; Marcantonio et al., 1995; Widom et al., 1999). Consequently, high Os concentrations make overprinting from low concentration alkali basalt unlikely, an important consideration given the abundance of post-shield stage alkali volcanism.

Isotopic heterogeneity in the mantle has been well-documented through studies of OIB and is thought to be the result of several distinct sources existing in the mantle such as recycled lithosphere, oceanic and continental crust, and the associated sediments that have been subducted into the mantle. These distinct sources produce a broad range of time integrated lithophile isotopic ratios, as well as $^{187}Os/^{188}Os$ (Day et al., 2009; Ireland et al., 2009; Simon et al., 2008; Waters et al., 2020; Widom et al., 1999). The observed fractionation of these parent-daughter isotopes makes it possible to infer the source components of the mantle sampled by OIB.

3.4.2 Petrogenesis of mafic and ultramafic Hawaiian xenoliths

Incorporation of Pacific mid-ocean ridge basalt (MORB) into Hawaiian lavas has been suggested and Pacific MORB gabbro xenoliths have been documented in several Hawaiian lava flows (Gao et al., 2016). Therefore, it is important to properly distinguish the gabbroic samples in this study from lower crustal gabbro originating from the Pacific plate. The five gabbro xenoliths examined here have petrologic characteristics, major and trace element compositions, and $^{187}Os/^{188}Os$ consistent with cumulate gabbros precipitated from a Kea-like melt. These xenoliths

have MgO, FeO(T) whole rock compositions, and Mg-numbers which fall within the ranges of gabbros precipitated from tholeiitic melts defined by Fodor and Vandermeyden (1988). Primitive mantle normalized REE patterns are similar to those calculated from clinopyroxenes by Sjoblom et al. (2023), showing relative REE enrichments, whereas LREE depletion would be typical of a MORB composition. Additionally, radiogenic $^{187}Os/^{188}Os$ ($\geq$0.213) for the crust underlying Hawai'i was reported by Peucker-Ehrenbrink et al. (2003), which is in strong contrast to the low $^{187}Os/^{188}Os$ (Avg = 0.1274 ±0.0064, 2 St. Dev.) for the Mauna Kea gabbros reported in this study and more reminiscent of previously reported Kea trend values (e.g.: Ireland et al., 2011).

Compatible and incompatible major elements for ultramafic xenoliths presented here correlate well with previously documented shield and post-shield stage tholeiites and picrites (**Figure 3.2 a-f**) plotting along regression trends, suggesting they are an accumulation of crystals fractionated from a genetically related melt. Deviations from the trends in Al_2O_3 and CaO for Mauna Kea gabbros are from the accumulation of plagioclase (**Figure 3.2a & b**). Parental melt MgO composition estimates for shield-stage tholeiites are significantly higher (~15-20 wt.%) (Ireland et al., 2009; Norman & Garcia, 1999) than most subaerially erupted basalts (<10 wt.%). This unusually high MgO content would likely lead to large volumes of olivine precipitating from the parent melt during magma storage. Gravity models of the Hawaiian volcanoes indicate the presence of high-density zones of material underlying many of the edifices. These cores correspond to depths ~10-14 km below present-day sea level at a modeled density of 3300 kg/m^3, consistent with voluminous olivine cumulate piles extending from crustal depths to within the volcanos (Kauahikaua et al., 2000). This idea is supported by the extensive number of picritic (olivine-rich) lava flows documented in Hawai'i. Many of these samples entrain olivine with primitive melt inclusions indicating that they are antecrysts scavenged from the cumulate pile

(Wieser et al., 2019). Clinopyroxene is the primary reservoir of the REE in peridotites and as such leverages the REE abundances. Depleted abyssal peridotites and Pacific MORB are characterized by strongly-depleted clinopyroxene REE patterns. Neither Loa nor Kea samples from this study reflect strong LREE depletions, having average $(La/Yb)_{PM}$ of ~2.0 ±1.6. Absolute and relative HSE abundances correspond well with other documented Hawaiian lavas (Pitcher et al., 2009; Ireland et al., 2009; Jackson et al., 2012) which in the case of the HSE, tend to be higher than Pacific MORB (Tatsumi et al., 1999). Due to their compatible behavior, the HSE fractionate to the residue during partial melting of the lithosphere, resulting in a melt with low HSE abundances. Incorporation of Pacific crust would have a dilutionary effect on HSE abundances. Likewise, Re is a moderately incompatible element and shows relative depletions in abyssal peridotites, whereas these samples, particularly from the Kea trend, have relative enrichments in Re with variable degrees of fractionation in the HSE. Given these factors a crustal or mantle origin for these xenoliths can be reasonably excluded. Instead, provided the similarities with a broad suite of Hawaiian lavas the stronger likelihood is these xenoliths crystalized from a shallow magma chamber(s) from a tholeiitic melt.

3.4.3 Patterns of HSE fractionation in Loa and Kea cumulates

Previous studies of the HSE in Hawaiian basalts have shown that HSE concentrations are broadly governed by olivine, and to a lesser degree spinel accumulation (Ireland et al., 2009; Pitcher et al., 2009), made evident by good positive or negative correlations with MgO (**Figure 3.4 a-f**). Selected HSE patterns also tend to be depleted versus PM estimates, with Re showing variable enrichment to moderate depletion, reflecting fractionation of the HSE from parental melts in the mantle. That holds true for most xenoliths reported here, with one notable exception

occurring in one aliquot of Hualālai sample HI1502C, which is slightly enriched in the HSE relative to PM. A second measurement of this sample shows strong depletions in Pd, Pt, and Ir. This disparity is most likely a result of nuggeting effects which can occur due to uneven distribution of micro sulfide minerals in whole rock powders. Other examples of PGE enrichment in the xenolith set are Hualālai samples HI1501, HI1503, and HI10-0, which show variable enrichments in Pt and Ir. HI1501 shows a moderate enrichment in Pt and Ir, near unity. Duplicate measurement of this sample reproduces similar Pt and Ir patterns, but does not show the same degree of enrichment relative to PM. HI1503 is more extreme with a duplicate measurement showing Pt near unity with PM and relative depletion in Ir. Sample HI10-01 is depleted in Pt with a strong enrichment in Ir. The PGE pattern of the Mauna Loa sample, ML1701, is more reflective of the broader Hualālai sample set. A possible cause of these fractionation patterns could be the trace presence of sub-microscopic platinum group minerals (PGM) entrained in olivine, however, Ru depletions relative to Pt and Ir cast doubt on this hypothesis. Another possible explanation could be equilibration of the cumulate pile with multiple pulses of magma fractionated from the parent melt.

Samples from Mauna Kea are much more uniform than those representing the Loa trend, Hualālai and Mauna Loa. HI1504F is the only sample with a modest enrichment in Pt relative to PM, the rest of the PGE throughout the suite are variably depleted. The IPGE for both the gabbro and peridotite xenoliths are broadly similar, while the PPGE shows variable degrees of fractionation between the two groups. Two of the xenolith samples, HI1504A and -D, show prominent Pd-Pt fractionation patterns (**Figure 3.5b**). These are also the most magnesian samples of the Kea set with the highest MgO and Mg-numbers, and both are at the upper range of Ni content. Previous studies have shown that IPGE have a strong affinity for mono-sulfide solid

solution (MSS) which is highly compatible in the mantle (e.g., Mungall & Brenan, 2014). The PPGE-rich Cu-sulfide phases are moderately incompatible during mantle melting, resulting in depletion of Pd and Pt, and a relative enrichment in Ru, Ir, and Os in mantle residues. This evidence along with elevated MgO and Ni contents might suggest a lithospheric origin for these two samples, however petrographic evidence does not correlate with this as both sample exhibit fine grain cumulate textures. The more likely scenario is that the HSE abundances of these samples are leveraged by their higher olivine and spinel content, consistent with the conclusion of Ireland et al. (2009).

The PM normalized Re concentrations are similar between published lavas and xenoliths from Loa and Kea. Because Re is moderately incompatible during magmatic differentiation, Re contents should be elevated in the melt versus cumulates, due to crystal-liquid fractionation. Relative Re abundances are only slightly elevated at best compared to the xenoliths. Previous studies have shown that extrusive lavas, particularly those from Hawai'i, can experience a draw-down in Re due to volatile loss if the sulfide phase hosting Re is not included within a silicate phase (Day, 2013; Ireland et al., 2009; Pitcher et al., 2009). This process can likely explain the similarity in relative Re concentrations between xenoliths and lavas given the xenoliths crystalized at depth, and so did not experience degassing during quenching. There is also very little correlation between absolute HSE abundances with melt depletion indicators such as Al_2O_3, Cao or La/Yb. Although when compared to the broader Hawaiian data set from the literature, a trend becomes apparent versus Al_2O_3 and CaO, but not La/Yb. Inter-PGE ratios also show a broad correlation with MgO, but none whatsoever with La/Yb and weak correlations with Al_2O_3 (**Figure 3.6 a & b**). Bulk rock MgO compositions are strongly leveraged by olivine abundance but Al_2O_3 and trace element ratios, such as La/Yb, are largely independent from olivine abundance as there are minimal

concentrations of incompatible elements in olivine. The primary driver of Al_2O_3 and La/Yb fractionation is the degree of melting. This suggests that the primary control on absolute and relative abundances of IPGE for Hawaiian samples is from olivine accumulation rather than melt depletion.

An estimated parental melt composition for the HSE in Hawai'i was modeled by Ireland et al. (2009) by linear regression to a MgO reference of 16 weight percent for each Hawaiian volcanic center. The estimated parental melt from each volcano was similar and therefore assumed to be derived from a common heterogeneous deep mantle source. This estimated composition is plotted with the data presented in this study in **Figure 3.5 a & b**. In most cases the peridotite IPGE abundances from both the Loa and Kea samples are variably enriched versus the parental melt estimate whereas the gabbros are generally depleted or near unity. Loa samples are generally Pt enriched and Pd depleted, while all the Kea peridotites and all but two gabbros are Pt and Pd depleted. This shows that IPGE behaved compatibly and PPGE behaved incompatibly during fractional crystallization and strengthens the argument of olivine (± included sulfides and PGM) accumulation being the predominant control over IPGE abundance. A key difference between the Loa and Kea samples is the behavior of Pt relative to the parent melt. A possible explanation for the Loa enrichment and Kea depletion could lie in the various mixing end members which have been attributed to the Loa and Kea trends and their and subsequent metasomatic effects. For example, Lassiter and Hauri (1998) proposed, based on radiogenic $^{187}Os/^{188}Os$ and heavy $\delta^{18}O$ isotope ratios, that the Loa trend end member incorporates recycled upper crust ±sediment, while the Kea trend incorporates recycled lithosphere and lower crust given the more mantle-like $^{187}Os/^{188}Os$ and low $\delta^{18}O$. A sedimentary and crustal mixing end member would be consistent with elevated Pt as well as elevated Cu composition which can be observed for Loa peridotites in **Figure**

3.2e. In contrast none of the Kea peridotites and the majority of gabbros show Pt depletions relative parental melt estimate. This is generally consistent with the idea of the Kea trend incorporating a more depleted component such as recycled lithosphere. Another possibility is the addition of Fe-Mn crustal material. Precipitation of Fe-Mn nodules can scavenge Pt from the seafloor, and their addition into the melt column could theoretically leverage HSE and Os isotopes (Baker & Jensen, 2004). This seems to readily explain the elevated Pt and radiogenic Os observed in the Loa samples. However, MnO content for the Loa samples remains considerably low and the slight correlation of FeO(T) with MgO is more likely a result of olivine content.

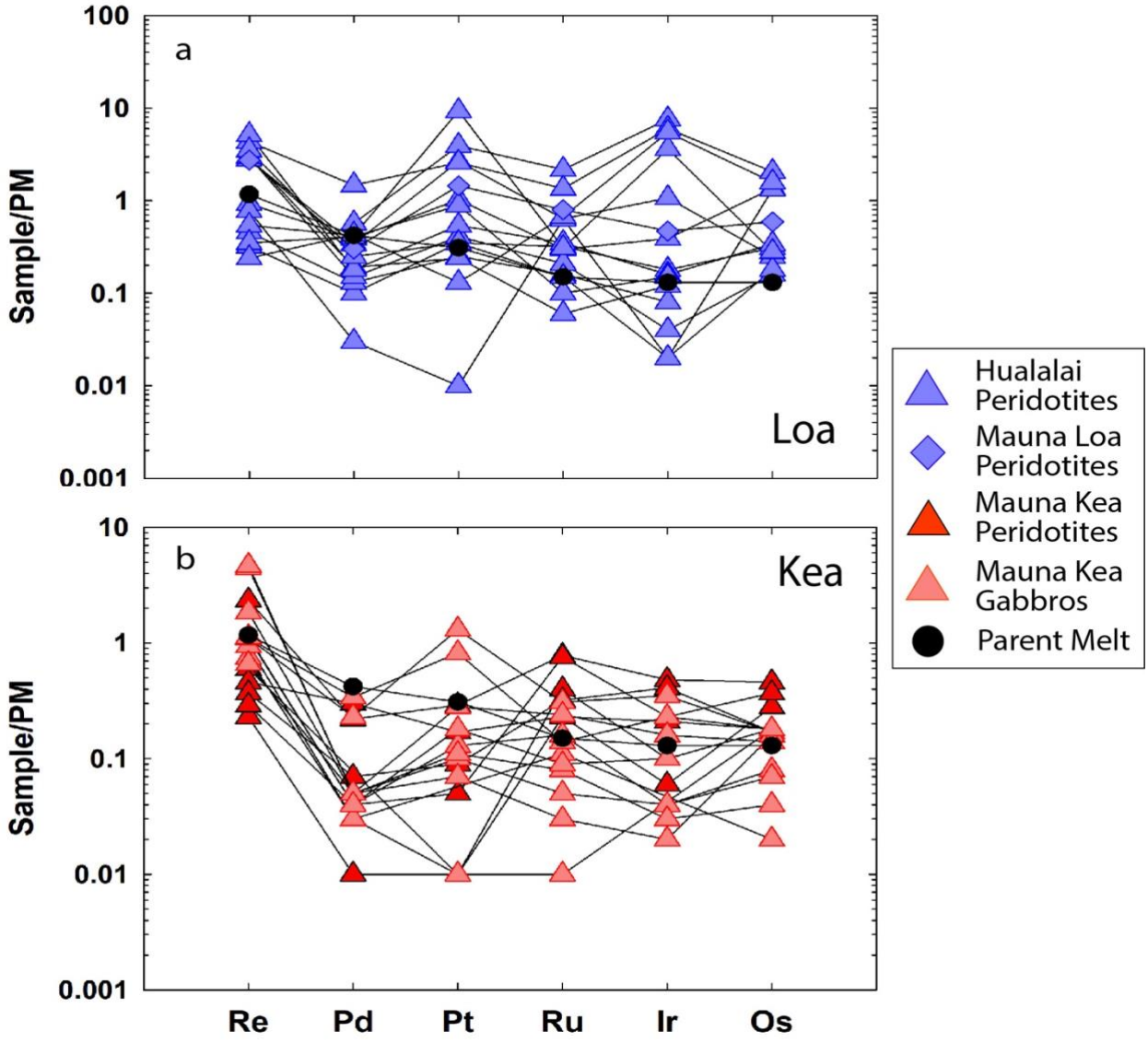

Figure 3.5 Primitive mantle normalized Re and PGE for (a) Hualālai and Mauna Loa cumulate peridotites and (b) cumulate peridotites and gabbros from Mauna Kea. The parent melt composition is from the estimate of Ireland et al. (2009). Primitive mantle normalization is from Day et al. (2017).

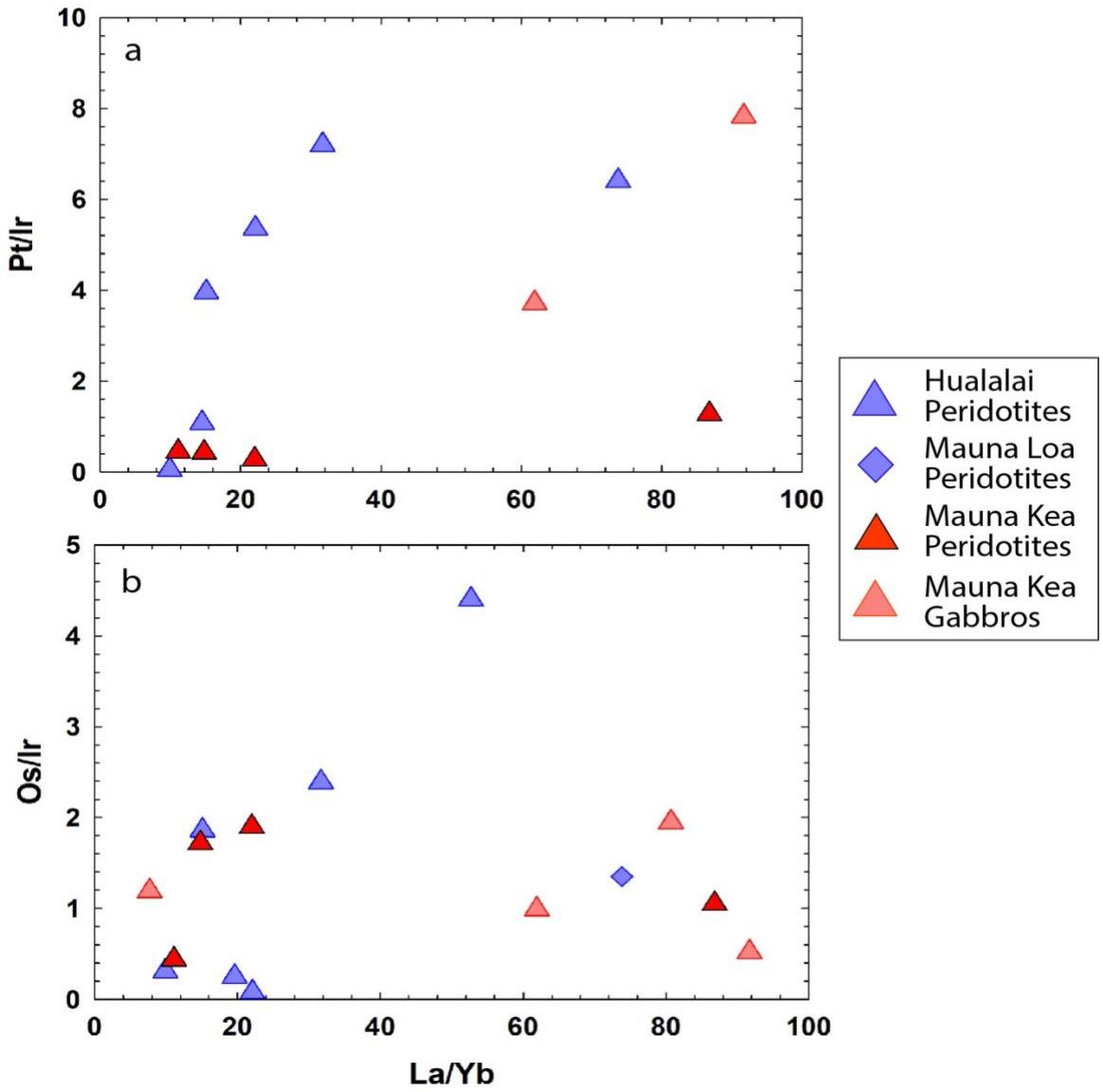

Figure 3.6 Inter-PGE ratio plots (a) Pt/Ir and (b) Os/Ir versus bulk rock melt depletion indicator La/Yb. No correlation is observed for either of the sample sets.

3.3.4. Osmium Isotopes and Source Endmembers of the Loa and Kea Trends

The bilateral Hawaiian trends have distinct isotopic endmembers. The Loa trend is characterized by radiogenic $^{187}Os/^{188}Os$, low $^{87}Sr/^{86}Sr$, low ε_{Nd}, and high $^{208}Pb^*/^{206}Pb^*$ reflective of the EM-1 mantle array component. The Kea trend show a depleted MORB-like signature with non-radiogenic Os, high $^{87}Sr/^{86}Sr$ at a given ε_{Nd}, and low $^{208}Pb^*/^{206}Pb^*$ (Abouchami et al., 2005; Weis et al., 2011; Williamson et al., 2019). Samples reported in this study show that the Loa (avg. $^{187}Os/^{188}Os$ = 0.1342 ±0.0043) and Kea (avg. $^{187}Os/^{188}Os$ = 0.1270 ±0.0062) trends define two distinct $^{187}Os/^{188}Os$ endmembers with minor overlap (i.e. Hualālai sample HI1503) (**Figure 3.7a**), consistent with the results of previous work (Bennett et al., 1996; Hauri et al., 1996; Lassiter & Hauri, 1998), but highlighting the distinction between the Loa and Kea trends with greater clarity. Several of these studies have also shown strong correlations between Os isotopes and lithophile isotopic systems like Pb, Nd, Sr, and Hf (Bennett et al., 1996; Bizimis et al., 2007; Hauri et al., 1996; Lassiter & Hauri, 1998), which suggests mixing of two or more mantle components with a common deep mantle source. These isotopic relationships have been attributed to mixing end members such as Pacific crustal contamination, metasomatized lithosphere, or recycled oceanic crust. Some authors have presented evidence for input from the outer core (Brandon et al., 1998) or exchange from the large low shear-wave velocity province (LLSVP) located at the core-mantle boundary beneath the Pacific plate (Weis et al., 2011).

Variations in $^{187}Os/^{188}Os$ are not affected by partial melting or olivine fractionation in the same manner as the HSE. Shown in **Figure 7a** are $^{187}Os/^{188}Os$ from this study and previous work has no definitive trend versus MgO. Whether the isotopic variations between the Loa and Kea trends are the result of mixing or strictly isolated to heterogeneity within the source, long-term Re/Os heterogeneity in one or multiple reservoirs is required to account for the disparity in

$^{187}Os/^{188}Os$ ratios. The poor correlation between $^{187}Re/^{188}Os$ and $^{187}Os/^{188}Os$ suggest that recent processes had to take place to decouple this relationship, such as partial melting or complex melt modification, as discussed previously (**Figure 3.7b**). Geochemical heterogeneity resulting from multiple episodes of melt depletion and refertilization is well documented in the upper mantle but is not as well constrained in the lower mantle where Hawaiian and most OIB melting originates. Pacific Ocean crust beneath Hawai'i is ~100 Ma so entrainment of this material could satisfy the time requirement and basaltic crust characteristically has high Re/Os. However, basaltic crust also has elevated concentrations of Pb and Sr, which Hauri et al. (1996) showed would skew the linear relationships with $^{187}Os/^{188}Os$ to a hyperbolic curve. Utilizing plutonic gabbro xenoliths from Hawai'i, Gao et al. (2016) concluded broad based assimilation of oceanic crust was unlikely given the large range of $\delta^{18}O$ in Hawaiian basalts versus the MORB-like $\delta^{18}O$ values of the Hualālai gabbro xenoliths. Additionally, if the Loa and Kea trends are part of a concentrically zoned plume, as suggested by Jones et al. (2017), it is unclear how Loa, the inner trend, entrains Pacific crust but the outer trend, Kea, does not. Therefore, large-scale addition of Pacific MORB may account for the radiogenic $^{187}Os/^{188}Os$ for Loa trend sample reported in this study and others but can likely be eliminated based on the lithophile isotopic observations and potential geometric problems assuming a concentric zoned plume.

Mantle metasomatism has been suggested as a mechanism for trace element fractionation and isotopic heterogeneity observed in OIB (Halliday et al., 1995), and a heterogeneously metasomatized mantle could, from a first order perspective, offer a physical explanation for bilaterally asymmetric trends. The problem this hypothesis encounters is metasomatism within the mantle typically removes Re thus lowering the Re/Os ratio of the residue which has been shown in abyssal peridotites (Day et al., 2017). While some studies have reported elevated Re/Os in

abyssal peridotites, these samples are typically restricted to the upper portion of the lithosphere nearer the lower crust where more melt/rock interaction is thought to occur. Hawaiian samples typically show lower Sm/Yb ratios suggesting the melts originated in deeper zones of the mantle. Cratonic and continental lithospheric xenoliths show evidence of metasomatism, but they typically have subchondritic $^{187}Os/^{188}Os$ whereas most of this sample set, particularly those representatives of the Loa trend have $\gamma Os > 0$, where γOs is defined as: $\gamma Os = ([^{187}Os/^{188}Os_{Sample} / {}^{187}Os/^{188}Os_{Primitive\ Mantle}] - 1)$ x 100. Therefore, while melts generated in a metasomatized upper mantle may account for Kea trend $^{187}Os/^{188}Os$ those same melts are unlikely to reproduce radiogenic Loa trend ratios and disagree with deep mantle TE ratios observed in both trends.

Based on elevated $^{186}Os/^{188}Os$ isotopic ratios Brandon et al. (1998) suggested chemical exchange between the core and the base of the Hawaiian as a possible initial source of melting. Unlike the Re-Os isotope system, ^{186}Os is the daughter product of ^{190}Pt decay. The Pt-Os system is an extremely long-lived radiogenic isotope system with a half-life ~ 100 times greater than the age of the Earth, although this is relatively poorly constrained relative more common isotopic systems (Brandon et al., 1999; Brandon et al., 1998; Ireland et al., 2011; Walker et al., 1997). Given the time required for ^{190}Pt to decay to ^{186}Os, melts should reflect near chondritic $^{186}Os/^{188}Os$. To produce a melt with elevated $^{186}Os/^{188}Os$ an input from an enriched Pt source such as the metallic core is required. Seismic velocity anomalies have been observed reaching the core-mantle boundary and/or LLSVP by French and Romanowicz (2015) with the highest resolution and least uncertainty of their study which supports the hypothesis of a core-mantle source. Weis et al. (2011) posits that sampling of the LLSVP and the core-mantle boundary could produce a bilaterally zoned plume tail thus explaining the asymmetrically bilateral trends observed in erupted lavas. However,

preservation of the isotopic integrity of the two plume tail sections throughout the melting column seems fortuitous.

A package of recycled oceanic lithosphere encompassing the depleted upper mantle to the upper crust and sediments was proposed by Lassiter and Hauri (1998) as a common mixing end member for both Loa and Kea trends. And although the LLSVP is compositionally unidentified, the prevailing hypothesis suggests the observed seismic anomaly could be the result of a large, subducted slab at or near the core-mantle boundary. The upper crustal and sedimentary section would have a high Re/Os ratio and typically have highly radiogenic $^{187}Os/^{188}Os$, all of which is requisite for Loa-type compositions. In addition, oceanic crust usually has radiogenic Sr isotopes with low Nd, which fits well with other isotopic characteristics of the Loa trend. Trends between Sr, Pb, and Os may also remain linear if enough Sr and Pb were lost to the mantle wedge when this hypothetical slab subducted. The same model accounts for the Kea trend composition by sampling from the depleted mantle and lower crustal section of the hypothetical subducted slab. This could provide a reservoir of subchondritic $^{187}Os/^{188}Os$ and is typically incompatible TE depleted so able to account for low isotopic Sr, -Pb, and -Nd. If chemical exchange with this slab occurs within the garnet stability field of the mantle, then TE ratios such as Sm/Yb observed in Hawaiian basalts could be preserved. However, Ireland et al. (2009) demonstrated that mixing of a quantity of subducted slab large enough to account for $^{187}Os/^{188}Os$ and HSE observations in Hawaiian samples could range from 20-30%. Mixing of that large a quantity would likely dilute the MgO content of the parent melt to a point that high forsterite olivine (Fo ≅ 88 – 90) (Hauri et al., 1996; Norman & Garcia, 1999) would not be in equilibrium with the melt, thus production of picritic basalts would be improbable.

Evidence of magma chambers at or above the Moho are provided from seismic and gravity models which suggest the presence of voluminous cumulate piles (Kauahikaua et al., 2000). The depth of magma storage varies for each edifice and are likely related to shield-stage volcanism with post-shield magma storage moving into the shallow lithosphere (Gao et al., 2022; Lassiter et al., 2022). Assimilation fractional crystallization (AFC) models indicate major element variability in shield stage basalts occurred at low pressure (<1 GPa). For example, Gao et al. (2022) showed that equilibration of Hualālai shield-stage xenoliths occurred at ~9 kbar and Mauna Loa and Mauna Kea xenoliths equilibrated within a range of ~2-3 kbar (Gaffney, 2002; Lassiter et al., 2022) These pressures correspond to near Moho depth at ~9 kbar and upper crustal to inter-edifice at ~2-3 kbar. Shallow magma storage within the lower to middle crust (Hualālai) and upper crust to inter-edifice (Mauna Loa and Mauna Kea) implies wall rock material is assimilated into the parent melts which could leverage Os isotopic compositions of Hawaiian lavas. However, the effect on lithophile isotopic compositions (particularly $^{87}Sr/^{86}Sr$ and $^{143}Nd/^{144}Nd$), major-, and trace-elements at ~10% wall rock assimilation is limited or possibly negligible (Gao et al., 2022; Lassiter et al., 2022). This also implies, by deduction, that transit time through the lithosphere may be minimal, thus input from the lithosphere is minimal. In fact the lithosphere may be modified by the upwelling melt column made evident by convex clinopyroxene REE patterns found in lithospheric xenoliths from Salt Lake Crater, Oahu (Bizimis et al., 2007). The gabbro samples from Mauna Kea presented in this study do not show the characteristics of lower crustal gabbros like gabbro xenoliths from Hualālai and the lack of documented lower crustal gabbro xenoliths from Mauna Kea suggest these samples originate from shallow magma chambers. Given the observations of voluminously large olivine cumulate piles proximal to Hualālai, Mauna Loa, and Mauna Kea the stronger probability allows the inference that the peridotite cumulates precipitated from similarly shallow magma

chambers. The comparatively non-radiogenic range of $^{187}Os/^{188}Os$ (0.12263 – 0.13063) for the Mauna Kea xenoliths seems to argue against any significant wall rock assimilation from the oceanic crust. But, if residence time in the crust was minimal and magma storage occurred inter-edifice as the Lassiter et al. (2022) model predicts then wall rock assimilation may be undetectable in terms of Os isotopes. However, the elevated $^{187}Os/^{188}Os$ observed in the Hualālai and Mauna Kea xenoliths open the possibility for radiogenic Os addition from wall rock of the oceanic crust, edifice, or Mauna Kea as that volcano predates Hualālai. Models from Gao et al. (2022) found that Hualālai xenoliths could experience $\gtrsim$7% increase in $^{187}Os/^{188}Os$ before any significant change in Sr isotopes was observed. In this case the average $^{187}Os/^{188}Os$ for Loa trend xenoliths are ~4% higher than the average Kea trend xenoliths which suggests the Hualālai or Mauna Loa melts could have assimilated a Kea-like component prior to forming the cumulate pile.

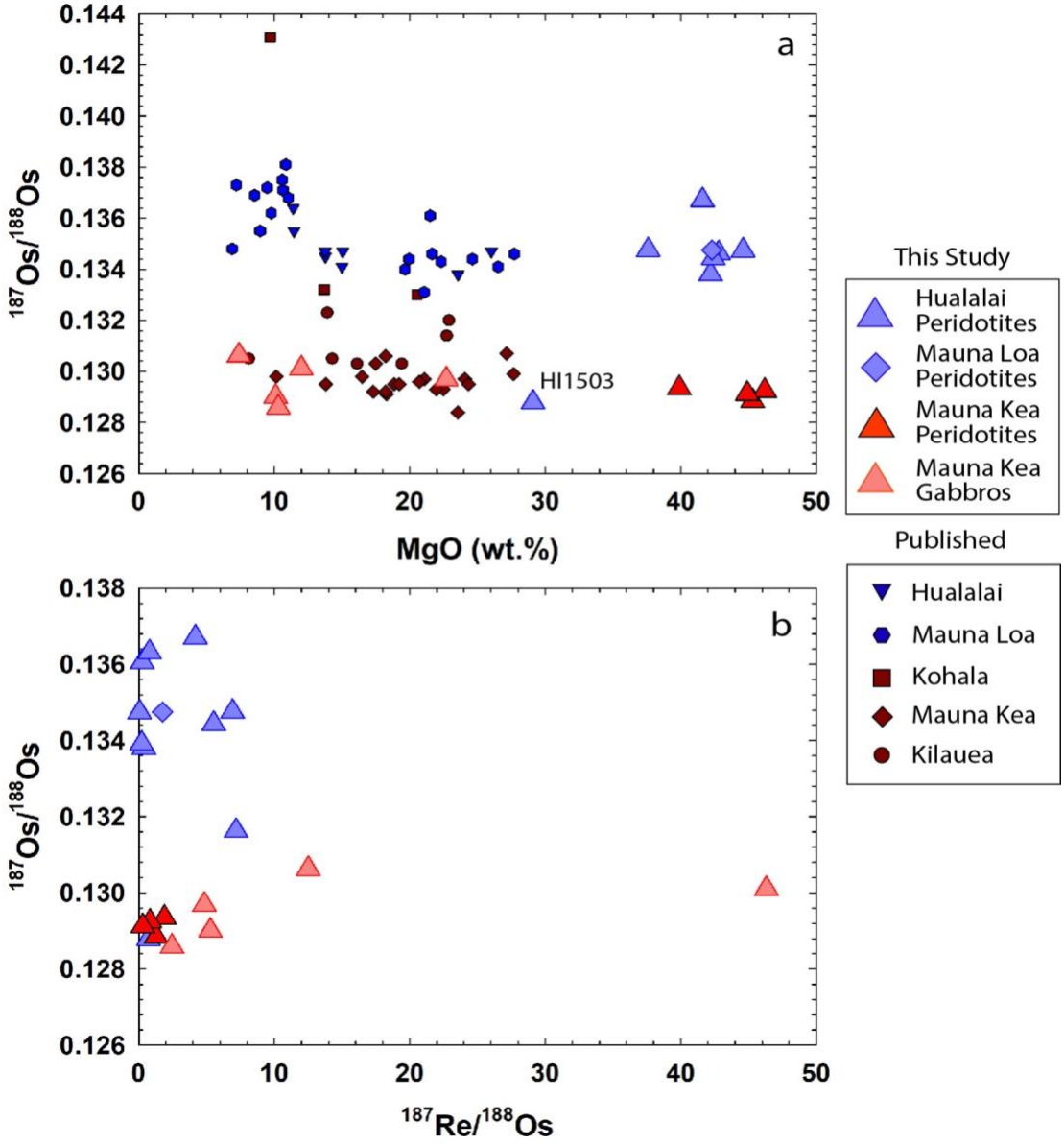

Figure 3.7 (a) $^{187}Os/^{188}Os$ as a function of MgO composition with published picrites and tholeiites for comparison (references provided in the Data Availability section). HI1503 is noted on the plot overlapping the range of the Kea trend (b) $^{187}Os/^{188}Os$ versus $^{187}Re/^{188}Os$ from this study shows a poor correlation for the Kea trend and no relevant correlation for the Loa trend samples.

3.4.5 Mixing of Loa and Kea Magmas Via Wall-Rock Assimilation and Shared Magma Chamber

Hualālai postdates Mauna Kea by ~90,000 years and detailed field mapping suggests Hualālai is buttressed on the southwestern flank of Mauna Kea (Lipman & Coombs, 2006). It is therefore likely that Hualālai erupted through and entrained Mauna Kea material. Several radiogenic isotope datasets as well as this study show some overlap between the predominantly Loa trend Hualālai and the Kea trend (i.e.: HI1502D and HI1503). Gravity modeling has shown shared density contours below 10-14 km between several of the Hawaiian volcanoes (Kauahikaua et al., 2000), which correspond to a mid to lower crustal depth and suggests magma could have exploited weak points in the crust, particularly during the island building stage. Although it is impossible to ascertain the efficiency of these hypothetical connections or their lifespan, the observation does raise the possibility that magma could transit between edifices within the crust theoretically resulting in hybridized melts. Using olivine xenocrysts to model the crystallization history of Hawaiian lavas, Yang et al. (2023) concluded that parent melts pond at the base of the lithosphere before percolating to the Moho and ponding again. The authors did not directly address any mixing hypotheses but such a large-scale process as their model suggests indirectly implies some mixing could occur. In 2019, ~1 year after the Kilauea caldera collapse, a series of earthquake swarms occurred near the predicted location of the Hawaiian hotspot. The seismicity was used to identify a complex structure of fluid-rich sills ~35-50 km deep which corresponds to the middle lithosphere given a Moho depth of ~13-18 km (Wilding et al., 2023). Observed seismicity bands extending upward from the sill complex are theorized to represent conduits of rapid magma transport supplying Mauna Loa and Kilauea (Wilding et al., 2023). These models place magma storage and transport at different depths but find commonality in their suggestion or implication

that Hawaiian magma chambers and transport systems may not be isolated to individual volcanic edifices. This seems to contradict hypotheses formed from geochemical and isotopic evidence that require magma storage and transport for the Loa and Kea trends to remain unique.

To test these geophysical observations, mixing models based on Os isotopic compositions were employed to examine mixing scenarios between Hualālai and Mauna Kea, and Kilauea and Mauna Loa. The initial melt compositions for the models are the calculated parent melts for Kilauea and Hualālai from Ireland et al. (2009). There is little difference between the parent melts of each edifice in terms of HSE abundances, which suggests a common source. This observation suggests the observed sill complex may act as a reservoir for both Kilauea and Mauna Loa. For each model the emphasis is placed on Os isotopic compositions rather than the Os concentrations because the Loa and Kea trends are defined as isotopic endmembers not by the concentration of Os or other HSE. Additionally, it has been shown in this study and others that Os concentration and IPGE composition in general is strongly controlled by the addition or removal of olivine. The first model tests the idea that older Mauna Kea edifice material is entrained by younger erupting Hualālai melts. In this scenario the Hualālai parent melt with a composition of 1 ng/g Os and $^{187}Os/^{188}Os$ of 0.135 is mixed with the average Mauna Kea composition, 0.7 ng/g Os and $^{187}Os/^{188}Os$ of 0.129 obtained from xenoliths in this study. The results show that ~10-20% addition of the average Mauna Kea composition to the Hualālai parent melt will generate $^{187}Os/^{188}Os$ that approximates the mean and median of the Hualālai sample set (**Figure 3.8a & b**). Adding ~55-60% of the Mauna Kea composition will drive the $^{187}Os/^{188}Os$ to the lower values of the Hualālai range. Sample HI1503 is not considered in this range because it sits outside 3 standard deviations of the Hualālai average Os isotopic range. However, samples such as this and HI1502D should not be completely discounted. If Hualālai erupted through the previously emplaced Mauna Kea it

would not be an unreasonable expectation for some Mauna Kea material to be incorporated into Hualālai eruptions with little equilibration, thus preserving a Kea-like signature. These results provide some validity to the hypothesis that Hualālai can entrain limited amounts of material from Mauna Kea and still retain Loa-like characteristics.

To examine the common source and potential shared transit system suggested by Wilding et al. (2023), two mixing models were created using the upper and lower $^{187}Os/^{188}Os$ values of the Mauna Loa range ($^{187}Os/^{188}Os$ ~0.134 – 0.138) from this study and literature data mixed with a parent melt estimate for Kilauea (0.65 ng/g Os; $^{187}Os/^{188}Os$ ~0.131) (Ireland et al., 2009). Beginning with the lower value the model shows that ~10-20% addition of a Mauna Loa composition can reproduce the lower values of the observed range but fails to reach the mean or median values unless there is no dilution from the Kilauea parent melt. Using the upper value from the Mauna Loa range shows the only 1-5% addition to the Kilauea parent is required to replicate the lower values in the range and ~10-20% is needed to achieve the mean and median values (**Figure 3.8a & b**). These results could imply that the Loa trend magmas could sample a crustal component resulting in highly radiogenic melts and that are diluted during storage and/or transport to a less radiogenic value that nonetheless remains elevated versus the Kea trend. Given the geographical and special alignment of these volcanoes it is difficult to envision a process where younger volcanoes erupting to the east of older volcanoes to the west do not entrain any material from the older volcanos. These results suggest this is a possibility for Hualālai and Mauna Kea and could be a viable hypothesis for Kilauea and Mauna Loa as well. To gain more resolution into these theories a deeper investigation involving the mixing of other lithophile isotopic systems, major elements, and HSE will be needed. Although the models presented here lack confirmation,

they do provide support for the geophysical observations suggesting chemical exchange between Loa and Kea trend magmas can occur.

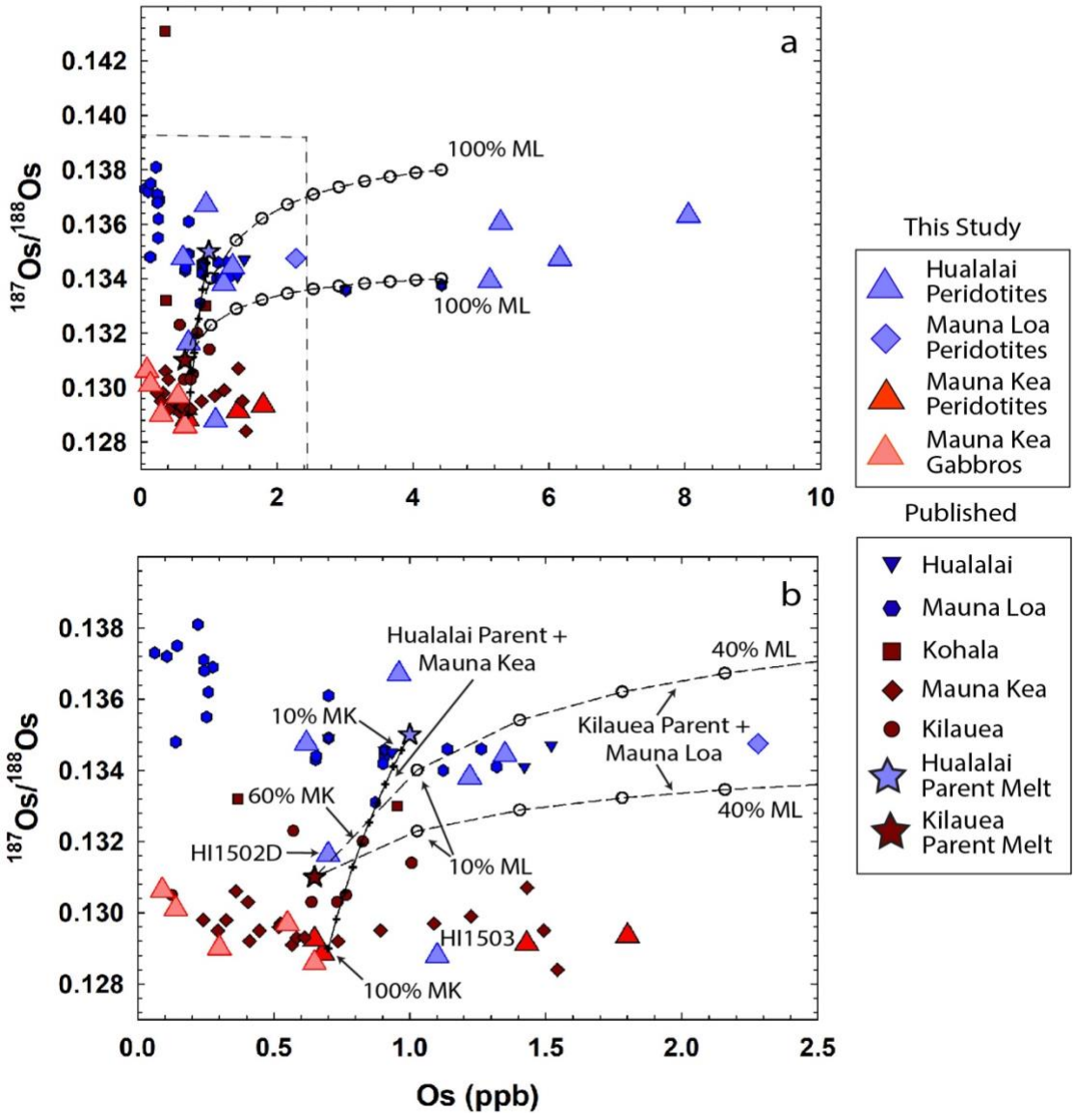

Figure 3.8 (a) $^{187}Os/^{188}Os$ as a function of Os concentration with mixing models of a Kilauea parent melt mixed with lowest and highest $^{187}Os/^{188}Os$ of the Mauna Loa range (dashed lines with open circles), and a Hualālai parent melt mixed with the mean Mauna Kea $^{187}Os/^{188}Os$ from this study (solid line with plusses). (b) Cutout of plot (a) dashed lines on (a) denote the bounds of (b). All models are marked in 10% increments. Parameters for the models are discussed in the text, parental melt estimates are from Ireland et al. (2009).

3.4 Conclusions

The samples presented in this study have characteristics consistent with cumulate gabbroic and peridotite xenoliths. For Mauna Kea gabbros xenoliths major element compositions, relative enrichments in PM normalized LREE, and non-radiogenic $^{187}Os/^{188}Os$ suggest these samples precipitated from Mauna Kea melts and are not fragments of oceanic crust entrained in the eruption column. Peridotite xenoliths representing both the Loa and Kea trends do not have strong LREE depletions typical of mantle derived ultramafic rocks and elevated relative and absolute HSE abundances suggests that these samples precipitated from a mafic melt. A conclusion can therefore be made that samples presented here represent cumulate piles from crustal or possibly inter-edifice magma chambers.

Absolute and relative abundances of HSE are diagnostic of processes broadly acting on Hawaiian cumulates and inductive of Loa and Kea trend processes. The broad correlations of IPGE with MgO coupled with the poor correlations with melt depletion indicators shows IPGE abundances are primarily controlled by olivine accumulation. This relationship also implies the host minerals for IPGE in the Hawaiian cumulates are sulfides and/or PGM included in olivine crystals. The poor correlation of Re and PPGE suggests these elements are hosted in interstitial sulfides and thus susceptible to mobilization and modification post emplacement in the cumulate pile. A lack of correlation between inter-HSE ratios and melt depletion indicators that are not leverage by olivine show that melt depletion has a smaller role in HSE fractionation that olivine abundance. Elevated Pt abundances relative parent melt estimates point toward a recycled crustal component as a Loa trend endmember. Likewise, depleted Pt abundances versus the same parent melt estimate suggest the Kea trend may incorporate a lithospheric component. Osmium-isotopic ratios presented in this study are likely reflective of source heterogeneity, however other factors

such as wall rock assimilation, especially from neighboring volcanoes, or sampling different endmembers in the mantle may have a meaningful impact. The mixing models presented here show that mixing between Loa and Kea edifices can occur without perturbing the distinct Loa and Kea Os isotopic compositions. Hualālai may incorporate ~10-20% of a Mauna Kea composition and perhaps up to 60% when considering the overlap of Hualālai samples with the Kea trend range. Likewise, a Kilauea parent melt could dilute a radiogenic Mauna Loa melt possibly during magma storage in the lithosphere or during transit in the lower crust.

3.5 Acknowledgments

Chapter 3 in part is currently being prepared for submission for publication of the material. Oller, Brian; Day, James M.D. The dissertation author was the primary researcher and author of this material.

CHAPTER 4 Source Heterogeneity and Geochemical Zoning of the Canary Islands Plume Inferred from the Highly Siderophile Elements and Osmium Isotopes

4.1 Abstract

Lherzolite, harzburgite and cumulate xenoliths from Tenerife, La Palma, and El Hierro along with basanites, basalts, and picrites from Lanzarote, Gran Canaria, Tenerife, La Palma, and El Hierro are characterized for their Os isotope compositions and major-, trace-, and highly siderophile element (HSE: Re, Pd, Pt, Ru, Ir, Os) abundances. Osmium isotope compositions for the lherzolite and harzburgite xenoliths (Avg. $^{187}Os/^{188}Os$ = 0.125 ±0.003; all uncertainties are 2 St. Dev.) and primitive mantle-normalized iridium platinum group elements (IPGE: Ru, Ir, Os) abundances are within the range of Atlantic abyssal peridotites. Cumulate xenoliths (Avg. cumulate $^{187}Os/^{188}Os$ = 0.156 ±0.013) are similarly radiogenic to lavas (Avg. lava $^{187}Os/^{188}Os$ = 0.150 ±0.033) with less fractionated HSE patterns. Fractionation of the HSE for most lavas can be explained by ~11% crystallization of olivine ±spinel and sulfide. The lavas show trace element characteristics similar to HIMU OIB with relative high field strength element enrichments and negative Pb anomalies. The estimated HSE composition of the parent melt based on ~15% MgO and ~10% Al_2O_3 (in ng/g: Re = 0.28 ±0.3, Pd = 1.6 ±2.5, Pt = 2.0 ±3.7, Ru = 0.56 ±0.75, Ir = 0.24 ±0.35, Os = 0.22 ±0.41, $^{187}Os/^{188}Os$ = 0.149 ±0.02) shows a high degree of variability and suggests variable melt sources for individual or groups of islands. New $^{187}Os/^{188}Os$ data is used to evaluate the extent of mixing between the estimated parent melt with possible contaminants from the lithosphere, lower crust, and sediments of the upper crust. Finally, potential geochemical zoning

patterns of the Canary Islands plume are investigated using new $^{187}Os/^{188}Os$ presented in this study combined with Sr-Nd-Pb-Os from literature sources.

4.2 Introduction

The Canary Islands form a broadly age-progressive hotspot chain with the oldest islands to the east constructed atop some of the oldest Atlantic oceanic crust (150 – 180 Ma) (Hoernle, 1998). Unlike many hotspot chains, the age progression does not conform to a uniform plate velocity or vector model (**Figure 4.1**). Of the seven islands that comprise the Canary Archipelago, La Palma and El Hierro, are in the shield building stage (Carracedo et al., 2001). Here, these islands have experienced virtually uninterrupted volcanic activity since subaerial emergence. The eastern islands, Lanzarote and Fuerteventura, as well as the central islands, Tenerife and Gran Canaria, are in the post-erosional stage of evolution where volcanism is less voluminous than the shield stage. La Gomera, between Tenerife and La Palma, is in a "gap-stage" of volcanism which may signal a transition to post-erosional rejuvenated style eruptions (Carracedo et al., 1998). The active hotspot is thought to be centered beneath the southwestern-most island El Hierro, a hypothesis supported by uplifted and, in the case of La Palma, subaerially exposed seamount structures (Hoernle & Schmincke, 1993). Holocene eruptions have been documented on all islands except La Gomera, and the western-most La Palma and El Hierro as well as the oldest and northeastern-most island, Lanzarote ~400 km away, have experienced historical eruptions (Carracedo et al., 2002) the most recent occurring on La Palma in 2021 (Day et al., 2022). This eruptive pattern differs from other well-known hotspot chains such as Hawai'i where historical activity is constrained proximal to the active hotspot.

Similar to many OIB chains, Canary Islands magmatism has been interpreted to be fed by a deep mantle source possibly originating at or near the core-mantle boundary (Carracedo et al., 1998; French & Romanowicz, 2015). Previous studies of OIB and the Canary Islands in particular have shown that lavas produced at these islands sample and preserve significant geochemical heterogeneity that exists within Earth's mantle (Day et al., 2009; Day et al., 2010; Day et al., 2022; Gurenko et al., 2006; Halliday et al., 1995; Hoernle et al., 1991). This mantle heterogeneity is generally categorized as endmembers defined by Sr-Nd-Pb systematics that show long-term (>1 Ga) incompatible trace element enrichment versus the depleted MORB mantle (DMM). These enriched endmembers sources are interpreted as EM1 (subducted continental crust with pelagic sediment and possibly sub-continental lithosphere), EM2 (subducted continental crust with terrigenous sediment), and HIMU (subducted oceanic crust with associated lithosphere) (Hofmann, 1997; Jackson & Dasgupta, 2008; Zindler & Hart, 1986). However, geochemical models of direct melting of these endmember materials does not account for the compositional ranges observed in OIB suggesting instead mixing of one or more endmembers with a depleted or primitive mantle source. Additionally, metasomatic and assimilation processes within the shallow lithosphere and/or crustal reservoirs can have a significant impact on the composition of OIB. Melting and mixing of variable proportions of endmembers combined with processes acting on the melt products during transit and storage through the lithosphere and crust is thought to be a primary factor behind observed geochemical zoning observed in genetically related OIB localities.

This study introduces new major-, trace-, and highly siderophile element (HSE: Re, Pd, Pt, Ru, Ir, Os) abundance data and $^{187}Os/^{188}Os$ compositions for lherzolite, harzburgite, and ultramafic cumulate xenoliths from Tenerife, La Palma, and El Hierro, as well as picrites, basalts, and basanites from Lanzarote, Gran Canaria, Tenerife, La Gomera, La Palma, and El Hierro. Due to

their compatible behavior, the HSE are advantageous for studies of mafic and ultramafic samples. Previous work has definitively shown that HSE and $^{187}Os/^{188}Os$ systematics can discriminate between mantle processes such partial melting, metasomatism, and slab recycling (Day, 2013; Day et al., 2017; Rehkamper et al., 1999). This study uses the advantages of the HSE "toolbox" to examine the nature of the Canary lithosphere and process that have acted upon it, estimate the HSE composition of the Canary parental melt, the mantle source end member components that contribute to the generation of Canary Islands lavas, and evaluate possible geographic zoning of the Canary plume.

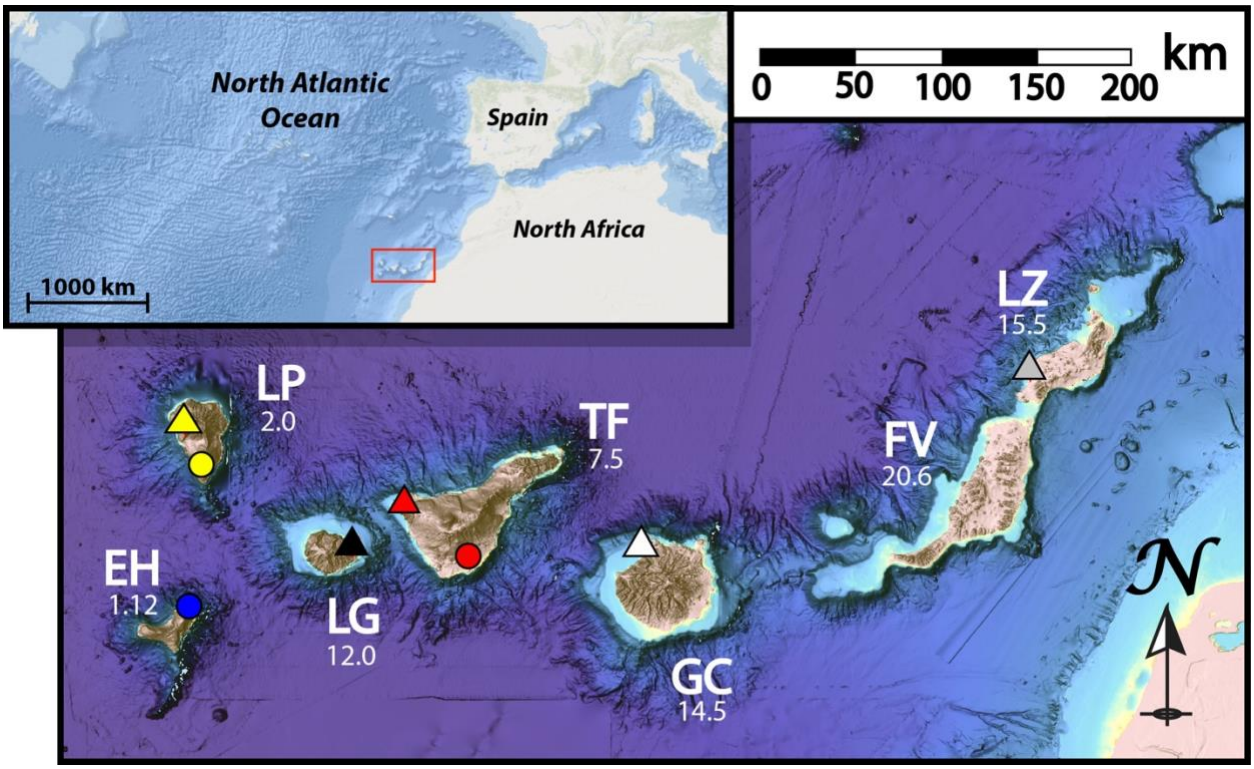

Figure 4.1 Map showing sample locations for xenoliths (circles) and lavas (triangles) for the Canary Islands. K-Ar ages for each island from Carracedo et al. (1998) are listed below the abbreviations in millions of years. (EH = El Hierro, LP = La Palma, LG = La Gomera, TF = Tenerife, GC = Gran Canaria, LZ = Lanzarote, FV = Fuerteventura)

4.3 Methods

Eighteen xenoliths from the islands of Tenerife (n = 6), El Hierro (n = 6), and La Palma (n = 6), along with nineteen shield building stage lavas from Lanzarote (n = 1), Gran Canaria (n = 2), La Gomera (n = 2), Tenerife (n = 2), El Hierro (n = 9), and La Palma (n = 4) were collected over various field trips and are reported here. The xenoliths varied in size from ~10 cm to ~20 cm in diameter. Petrography for the xenoliths was determined at the *Scripps Isotope Geochemistry Laboratory (SIGL)* using prepared sections ground to ~60μm in thickness. For generation of bulk rock powders, ~100 to 200 g fractions of samples were sawn, buffed with corundum paper, and washed to remove saw marks, dust, and debris before being crushed using an alumina jaw crusher followed by powdering using a SPEX™ alumina shatterbox. All equipment was thoroughly cleaned between samples to avoid cross contamination.

Major element compositions for the lavas and xenoliths were measured by X-ray fluorescence (XRF) at Franklin and Marshall College using a *PW 2404 PANalytical* XRF vacuum spectrometer following the procedures outlined in Boyd and Mertzman (1987). Major element analyses by XRF involved standard lithium tetraborate fusion techniques using 3.6:0.4 g $LiBO_4$:sample powder. Ferrous iron concentrations were determined by titration with potassium dichromate. Precision and accuracy are estimated using repeat analyses of standards, and the long-term precision and reproducibility are reported in Day et al. (2017).

Whole-rock trace element compositions were determined at the SIGL using methods described in Day et al. (2014). One hundred milligram aliquots of sample powder was precisely weighed and digested in a 1:4 mixture of Teflon-distilled HNO_3:HF for >72 hours at 150˚C on a hotplate. Rock standards (BHVO-2, BCR-2, HARZ-01) and total procedural blanks were prepared along with the samples. After drying down and sequential HNO_3 dry-down steps to break-down

fluorides, sample solutions were diluted by a factor of 5000 in 2% HNO_3 and spiked with a 1 ppb indium solution to monitor instrumental drift. Solutions were measured using a *Thermo Scientific* iCAPq c quadrupole ICP-MS in standard mode. The reproducibility of the reference materials was better than 7.1% RSD, and elemental abundances were within error of the recommended ranges.

Osmium isotope and HSE (Re, Pd, Pt, Ru, Ir, Os) abundances for eighteen xenoliths and nineteen lavas were measured at *SIGL* using the methods described in Day et al. (2015). The sample powders were well homogenized, precisely weighed, then digested in sealed borosilicate Carius tubes with Os isotope and HSE "spikes" and 10 mL of a 2:3 mixture of Teflon-distilled HCl and Teflon-distilled HNO_3 that had been purged of Os. The samples were digested at 240°C for 72 hours. Osmium was then triply extracted from the acid using CCl_4, back-extracted into HBr and purified by micro-distillation. Rhenium and platinum group elements were separated from the solution with anion exchange columns, then measured on a *Thermo Scientific* iCAPq-c ICPMS in standard mode. Osmium isotopic compositions were measured on a *Thermo Scientific* Triton thermal ionization mass spectrometer by peak-jumping in negative ion phase. The measurements were corrected for oxide and fractionation using a ratio $^{192}Os/^{188}Os = 3.08271$. Osmium concentrations were determined using ^{190}Os spike deconvolution and were blank-corrected. 70pg UMCP Johnson-Matthey standards were used to monitor instrument precision. For the eighteen xenoliths, measurements of the standards averaged 0.1141 ±0.00013 (2σ, n = 2) and for the nineteen lavas standards averaged 0.11371 ±0.00022 (2σ, n = 22). Procedural blanks for Os analyses (n = 2) had an average corrected $^{187}Os/^{188}Os$ of 0.140 ±0.0007 and [Os] of 1.6 ±1.8 pg for the xenolith samples. Total procedural blanks for lava samples for both Carius tube and high pressure asher digestions had average (n = 5) corrected $^{187}Os/^{188}Os$ of 0.189 ±0.139 and [Os] of 0.3 ±0.3 pg. For both xenolith and lava sample sets measured HSE isotope dilution isotopic ratios

were corrected for mass fractionation using the deviation of the standard average run on the day over the natural ratio for the element, and all reported values are blank corrected. The average HSE abundances of the xenolith blanks (n = 2) were: Re = 53 pg, Pd = 374 pg, Pt = 10 pg, Ru = 281 pg, Ir = 9 pg. For the lava blanks (n = 5) the average HSE abundances were: Re = 2.4 ±2.2 pg, Pd = 13.5 ±32.5 pg, Pt = 3.2 ±5.8 pg, Ru = 3.6 ±6.2 pg, Ir = 2.1 ±3.9 pg.

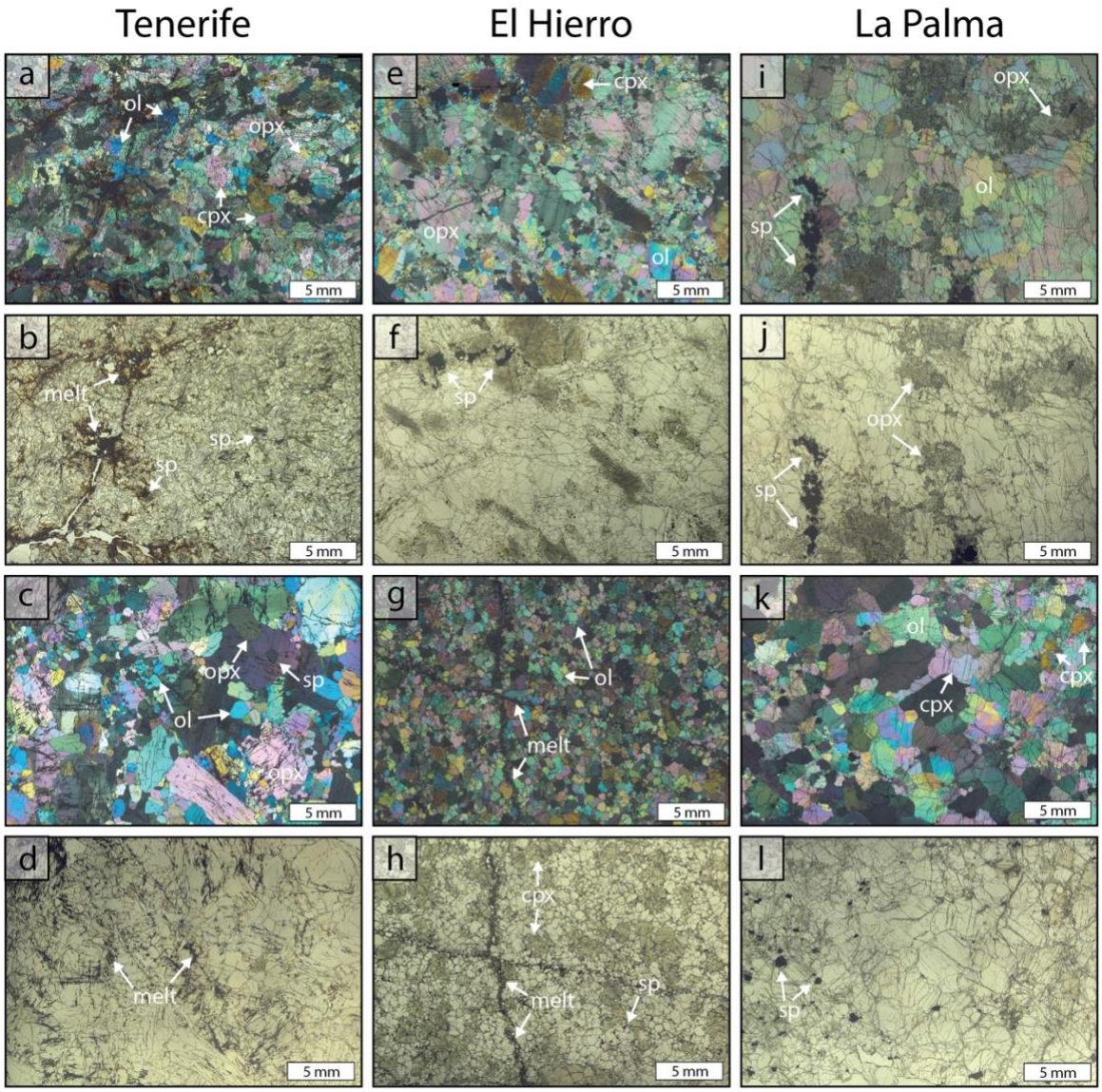

Figure 4.2 Photomicrographs of selected xenoliths from Tenerife (a & b: TF1601A; c & d: TF1601F), El Hierro (e & f: EH1601B; g & h: EH1601C), and La Palma (i & j: LP1603B; k & l: LP1603C). XPL images are placed above conjugate PPL images for each sample, slides are ground to 60 µm thick.

4.4 Results

4.4.1 Petrography of Tenerife, El Hierro, and La Palma Xenoliths

Six petrographic thin sections were prepared for the Tenerife and La Palma xenoliths, and due to size constraints, three of six samples for El Hierro. Each section was ground and polished to a thickness of 60 µm. Modal abundances for the sections were obtained by photo analysis using the methods described in Oller et al. (2022), the results are presented in **Table S4.3**. Xenoliths from Tenerife and La Palma are dominantly spinel harzburgites (Tenerife: 42.4 to 74.6 modal % olivine, 17.4 to 39.8 modal % orthopyroxene, 3.4 to 16.4 modal % clinopyroxene, 1.2 to 5.8 modal % spinel; La Palma: 51.7 to 72.0 modal % olivine, 35.1 to 20.6 modal % orthopyroxene, 5.0 to 10.5 modal % clinopyroxene, 0.6 to 2.3 modal % spinel) with a few examples of spinel lherzolites (TF1601E, -F, and LP1603B, -E). One of the three El Hierro xenoliths one is a spinel harzburgite (EH1601B), the other two (EH1601A, -C) have textures consistent with cumulate xenoliths. Aside from the cumulates, all the xenoliths can be broadly classified as the OI2-u group defined by Simon et al. (2008). Some key characteristics of OI2-u xenoliths are: porphyroclastic to protogranular textures with some poikilitic minerals, visual evidence of melt-rock reaction, and a lack of primary clinopyroxene.

Tenerife xenoliths have generally protogranular textures with average grain sizes of major rock forming minerals ~2.8 ±2.1mm, although some have porphyroclasts of olivine approaching or exceeding 5mm about the long axis. All of these xenoliths feature sub-rounded to euhedral spinel grains with average sizes of ~1.0 ±0.3mm occurring along grain boundaries of olivine. TF1601B, -D, and -E also have anhedral porphyroclasts of spinel associated with melt veins and/or melt reacted orthopyroxene. These spinels are ~0.5 – 1.5mm occurring in clusters enveloping fine

grained clinopyroxenes. Tenerife shows the most melt infiltration of the entire xenolith sample set with modal melt inclusions ranging from 2 to 8.5% (**Table S4.3, Figure 4.2b**). The melt forms veins along grain boundaries and shows strong reaction textures with orthopyroxene and exsolution of clinopyroxene.

La Palma xenoliths show more textural variability than Tenerife. LP1603B, -C, and -E have protogranular textures similar to Tenerife, while LP1603A, -D, and -F have fine grain granoblastic textures encompassing units of small (<1mm) anhedral olivine ±orthopyroxene. Melt infiltration is less apparent in La Palma samples, with LP1603A, -B, and -E showing ~0.9%, 0.7%, and 8.5% melt respectively. All of the samples in this set have anhedral porphyroclasts of spinel, broadly similar to those observed in the Tenerife samples. These spinels tend to be some of the larger minerals in the granoblastic samples, occurring along lineations of fine grain, sub-round pyroxenes and smaller spinel. In protogranular samples the spinels are oriented along grain boundaries, normally adjacent to orthopyroxenes. Despite showing less visible melt infiltration than Tenerife samples, the protogranular La Palma xenoliths have orthopyroxenes showing textural evidence of melt reaction similar to orthopyroxenes observed in the Tenerife samples (**Figure 4.2i & j**). Clinopyroxene tends to be small (<1mm) occurring as reaction and/or exsolution with orthopyroxenes. LP1603E is an exception, here euhedral clinopyroxene is ~2mm dispersed among olivine.

Of the three El Hierro xenolith one (EH1601B) has textural characteristics similar to Tenerife and La Palma and EH1601A and -C have characteristics consistent with cumulate xenoliths. Sample EH1601B has a protogranular texture with phenocrysts of olivine and orthopyroxene showing evidence of melt reaction (**Figure 4.2e & f**). This sample has a mixture of course and fine olivine and orthopyroxene that average ~3.5 ±0.6mm and 0.5 ±0.1mm respectively.

Clinopyroxenes tend to be smaller and are generally distributed among melt-reacted crystals. As with the previously described samples, EH1601B has large spinel grains (avg: ~1.2 ±0.3mm) occurring alongside and within melt reacted orthopyroxene (**Figure 4.2f**). Samples EH1601A and -C are finer grained than previously described samples with an average size of ~1.0 ±0.3mm. These samples tend to be much more equigranular with more euhedral crystals that form ~120° triple junctions, particularly in the case of EH1601C (**Figure 4.2g**).

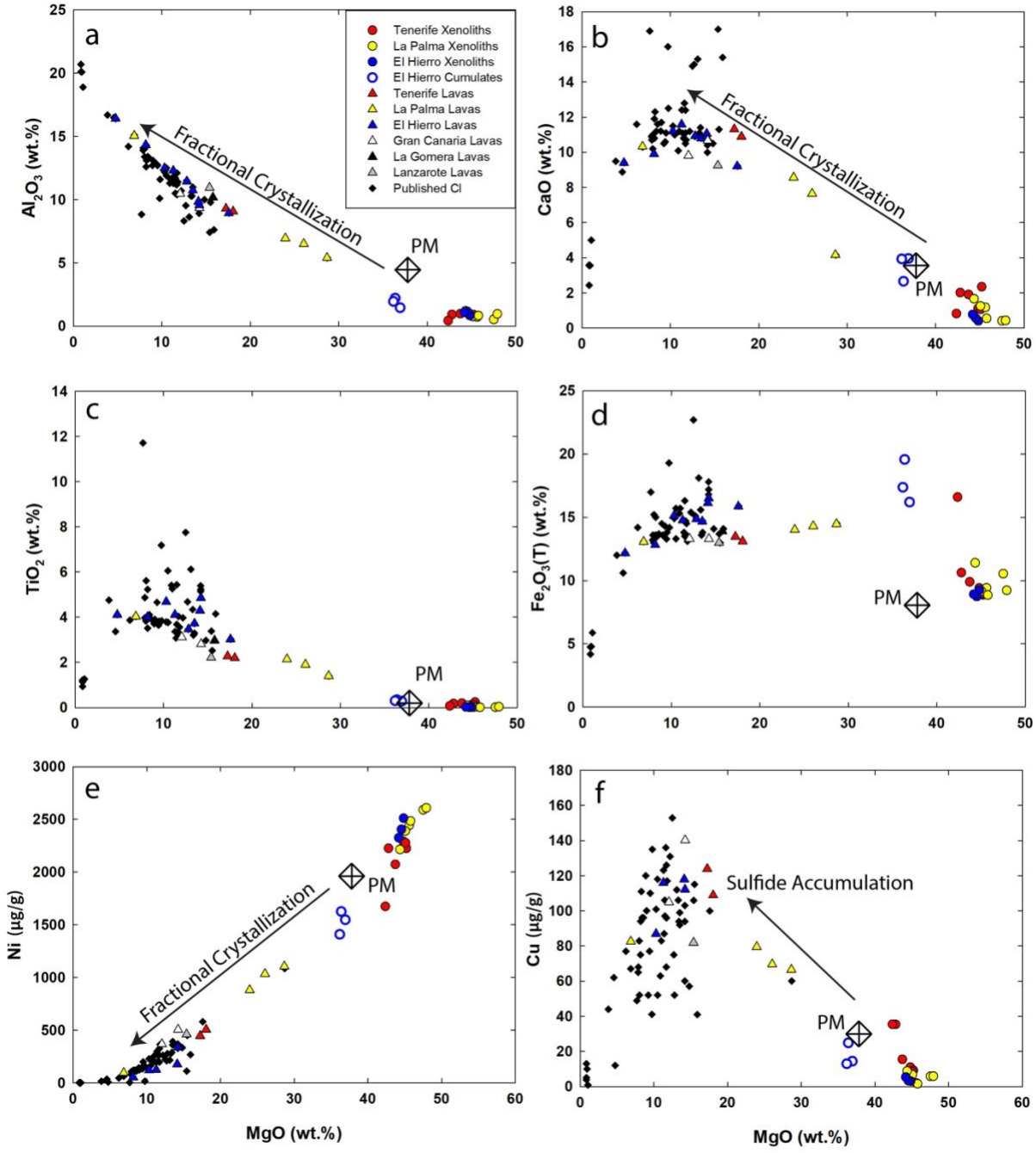

Figure 4.3 Harker diagram for Canary Islands xenoliths and lavas showing fractional crystallization and melt depletion trends (a – e) and sulfide accumulation (f). Published data is from Day et al. (2010). (PM = primitive mantle from McDonough and Sun (1995))

4.4.2 Bulk-Rock Major & Trace Element Compositions

Bulk rock major and trace element abundances for the Canary Islands lavas and xenoliths are reported in **Table S4.2**. Three of the El Hierro xenoliths (EH1601A, -C, and -F) have major and trace element characteristics consistent with petrographic observations discussed in the previous section indicative of cumulate xenoliths. Contents of MgO for EH1601A, -C, and -F are lower (36.2 to 36.9 wt.%) than the other El Hierro samples, as well as the broader Canary Islands xenolith samples. Corresponding Mg-numbers for these xenoliths range from 78.7 to 81.9. Incompatible major element compositions, such as Al_2O_3 and CaO are elevated (Al_2O_3: 2.0 to 2.2, and CaO: 2.7 to 3.9) relative to other El Hierro, La Palma, and Tenerife xenoliths and compatible elements Co and Ni are low. These samples plot between the lithospheric xenoliths and lavas on fractional crystallization trends such as Al_2O_3, CaO, and TiO_2 versus MgO (**Figure 4.3**). LOI for these three samples are negative (-0.98 to -0.66) suggesting they experienced little to no post emplacement alteration. Negative LOI values, in general, represent the change from ferrous to ferric Fe during the heating process for LOI analysis. Primitive mantle normalized incompatible trace element (ITE) patterns for these cumulates are similar to the broader xenolith suite but are typically more enriched than the lithospheric El Hierro counterparts with increasing compatibility. Other noteworthy observations are a prominent negative Pb anomaly and a modest negative Y anomaly reflective of the lava samples presented in this study (**Figure 4.4a**). Primitive mantle normalized rare earth element (REE) patterns have an upward convex pattern, showing relative depletions in LREE versus Nd, then becoming steeper approaching the HREE, with La/Yb = 2.79 to 7.95, while La/Sm is closer to unity (La/Sm = 0.82 – 1.94). These samples are more enriched in HREE than the lithospheric El Hierro samples.

Lithospheric xenoliths include all the Tenerife and La Palma samples, and EH1601B, -D, and -E from the El Hierro set. Mg-numbers from all three sample sites are high and uniform, El Hierro average = 90.78 ±0.21, La Palma average = 90.34 ±0.99, and Tenerife is more variable, average = 89.07 ±2.84. All three sets have high MgO contents (42.4 to 47.9 wt.%) well correlated with low Al_2O_3 (0.43 to 1.21 wt.%) and shows good negative correlation with Fe_2O_3(T) ($r^2 = 0.77$), and positive correlation with Ni ($r^2 = 0.87$) (**Figure 4.3**). La Palma and El Hierro xenoliths are unaltered with loss on ignition (LOI) ranges from -0.14 to -0.61 wt.% and -0.12 to -0.98 wt.% respectively. Tenerife xenoliths show slightly more, but minimal alteration spanning -0.07 to 0.35 wt.%. Incompatible trace elements patterns between the three sets are variable. El Hierro lithospheric xenoliths are ITE depleted relative to Nb. They generally trend down toward more compatible TE with prominent depletions in Pb, Hf, and Ti (**Figure 4.4a**). These xenoliths overlap their cumulate counterparts, diverging at Nd, with lithospheric xenoliths falling below the cumulates. Nb/Ta ratios for the three islands are very uniform and distinctly subchondritic (average Nb/Ta = 0.07 ±0.02). Average Zr/Hf ratios for La Palma (average Zr/Hf = 66.24 ±40.77) and El Hierro (average Zr/Hf = 61.32 ±5.74) lithospheric xenoliths are similar, although La Palma xenoliths show much greater variability. Tenerife has lower average Zr/Hf (average Zr/Hf = 38.67 ±7.12). All three islands show highly variable Sr/Pb ratios. El Hierro is the highest (average Sr/Pb = 354.13 ±127.22), and Tenerife and La Palma are more similar (average Sr/Pb = 130.06 ±66.75; 157.42 ±170.4 respectively) with La Palma having the highest variability and Tenerife the lowest. Primitive mantle normalized REE patterns are similar between Tenerife and La Palma with both showing relative enrichments in LREE and generally flat downward trending slopes that suggest melting in the presence of garnet (**Figure 4.5a**). The La Palma slope is steeper than Tenerife, average La/Yb ratios for Tenerife and La Palma are 5.37 ±1.88 and 18.34 ±8.69 respectively. El

Hierro REE patterns have an N-MORB like shape with depletions in LREE relative to Nd. La/Yb ratios for El Hierro fall between Tenerife and La Palma (average La/Yb = 11.75 ±4.85).

Lava samples from the five islands have foidite to trachy-basalt compositions based on the total alkali-silica classification of Le Bas et al. (1986). Total alkalis ($Na_2O + K_2O$) range from 0.05 to 6.57 wt.% and correlate well with MgO ($r^2 = 0.77$). Three samples (03-PAL-05, 04-PAL-05, JMDDLP03) have picritic compositions with elevated MgO from 23.95 to 28.66 wt.%, and only three samples in the sample suite fall below 10 wt.% (JMDD LP19 = 6.87 wt.%, JMDD EH02 = 4.76 wt.%, and EH06-04 = 8.16 wt.%); the remainder range from 10.29 to 18.05 wt.%. Mg-numbers for the lavas range from 43.7 – 79.7 with the highest values corresponding to the La Palma picrites. Fe_2O_3(T) contents are homogenous (Avg = 14.52 wt.% ±1.2) with slightly more variable Al_2O_3 (Avg = 10.49 wt.% ±2.8). Incompatible major elements (Al_2O_3, CaO, TiO_2) show a good negative correlation with MgO, while the same relationships with Fe_2O_3(T) are more variable (**Figure 4.3a - f**). Alteration of the lavas are generally minimal. Loss on ignition (LOI) is low across the lava suite (Avg = 0.93 wt.% ±1.68) with JMDD LP03 showing the highest post-emplacement alteration at 6.93 wt.%. Aside from that sample, LOI makes a narrow range from -0.57 to 2.5 wt.%.

Compatible trace elements (Cr, Co, Ni) are strongly correlated with melt depletion indicators MgO and Al_2O_3. Nickel and Cr have broad compositional ranges (202 – 1714 μg/g; 55 – 1106 μg/g respectively) with Co showing a significantly more confined range (31 – 119 μg/g). Absolute and relative trace element abundances from all five islands are similar to previous Canary Island studies (Day et al., 2010; Simon et al., 2008; Widom et al., 1999) as well as other HIMU-like OIB, showing elevated U, Th, Nb, and Ta with strongly depleted Pb. Primitive mantle (PM) normalized incompatible trace element (ITE) patterns are generally similar for all lava samples.

Highly incompatible elements are relatively depleted with strong enrichments in high field strength elements Nb and Ta making a convex pattern. Samples show negative Pb anomalies with notable exceptions from El Hierro (EH06-01, -02, -03) and Lanzarote (LZ06-01). The patterns show a negative slope becoming more homogeneous with increasing compatibility (**Figure 4.4b**). Ratios of Nb/Ta overlap the chondritic average, ranging from 15.4 to 18.01 (Nb/Ta Chondrite = 17.6; (Weyer et al., 2002)), whereas Zr/Hf ratios (39.7 to 46.0) are elevated relative to chondrites (Zr/Hf Chondrite = 36.6 (Jochum et al., 1986), and 34.2; (Weyer et al., 2002)). Primitive mantle normalized rare earth elements (REE) patterns have a dominantly negative slope with a La/Yb range from 12.91 to 33.8 and a La/Sm range from 3.05 to 6.14. Three of the El Hierro samples (EH06-01, -02, -03) have PM normalized La depleted relative Ce making a discrete convex LREE pattern that slopes negatively into MREE, consistent with the broader lava suite (**Figure 4.5b**).

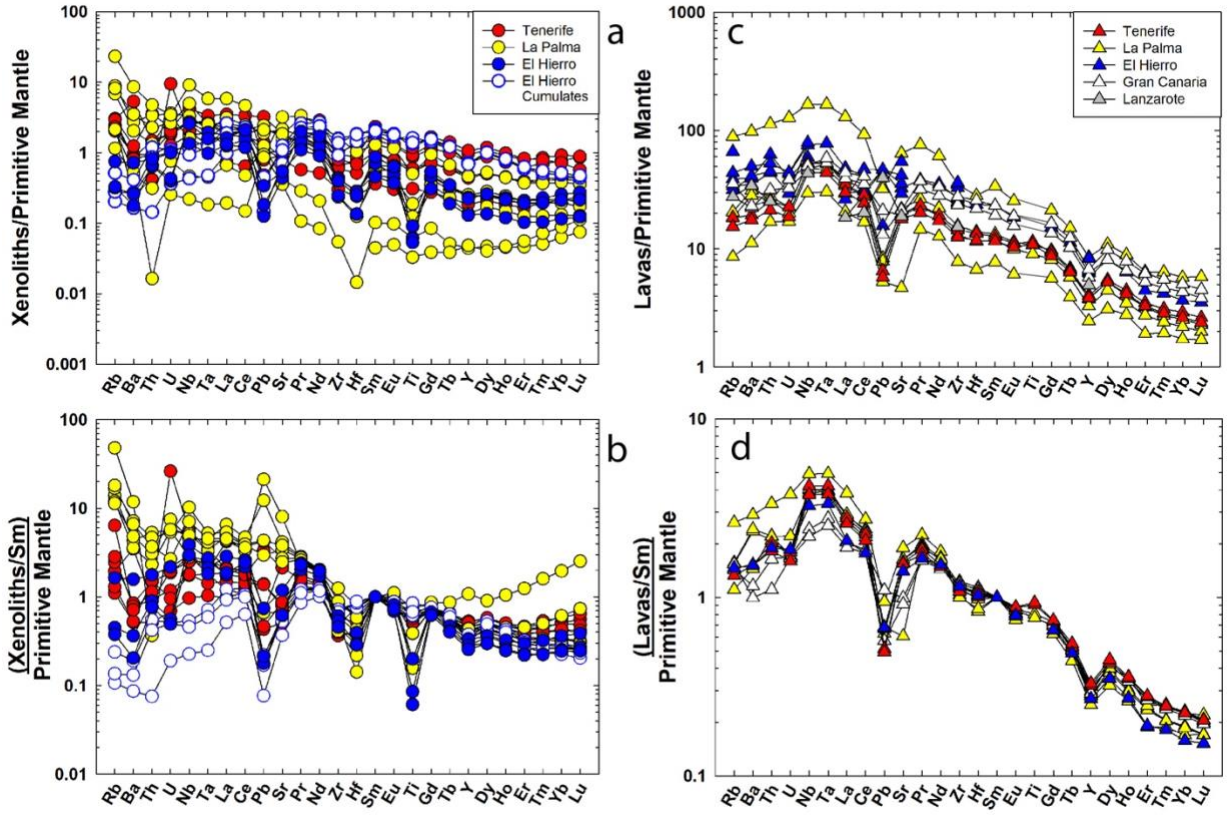

Figure 4.4 (a) Primitive mantle normalized trace element diagram for Tenerife, La Palma, and El Hierro ultramafic xenoliths. (b) Xenolith trace elements double normalized to Sm to highlight dispersion of light and fluid mobile TE within the sample set and LP1603e showing HREE enrichment. (c) Primitive mantle normalized trace element diagram for Tenerife, La Palma, El Hierro, Gran Canaria, and Lanzarote shield-stage lavas. (d) Trace elements double normalized to Sm for shield stage lavas from Gran Canaria, Tenerife, La Palma, and El Hierro. Primitive mantle normalization from McDonough and Sun (1995).

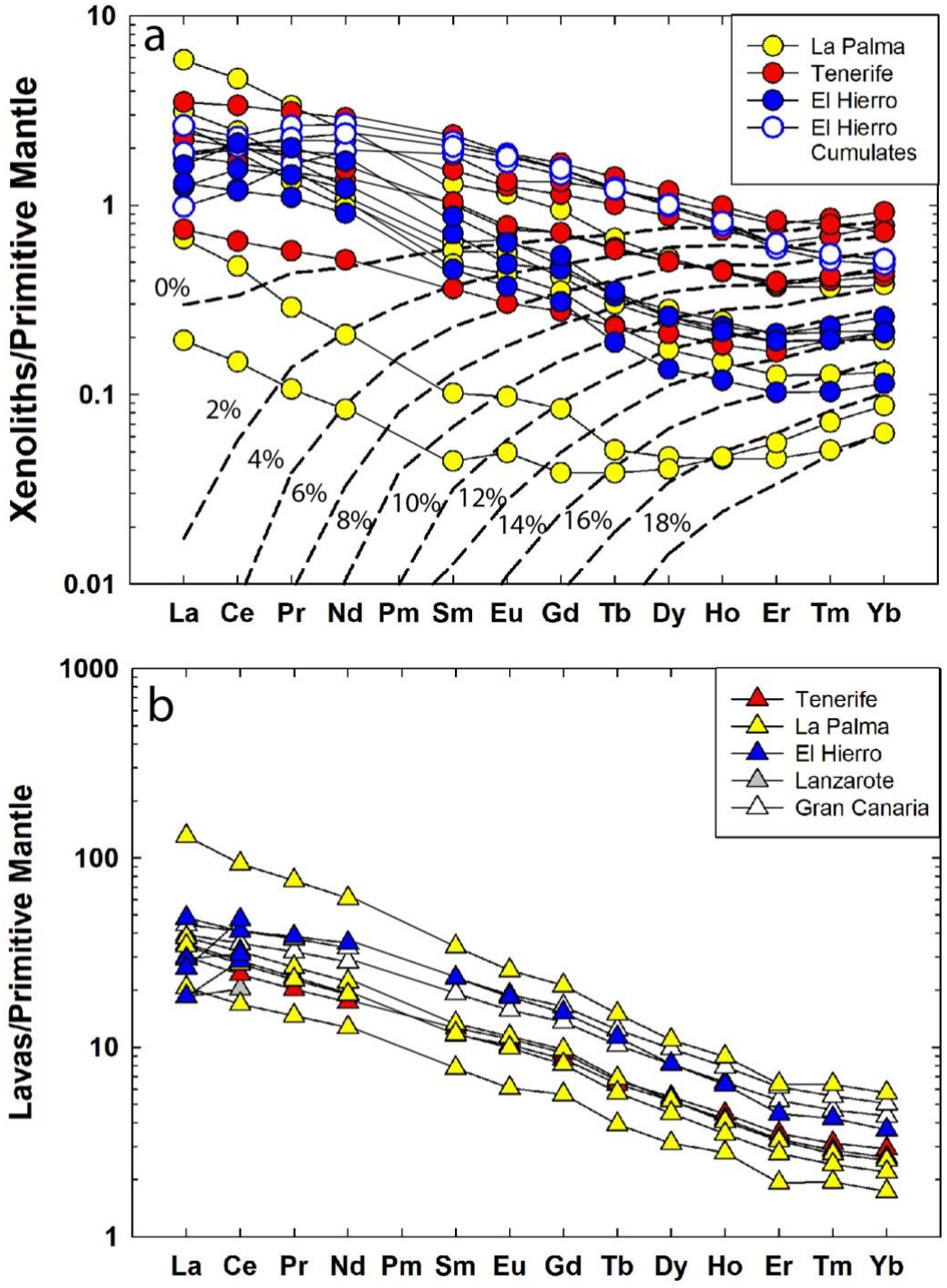

Figure 4.5 (a) Primitive mantle normalized rare earth element diagram for Tenerife, La Palma, and El Hierro. Melt depletion curves from Warren (2016) are in 2% increments from 0 – 18%. (b) Primitive mantle normalized rare earth element diagram for Tenerife, La Palma, El Hierro, Gran Canaria, and Lanzarote. Primitive mantle normalization from McDonough and Sun (1995).

4.4.3 Osmium Isotopic Ratios & Highly Siderophile Element Abundances

El Hierro cumulate xenoliths have absolute HSE abundances below primitive mantle estimates, with the exception of EH1601F which shows a relative enrichment in Pd. The cumulates are near parity with regard to Re and Pd compared to lithospheric xenoliths from this study, but they are comparatively depleted in Pt, Ru, Ir, and Os. The broader HSE profiles of these samples are depleted compared to Atlantic lithosphere (Day et al., 2017) (**Figure 4.6a**). These samples have a broad negative correlation with Pd, Pt, Ru, Ir, and Os, and a positive correlation with Re. Nickel is negatively correlated with Re and Pd and positively correlated with the compatible HSE. Inter-HSE ratios are generally low (average Pd/Ir = 3.8 ±8.4; average Pt/Ir = 1.7 ±1.6; average Ru/Ir = 2.1 ±1.4) which suggests a lesser degree of fractionation than the lavas. Os compositions are well above the 50 pg/g threshold (average Os = 4.78 ng/g ±7.8) suggesting that early crystalizing phases may act as a control on Os concentrations and Os isotope ratios. The $^{187}Os/^{188}Os$ ratios for the El Hierro cumulates define a narrow range inside that of the lavas but more radiogenic than the lithospheric xenoliths (0.14896 – 0.16196; average = 0.15599 ±0.0132). These samples generally become less radiogenic with increasing Os concentration. They have a broad negative correlation with MgO and are well correlated negatively with Ni.

Rhenium-Os isotopes and highly siderophile element (HSE: Os, Ir, Ru, Pt, Pd, Re) abundances were determined for all the xenoliths and lavas and are reported in **Table 4.1**. Primitive mantle normalized HSE profiles for lithospheric xenoliths from Tenerife, El Hierro, and La Palma are flat with respect to compatible HSE, with notable depletions in Re and variable Pd. Incompatible HSE abundances are generally flat with respect to MgO for xenoliths from Tenerife, La Palma, and El Hierro while compatible HSE are more scattered. Nickel content shows a positive trend across HSE although poorly correlated. $^{187}Os/^{188}Os$ are more reflective of mantle values

(0.11910 – 0.13087) and have a good negative correlation between MgO and $^{187}Os/^{188}Os$ (r^2 = 0.87). $^{187}Re/^{188}Os$ overall have a high degree of variation ranging from 0.01 to 29.56 (average = 2.43 ±15.1) and are typically flat with respect to MgO and Ni.

Similar to the xenoliths, absolute HSE abundances for the lavas from the five islands in this study are generally below primitive mantle estimates (Becker et al., 2006; Day et al., 2017), with the exception of Gran Canaria lavas which show relative enrichments in incompatible HSE (Re, Pd, Pt). The entire sample set of lavas shows relative enrichments in incompatible HSE versus depletions in compatible HSE (Ru, Ir, Os) making a negative sloping HSE profile (**Figure 4.6b**). The largest disparity in the HSE profile for Canary lavas is the enriched Gran Canaria picrites and two lavas from El Hierro and La Palma which show prominent depletions in Pt and Ru. Palladium shows a good negative correlation with Cu (r^2 = 0.7) (average Pd/Cu = 0.013 ±0.02). Re is negatively correlated with MgO and Ni and positively correlated with TiO_2. Palladium and Pt are negatively correlated with MgO and TiO_2, and positively correlated with Ni. Ru, Ir, and Os are positively correlated with MgO and Ni, and negatively correlated with TiO_2. Although these correlations are clearly apparent, there is considerable scatter in all the patterns. Inter-HSE ratios provide evidence of fractionation (average Pd/Ir = 7.8 ±9.6; average Pt/Ir = 7.4 ±12.4). Osmium concentrations for the entire sample set are above the 50 pg/g threshold observed by several workers (Day et al., 2010; Marcantonio et al., 1995; Widom et al., 1999). Concentrations below this threshold are highly susceptible to contamination and typically show extremely radiogenic $^{187}Os/^{188}Os$ ratios (Reisberg et al., 1993). Nonetheless, $^{187}Os/^{188}Os$ ratios for these Canary lavas define a broad range from 0.12870 – 0.19740 with an average of 0.15030 ±0.034.

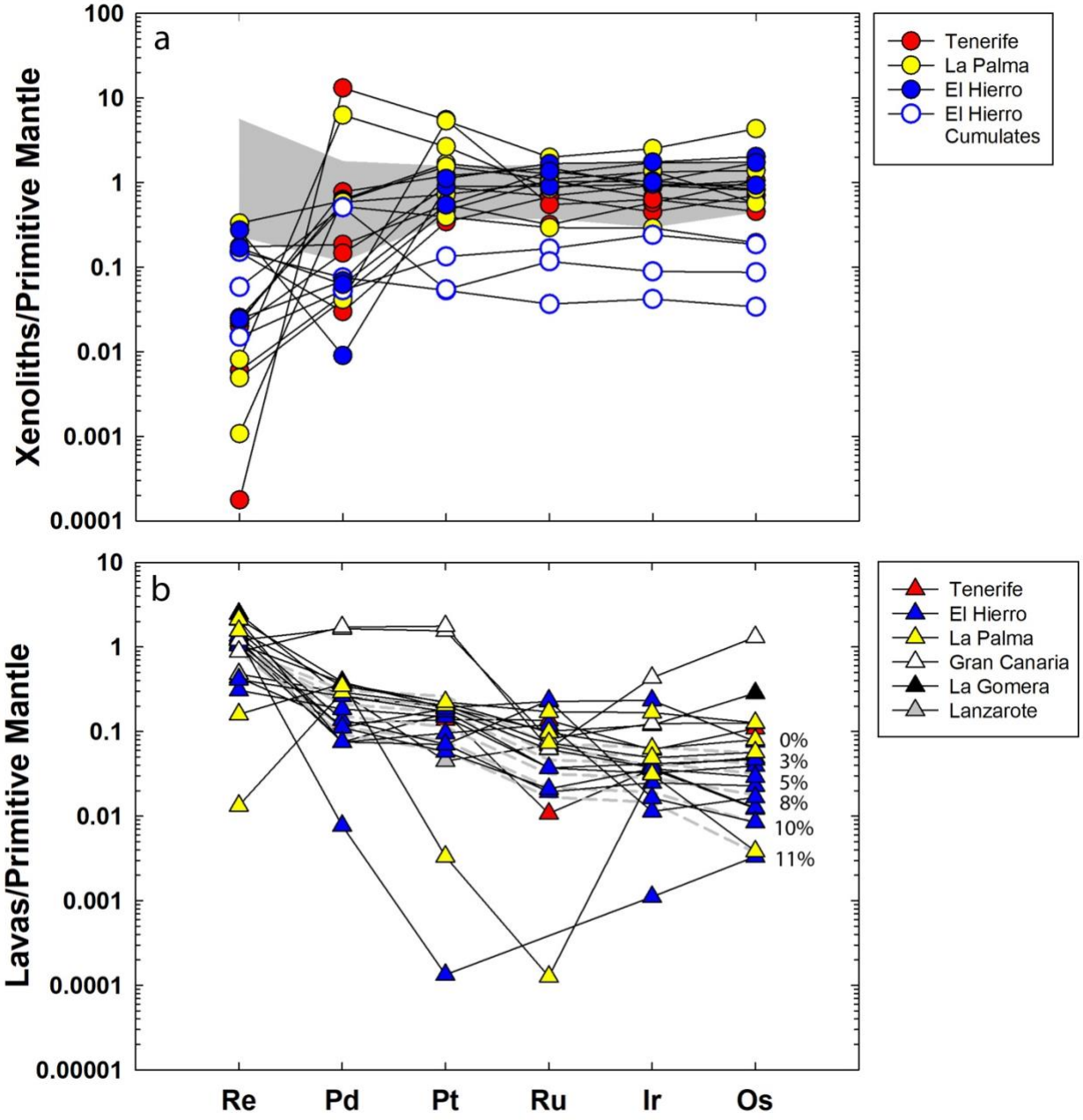

Figure 4.6 (a) HSE abundances for Tenerife, La Palma, and El Hierro ultramafic xenoliths. The grey shaded area is a global compilation of abyssal peridotites from Day et al. (2017) and references therein. (b) HSE abundances for Tenerife, La Palma, El Hierro, Gran Canaria, and Lanzarote. Crystallization model shows the results of 0 – 11% co-crystallization of olivine, spinel, and sulfide. See main text for detailed model parameters. Primitive mantle normalization from Day et al. (2017).

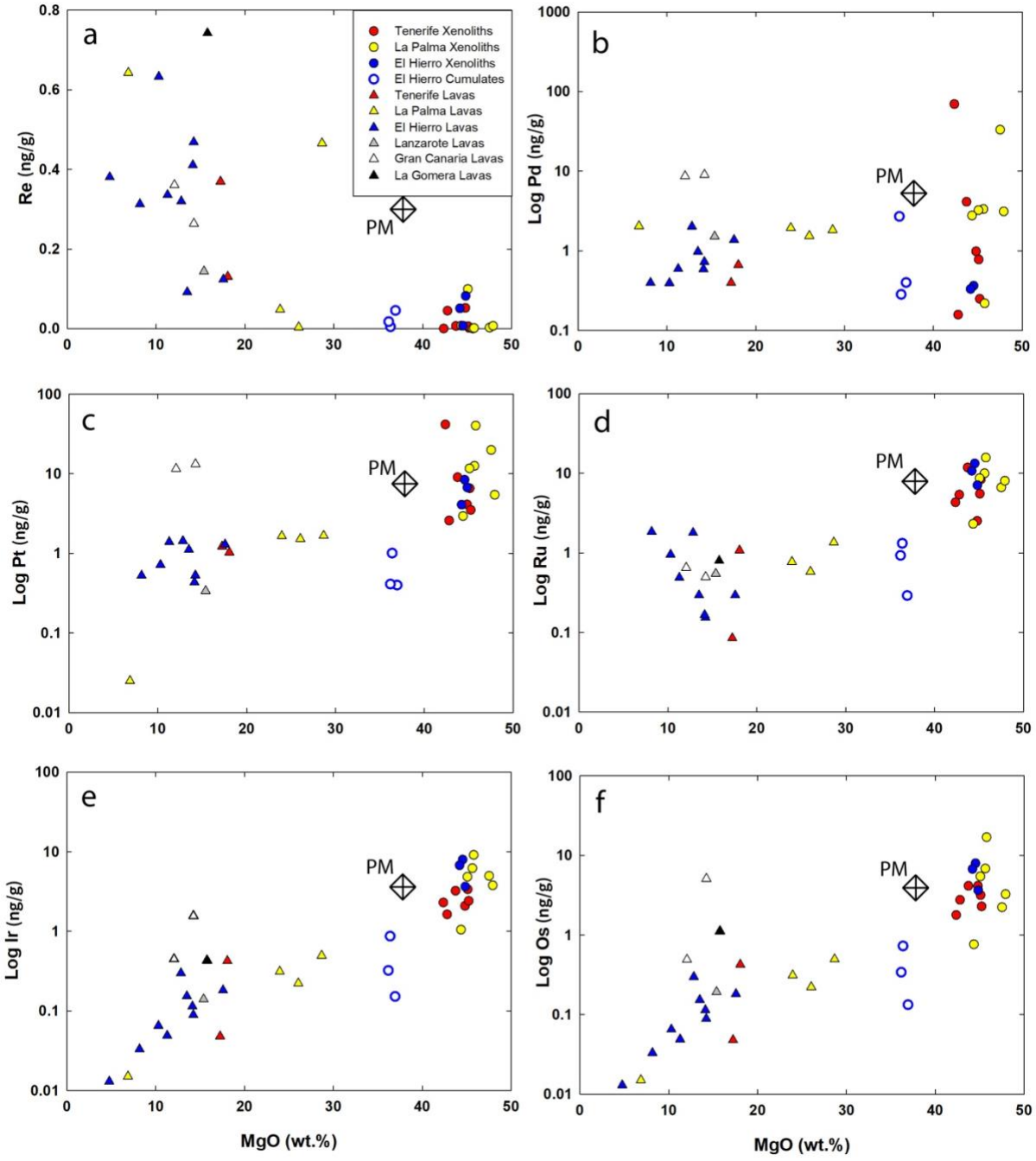

Figure 4.7 HSE versus MgO Harker diagram for Canary Islands ultramafic xenoliths and lavas. (PM = primitive mantle estimate from McDonough and Sun (1995) and Day et al. (2017))

Table 4.1 Whole-rock Re-Os isotope and highly siderophile element (ng g^{-1}) abundances for Canary Islands xenoliths and lavas.

	Location	Lithology	MgO (wt.%)	Al_2O_3 (wt.%)	Re	Pd
Xenoliths						
TF1601A	Tenerife	Harz	42.8	0.9	0.04	0.16
TF1601B	Tenerife	Harz	43.7	1.0	0.01	4.12
TF1601C	Tenerife	Harz	44.8	0.8	0.05	0.98
TF1601D	Tenerife	Lhz	45.2	0.9	0.00	0.25
TF1601E	Tenerife	Lhz	45.1	0.8	0.01	0.78
TF1601F	Tenerife	Lhz	42.4	0.4	0.00	69.67
EH1601A	El Hierro	Cumulate	36.4	2.2	0.00	0.28
EH1601B	El Hierro	Harz	44.8	0.9	0.08	0.05
EH1601C	El Hierro	Cumulate	36.9	1.5	0.05	0.40
EH1601D	El Hierro	-	44.5	1.2	0.01	0.36
EH1601E	El Hierro	-	44.2	1.1	0.05	0.33
EH1601F	El Hierro	Cumulate	36.2	2.0	0.02	2.70
LP1603A	La Palma	Lhz	45.6	0.7	0.00	3.34
LP1603B	La Palma	Lhz	45.1	0.8	0.10	3.23
LP1603C	La Palma	Harz	47.5	0.5	0.00	33.18
LP1603D	La Palma	Harz	47.9	1.0	0.01	3.11
LP1603E	La Palma	Lhz	45.8	0.8	0.00	0.22
LP1603F	La Palma	Lhz	44.4	1.2	0.01	2.76
Lavas						
LZ06-01	Lanzarote	Picro-Basalt	15.4	11.0	0.14	1.52
GC0901	Gran Canaria	Basalt	12.1	10.5	0.36	8.72
GC0902	Gran Canaria	Basalt	14.2	9.3	0.26	9.08
9C-TEN-05	Tenerife	Picro-Basalt	17.2	9.3	0.37	0.40
9E-TEN-05	Tenerife	Picro-Basalt	18.1	9.1	0.13	0.67
1F-GOM-05	La Gomera	Basanite	15.8	10.2	0.74	1.39
JMDD LP19	La Palma	Basanite	6.9	15.1	0.64	2.05
03-PAL-05	La Palma	Picro-Basalt	24.0	7.0	0.05	1.94
04-PAL-05	La Palma	Picro-Basalt	26.0	6.5	0.00	1.55
JMDD LP03	La Palma	Foidite	28.7	5.4	0.47	1.83
JMDD EH01	El Hierro	Foidite	14.2	9.6	0.47	0.73
JMDD EH02	El Hierro	TrachyBasalt	4.8	16.4	0.38	0.04

Table 4.1 Whole-rock Re-Os isotope and highly siderophile element (ng g^{-1}) abundances for Canary Islands xenoliths and lavas. (Continued)

	Location	Lithology	MgO (wt.%)	Al_2O_3 (wt.%)	Re	Pd
JMDD EH03	El Hierro	Basanite	12.8	11.5	0.32	2.03
JMDD EH12	El Hierro	Basanite	13.5	10.7	0.09	0.98
JMDD EH15	El Hierro	Picro-Basalt	17.6	8.9	0.12	1.38
EH06-01	El Hierro	Picro-Basalt	14.1	9.9	0.41	0.59
EH06-02	El Hierro	Basanite	11.3	12.3	0.34	0.60
EH06-03	El Hierro	Basanite	10.3	12.5	0.63	0.40
EH06-04	El Hierro	Basanite	8.2	14.3	0.31	0.40

	Pt	Ru	Ir	Os	Pd/Ir	Ru/Ir
Xenoliths						
TF1601A	2.58	5.38	1.62	2.75	0.10	3.31
TF1601B	9.03	11.76	3.21	4.12	1.28	3.66
TF1601C	4.11	2.52	2.08	4.12	0.47	1.21
TF1601D	3.50	8.36	2.39	2.27	0.10	3.49
TF1601E	6.55	5.51	3.35	3.15	0.23	1.64
TF1601F	41.47	4.31	2.29	1.77	30.45	1.89
EH1601A	1.00	1.31	0.87	0.73	0.33	1.52
EH1601B	6.71	7.07	3.43	3.62	0.01	2.06
EH1601C	0.40	0.29	0.15	0.13	2.64	1.92
EH1601D	8.38	13.25	6.28	7.90	0.06	2.11
EH1601E	4.07	10.72	3.65	6.71	0.09	2.94
EH1601F	0.41	0.92	0.32	0.34	8.40	2.87
LP1603A	12.56	9.99	6.19	6.80	0.54	1.61
LP1603B	11.63	8.65	4.81	5.42	0.67	1.80
LP1603C	19.87	6.64	4.94	2.22	6.71	1.34
LP1603D	5.43	8.02	3.76	3.24	0.83	2.13
LP1603E	40.19	15.69	9.07	16.85	0.02	1.73
LP1603F	2.94	2.31	1.04	0.76	2.65	2.22
Lavas						
LZ06-01	0.34	0.55	0.14	0.19	10.86	3.91
GC0901	11.60	0.65	0.45	0.49	19.51	1.45
GC0902	13.23	0.50	1.56	5.11	5.83	0.32
9C-TEN-05	1.23	0.09	0.13	0.05	3.08	0.66
9E-TEN-05	1.03	1.08	0.22	0.43	3.07	4.95
1F-GOM-05	1.47	0.80	0.43	1.11	3.24	1.86

Table 4.1 Whole-rock Re-Os isotope and highly siderophile element (ng g^{-1}) abundances for Canary Islands xenoliths and lavas. (Continued)

JMDD LP19	0.03	0.00	0.11	0.02	18.33	0.01
03-PAL-05	1.65	0.77	0.23	0.31	8.56	3.40
	Pt	Ru	Ir	Os	Pd/Ir	Ru/Ir
04-PAL-05	1.53	0.58	0.18	0.22	8.78	3.28
JMDD LP03	1.67	1.35	0.60	0.50	3.04	2.25
JMDD EH01	0.53	0.15	0.09	0.09	8.18	1.71
JMDD EH02	0.00	0.00	0.00	0.01	10.25	0.00
JMDD EH03	1.44	1.79	0.84	0.30	2.41	2.13
JMDD EH12	1.12	0.29	0.12	0.15	8.46	2.53
JMDD EH15	1.30	0.29	0.15	0.18	9.21	1.96
EH06-01	0.43	0.17	0.13	0.11	4.52	1.27
EH06-02	1.40	0.49	0.14	0.05	4.41	3.60
EH06-03	0.72	0.96	0.04	0.07	9.66	23.29
EH06-04	0.53	1.85	0.06	0.03	6.76	31.34

	$^{187}Re/^{188}Os$	2s	$^{187}Os/^{188}Os$	2s	T_{RD} (Ma)	γOs
Xenoliths						
TF1601A	0.07871	0.002	0.12335	0.00014	891	-
TF1601B	0.07864	0.003	0.12522	0.00009	625	-
TF1601C	0.10639	0.119	0.12412	0.00015	779	-
TF1601D	3.97781	0.003	0.12324	0.00010	910	-
TF1601E	0.11292	0.004	0.12412	0.00009	782	-
TF1601F	0.13401	0.003	0.13087	0.00011	99	-
EH1601A	0.63292	0.033	0.14896	0.00016	-	-
EH1601B	1.08700	0.056	0.12718	0.00012	352	-
EH1601C	1.85600	0.887	0.15705	0.00028	-	-
EH1601D	29.56020	0.004	0.12673	0.00014	409	-
EH1601E	0.12587	0.019	0.12675	0.00015	407	-
EH1601F	0.63506	0.087	0.16196	0.00021	-	-
LP1603A	0.11036	0.001	0.12443	0.00008	732	-
LP1603B	0.02993	0.022	0.12589	0.00009	529	-
LP1603C	0.73161	0.004	0.12647	0.00010	457	-
LP1603D	0.12755	0.004	0.11910	0.00012	1478	-
LP1603E	0.14131	0.000	0.12098	0.00010	1210	-
LP1603F	0.01465	0.019	0.12584	0.00010	578	-
Lavas						

Table 4.1 Whole-rock Re-Os isotope and highly siderophile element (ng g^{-1}) abundances for Canary Islands xenoliths and lavas. (Continued)

LZ06-01	3.63057	0.082	0.16138	0.00019	-	26.0
GC0901	3.55182	0.079	0.12999	0.00006	-	1.8
GC0902	0.24903	0.000	0.12870	0.00006	-	0.9
9C-TEN-05	37.25791	0.860	0.14977	0.00016	-	14.5
9E-TEN-05	1.48797	0.014	0.14012	0.00006	-	9.8
	$^{187}Re/^{188}Os$	2s	$^{187}Os/^{188}Os$	2s	T_{RD} (Ma)	γOs
1F-GOM-05	3.23081	0.065	0.13893	0.00017	-	8.9
JMDD LP19	207.06009	8.900	0.14479	0.00017	-	13.5
03-PAL-05	0.74325	0.003	0.14602	0.00006	-	14.5
04-PAL-05	0.08703	0.000	0.14432	0.00019	-	13.1
JMDD LP03	4.54654	0.128	0.14344	0.00007	-	12.3
JMDD EH01	27.06295	0.320	0.14185	0.00009	-	11.2
JMDD EH02	142.53491	4.200	0.19740	0.00137	-	54.7
JMDD EH03	10.98559	0.058	0.17034	0.00007	-	33.4
JMDD EH12	2.91596	0.053	0.17508	0.00006	-	37.2
JMDD EH15	3.29483	0.067	0.15376	0.00009	-	20.5
EH06-01	20.17684	0.546	0.15085	0.00019	-	18.2
EH06-02	33.15850	0.680	0.15320	0.00022	-	20.1
EH06-03	47.09304	1.370	0.15346	0.00011	-	20.3
EH06-04	45.74018	1.300	0.13225	0.00326	-	3.7

4.5 Discussion

4.5.1 Distinguishing cumulate from lithospheric xenoliths

Mantle xenoliths and ultramafic cumulates can share some similarities such as modal minerology or depleted ITE patterns, however, the processes that formed them and information that can be gleaned from them are substantially different. Mantle xenoliths represent the ultramafic residue remaining after MORB extraction, whereas ultramafic cumulate xenolith are precipitate products of basaltic melts which can occur anywhere from the upper mantle, crust, or within the volcanic edifice. Therefore, it is important to clearly define the two groups represented in this study. Of the eighteen xenoliths analyzed here, three are interpreted as cumulate xenolith (EH1601A, -C, -F). The remaining fifteen xenoliths are harzburgites and lherzolites, highly melt-depleted refractory mantle fragments based on their petrographic textures, major and trace element compositions and $^{187}Os/^{188}Os$ that suggest stabilization ages >700 Ma.

Available thin sections (EH1601A, -C) are dominantly fine grained with evidence of melt infiltration, as opposed to the other xenoliths which are typically coarse-grained spinel harzburgites and lherzolites with ~120° triple junctions suggesting long-term equilibration at elevated temperature and pressure. The cumulate samples show substantially less MgO (36.18 to 36.94 wt.%), elevated Al_2O_3 (1.45 to 2.21 wt.%), and elevated $Fe_2O_{3(T)}$ (16.19 to 19.56 wt.%) than the lithospheric xenolith samples. This disparity is best illustrated by Mg-number for the two sample subsets where elevated Mg-numbers for the lithospheric samples shows that they are Mg rich, and Fe depleted (Avg. Mg-number = 90.0 ±4.0) within the range of DMM, versus the significantly lower cumulate samples (Avg. Mg-number = 80.4 ±3.2). In addition, major and trace element co-variation diagrams show the cumulate xenoliths are enriched in incompatible elements

relative the PM and typically plot between the lava and lithospheric samples, whereas lithospheric xenoliths consistently plot below PM estimates (**Figure 4.2**).

Absolute REE abundances are broadly similar between the cumulates and the most enriched lithospheric samples however, PM normalized patterns for the cumulates show LREE depletion relative to the MREE which suggests crystal-liquid fractionation of LREE and accumulation of clinopyroxene. The strong LREE enrichment in the lithospheric xenoliths are consistent with metasomatic processes post melt-depletion which is commonly observed in abyssal peridotites (e.g., Niu, 2004; Warren, 2016), as well as HFSE fractionation. This will be discussed in detail for the lithospheric xenoliths in the following sections, but it is important to note for comparative purposes the subchondritic Zr/Hf for the cumulates versus the suprachondritic Zr/Hf for the lithospheric samples. This suggests the HFSE were uniformly fractionated into the liquid phase resulting in subchondritic Zr/Hf for the cumulates, whereas the highly variable suprachondritic Zr/Hf for the xenoliths reflect melt-rock reaction.

Relative HSE abundances for the cumulate samples are depleted relative to the primitive mantle estimate with flatter patterns compared to the lithospheric xenoliths. Like the lavas, these three cumulates show enrichments in Re, Pd, and Pt relative the lithospheric samples. They also have the lowest Os concentrations (Os = 0.13 – 0.73 ng/g) and are the most radiogenic ($^{187}Os/^{188}Os$ = 0.1487 – 0.1620) of the entire xenolith suite. This is much more comparable to the average lava from this study (Avg. Os = 0.5 ±2.4 ng/g; Avg. $^{187}Os/^{188}Os$ = 0.1503 ±0.0334) and previously published Canary lavas (Avg. Os = 0.07 ng/g ±0.12; Avg. $^{187}Os/^{188}Os$ = 0.1520 ±0.0308 (Widom et al., 1999) and (Avg. Os = 0.07 ng/g ±0.1; Avg. $^{187}Os/^{188}Os$ = 0.1455 ±0.0116 (Day et al., 2009; Day et al., 2010; Day et al., 2022)). As for the lithospheric xenoliths, HSE patterns, in most cases, overlap those of Atlantic (Day et al., 2017) and Pacific (Paquet et al., 2022) abyssal peridotites

(**Figure 4.6a**). Osmium isotopic compositions range from 0.119 to 0.131 consistent with global averages for $^{187}Os/^{188}Os$ for abyssal peridotites (e.g., Day et al., 2017; Paquet et al., 2022; Snortum et al., 2019) and depleted mantle in general (e.g., Armytage et al., 2014; Harvey et al., 2012).

4.5.2 Metasomatism of Canary Island xenoliths

Evidence of metasomatic melt-rock reaction is provided by the elevated LREE abundances observed in the lithospheric samples. All of the xenoliths presented here have highly variable whole-rock $(La/Yb)_{PM}$ >1 which are indicative of clinopyroxene addition and/or melt infiltration. Clinopyroxene exhibits a strong control over the bulk partition coefficients of the LREE as well as HFSE Zr and Hf (Hart & Dunn, 1993), thus any addition of clinopyroxene by migrating melts can strongly leverage REE patterns. This effect is evident in figure 5a as the LREE do not follow the predicted melting patterns and in some cases are elevated above the PM estimate. This type of enrichment, which favors LREE over more compatible trace elements and HREE, requires reaction between the residue and low degree partial melt that will not over-print the entire system (e.g., d'Errico et al., 2016; Harvey et al., 2006). This LREE enrichment versus HREE is most evident in the four lherzolite samples (TF1601E, -F, LP1603B, and -E) where clinopyroxene likely crystalized as a secondary phase within refractory harzburgites. Melt infiltration is most apparent in the Tenerife samples and EH1601C where modal analysis of petrographic sections show ~2 to 7% melt. However, elevated clinopyroxene and melt do not directly correspond to high $(La/Yb)_{PM}$ ratios. In fact, the highest $(La/Yb)_{PM}$ occur in the La Palma samples which are a mix of lherzolites and harzburgites and have no optically detectable melt infiltration veins. There are two plausible explanations for this disparity. First, modal analysis of a particular this section is limited to a small area compared to whole-rock geochemical analysis which involves homogenization of several

grams (>50) of rock powder. Melt veins could be present in the broader sample but not sampled by a particular thin section. Second, melt-rock reaction that results in the addition of clinopyroxene and/or melt that isn't visually obvious referred to as cryptic metasomatism (e.g., Warren, 2016). This type of metasomatism is normally made apparent by U-shaped REE patterns where initial melting depletes LREE-MREE followed by low degree melt infiltration that enriches the LREE. Ideally, cryptic metasomatism should produce a U-shaped LREE pattern with $(La/Yb)_{PM}$ at or near unity. In this case none of the samples have $(La/Yb)_{PM}$ at unity but four sample are less than 3 and another five samples show $(La/Yb)_{PM}$ less than 5 making for an asymmetric U-shaped REE pattern.

To place some constraints on the degree of melt addition to the Canary lithosphere a simplified two-component mixing model, similar to Oller et al. (2022), was used to test the effect of a low degree Canary melt on the depleted lithosphere. The initial composition is an idealized refractory lithosphere that has experienced 10 to 15% melt depletion. Added to this is the average of lavas from this study with MgO and Al_2O_3 composition near that of the calculated parent melt of 15 wt.% and 10 wt.% respectively. The model shows that the addition of 0.5 to 13% of an enriched Canary lava produces a good fit with the observed REE patterns (**Figure 4.8**). Melt addition over 4% may be considered high, however, given the extent of erupted lava that comprises the Canary Islands and the extent of melt infiltration observed in some xenoliths this possibility cannot be excluded.

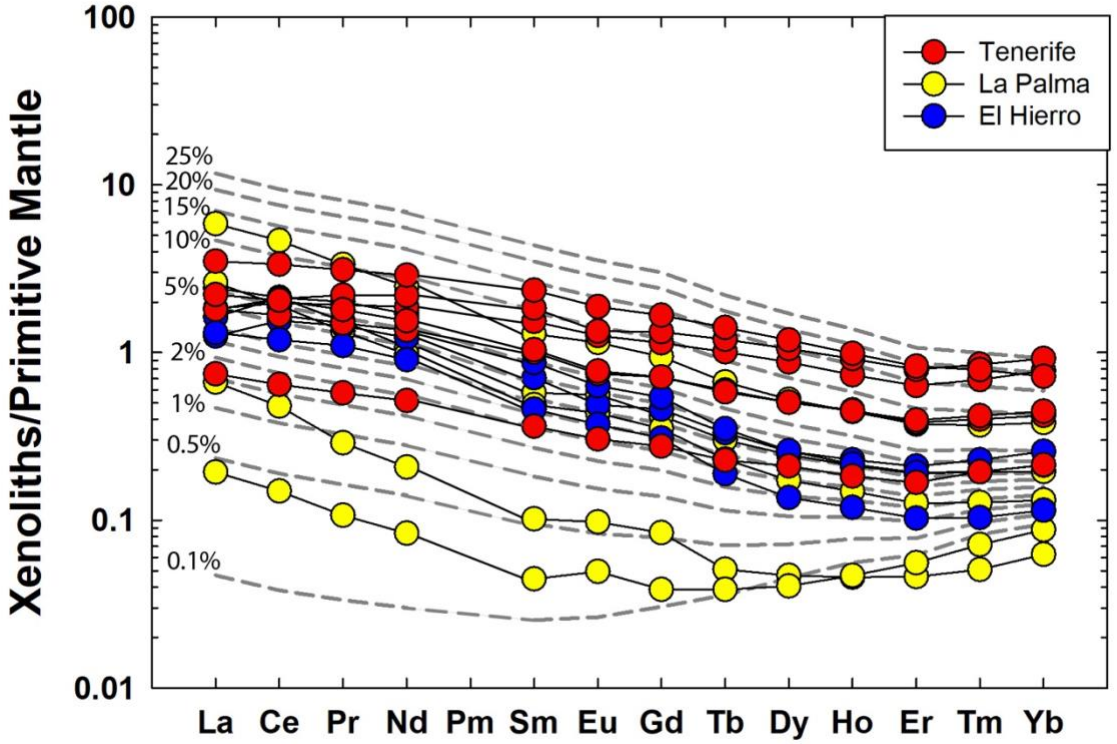

Figure 4.8 Rare Earth element melt addition model for Canary ultramafic xenoliths. Melt addition curves from 0.1% - 25% are relative to the most REE depleted (LP1603E). Primitive mantle normalization from McDonough & Sun 1995.

4.5.3 HFSE fractionation in the Canary lithosphere

High field strength element (HFSE: Nb, Ta, Zr, and Hf) fractionation is a common characteristic of mantle peridotites that have been exposed to melt-depletion and metasomatism in the spinel facies (e.g., Niu, 2004; Pfänder et al., 2007; Weyer et al., 2003). For the Canary Islands samples the element pairs Zr-Hf show highly variable degrees of fractionation between the Tenerife (Avg. Zr/Hf = 38.7 ±14.2), El Hierro (Avg. Zr/Hf = 61.3 ±11.4), and La Palma (Avg. Zr/Hf = 76.7 ±71.0) data sets. For El Hierro and La Palma these ratios are nearly double chondritic ratios with La Palma values showing extreme variation (LP1603C Zr/Hf = 139.5), while Tenerife

ratios are just slightly elevated. Ratios of Nb/Ta are also significantly elevated above chondrites (Tenerife +15%, El Hierro and La Palma +47%). Partial melting of spinel facies mantle should produce low Nb/Ta and Zr/Hf given the lower compatibility of Nb and Zr versus Ta and Hf. Melt-depletion should produce a positively correlated trend between Zr/Hf and Zr concentration in mantle residue because clinopyroxene/melt partition coefficients predict $D_{Hf} > D_{Zr}$ (Hart & Dunn, 1993), but the observation made here shows a negative correlation. The same idea holds for Nb/Ta versus Nb which, in this case, Nb/Ta does decrease with decreasing Nb concentration, albeit with a poorly correlated trend. These observed relationships which contradict model predictions suggest other process(es) besides simple MORB extraction have affected these samples. Metasomatic enrichment from a low degree asthenosphere partial melt would increase the concentration of Nb relative to Zr given Nb is more incompatible than Zr, and Zr is compatible in the garnet stability field. This should produce a positive correlation between Zr/Nb and Zr with relatively uniform Nb/Ta ratios, which is observed in the Canary xenoliths, which suggests that a more homogenously enriched Nb melt reacted with the depleted lithosphere in the spinel stability field (Weyer et al., 2003). The lavas presented in this study show chondritic Nb/Ta (Avg. Nb/Ta = 17.2 ±2.0) with more homogeneous Nb concentration (Avg. Nb = 36.0 ppm ±19.6) excluding one extreme outlier (JMDD LP19). The suprachondritic Nb/Ta in the Canary xenoliths may reflect an elevated ratio of this parent melt to residue which the previously discussed simplified REE addition model suggested could be as high as 10%.

4.5.4 Melt-depletion of Canary xenoliths

Elevated degrees of melt depletion is a key characteristics of the oceanic lithosphere (REF). The removal of basaltic material to form oceanic crust leaves a residue depleted in incompatible

elements, followed by re-enrichment by low degree percolating melts. This latter re-enrichment is normally manifested in relatively elevated LREE abundances preserved within metasomatic clinopyroxene and interstitial melt (e.g., Johnson et al., 1990). The melt-depletion process has been well documented globally, particularly for the Atlantic basin. For example, abyssal peridotites from the Gakkel Ridge and Mid-Atlantic Ridge are estimated to have experienced between 4 and 16% melt removal (d'Errico et al., 2016; Harvey et al., 2006). The effects of melt depletion on the Canary Islands xenoliths are best illustrated by major and trace element variations shown in **Figure 4.2**. The divergence of these samples from the PM estimate shows the removal of incompatible major and trace elements and subsequent concentration of highly compatible MgO. Depleted REE patterns are another good indicator of melt depletion for lithospheric samples as incompatible REE will be partition to the liquid phase proportionally based on the degree of melt removal. The melt depletion model of Warren (2016) was used to quantify the degree of melt removal for these samples. Based on HREE abundances, the model shows that the Canary Islands lithospheric xenoliths have experienced 6 to 18% melt removal, consistent with MORB-like melt depletion of upper mantle peridotite (Day et al., 2017; Hellebrand et al., 2002; Oller et al., 2022) (**Figure 4.5a**).

Osmium isotopes and HSE abundances are good indicators of mantle melting and metasomatic processes. Osmium concentrations greater than 50 pg/g typically preserve melt depletion signatures despite metasomatism or contamination from crustal sources (Day, 2013; Marcantonio et al., 1995; Widom et al., 1999). Samples beneath this threshold are highly susceptible to over-printing, which is advantageous for ultramafic xenolith studies because of the compatible behavior of Os and the tendency for olivine to enclose Os rich sulfides, thus the samples typically exceed 50 pg/g Os. In addition, HSE (Re, Pd, Pt, Ru, Ir, Os) are useful elements for elucidating mantle processes given their tendency to variably fractionate from one another

under various melting conditions (Rehkamper et al., 1999). Unlike major and trace elements, the HSE are dominantly controlled by sulfide phases and to a lesser degree oxides such as Cr-spinel. Rhenium is an exception to this as Re concentrations are less dependent on the abundance of sulfide phases and typically shows behavior broadly similar to ITE. Platinum-PGE (PPGE: Pd, Pt) tend to accumulate in Cu-sulfide phases and along with Re are the more incompatible HSE. Under most circumstances these phases form interstitially along grain boundaries from metasomatic sulfide rich alkali melts. By contrast, Iridium-PGE (IPGE: Ru, Ir Os) are hosted by primary sulfide phases which are subsequently hosted in early crystalizing lithophile phases such as olivine and/or opx (Luguet et al., 2007) and thus have more compatible behavior. These are commonly referred to as Type 1 sulfides by the population classification of Luguet and Pearson (2019), while the former are classified as Type 2, both of which are observed in Tenerife, El Hierro, and La Palma petrography.

Because of the high concentration of sulfide phase, and subsequently of the HSE, in peridotites versus melts, relative and absolute HSE abundances in whole-rock peridotites preserve long-term melt-depletion signatures well (Brandon et al., 2000; Day et al., 2017; Luguet et al., 2001; Paquet et al., 2022). Primitive mantle normalized HSE patterns show depletions in Re, Pd, ±Pt relative Ru, Ir, and Os for the majority of lithospheric samples. These patterns suggest sulfide melt was removed with silicate melt. Zhang and Hirschmann (2016) experimentally showed that Cu-Ni sulfide is partially or totally liquid at upper mantle conditions which results in the extraction of PPGE and concentration of IPGE in monosulfide solid solution (MSS) (e.g., Alard et al., 2000; Ballhaus et al., 2006; Luguet et al., 2003). However, no MSS were observed in any of the samples analyzed in this study which suggests HSE abundances are controlled by metasomatic secondary sulfide phases (Luguet & Reisberg, 2016). Copper abundance is a proxy for Cu-Ni sulfide, thus in

the case of metasomatic sulfide addition, should correlate positively with HSE abundances. This correlation is not observed in the sample set, nor is any correlation observed between absolute HSE abundance of intra-HSE ratios (Pd/Ir, Pt/Ir) and fertility indicators Al_2O_3 and La/Yb. Only five samples (TF1601B, -F, LP1603B, -C, -E) have Pd/Ir and/or Pt/Ir in excess of chondritic ratios but none of these samples correspond to anomalously high Cu, Al_2O_3, or La/Yb. Because these unusually high HSE ratios show no correspondence to broader indicators of metasomatism it is likely the high Pd ±Pt observed here are the result of a sulfide "nuggeting" effect that occurs only at the hand-sample level. Additionally, the lack of correspondence between HSE, sulfide and silicate metasomatism indexes suggest the effect of metasomatism on these sample is minor at best and very unlikely to leverage $^{187}Os/^{188}Os$.

For Os rich residuum (Os > 50 pg/g) $^{187}Os/^{188}Os$ ratios are not heavily affected by partial melting. Instead, partial melting fractionates the parent Re from the daughter Os thus locking the $^{187}Os/^{188}Os$ at the time of melting. As such, there is no definitive relationship between $^{187}Os/^{188}Os$ and other lithophile melt depletion indicators such as MgO in this sample set. The $^{187}Os/^{188}Os$ for lithospheric xenoliths presented in this study are unradiogenic (Avg. $^{187}Os/^{188}Os$ = 0.1252 ±0.0058) which compares very closely to the values obtained by Simon et al. (2008) for mantle xenoliths from the Canary Islands (Avg. $^{187}Os/^{188}Os$ = 0.1251 ±0.0024). These values also fall within the range of average abyssal peridotite Os isotopic compositions (Avg. $^{187}Os/^{188}Os$ = 0.1263 ±0.0198) (Lassiter et al., 2014), (Avg. $^{187}Os/^{188}Os$ = 0.1275 ±0.0306) (Day et al., 2017) and Salt Lake Crater peridotites from Oahu, Hawai'i (Avg. $^{187}Os/^{188}Os$ = 0.1226 ±0.0074) (Bizimis et al., 2007). Additionally, this is below the time-integrated primitive mantle $^{187}Os/^{188}Os$ value determined by Meisel et al. (2001) ($^{187}Os/^{188}Os$ = 0.1296) which suggests long-term fractionation of Re-Os. To provide insight into the timing of melt-depletion and constrain the *minimum* age of

lithosphere stabilization a Re depletion model age (T_{RD}) can be calculated from $^{187}Os/^{188}Os$ where T_{RD} is defined as: $T_{RD} = 1/1.67 \times 10^{-11} \times \ln [[(0.1269 - {}^{187}Os/^{188}Os_{sample})/0.40186] + 1]$. While T_{RD} ages are useful there are some important considerations when evaluating these model ages. T_{RD} only reports the most recent significant melting event where a significant melting event is defined as sufficient melt depletion to remove Re from the system in question. This fundamental assumtion implies that that many other melting events could have occurred prior to the reported T_{RD} especially if the lithosphere experienced refertilization of Re (Rudnick & Walker, 2009). Nevertheless, $^{187}Os/^{188}Os$ applied to T_{RD} for the Canary lithospheric xenoliths show an average stabilization age of 717.2 ±365.6 Ma with two sample from La Palma exceeding 1 Ga (LP1603D = 1478.5 Ma, LP1603E = 1210.1 Ma). Results reported by Simon et al. (2008) for Canary xenoliths and Bizimis et al. (2007) for Oahu xenoliths are very similar showing an average model age of 630.8 ±173.3 and 711.1 ±487.2 Ma respectively, although seven examples from the Oahu data set show ages exceeding 1 Ga with one example ~1.9 Ga. These relatively low $^{187}Os/^{188}Os$ and typically ancient model ages suggest that at least some ancient, depleted oceanic lithosphere exist beneath the Canary Islands despite the ongoing exposure to an isotopically enriched plume and clear and extensive melt-rock interaction processes.

4.5.5 Fractional Crystallization Processes in Canary Island Lavas

Canarian Archipelago lavas from this and previous studies show a broad compositional range (e.g., Carracedo et al., 2002; Day et al., 2009; Marcantonio et al., 1995) that suggests both partial melting and fractional crystallization are significant factors in the evolution of the parental melt(s). For example, picrites (03-PAL-05, 04-PAL-05, JMMD LP03) and cumulate xenoliths (EH1601A, -C, -F) presented in this study and those documented in other studies (e.g., Day et al.,

2010; Marcantonio et al., 1995) strongly suggest crystallization of spinel ± sulfide is a significant factor in affecting the composition of Canary lavas. Linear co-variation of major elements with MgO suggests fractional crystallization plays an important role in Canary lavas and likely acts as a control on HSE abundances (**Figure 4.2**). Steep primitive mantle normalized trace element and REE patterns also show the effect of fractionation with ITE abundances 10 to 100 × primitive mantle (**Figure 4.3**) and suggest partial melting in the presence of garnet. An estimate of the depth and degree of partial melting can be obtained through relative REE ratios. In this case a polybaric model using the relationship between $(Dy/Yb)_N$ and $(La/Yb)_N$ suggests ~2% - 7% partial melting at or near the garnet stability field (**Figure 4.9**) similar to previous estimates (Day et al., 2010; Gurenko et al., 2006), and consistent with the sediment-load corrected gravity study showing ~95 km thick lithosphere near the continental margin of Africa (Winterbourne et al., 2009). Several studies have shown that early precipitating mineral phases, such as olivine, can strongly control HSE abundances (Barnes et al., 1985; Ireland et al., 2009; Pitcher et al., 2009). Olivine control of HSE abundance is made evident for these data in HSE versus MgO variation diagrams (**Figure 4.7**). Here, the PGE (Pd, Pt, Ru, Ir, & Os) trend positively with MgO, albeit with variable degrees of correlation, which generally shows compatibility of PGE. Rhenium trends negatively with MgO and positively with TiO_2 although poorly correlated in both spaces, which suggests generally incompatible behavior. Unusually elevated Pd and Pt in Gran Canaria lavas (GC0901, GC0902) correspond to high Cu abundance, and in the case of GC902 the highest Cu abundance observed in these lavas. Using Cu as a proxy for sulfide content suggests these high PPGE abundances are the result of sulfide accumulation in these samples.

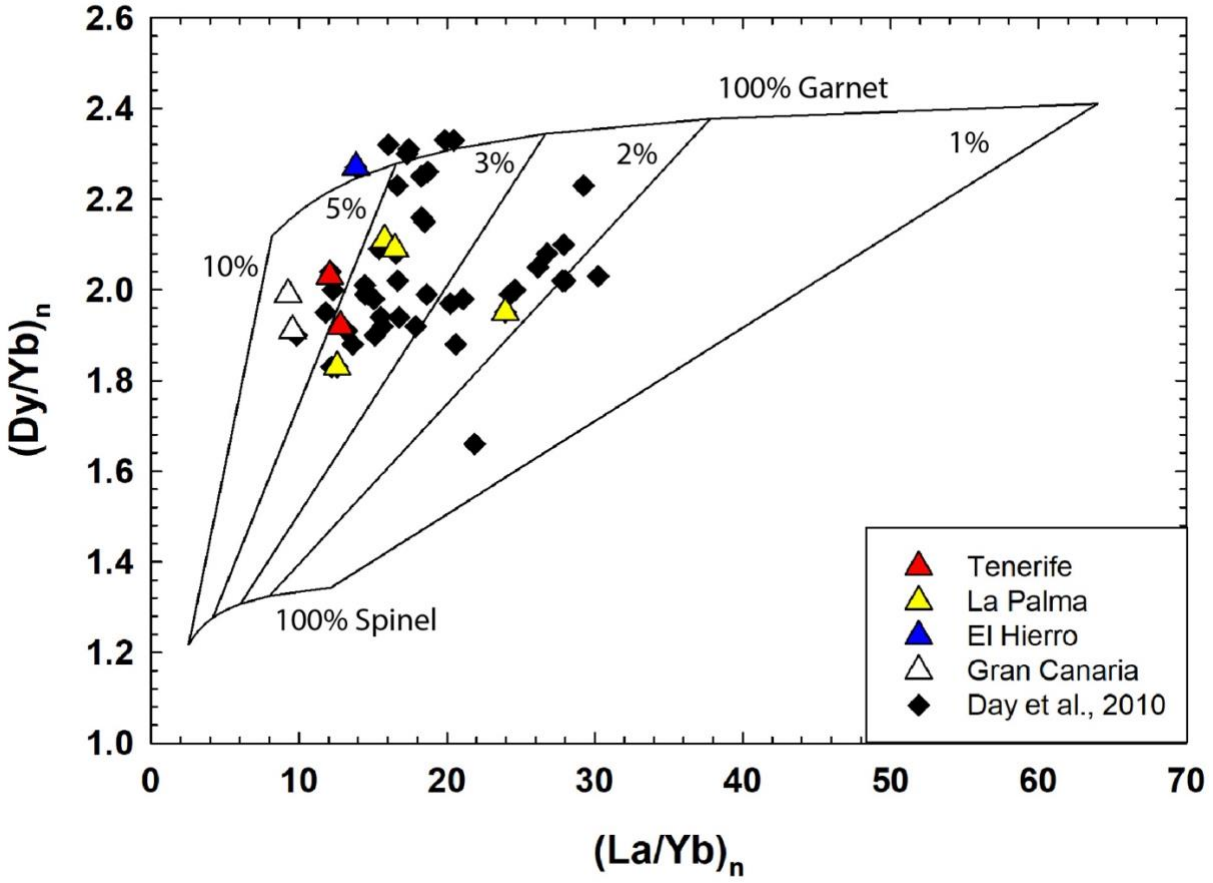

Figure 4.9 Estimates of partial melting for Tenerife, La Palma, El Hierro, and Gran Canaria lavas from this study versus published La Palma and El Hierro lavas from Day et al. (2010). This model assumes a primitive mantle source composition from McDonough and Sun (1995), partition coefficients from McKenzie and O'Nions (1991), and garnet and spinel peridotite modal proportions from Day et al. (2022).

Patrial melting is the primary driver of HSE fractionation in low degree partial melts due to incomplete melting of sulfides in the source material (Barnes et al., 1985; Rehkamper et al., 1999). Fractionation of HSE in the Canary lavas is shown by the separation of IPGE from PPGE and inter-HSE ratios (Pd/Ir and Pt/Ir) that exceed those chondritic values. To constrain the degree of fractionation an estimated parental melt composition was derived from the measured lavas using the method of Norman and Garcia (1999) whereby the inflection point on a log-log variation diagram of Al_2O_3 versus MgO represents the parental composition. This calculation includes data

from this study and those from Day (2013). In this case, the intersect of two linear regression lines shows MgO ~15.2 wt.% and Al_2O_3 ~10.0 wt.%. These figures are within the range of prior estimates of Canary Islands parent melt compositions calculated from olivine-bulk rock equilibrium relationships by Nicklas, Hahn, et al. (2022) and Day et al. (2022) (MgO ~8 to 17 wt.%). Applying the calculated parental MgO of ~15% to a linear regression of measured HSE shows parental melt HSE compositions for the Canary Islands are (in ng/g: Re = 0.28 ± 0.3, Pd = 1.6 ± 2.5, Pt = 2.0 ± 3.7, Ru = 0.56 ± 0.75, Ir = 0.24 ± 0.35, Os = 0.22 ± 0.41, $^{187}Os/^{188}Os$ = 0.149 ± 0.02). It should be noted however that the HSE versus MgO trends are not tightly correlated and in the case of Re poorly correlated. This and the broad range of parental melt MgO calculations from other studies suggest significant variability in the calculated parental melt HSE composition. Alternatively, this observed uncertainty could point to distinct source compositions for each island or groups of islands. Samples with < 50 pg/g were omitted from the regression models as these low Os samples are generally considered highly susceptible to contamination (Day, 2013; Reisberg et al., 1993; Widom et al., 1999), as were data points that exceed two standard deviations of the mean. A comprehensive list of parental melt HSE compositions for the range of calculated MgO is provided in **Table S4.4**. Many of the HSE values in this study exceed the predicted parental melt values, even when considering the most extreme parental MgO content of 17% despite the samples having less MgO themselves. A possible explanation for this is accumulation of sulfide ±olivine. Whole rock Mg-numbers, a general proxy for olivine content, also show little correspondence to samples with elevated HSE abundances, which casts doubt on olivine accumulation alone. Nonetheless, these parental HSE estimates can be used to model HSE variations observed in these lavas. Using the hypothetical parental melt with 15% MgO as a starting composition and partitioning coefficients for olivine, chromite, and sulfide defined by Day (2013) shows ~11%

fractionation of a mineral assemblage consisting of 98% olivine, 1.9% Cr-spinel, and 0.1% sulfide constrains PGE abundances for all but the most extremely fractionated samples (JMMD LP17 and JMMD EH02), particularly for IPGE, (**Figure 4.5a**). These two samples have prominent depletions in Pt and Ru (Ru is below detection limits in JMMD EH02) relative HSE. Ruthenium has been shown to behave compatibly in Cr-spinel thus the large anomalies can likely be explained by the segregation of Cr-spinel from these melts (e.g., Day, 2013; Paquet et al., 2019). Rhenium shows a high degree of variability compared to the model which suggests fractional crystallization is not a significant factor controlling absolute Re abundance. Twelve samples have Re concentrations above the calculated parental melt value which is reasonable given the highly incompatible behavior of Re and suggests that Re abundances in these samples are a function of partial melting processes rather than crystal-liquid fractionation. The remaining six samples are variably depleted relative the calculated parent melt and the most fractionated model. A possible explanation for this is magmatic degassing during subaerial eruption. Studies of Hawaiian subaerial versus submarine tholeiites have shown consistent depletions in Re concentration of subaerially erupted lavas compared to submarine lavas samples by drill core (Ireland et al., 2009; Lassiter, 2003).

4.5.6 Osmium Isotopic Composition of Canary Lavas

Osmium isotopes in OIB are sensitive indexes of contamination from lithospheric, crustal, or sedimentary inputs because of the contrast in Os concentration with the lithosphere (≥1 ng/g Os) and the contrast in $^{187}Os/^{188}Os$ composition with MORB crust (<0.18) and sediment (>0.4) (Marcantonio et al., 1995; Peucker-Ehrenbrink et al., 2003; Peucker-Ehrenbrink et al., 2012; Reisberg et al., 1993; Widom et al., 1999). Recently, Day et al. (2022) proposed a magma transit

model based on observations from the 2021 Cumbre Vieja, La Palma eruption. Here, earthquake focal depths suggest magma ponding and/or storage zones within the lithosphere, crust, and sediment apron underlying La Palma which provide potential for contamination of ascending melts. While this model is specific to the island of La Palma, it will be applied as a general analog for the entire archipelago for this discussion.

Ocean island alkali basalts with low Os concentration are highly susceptible to contamination from peridotite (e.g., Day, 2013) and magma storage within the lithosphere has been proposed as a source of contamination for Canary lavas (Widom et al., 1999). However, the degree of potential lithospheric contamination appears to be minimal. Mantle xenoliths from Lanzarote, Tenerife, La Palma, and El Hierro tend to have low Re (avg: <0.026 ng/g), high Os (avg: >2 ng/g), and relatively non-radiogenic $^{187}Os/^{188}Os$ (avg: <0.126) (Day et al., 2008; Simon et al., 2008; this study). Model (i) in **Figure 4.10** shows modeled assimilation of Canary Islands lithosphere material with lavas from this study and the literature. The end-members for this model are the average composition of the Canary lithosphere and the lava sample with the highest degree of HSE fractionation (JMDD EH02). The results show that assimilation of oceanic lithosphere is minimal (≤1.5%) for the majority of the lava samples. Two picritic samples from Gran Canaria (GC0901, GC0902) and the El Hierro cumulate xenoliths (EH1601A, -C, -F) exceed this threshold requiring ~3% lithospheric assimilation. Given the high abundance of olivine in these rocks and their high relative HSE abundances, these results raise the possibility that the samples entrained a small fraction of lithospheric olivine ±Cr-spinel xenocrysts. However, the broader tenor of the mixing model indicates that even in the more extreme circumstances the addition of oceanic lithosphere was minor and does not have a significant dilutionary effect on the Os isotope composition of the lavas.

The Canary Islands are emplaced atop some of the oldest oceanic crust in the world (150 – 180 Ma; Hoernle (1998)) with a thick (5 - 7 km) sediment apron (Straume et al., 2019). Both reservoirs are potential sources for contamination during magma transit and especially during a prolonged storage period. Samples with <50 pg/g Os are the most susceptible to crustal contamination while samples that exceed this Os threshold are considered highly resistant to significant contamination. The lowest Os concentrations of this sample set correspond to some of the highest $^{187}Re/^{188}Os$ which suggests interaction with a high Re reservoir such as crustal material. Model (ii) in **Figure 4.10** shows a binary mixture of JMMD EH02 and Atlantic MORB crust with low Os (0.354 ng/g) and radiogenic $^{187}Os/^{188}Os$ (0.15) (Blusztajn et al., 2000) begins to reproduce some of the observed range at ~20% crustal assimilation. A crustal input of this magnitude would likely have a dilutionary effect on HSE abundances and would be evident in major and trace elements which is not observed in these data. In addition, Gurenko et al. (2006) found that an unrealistically large (>70%) addition of crust would be required to produce the $^{87}Sr/^{86}Sr$ from Gran Canaria, which is not supported by Pb, Nd, or O isotope systematics. Therefore, these results suggest the addition of Atlantic MORB crust may have had a cursory effect on $^{187}Os/^{188}Os$ for the lowest Os concentration samples the large-scale mixing required for the full breadth of the sample set is not supported by complementary data.

A third source of potential contamination is the upper MORB crust and sediment apron. Here Os signatures would likely be dominated by high Os concentration, radiogenic $^{187}Os/^{188}Os$ Fe-Mn crust formed on pillow basalts in the deep ocean. Assimilation of similar material has been considered for Hawai'i but found to be insignificant (Ireland et al., 2009). Nonetheless, surficial Fe-Mn deposits have been documented by Marcantonio et al. (1995) on La Palma pillow basalts and are thus worth consideration for these models. Model (iii) **Figure 4.10** shows the average Os

composition for Fe-Mn crusts from the Atlantic (Os = 1.9 ng/g; $^{187}Os/^{188}Os$ = 1.054; Burton et al. (1999)) assimilated by the calculated parent melt from this study shows that ≤0.5% addition of Fe-Mn crust exceeds the upper bounds of $^{187}Os/^{188}Os$ for the Canary data which are represented by El Hierro lavas and cumulate xenoliths. If the parental melt is assumed to be the same composition for the archipelago, then this model suggest El Hierro is the only island to incorporate Fe-Mn crust. This scenario is not supported by MnO or Fe_2O_3 relationships with MgO or Al_2O_3. In fact, there is no correspondence between MnO and MgO or HSE for the entire data set which suggests assimilation of upper crust and oceanic sedimentary material has had an insignificant impact on Os-isotopic and HSE abundances. In conclusion, lithospheric assimilation is the most likely source for contamination reflected in $^{187}Os/^{188}Os$, albeit to a small degree. This may also be reflected in HSE abundance where samples exceed parental melt estimates and cannot be reconciled by fractional crystallization.

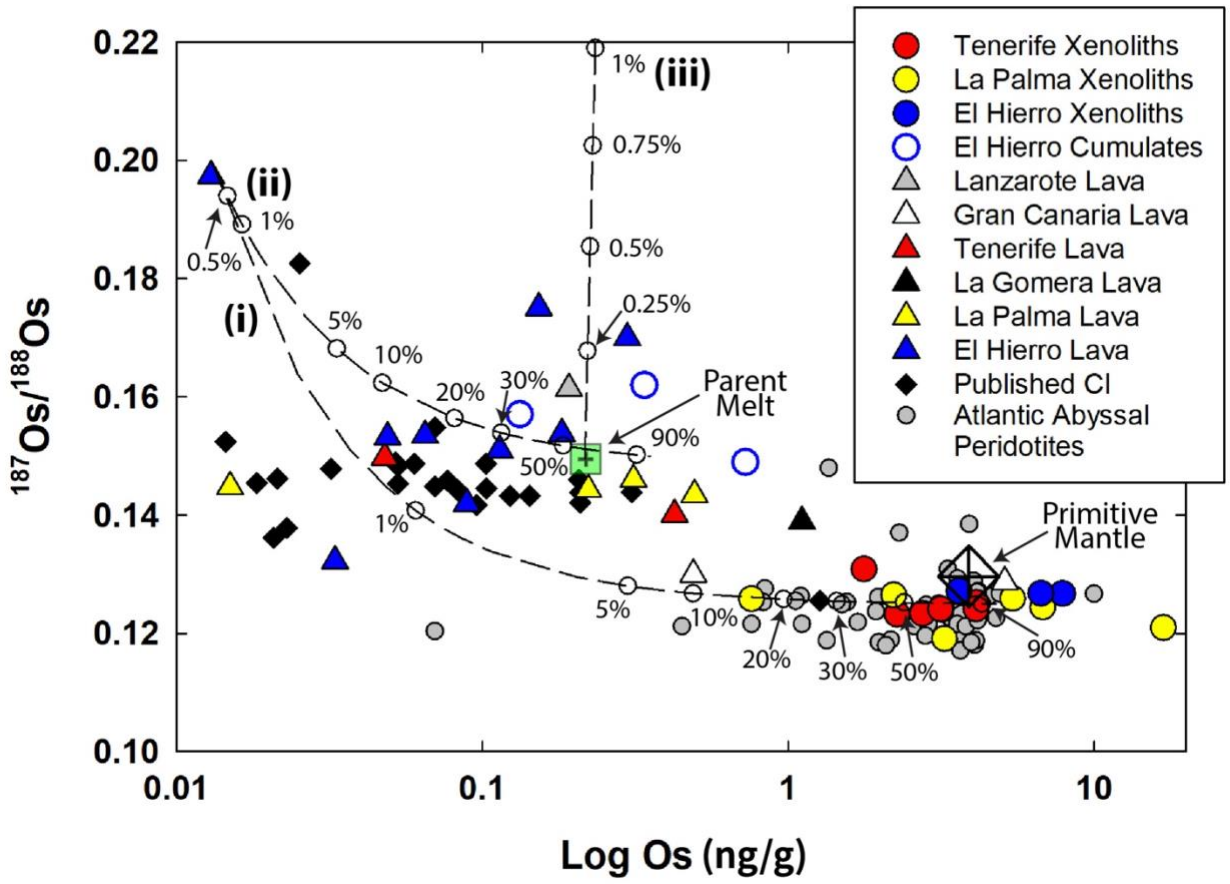

Figure 4.10 $^{187}Os/^{188}Os$ versus Os for Canary Islands lavas and ultramafic xenolith compared to published Canary Islands data with binary mixing curves showing the effects of: Model (i), assimilation of highly fractionated Canary lava with average Canary Island lithosphere represented by mantle xenoliths from this study. Model (ii), assimilation of highly fractionated Canary lava with lower crustal material from Blusztajn et al., 2000. Model (iii) assimilation of Canary Islands estimated parent melt (this study) with Fe-Mn pillow rind material from Marcantonio et al. (1995). Published data for the Canary Islands: Day et al. (2009); Simon et al. (2008); Widom et al. (1999) and Atlantic lithosphere from the compilation in Day et al. (2017) (references therein).

4.5.7 Geographical Distribution of $^{187}Os/^{188}Os$

Geochemically distinct zoning has been observed in mantle plumes throughout the Pacific basin, typically as subparallel trends. Hawai'i, the Society Islands, Marquesas Islands, Foundation

Seamount chain, Samoa Islands, and Galapagos Islands have more radiogenic Pb, Sr, and Os with less radiogenic Nd in their southern liniments relative the northern (Abouchami et al., 2005; Chauvel et al., 2012; Harpp & Weis, 2020; Huang et al., 2011; Jackson et al., 2014; Nicklas, Day, et al., 2022; O'Connor et al., 2001; Paquet et al., 2022; Payne et al., 2013). The isotopically enriched Loa and isotopically depleted Kea trends of Hawai'i are the most thoroughly documented of the Pacific plumes. Here Abouchami et al. (2005) argued for a bilaterally zoned plume head and Weis et al. (2011) proposed distinct sources where the Loa trend samples the large low shear velocity province (LLSVP) at the core-mantle boundary, and the Kea trend samples more depleted lower mantle material. Earlier models for Hawai'i suggest a concentrically zoned plume (Hauri et al., 1996; Lassiter & Hauri, 1998) which Jones et al. (2017) invoked as part of a plate motion model to explain the geographic orientation and timing of the Loa and Kea trends as well as the Society, Marquesas, and Samoa Islands, and the Foundation Seamount chain. There is a general consensus that the enriched component of mantle plume originates from the deep mantle, but several different models can be evoked to explain the depleted component: First, subducted ancient lithosphere (e.g.: Castillo, 2015; Day, 2013); second, metasomatized lithosphere (e.g.: Pilet et al., 2008); third, entrained upper mantle or DMM (e.g.: Lassiter et al., 2000); fourth, intrinsic characteristic of the plume (e.g.: Yang et al., 2003).

The Canary Islands do not show well-defined double volcanic liniments like most of their Pacific counterparts despite good sample resolution for Pb, Sr, Nd, and Os isotopic systems. However, clear patterns can be observed between the islands based on longitude. Using compiled published data (sources provided in the Data Availability section) average $^{87}Sr/^{86}Sr$ generally becomes less radiogenic from east (Lanzarote average $^{87}Sr/^{86}Sr = 0.70364 \pm 0.00094$ n = 14) to west (La Palma average $^{87}Sr/^{86}Sr = 0.70310 \pm 0.00014$, n = 57; and El Hierro average $^{87}Sr/^{86}Sr =$

0.70299 ±0.00014, n = 9). Average $^{143}Nd/^{144}Nd$ shows more radiogenic values with the same westerly trend although not as well defined as the $^{87}Sr/^{86}Sr$ trend. In this case the lowest average $^{143}Nd/^{144}Nd$ is Fuerteventura (average $^{143}Nd/^{144}Nd$ = 0.51286 ±0.00013, n = 37) while El Hierro is the most radiogenic (average $^{143}Nd/^{144}Nd$ = 0.51296 ±0.00003, n = 9). Lanzarote breaks this trend having average $^{143}Nd/^{144}Nd$ near the El Hierro value (Lanzarote average $^{143}Nd/^{144}Nd$ = 0.51291 ±0.00004, n = 16). The Pb isotope systems $^{208-}$ $^{206}Pb/^{204}Pb$ share very similar asymmetric convex east-west patterns. The eastern islands, Lanzarote and Fuerteventura, have the least radiogenic average values and the central islands Tenerife and La Gomera comprise the highest values of the range. The westernmost islands La Palma and El Hierro have disparate average values with El Hierro near Fuerteventura at the bottom of the range and La Palma near the center of the range, similar to Gran Canaria. This trend however breaks down when examined as $^{208}Pb^*/^{206}Pb^*$, which represents time-integrated $^{232}Th/^{238}U$ since the formation of Earth. To analyze $^{187}Os/^{188}Os$ compositions a weighted average based on Os concentration was used to dilute the effect of strongly radiogenic, low concentration samples which are susceptible to contamination. Application of a weighted average thus provides greater emphasis for higher concentration samples while preserving the best possible sample size for statistical analysis. Here $^{187}Os/^{188}Os$ increase from the central island, Gran Canaria to more radiogenic values west to La Palma and El Hierro. The easternmost, Lanzarote and Fuerteventura, approximate the average value for La Palma however, one standard deviation of these averages spans nearly the entire range of the archipelago (**Figure 4.11**).

Considering the east-west distribution of the Nd-Pb-Os isotope systems an argument can be made for a concentrically zoned plume with less radiogenic Pb and more radiogenic Nd and Os toward the periphery. Strontium isotopes however don't fit this model making a more liner trend,

becoming less radiogenic east-west. Nonetheless, it is not unusual for one isotopic system to deviate from a defined geographic trend. A well-defined Sr-Nd-Pb bilateral trend has been observed in the Marquesas Islands in the South Pacific (Chauvel et al., 2012) but thus far the trend is not observed in $^{187}Os/^{188}Os$ (Nicklas, Day, et al., 2022). It is also difficult to envision the dynamics of a concentrically zoned plume centered on the central Canary Islands given the active hotspot is inferred to be beneath the El Hierro – La Palma region of ~17.85° longitude (Carracedo et al., 1998) and the most resent eruption occurred on La Palma in 2021 (Day et al., 2022). Given these challenges to a zoned plume model for the Canaries it may be better to evaluate the geographic distribution of these isotopic systems in terms of source heterogeneity within the mantle. Based on HFSE and LILE ratios, and O-Sr-Nd-Pb-Os systematics the western Canary Islands, El Hierro and La Palma, were shown to sample variable proportions of a young HIMU source from recycled oceanic crust and/or lithosphere (Day et al., 2009; Day et al., 2010). The variably elevated $^{187}Os/^{188}Os$ presented here for El Hierro and La Palma relative the other islands support this conclusion whereby relatively young (<2 Ga) recycled crust is a source for more radiogenic $^{187}Os/^{188}Os$. The source for Gran Canaria was inferred to incorporate continental sedimentary material (Thirlwall et al., 1997), similar to an EM2 composition, which would imply a radiogenic $^{187}Os/^{188}Os$ signature. The raw average of Os isotope data support this conclusion (Avg Gran Canaria lava: ~0.l3870; Widom et al. (1999); this study). However, the low concentration of Os expected in continental sediments would easily be overwhelmed by the high concentration, non-radiogenic Os found in mantle melts, which becomes more apparent when using a weighted average. The eastern Canaries, Lanzarote and Fuerteventura, likely sample a proportion of enriched lithosphere (Hoernle & Tilton, 1991) or oceanic sediment (Thirlwall et al., 1997) based on $^{207}Pb/^{204}Pb$, which is consistent with the more elevated and highly variable

$^{187}Os/^{188}Os$ shown in this study. Overall these data depict an ocean island chain that samples a highly heterogenous mantle across a span of ~400 km, and in the case of El Hierro and La Palma preserves heterogeneity over a distance as small as ~50 km (Day et al., 2010). This small-scale heterogeneity is similar to Hawai'i's Loa and Kea trends which are well defined by multiple isotopic systems over a similarly small geographic space (~50 km) (Abouchami et al., 2005). Similar to the Canary Islands, the Juan Fernandez Islands west of Chile show no strong evidence of geochemical zoning or bilateral trends. Geochemical differences between Alexander Selkirk Island (west) and Robinson Crusoe Island (east) can be attributed to sampling variable proportions of FOZO (convergence zone) and DMM in conjunction with variable degrees of partial melt related to the position of the hotspot (Paquet et al., 2019). The Marquesas Islands sample a deep mantle component with variably small proportions of EM2-like recycled sediment, broadly analogous to Gran Canaria. Lavas studied here have mildly radiogenic $^{187}Os/^{188}Os$ (avg = 0.131) (Nicklas, Day, et al., 2022), less radiogenic than Gran Canaria (avg ~0.l39; Widom et al. (1999); this study). Lavas from the Azores show distinct geographical differences in HSE abundances with a slight variation in $^{187}Os/^{188}Os$ (Waters et al., 2020) while intra-island HSE abundance disparities are not obvious in the Canary Islands. Waters et al. (2020) attributes this distinction in the Azores to variable degrees of partial melting of a heterogeneous source related to ridge proximity and plate thickness. The more ridge proximal Azorean islands likely experience an increase in degree of partial melting related to adiabatic decompression from the ridge axis than do the more ridge distal islands. In contrast, the Canary Archipelago is emplaced atop uniformly thick, old lithosphere and show similar degrees of partial melting throughout the island chain.

In conclusion, the geographical disparities between the Canary Islands are not as well defined as many Pacific Island chains. The isotopic variations are not easily resolved by proximity to the

hotspot, plate thickness disparities, or a uniform plate motion velocity model. Previous studies have suggested that the Canary plume samples at least some fraction of recycled crust made evident by elevated $^{238}U/^{204}Pb$ ratios (HIMU) (Day et al., 2009; Day et al., 2010; Widom et al., 1999). A recycled crustal component can also be invoked explain the highly radiogenic, low Os concentrations from the eastern Canary Islands observed in this study and others. Geographic zoning of the Canary plume can best be described by mixing of mantle components from east to west. Variable proportions of a primitive mantle-like component seem to be a common factor in the source melts of Canary Archipelago with fractions of recycled sediments in the eastern Canaries to La Palma and a recycled crustal component represented as HIMU becoming more prominent west toward El Hierro.

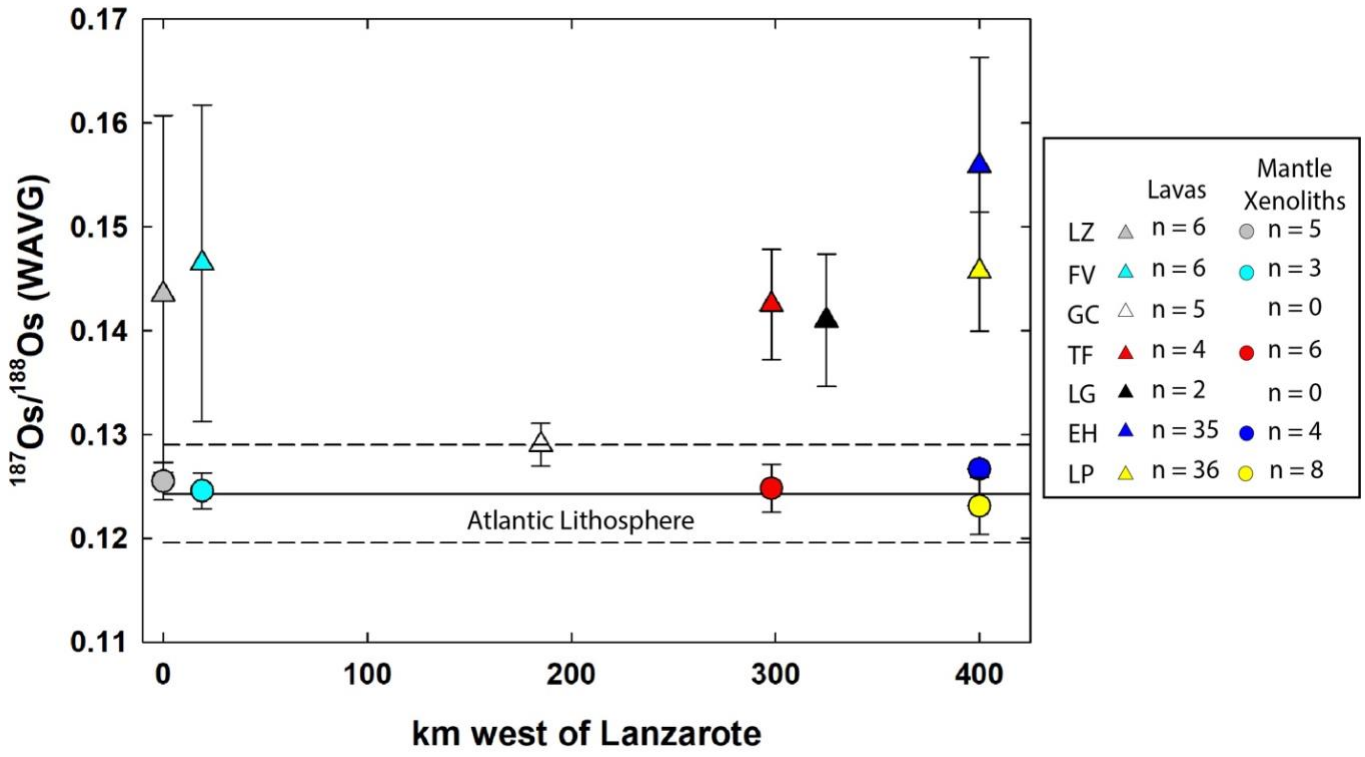

Figure 4.11 Geographic distribution of average $^{187}Os/^{188}Os$ for the Canary Islands from Lanzarote to La Palma (this study and published data). $^{187}Os/^{188}Os$ is a weighted average based on Os concentration. Average Atlantic lithosphere is from the compilation of Day et al. (2017), dashed lines are 2 SD. Sample sizes are provided in the key, error bars represent 2 SD. Where error bars are not shown, they are within the marker. (Abbreviations: LZ = Lanzarote; FV = Fuerteventura; GC = Gran Canaria; TF = Tenerife; LG = La Gomera; EH = El Hierro; LP = La Palma) A comprehensive list of data sources for Canary Islands lavas is in the Data Availability section.

4.6 Conclusions

Xenolith samples analyzed in this study from Tenerife, La Palma, and El Hierro show high degrees of melt depletion, up to 18%, followed by significant metasomatism. Evidence of metasomatism is provided by elevated LREE and HFSE fractionation. Zr/Hf vs. Zr and Nb/Ta vs. Nb patterns are inconsistent with MORB extraction and suggest melt addition from a low degree

asthenospheric melt. Melt addition modeling shows ~0.5 – 13% addition of the Canary parental melt replicates REE patterns observed in the xenolith suite. Non-radiogenic $^{187}Os/^{188}Os$ and ancient T_{RD} ages suggest an Atlantic oceanic lithosphere domain underlying Tenerife, La Palma, and El Hierro that has experienced moderate to significant melt modification from hotspot interaction.

Polybaric melt modeling for Canary Islands lavas presented here suggest these melts were produced by 2 – 7% partial melting near the garnet stability field for peridotite. An estimated HSE composition for an aggregate parent melt can be derived from log-log variation of MgO versus Al_2O_3. Relating the observed HSE compositions from the lavas to the estimated MgO composition from the parent melt yields in ppb: Re = 0.28 ± 0.3, Pd = 1.6 ± 2.5, Pt = 2.0 ± 3.7, Ru = 0.56 ± 0.75, Ir = 0.24 ± 0.35, Os = 0.22 ± 0.41, $^{187}Os/^{188}Os$ = 0.149 ± 0.02. However, there is strong evidence that parent melts are variable between islands. HSE compositions for most of the lavas can be accounted for by ~11% fractionation of olivine, Cr-spinel, and sulfide from the estimated parent melt. Mixing models for $^{187}Os/^{188}Os$ between lava samples from this study and the average for Canary lithosphere show up to 3% assimilation of lithospheric material. The effect of assimilation of upper or lower oceanic crust or marine sediment appear minimal thus unlikely a significant contribution to the $^{187}Os/^{188}Os$ composition of Canary Island lavas.

Geographical zoning of the Canary plume is not as distinct as many Pacific plumes and is not well resolved by standing geodynamic models. However, heterogeneous source components can be used as a basis for explaining isotopic differences observed between the Canary Islands where the eastern Canary Islands show a recycled sediment EM2-like component, and the western Canary Islands have a dominantly HIMU signature from recycled crustal material.

4.7 Acknowledgments

Chapter 4 in part is currently being prepared for submission for publication of the material. Oller, Brian; Day, James M.D. The dissertation author was the primary researcher and author of this material.

CHAPTER 5 New Insight into the Mantle Source Composition of the Big Pine Volcanic Field from Cumulate Xenoliths Using Osmium Isotopes and Highly Siderophile Elements

5.1 Abstract

Pyroxenite and peridotite cumulate xenoliths along with high Mg alkali basalt host lavas from the Papoose Canyon monogenic vent in the Big Pine Volcanic Field (BPVF) were analyzed for their major-, trace-, and highly siderophile-element abundances (HSE: Re, Pd, Pt, Ru, Ir, Os), and $^{187}Os/^{188}Os$ compositions. In addition, major- and trace-element abundances were obtained by laser ablation inductively coupled plasma mass spectrometry (LA-ICP-MS) and electron microprobe analysis for olivine, clinopyroxene, orthopyroxene, and spinel mineral separates from three peridotite samples. This study presents new HSE and $^{187}Os/^{188}Os$ data that offer insights into the mantle source for the BPVF and the effects of crustal assimilation on interpretation of these data. Osmium isotopic compositions are less radiogenic for peridotites ($^{187}Os/^{188}Os$ = 0.145 ±0.010 (weighted to Os = 0.142); $\gamma_{Os}i$ = 13.3 ±7.9; n = 11) and pyroxenites ($^{187}Os/^{188}Os$ = 0.194 ±0.068 (weighted to Os = 0.214); $\gamma_{Os}i$ = 51 ±54; n = 8) than lavas or xenoliths from previous BPVF studies. Peridotite HSE patterns show three distinct patterns; Pd enriched, fractionated Ir/Os, and relative Pd depleted. Pyroxenite HSE patterns are more coherent showing higher degrees of variation in Pt and Ir. The V-in-olivine oxybarometer shows average fO_2 > +2.3 ΔFMQ for the peridotite cumulates that suggests an oxidized mantle source, likely from Farallon slab contributions. Two-pyroxene thermobarometery shows the average depth of equilibration for the cumulates is at or near Moho depths. These new data and previously published models are used to conceptualize the structure of the Owens Valley lithosphere from the Coso volcanic field to the BPVF and are then

discussed in the broader context of the Walker Lane and Gulf of California rifting. Finally, the Owens Valley is examined against the East African Rift, a well-documented continental rift system.

5.2 Introduction

Previous work has shown that basalts are often mixtures of multiple batches of magma generated through polybaric melting, often originating from different sources that are homogenized during transit and/or storage prior to eruption (e.g., Anderson, 1976; Turner & Campbell, 1986). These homogenization processes can obscure the source composition and make it challenging to constrain the true nature of parental melt mantle sources. Furthermore, during transit and storage it is not uncommon for magmas to assimilate lithospheric or crustal material, which can further or even totally obscure the source composition (e.g., Carlson et al., 1981; Cox, 1980; Day, 2016). Ultramafic cumulate xenoliths harbor some of the earliest crystalizing phases from these complex magma mixtures thus potentially segregating these crystals from further assimilation equilibration with other mixing agents and contaminants, offering an alternative means by which to understand magma genesis (e.g., Peters et al., 2016).

Basalts from the BPVF have been considered unique among Basin and Range volcanic rocks due to their often relatively magnesian compositions. Previous studies have highlighted features such as their average high MgO content (Mg-number ≅ 70), high equilibration pressures and temperatures, and an abundance of ultramafic xenoliths to strengthen arguments that BPVF basalts, including those from the Papoose Canyon monogenic vent, represent primary mantle melts (Beard & Glazner, 1995; Blondes et al., 2008; Gazel et al., 2012; Mordick & Glazner, 2006). The high temperatures and pressures along with the presence of mantle xenoliths are thought to be

indicative of rapid transit from the mantle to the surface, thus limiting crustal contamination (e.g., Reiners, 2002), leading to the point of view that the BPVF acts as a window to the mantle beneath the extensional Walker Lane and eastern Sierra Nevada. However, more recent research has called this interpretation into question. Gao et al. (2017) demonstrated that Papoose Canyon basalts in particular likely experienced significant crustal ponding during which time the magma chamber(s) was recharged and assimilated crustal wall rock. Prior conclusions regarding compositional temporal variation in the Papoose Canyon and other monogenic vents are typically attributed to mantle heterogeneity where melts are sourced from enriched (pyroxenite) and depleted (peridotite) end-members (Blondes et al., 2008; Reiners, 2002). These more recent results from Gao et al. (2017) raise possible doubts about such interpretations.

This study utilizes the abundant peridotite and pyroxenite cumulate xenoliths from the Papoose Canyon coupled with the inherent advantages of HSE abundances and Re-Os isotope systematics to identify source composition versus contamination. Ultramafic cumulate xenoliths are ideal for this task because of the compatible behavior of the HSE during partial melting, meaning HSE will be concentrated in these early crystalizing phases relative to the host basalt (e.g., Peters et al., 2016). The HSE and Os isotopes have shown their utility in discerning partial melting, metasomatism, refertilization, and slab recycling (Day, 2013; Day et al., 2017; Rehkamper et al., 1999). Here the HSE are used to evaluate potential source characteristics of the Papoose Canyon that may otherwise be obscured using more conventional lithophile element systematics. Because Os is a sensitive tracer of crustal contamination, especially at low concentrations (e.g., Reisberg et al., 1993), Os isotope mixing models are used to evaluate the magnitude of continental crust assimilated by the cumulate xenoliths. Finally, Owens Valley

magmatism is compared to other continental rift systems and a conceptual model is developed based on data presented here and recent geochemical and geophysical research.

5.3 Geologic Setting

The BPVF is located in the Owens Valley, an oblique strike-slip fault bounded graben that defines the western-most basin of the Walker Lane geomorphic province (**Figure 5.1a**). The Owens Valley is bound to the west by the Sierra Nevada Mountains and the Southern Sierra Nevada and Owens Valley Faults. The eastern perimeter is the Inyo-White Mountain Range controlled by a diffuse normal fault boundary, the White Mountains Fault (**Figure 5.1b**) and volcanism in the valley occurs along or in close proximity to these fault boundaries. There are ~40, primarily mafic, flows and scoria cones with one silicic dome that comprise ~0.5 km^3 of volume (Beard & Glazner, 1995). Eruption activity occurred in the middle to late Pleistocene from ~1.2 to 0.1 Ma (Bierman et al., 1991; Blondes et al., 2008; Gillespie et al., 1984) with most of the activity limited to the late Pleistocene, although the Owens Valley remains seismically active. The Coso Volcanic Field (CVF) is located ~120 km south of BPVF in the southern-most extent of the Owens Valley (**Figure 5.1a**). A full range of volcanic eruptions occurred here from basaltic to rhyolitic, producing ~35 km^3 of material over the course of 4.5 to 0.1 Ma. Prior to ~5 Ma the dominant tectonic setting in this region was subduction of the Farallon plate after which dextral shearing and extension in response to the evolution of the San Andreas fault became dominant (Atwater, 1970; Nicholson et al., 1994; Ormerod et al., 1991). Volcanism in the BPVF and CVF has been attributed to lithospheric thinning in response to this extension (Beard & Glazner, 1995; Gazel et al., 2012) or removal/delamination of the lithosphere from foundering of the Farallon slab (Ducea & Saleeby, 1996; Lee et al., 2000; Lee et al., 2001).

The mafic flows show a range of compositions from basanites to alkalic and sub-alkalic basaltic lavas (Bierman et al., 1991; Blondes et al., 2008; Gao et al., 2017) with silica content generally increasing through time from ~44 to 53 wt.% (Blondes et al., 2008; Ormerod et al., 1991). Incompatible trace element compositions show a broad range throughout the volcanic field with negative high field strength element (HFSE: Nb, Ta, Zr, Hf) anomalies. Strontium concentrations range from 837 to 2180 μg/g with a relatively limited but radiogenic isotopic range of $^{87}Sr/^{86}Sr$ (0.70552 to 0.70634: (Beard & Glazner, 1995; Blondes et al., 2008; Gao et al., 2017; Mordick & Glazner, 2006; Ormerod et al., 1988; Ormerod et al., 1991). Earlier studies have attributed the broad compositional range observed in the BPVF to variable degrees of partial melting of continental lithosphere (Ormerod et al., 1991) however, this is not supported by the Sr isotopic data. Based on HFSE and large ion lithophile element (LILE) ratios Beard and Glazner (1995) suggested a metasomatized continental lithosphere melt source, consistent with the regional subduction history. Based on high H_2O content Gazel et al. (2012) concluded the BPVF incorporated an asthenosphere component resulting from upwelling due to extension or counter-flow from a foundering slab.

The Papoose Canyon volcanic sequence is located in the southeastern area of the Big Pine Volcanic Field, on the east side of U.S. Highway 395 (**Figure 5.1b**). The volcanic sequence is bisected by the Papoose Canyon which incises the flank of the Inyo-White Mountains. This is one of the older vents in the BPVF with an average $^{39}Ar/^{40}Ar$ age of 760.8 ±22.8 ka and is partially overlain by the younger Jalopy (469.4 ±9.2 ka) and Quarry (90.5 ±17.6) cones (Blondes et al., 2008). The Papoose Canyon shows major and trace element and isotopic temporal-compositional variation that reflects the range of the broader BPVF. For example, LREE (La, Ce, Nd) concentrations in Papoose Canyon samples show an approximately two times variation becoming

more depleted with decreasing age (Blondes et al., 2008; Gao et al., 2017) and ITE compositions span nearly the entire range of the BPVF. Limited $^{187}Os/^{188}Os$ are highly radiogenic with low absolute and relative Os concentrations which has been interpreted as evidence of crustal contamination (Blondes et al., 2008; Gao et al., 2017) however, a heterogeneous mantle source of peridotite and pyroxenite cannot be ruled out.

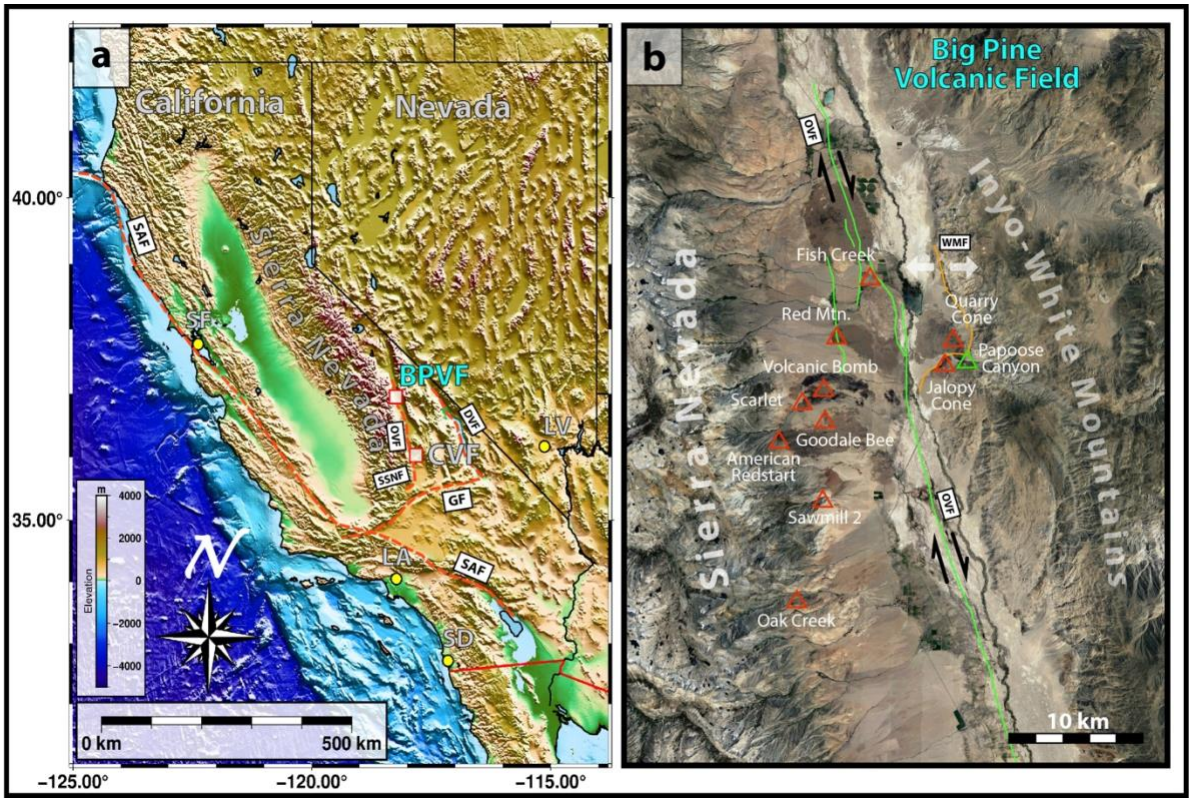

Figure 5. 1 (a) Regional elevation map of the southwest United States showing the study area (BPVF), Coso Volcanic field and major fault zones and fault zones relevant to the study area. (b) Zoomed in satellite image of the Big Pine Volcanic Field. Previously studied volcanic edifices are noted by red triangle, Papoose Canyon (this study) is a green triangle. Fault zones are marked in green and orange with arrows showing the sense of shear. (Abbreviations: SD = San Diego, LA = Los Angeles, LV = Las Vegas, SF = San Francisco, CVF = Coso Volcanic Field, BPVF = Big Pine Volcanic Field, SAF = San Andreas Fault, GF = Garlock Fault, SSNF = Southern Sierra Nevada Fault, OVF = Owens Valley Fault, DVF = Death Valley Fault, WMF = White Mountains Fault) (a) created with GMT 6 open source software (Wessel et al., 2019).

5.4 Methods

Nineteen ultramafic cumulate xenoliths, 11 of which were peridotic and eight of which were pyroxenitic to transitional in composition, and six lava samples hosting the xenoliths from the Papoose Canyon monogenic vent in Owens Valley, California were analyzed for this study. For whole rock powders, 30 to 60 g of sample were sawn and buffed with corundum paper, then washed to remove dust and debris prior to being crushed using an alumina jaw crusher followed by powdering using a SPEX™ alumina shatterbox. All crushing and powdering equipment were thoroughly cleaned between samples to prevent cross contamination.

Major element compositions for all whole rock samples were measured at Franklin and Marshall College using a *PW 2404 PANalytical* XRF vacuum spectrometer according to the procedures of Boyd and Mertzman (1987). Determination of major elements used standard lithium borate fusion techniques with 3.6:0.4 g $LiBO_4$:sample powder. Ferrous iron concentrations were obtained by titration with potassium dichromate. Precision and accuracy are estimated using repeat analyses of standards, and the long-term precision and reproducibility are reported in Day et al. (2017). Absolute standard deviations (2σ, n = 13) in wt. % are: SiO_2 ± 0.13, TiO_2 ± 0.01, Al_2O_3 ± 0.09, FeO ± 0.63, Fe_2O_3 ± 0.47, Fe_2O_3(T) ± 0.10, MnO ± 0.01, MgO ± 0.04, CaO ± 0.07, Na_2O_3 ± 0.03, K_2O ± 0.01, P_2O_5 ±< 0.01. For the average of thirteen runs of BHVO-2 standard powder versus USGS values the accuracy is better than .2% for SiO_2 and TiO_2, < 1.0% for Al_2O_3, Fe_2O_3(T), MnO, MgO, CaO, Na_2O_3, P_2O_5, and < 3.0% for K_2O.

Whole-rock trace element compositions were determined at the Scripps Isotope Geochemistry Laboratory (SIGL) using methods described in Day et al. (2014). One hundred milligram aliquots of sample powder was precisely weighed and digested in a 1:4 mixture of Teflon-distilled HNO_3:HF for >72 hours at 150˚C. Total procedural blanks (n = 2) and rock

standards (BHVO-2, BCR-2, HARZ-01) were prepared alongside the samples. These data are reported in **Table S5.2**. After drying down and sequential HNO_3 steps to break-down fluorides, sample solutions were diluted by a factor of 5000 in 2% HNO_3 and spiked with a 1 ng/g indium solution to monitor instrumental drift. Solutions were measured using a *Thermo Scientific* iCAPq c quadrupole ICP-MS in standard mode. The reproducibility of the reference materials was better than 5% RSD, and elemental abundances were within error of the recommended ranges.

In situ major element abundances were determined at the University of Nevada, Las Vegas (UNLV) using the JEOL JXA-8900 electron microprobe. Spot analysis of the minerals were performed using a 15 kV accelerating voltage with a 20 nA beam current and a spot size of 2 mm. Data were reduced using standard ZAF corrections. Peak counting times were 20 s for Na; 30 s for Si, Mg, Fe, Mn, Ni, and Cr; 49 s for Ca; and 60 s for Al, Ti, and P. Natural and synthetic mineral standards were used for calibration. These standards included olivine (Si, Mg, Ni), augite (Mg, Fe), ilmenite (Fe, Mn, Ti), plagioclase (Si, Al, Ca), chromite (Cr), albite (Na), microcline (K), and apatite (P). Estimated uncertainties on major oxide concentrations were ~2%.

Trace element analyses for olivine and clinopyroxene were conducted at the SIGL using inductively coupled plasma mass spectrometry (LA-ICP-MS) with a *New Wave* UP213 213 nm laser ablation system coupled to a *Thermo Scientific* iCAPq c quadrupole ICP-MS with a frequency of 5 Hz, a fluence control between 3 – 3.5 J/cm^2, and a 100 nm spot size. Silicon abundances obtained by electron microprobe at UNLV were used as an internal standard and United States Geological Survey (USGS) standard reference glasses BHVO-2g, BIR-1g, and BCR-2g were used as external standards. Analyses consisted of ~20 s of background and ~40 s of data collection. Raw data were corrected using a Python based algorithm developed at SIGL and limits of detection were defined as three standard deviations above the mean background.

Osmium isotope and HSE (Re, Pd, Pt, Ru, Ir, Os) abundances were measured at SIGL using the methods outlined in (Day et al., 2016). The sample powders were well homogenized, precisely weighed, then digested in sealed borosilicate Carius tubes with Os isotope and HSE "spikes" and 10 mL of a 2:3 mixture of Teflon-distilled HCl and Teflon-distilled HNO_3, that had been purged of Os, then were digested at 240°C for 72 hours. Osmium was then triply extracted from the acid using CCl_4, back-extracted into HBr and purified by micro-distillation. Rhenium and platinum group elements were separated from the solution with anion exchange columns, then measured on a *Thermo Scientific* iCAPq-c ICPMS in standard mode. Osmium isotopic compositions were measured on a *Thermo Scientific* Triton thermal ionization mass spectrometer by peak-jumping in negative ion phase. The measurements were corrected for oxide and fractionation using a ratio $^{192}Os/^{188}Os = 3.08271$. Osmium concentrations were determined using ^{190}Os spike deconvolution and were blank-corrected. 70pg UMCP Johnson-Matthey standards were used to monitor instrument precision. Measurements of the standards averaged 0.11379 ±0.00008 (2σ, n = 10). Procedural blanks for Os analyses (n = 2) had an average corrected $^{187}Os/^{188}Os$ of 0.187 ±0.004 (2σ) and 0.171 ±0.007 (2σ), and [Os] of 5.5 and 2.4 pg. Measured HSE isotope dilution isotopic ratios were corrected for mass fractionation using the deviation of the standard average run on the day over the natural ratio for the element, and all reported values are blank corrected. The average HSE abundances of these blanks (n = 4) were: Re = 15 pg, Pd = 46 pg, Pt = 22 pg, Ru = 33 pg, Ir = 2 pg. These values represent <10% of the total analyte with the exception of Re and Pt that are <18% and 23% in the worst cases respectively.

Parental melt compositions were calculated for peridotite samples PC1501b, -d, and -e using the methods discussed in Nicklas et al. (2022). The MgO composition of the parent melt is first calculated from the bulk-rock FeO composition and the olivine MgO and FeO composition

assuming $K_{D\frac{FeO}{MgO}}^{MgO/liq}$ = 33.0 ±0.02 (Toplis, 2005). The remaining major elements and V are calculated by addition or subtraction of the average olivine composition from the bulk-rock until the MgO is equal to the calculated parent melt. Finally, parent melt SiO_2 compositions are calculated by deduction of total oxides from 100%.

5.5 Results

5.5.1 Textures and Mineral Compositions

Papoose Canyon peridotite and pyroxenite xenoliths are fine grained with poikilitic textures featuring generally rounded grain boundaries. Average grain sizes for PC1501b, -d, and -e along the long axis are: PC1501b: 1427 μm ±650, 1σ (n = 32); PC1501d: 1141 μm ±428, 1σ (n = 45); PC1501e: 1763 μm ±574, 1σ (n = 30). Textural features consistent with a mantle origin, such as ~120° triple junctions are absent (**Figure 5.2a, b, c**). Olivine-dominant ultramafic xenoliths (peridotites) are ~80 to 90 modal% olivine, ~5 to 10 modal% clinopyroxene, with minor orthopyroxene and oxides that range from spinel to magnetite compositions. Clinopyroxene dominant ultramafic xenoliths (pyroxenites) are 70 to 85 modal% clinopyroxene, 10 to 20 modal% olivine, with minor orthopyroxene. In the peridotites, clinopyroxene is often observed forming at the expense of orthopyroxene and in fewer cases olivine. Oxides in these samples dominantly occur as interstitial grains but in a few cases intergranular oxides are observed. No sulfide grains were observed suggesting they are smaller than the limit of magnification.

Major and trace element compositions for Papoose Canyon olivines, clinopyroxenes, orthopyroxenes, and oxides from peridotite samples PC1501b, -d, and -e are reported in **Table S5.3, S5.4, S5.5, & S5.6**.

Olivine

Magnesium-numbers for olivines (Mg-number = 80 to 87; Avg = 86.0 ±1.0, 1σ) are within the range for ultramafic cumulate xenoliths reported by Gao et al. (2017) (Mg-number = 73 to 87) and overlap the reported range for olivine phenocrysts in basalts (Mg-number = 77 to 89) (Gao et al., 2017; Mordick & Glazner, 2006). Peridotite samples presented in this study tend to be more homogeneous than previously reported xenolith or phenocryst olivines (Blondes et al., 2012; Gao et al., 2017; Gazel et al., 2012). Nickel content for PC olivines is also very uniform (2060 to 1129 μg/g), making a strong positive correlation with Mg concentration. Calcium concentrations are highly variable from 9479 to 518 μg/g, which suggests some olivines may be mantle xenocrysts, based on the global classification <700 μg/g Ca (Foley et al., 2013). Iron/manganese ratios range from 79 to 66, mostly above the predicted range for peridotite derived melts (Herzberg, 2011). Calculated parent melt compositions for the three samples studied by EMPA are presented in **Table S5.7**. Average MgO and SiO_2 compositions range from 9.4 to 13.3% wt. and 46.0 to 49.2 wt.% respectively, which are within the calculated parent melt ranges for PC basalts (Gazel et al., 2012). However, calculated TiO_2 and CaO exceed the published calculations by ~70% and Al_2O_3 from this study is ~75% less than those of Gazel et al. (2012).

Vanadium concentrations for olivine are homogeneous showing an average of 3.7 ±0.6 μg/g, with a positive correlation with [Mg] but no variation with Mg-number. Vanadium exists as several species in melts (V^{3+} to V^{5+}) and compatibility in olivine increases as valence state decreases toward V^{3+}, which is the most compatible species over a broad range of temperatures, pressures, or compositions (Canil, 1997; Wang et al., 2019). Partitioning of these species in melt is a function of fO_2, such that the partitioning of V into olivine can be calibrated to constrain fO_2 (e.g.: Nicklas et al., 2022). Using the empirical equation derived by Wang et al. (2019) the PC olivines show a

grand average fO_2 $+2.63^{+0.044}_{-0.043}$ ΔFMQ, which is significantly above the values for adjacent Quarry (+0.9 ΔFMQ) and Jalopy (+1.6 ΔFMQ) cones reported by Gazel et al. (2012) and similar but slightly higher than values for the Canary Islands: Gran Canaria (+2.6 ΔFMQ) and La Palma (+2.2 ΔFMQ) (Nicklas et al., 2022). Petrographic analysis shows the Papoose Canyon samples have less than 30% clinopyroxene, thus the effect of pyroxene accumulation on the fO_2 calculations can be assumed to be minimal (see discussion in Nicklas et al., 2022).

Pyroxenes

Pyroxenes from Papoose Canyon ultramafic xenoliths range in composition from enstatite (orthopyroxene) to diopside (clinopyroxene) (**Figure 5.2e**). The orthopyroxenes are homogeneous ($En_{75-77}Wo_{2-3}Fs_{20-22}$) with relatively uniform MgO composition and clinopyroxenes are more compositionally heterogeneous with a range of MgO from augites to diopside ($En_{37-54}Wo_{30-51}Fs_{10-16}$), similar to BPVF pyroxenes from Mordick and Glazner (2006). Orthopyroxenes have average Mg-number of 86.5 ±0.4 and clinopyroxenes have average Mg-number of 85.9 ±1.0 which falls within, but defines a more restricted range (Mg-number = 73 to 88) for clinopyroxenes from ultramafic xenoliths shown by Gao et al. (2017). Primitive mantle normalized trace element patterns for clinopyroxenes have predominantly convex trends (**Figure 5.5d**) with more dispersion in the incompatible trace elements (e.g.: Rb, Ba, Th, U, La, Ce) and variably enriched and depleted Pb (**Figure 5.5e**). These samples also show negative anomalies for high field strength elements (HFSE) consistent with subduction arc lavas.

Spinel

The majority of spinels are limited to sample PC1501e, although some examples were found and analyzed in PC1501b and -d. These minerals have a narrow range of Mg-number (42.5 to 58.3) compared to a much broader range of Cr# (7.3 to 35.2), where Cr# = [Cr / (Cr × Al) × 100], and

FeO content is between 14 to 22 wt.%. Spinel Cr#'s have strong positive correlations with FeO and TiO_2 (r^2 = 0.84 and 0.74, respectively). Spinel Mg-numbers correlate positively with olivine and clinopyroxene Mg-numbers which suggests concurrent crystallization of these phases.

5.5.2 Thermobarometery Models

Temperatures and pressures were calculated for three samples based on in-situ measurements of major element compositions of orthopyroxenes and clinopyroxenes. The calculations were made by iterating equations 36 (T) and 39 (P) from Putirka (2017) using the Python3 tool Thermobar (v.0.07) from Wieser et al. (2022). Here equilibrium between the two pyroxene phases is determined by the calculated Fe^{2+}/Mg exchange which was set using the criteria from Putirka (2017) at K_D = 1.09 ±0.14; results that fell outside this range were rejected. This filter shows an average equilibration pressure of 0.85 ±0.38 GPa and an average temperature of 1081° C ±58° from 1322 possible matches. Applying a narrower filter, K_D = 1.0 ±0.08, yielded nearly identical average pressures and temperatures with 782 possible matches. This range of pressures corresponds to an average depth of ~32 ±7 km assuming constant crustal density $\rho = 2750 \text{kg/m}^3$ (Wang et al., 2002), in accordance with previous BPVF studies (Gao et al., 2017; Gazel et al., 2012; Mordick & Glazner, 2006). The pressure results from two-pyroxene matching presented here are slightly higher than 0.5 to 0.7 GPa based on clinopyroxene Mg-numbers from Gao et al. (2017). However, pressure and temperature models based on Si activity and olivine-melt equilibrium respectively, for lavas >500 ka (Papoose Canyon sequence specifically) shown by Gazel et al. (2012) (2.2 GPa at ~1350° C to 1.7 GPa at ~ 1280° C) exceed the figures shown here. Similarly, results from this study are lower than those from

Mordick and Glazner (2006) (1.4 ±0.3 GPa at ~1250° C ±100°) which used a clinopyroxene-liquid thermobarometer calibrated for anhydrous melts.

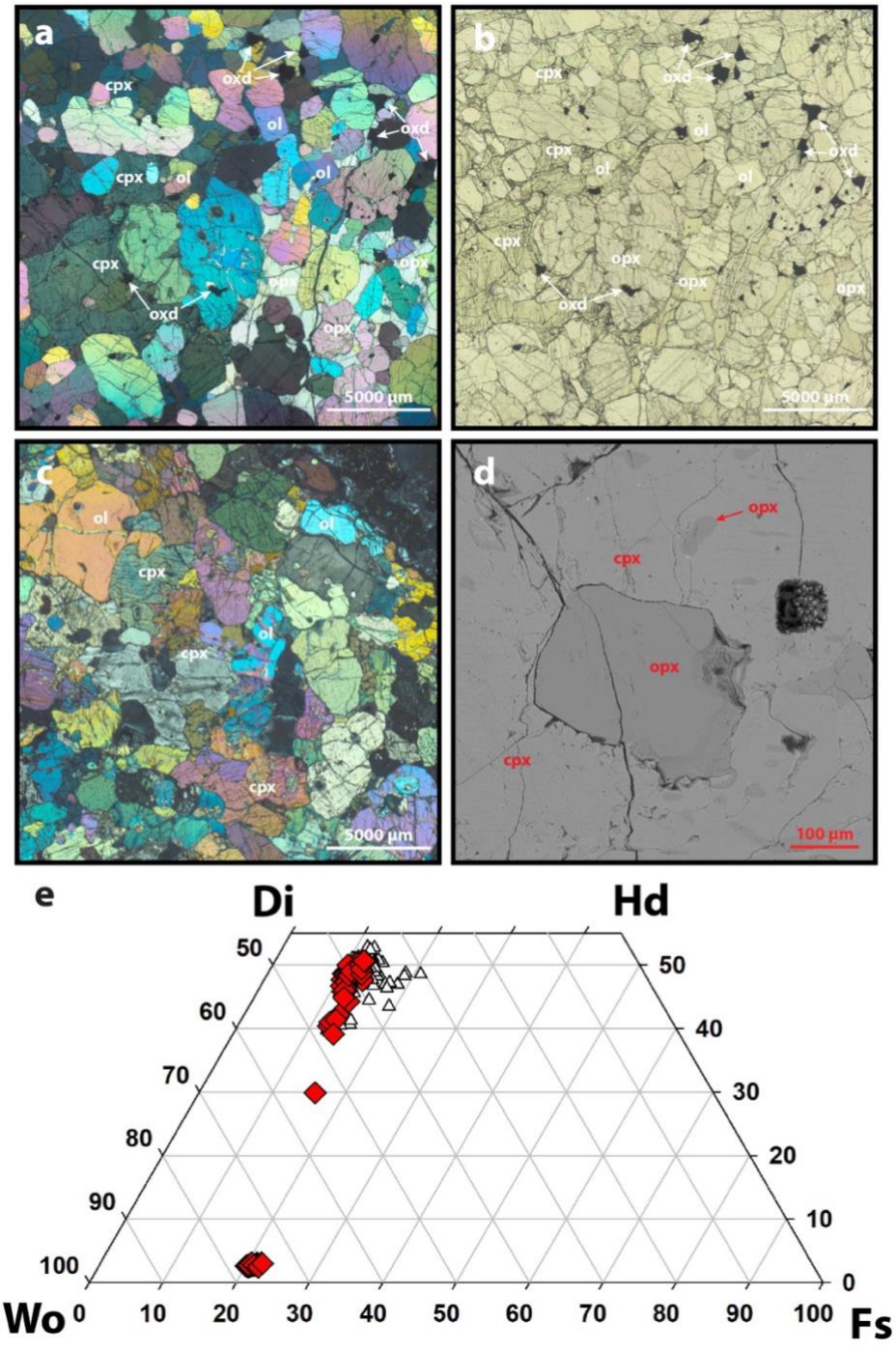

Figure 5.2 Photomicrographs of peridotite xenoliths (a & b: PC1501e xpl and ppl; c & d: PC1501d xpl and bse) Slides are ground to 60 µm thick. (e) Pyroxene ternary diagram for PC pyroxenes from this study (red diamonds) and Gao et al. (2017) (white triangles). Wo = wollastonite; Di = diopside; Hd = hedenbergite; Fs = ferrosilite.

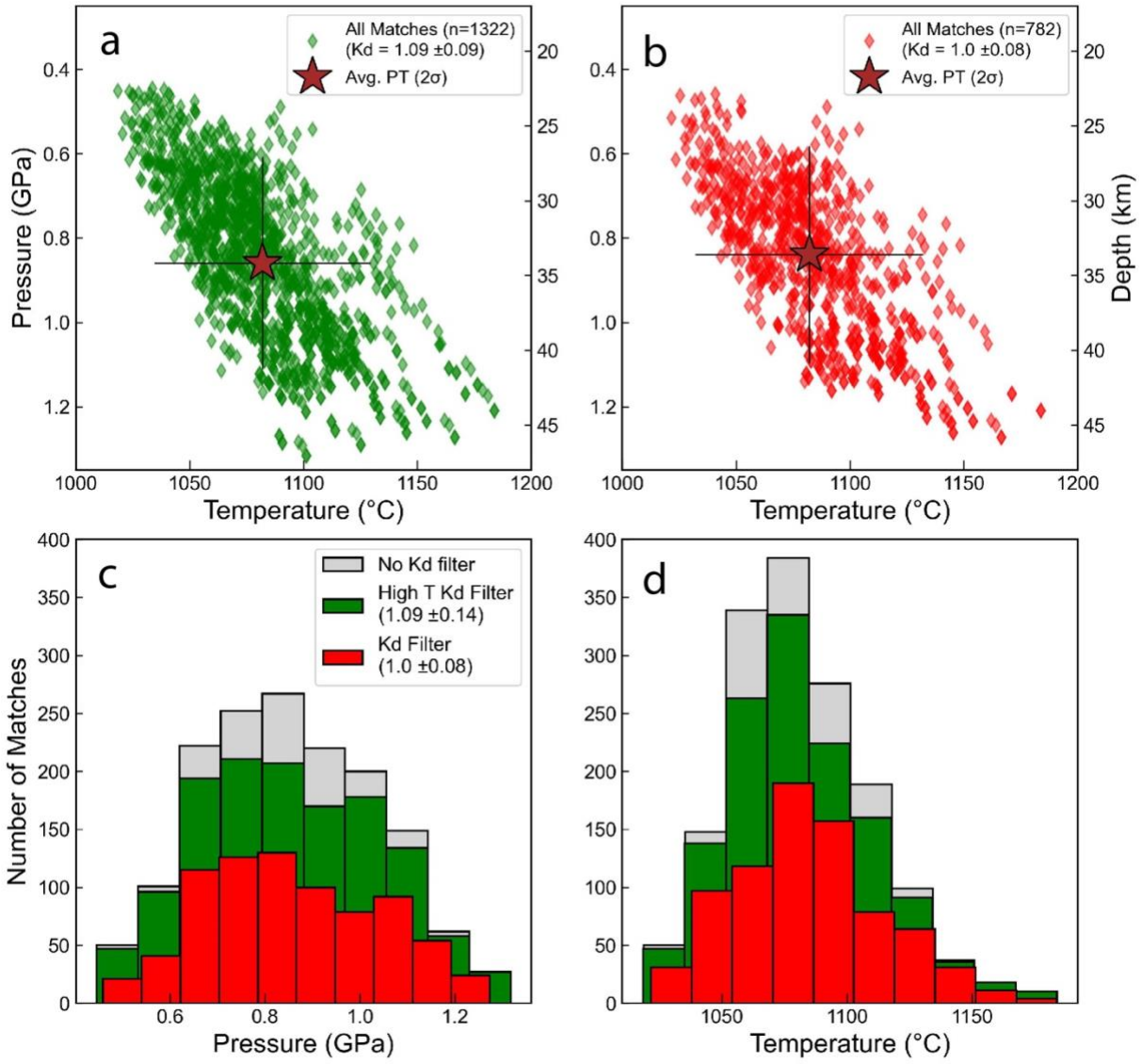

Figure 5.3 Pressure and depth versus temperature for two-pyroxene matching from Putirka (2017). (a) is a high K_d filter set to 1.09 ±0.09 yielding 1322 opx-cpx matches, (b) is a tight K_d filter set to 1.0 ±0.08 yielding 782 opx-cpx matches. (c) & (d) histogram plots showing number and distribution of opx-cpx matches for (c) pressure and (d) temperature with no filter (gray), high K_d filter (green), and tight K_d filter (red). The plots were generated using the open source Python3 tool Thermobar (v.0.07) from Wieser et al. (2022).

5.5.3 Bulk-Rock Major and Trace Element Compositions

Bulk rock peridotite xenolith compositions have generally high MgO contents (27.5 to 40.3 wt.%) with low SiO_2 (37.7 to 45.4 wt.%) with a broader range of CaO contents (10.9 to 1.6 wt.%), reflective of clinopyroxene abundance. Pyroxenite xenoliths have characteristically lower MgO contents (14.9 to 21.3 wt.%), higher SiO_2 (43.2 to 50.1 wt.%), and CaO contents (13.6 to 17.5 wt.%) all defining more restricted ranges. Compositions of Al_2O_3 define a narrow range for both peridotite (2.5 to 5.4 wt.%) and pyroxenite xenoliths (5.3 to 7.2 wt.%) apart from pyroxenite samples PC1601j and -k (14.1 and 11.8 wt.% respectively). Major and trace element compositions for these lava samples are homogeneous and within the ranges defined in previous studies of BPVF lavas (**Figure 5.4a-f**) (Blondes et al., 2008; Gao et al., 2017; Gazel et al., 2012). Host lavas for the ultramafic xenoliths presented here plot in the fields of trachybasalts to basanites based on the total-alkalis (TAS) versus silica classification (Le Bas et al., 1986) (total-alkalis = $Na_2O_2 + K_2O$ = 5.4 to 5.7 wt.%; SiO_2 = 45.9 to 46.8 wt.%). However, these samples have uniformly high MgO (9.0 to 9.4 wt.%), similar to primitive melts from Papoose Canyon and other BPVF vents and flows, which implies a better classification for these samples would be high MgO alkali basalts. Major-element covariation diagrams both fractional crystallization from the parent melt as well as mixing as assimilation processes. The logarithmic trends between Al_2O_3, TiO_2, and Fe_2O_3(T) versus MgO are generally indicative of fractional crystallization (**Figure 5.4a, c, & d**) and the linear trend between CaO versus MgO is indicative of crustal assimilation (**Figure 5.4b**).

Concentrations of the rare earth elements (REE) for cumulate peridotites are depleted relative to the pyroxenites and lavas. The pyroxenites however, have similar heavy REE (HREE) and incompatible trace element (ITE) profiles to the range of BPVF lavas while showing relative depletions in light REE (LREE) and ITE (**Figure 5.5a, e**). Blondes et al. (2008) observed a

systematic decrease in REE and ITE correlated with age. For example, the reported range of La/Yb decreases from 27.9 to 14.1 as lavas decrease in age through the Papoose sequence. Lavas from this study have homogeneous REE and ITE concentrations and fall within the field of BPVF lavas and are similar to the middle to younger age Papoose sequence reported by Blondes et al. (2008). They show no notable Eu enrichments relative primitive mantle and are similar to the broader BPVF lavas with the exception of Fish Creek and adjacent Jalopy Cone which have positive Pb anomalies. All the sample presented here have negative HFSE, Ti and Pb anomalies except for peridotite 1501f which shows a slight positive Pb anomaly. Cumulate xenoliths show higher degrees of inter-sample variation in LILE and LREE than moderately incompatible TE and HREE. The HFSE and Ti are variably depleted, and samples have both positive and negative inter-sample Pb anomalies (**Figure 5.5b**). Nickel concentrations show a strong positive linear trend with MgO throughout the sample set reflecting accumulation of olivine (**Figure 5.4e**). Light and heavy REE show positive linear correlations (i.e.: La versus Sm), particularly for lavas, consistent with results from Gao et al. (2017), and indicative of crustal assimilation. However, ratios of LREE and fluid mobile elements show distinct trends between lavas and cumulates (**Figure 5.4f**).

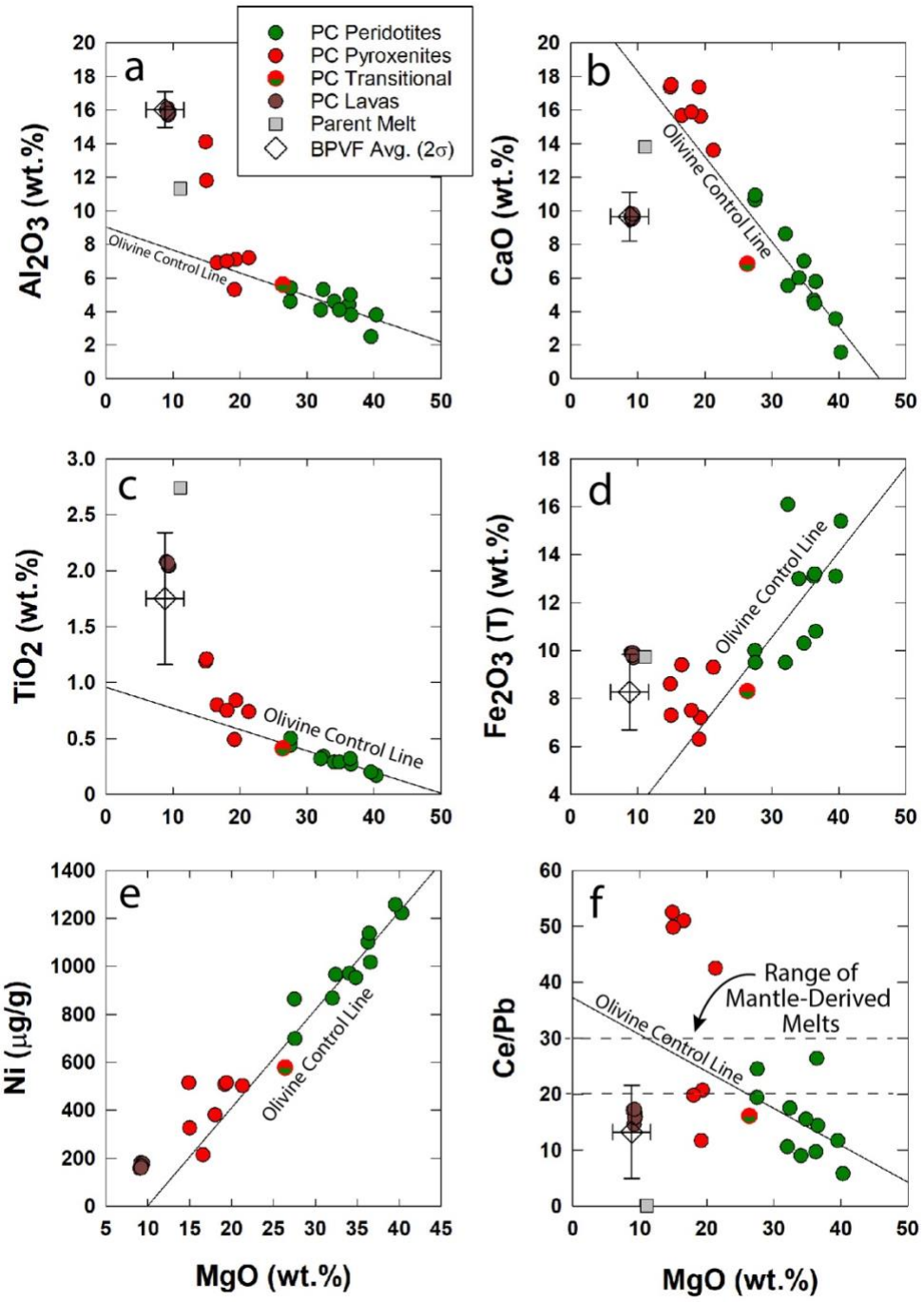

Figure 5.4 Variation diagrams of major (a – d) and trace elements (e & f) versus MgO for PC peridotites, pyroxenites, and lavas. Average lava composition for the BPVF is represented by a diamond with two standard deviation error bars. The calculated parent melt from this study is shown as a grey square marker. Published BPVF data from Blondes et al. (2008), Gao et al. (2017) and (Gazel et al., 2012).

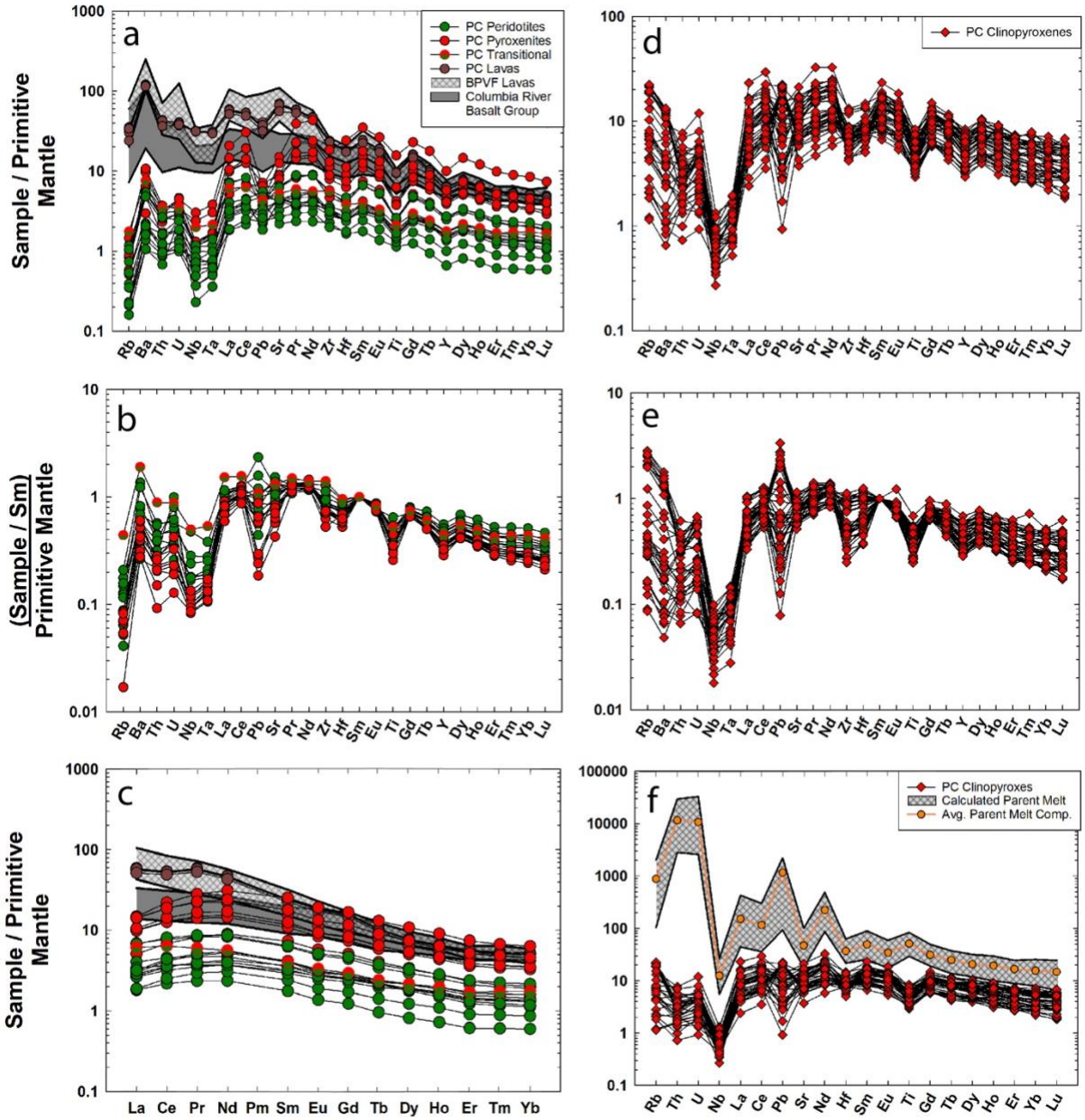

Figure 5.5 (a) Incompatible trace element (ITE) diagram for PC peridotites, pyroxenites, and lavas from this study with the ranges of published data for BPVF lavas (Blondes et al., 2008; Gazel et al., 2012) and the lower and upper Steens Formation of the Columbia River Basalt Group (Day et al., 2021). (b) Double normalization ITE diagram for PC peridotites and pyroxenites. (c) Rare earth element (REE) diagram for PC peridotites, pyroxenites, and lavas from this study (fields are the same as (a)). (d) ITE diagram for PC clinopyroxene mineral separates. (e) double normalization ITE diagram for PC clinopyroxene mineral separates. (c) Rare earth element (REE) diagram for PC peridotites, pyroxenites, and lavas from this study and the range of published data for BPVF lavas. (f) Calculated parent melt based on PC clinopyroxene compositions for Papoose Canyon. Partition coefficients from McKenzie and O'Nions (1991). Published BPVF data from Blondes et al. (2008), Gao et al. (2017) and (Gazel et al., 2012). Primitive mantle normalization values from McDonough and Sun (1995).

5.5.4 Osmium Isotopic Ratios & Highly Siderophile Element Abundances

Osmium isotopic and HSE data for Papoose Canyon whole rock powders are reported in **Table 5.1**. Papoose Canyon cumulate peridotites have Re concentrations ranging from 0.08 to 0.21 ng/g with broader ranges for Pd (0.48 to 31.0 ng/g) and Pt (0.22 to 6.7 ng/g). Cumulate pyroxenites have similar concentrations and ranges of Re (0.09 to 0.45 ng/g) and Pd (0.4 to 13.8 ng/g) compared to the peridotites with a generally elevated and broader range for Pt (0.14 to 148.2 ng/g). Iridium platinum group element (IPGE = Ru, Ir, Os) concentrations for cumulate peridotites have more restricted ranges of Ru (0.29 to 0.74 ng/g) and broader ranges of Ir (0.01 to 1.4 ng/g) with higher absolute concentrations of Ru than peridotite PPGE, whereas Os (0.003 to 0.227 ng/g) has a more restricted range and lower absolute concentration. Pyroxenite Ru and Ir concentrations define a narrower range and lower absolute concentrations than the peridotites (Ru = 0.23 to 0.55 ng/g; Ir = 0.02 to 12.9 ng/g), and Os has a range and concentration (Os = 0.004 to 0.27 ng/g). Inter-element HSE ratios show highly variable degrees of fractionation that range from supra-chondritic to sub-chondritic in both peridotites and pyroxenites. Pyroxenites and transitional sample (PC1501g) tend to have lower degrees of fractionation in Pd and Ru (Avg Pd/Ir = 22.6 ±49.4, 1σ; Avg Ru/Ir = 3.4 ±8.5, 1σ) than peridotites (Avg Pd/Ir = 140 ±158, 1σ; Avg Ru/Ir = 8.1 ±8.6, 1σ). The two sample sets are more similar with regard to Pt and Os fractionation with pyroxenite (Avg Pt/Ir = 6.4 ±3.6, 1σ; Avg Os/Ir = 0.05 ±0.08, 1σ) compared to peridotite (Avg Pt/Ir = 7.5 ±5.0, 1σ; Avg Os/Ir = 0.6 ±0.3, 1σ). Absolute HSE concentrations nor inter-element ratios show any quantifiable correlation with melt-depletion indicators, such as MgO and Al_2O_3, or sulfide accumulation indicators such as Ni and Cu. Primitive mantle normalized HSE diagrams for the cumulate peridotites form three distinct patterns. First, strongly enriched in Pd and variably

depleted in Ir and Os (**Figure 5.6c**). Second, unfractionated Pd and Pt with fractionated IPGE forming an Ir enriched “saw tooth” like pattern (**Figure 5.6d**). Third, PPGE – IPGE fractionated with depleted Pd relative patterns 1 and 2. These are similar to fractionation patterns observed in areas such as Izu-Bonin (e.g., Woodland et al., 2002) (**Figure 5.6e**). The pyroxenites and transitional xenolith form more cohesive patterns that are not easily sub-divided into groups. Here, Pd shows similar dispersion which falls within the range of the peridotites. In most cases Pt is enriched versus Pd and the transitional sample shows the highest absolute and relative Pt abundance of the sample set. Pyroxenite IPGE patterns reflect the Ir – Os fractionated "saw tooth” patterns of the pattern 2 peridotites with the exception PC1601c which is more similar to pattern 3. Both the peridotites and pyroxenites, excluding Ir for the transitional sample, are depleted in IPGE versus mantle xenoliths reported by Lee (2002), which are in turn slightly depleted relative primitive mantle (e.g., Becker et al., 2006; Day et al., 2017) (**Figure 5.6a & b**). Relative abundances of PPGE for both peridotites and pyroxenites generally fall within the range for Piton Chisny and Piton de la Fournaise cumulate xenoliths from Réunion Island (Peters et al., 2016). Osmium and Ru for pyroxenite and peridotites are depleted relative Réunion cumulates and Ir shows more variability versus this range.

Osmium isotopic compositions for cumulate peridotites are less radiogenic (0.1433 to 0.2403) than pyroxenites (0.1640 to 0.4076). These values span a larger range than previous studies (0.2135 to 0.3074; Blondes et al. (2008), and 0.1830 to 0.2870; Gao et al. (2017)), and trend to less radiogenic values. The entire sample set, however, is considerably more radiogenic than primitive mantle (0.1296 ±0.0008; Meisel et al. (2001)). Elevated $^{187}Os/^{188}Os$ have been well documented in HIMU-type OIB and the measured and previously reported $^{187}Os/^{188}Os$ ranges overlap the upper global HIMU range (e.g., Day, 2013; Day et al., 2009; Day et al., 2010; Ireland

et al., 2011; Ireland et al., 2009; Lassiter, 2003). These $^{187}Os/^{188}Os$ show little correlation versus melt-depletion and/or magmatic fractionation indicators MgO or Ni but show a good positive co-variation ($r^2 = 0.67$) with Cu. The $^{187}Re/^{188}Os$ for peridotite samples varies from 3.9 to 66 with an average of 21 ±35 2σ. The pyroxenites form a much broader range from 32.2 to 562 with an average of 194 ±373 2σ, and the transitional xenolith has the lowest $^{187}Re/^{188}Os$ of the entire sample set with a value of 2.6.

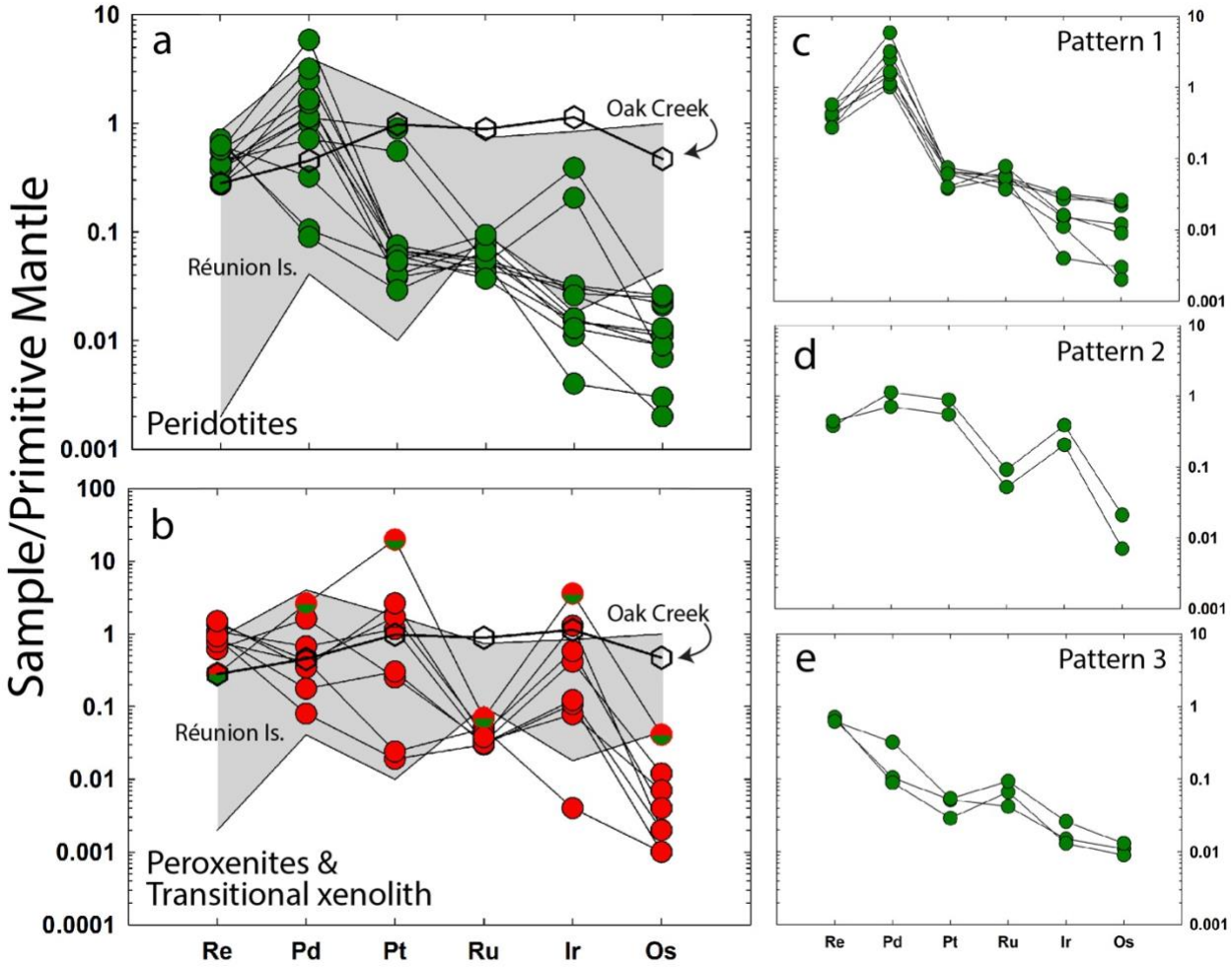

Figure 5.6 Primitive mantle normalized HSE diagram for Papoose Canyon cumulate peridotites (a) and pyroxenites (b) with spinel facies xenoliths from Oak Creek, BPVF and cumulate xenoliths from Piton Chisny and Piton de la Fournaise, Réunion Island (gray field) (Peters et al., 2016) on both plots for comparison (Lee, 2002). (c, d, & e) Peridotite samples from (a) divided into respective patterns, see text for further details. Primitive mantle normalization from Day et al. (2017).

Table 5.1 Whole-rock Re-Os isotope and highly siderophile element (ng g^{-1}) abundances for 0.761 Ma Papoose Canyon cumulate xenoliths.

	MgO (wt.%)	Al_2O_3 (wt.%)	Re	Pd	Pt	Ru	Ir
Peridotites							
PC1501a	32.4	5.3	0.083	5.34	0.28	0.43	0.01
PC1501b	27.5	4.6	0.114	5.98	6.68	0.73	1.40
PC1501d	27.6	5.4	0.133	3.77	4.15	0.41	0.74
PC1501e	34.1	4.6	0.129	6.04	0.49	0.36	0.11
PC1501f	40.3	3.8	0.168	31.00	0.50	0.42	0.10
PC1601a	32.0	4.1	0.114	8.13	0.50	0.45	0.05
			0.199	0.55	0.39	0.33	0.05
PC1601d	36.3	4.4	0.082	13.35	0.56	0.43	0.11
PC1601e	39.5	2.5	0.127	16.83	0.46	0.29	0.04
PC1601g	36.6	3.8	0.172	8.78	0.30	0.62	0.06
PC1601h	34.8	4.1	0.212	0.48	0.22	0.53	0.05
PC1601i	36.4	5.0	0.188	1.71	0.41	0.74	0.10
Pyroxenites							
PC1501c	16.6	6.9	0.325	3.56	8.71	0.26	1.49
PC1501g (transitional)	26.4	5.6	0.085	13.82	148.23	0.55	12.90
PC1501h	19.2	5.3	0.186	8.55	1.88	0.26	0.28
PC1601b	19.4	7.1	0.261	0.42	0.14	0.23	0.39
PC1601c	18.0	7.0	0.414	2.30	0.18	0.39	0.02
PC1601f	21.3	7.2	0.230	2.18	12.87	0.34	2.08
PC1601j	14.9	14.1	0.276	0.94	2.28	0.24	0.44
PC1601k	15.0	11.8	0.448	1.83	19.73	0.30	4.66

Table 5.1 Whole-rock Re-Os isotope and highly siderophile element (ng g^{-1}) abundances for 0.761 Ma Papoose Canyon cumulate xenoliths. (Continued)

	Os	Pd/Ir	Ru/Ir	$^{187}Re/^{188}Os$	2s	$^{187}Os/^{188}Os$	2s	γOsi
Peridotites								
PC1501a	0.011	5.3	0.083	5.34	0.28	0.43	0.01	13
PC1501b	0.083	4.6	0.114	5.98	6.68	0.73	1.40	22
	0.048							-0.4
PC1501d	0.026	5.4	0.133	3.77	4.15	0.41	0.74	17
	0.227							0.0
PC1501e	0.087	4.6	0.129	6.04	0.49	0.36	0.11	12
PC1501f	0.098	3.8	0.168	31.00	0.50	0.42	0.10	18
	0.023							17
PC1601a	0.046	4.1	0.114	8.13	0.50	0.45	0.05	18
	0.043		0.199	0.55	0.39	0.33	0.05	-4
	0.003							16
PC1601d	0.101	4.4	0.082	13.35	0.56	0.43	0.11	20
PC1601e	0.009	2.5	0.127	16.83	0.46	0.29	0.04	20
PC1601g	0.037	3.8	0.172	8.78	0.30	0.62	0.06	13
PC1601h	0.036	4.1	0.212	0.48	0.22	0.53	0.05	13
PC1601i	0.050	5.0	0.188	1.71	0.41	0.74	0.10	20
Pyroxenites								
PC1501c	0.047	6.9	0.325	3.56	8.71	0.26	1.49	36
PC1501g	0.161	5.6	0.085	13.82	148.23	0.55	12.90	88
(transitional)	0.178							83
	0.269							58
PC1501h	0.028	5.3	0.186	8.55	1.88	0.26	0.28	2.4
	0.009							38
	0.007							34
PC1601b	0.005	7.1	0.261	0.42	0.14	0.23	0.39	26
PC1601c	0.004	7.0	0.414	2.30	0.18	0.39	0.02	27
PC1601f	0.015	7.2	0.230	2.18	12.87	0.34	2.08	209
PC1601j	0.009	14.1	0.276	0.94	2.28	0.24	0.44	22
	0.009							20
PC1601k	0.009	11.8	0.448	1.83	19.73	0.30	4.66	21

5.6 Discussion

5.6.1 Pressure Temperature Constraints on Equilibration Depth

Thermobarometery models provide quantitative constraints on the pressure and temperature conditions of crystallization in magmatic systems. However, these models cannot account for conditions during melting such as fractional versus batch melting. As such, this model only offers insight to the final conditions of equilibration for pyroxenes, not a depth of melt generation. Thermobarometery models are calibrated assuming equilibrium between phases and/or crystal-liquid compositions. Previous studies have shown BPVF lavas have likely experienced crustal assimilation, and disequilibrium between phenocryst-liquid compositions (Gao et al., 2017). Because these lavas would represent the liquid composition, a clinopyroxene-liquid thermobarometer would likely overestimate temperature and pressure. Furthermore, olivine melt inclusions show a water content of ~1.5 to 3.0% for the BPVF (Gazel et al., 2012) and clinopyroxene-liquid thermobarometers, such as Putirka et al. (1996), are calibrated for anhydrous melts. Olivine, clinopyroxene, and orthopyroxene in the cumulate xenoliths from this study have similar Mg-numbers suggesting concurrent crystallization of these phases, making the two-pyroxene thermobarometer a more ideal model.

To place pressure and temperature results in context it is helpful to have some constraints on the depth of mechanical and rheological boundaries of the BPVF. Previous geophysical studies have shown evidence for thin lithosphere or lithosphere removal beneath the Eastern Sierra Nevada and Owens Valley, extending east into the Walker Lane (e.g.: Boyd et al., 2004; Ducea & Saleeby, 1996; Frassetto et al., 2011; Shen et al., 2013). In either case the implication is an exceptionally shallow asthenosphere for a continental setting, which has implications to the interpretation of thermobarometery results. High Vp/Vs values and receiver functions point to a crustal thickness

between 35 to 40 km for the southern Owens Valley (Frassetto et al., 2011; Wang et al., 2002) and thermobarometery models based on Ca in orthopyroxene of spinel facies mantle xenoliths from Oak Creek suggest shallow equilibration at relatively high temperature (1.5 GPa; 1000° to 1200° C) (Ducea & Saleeby, 1996; Lee et al., 2001).

Two-pyroxene thermobarometery results (Putirka, 2017) record average equilibration pressures of the Papoose Canyon cumulate xenoliths of 0.85 ±0.38 GPa and an average temperature of 1081° C ±58°. Based on a the same crustal density model used for depth estimates from Gao et al. (2017) and Gazel et al. (2012) ($\rho = 2750$ kg/m^3 (Wang et al., 2002)) this pressure corresponds to an average equilibration depth of 32 ±7.0 km. These results are less than the estimate of Mordick and Glazner (2006) (~1.4 ±0.3 GPa; 1250° C ±100°) but similar to Gao et al. (2017) and the broader estimates from Gazel et al. (2012) (~0.5 to 0.7 GPa), which corresponds to ~38 ±7.0 km. However, Gazel et al. (2012) grouped BPVF lavas into young (< 500 ka) and old (> 500 ka) categories of which Papoose Canyon (~760 ka) was grouped as old. These > 500 ka lavas show pressure results that suggest ~70 km depth of equilibration at ~1220° C, which was interpreted as the lithosphere asthenosphere boundary (LAB) ~500 ka (Gazel et al., 2012). The pressures and temperatures presented in this study are consistent with equilibration at or near the Moho based on receiver function analysis showing a crustal thickness of ~35 to 40 km (Frassetto et al., 2011). Crustal thickness constrained to this range also provides better agreement with the mantle xenolith equilibration temperatures from Lee et al. (2001) and Ducea and Saleeby (1996) as these provide a rough ceiling for maximum equilibration temperature of the cumulate xenoliths at this depth.

The results from Gazel et al. (2012) suggest a deep mantle source for Papoose Canyon melts and the pressure and temperature models presented here do not necessarily preclude that

possibility. In fact, Gazel et al. (2012) proposed melts stalled at the LAB prior to ascending to the Moho, possibly as a result of lithospheric thinning in this region. The present-day LAB is ~55 – 60 km (Rau & Forsyth, 2011) which implies the Owens Valley experienced 20 – 30% reduction in lithospheric thickness from ~70 km inferred from the phenocryst-liquid equilibration depth over < 2 Ma. An asthenospheric source is possible considering the overall lack of lithospheric geochemical characteristics for these cumulate xenoliths. For example, lithospheric olivine typically have Mg-numbers from 89 to 92, whereas olivines from this study range from 80 to 87 (Avg Mg-number = 86.0 ±1.0, 1σ) and spinel Cr# versus Mg-number are outside the field of spinel facies xenoliths (Warren, 2016). Trace element ratios such as Ce/Pb plot outside the range of mantle-derived melts (Hofmann et al., 1986) and $^{187}Os/^{188}Os$ ratios are far more radiogenic than the lithosphere (e.g., d'Errico et al., 2016; Day et al., 2017; Lee, 2002; Warren, 2016). This evidence will be discussed in greater detail in the following sections, but the sum of the evidence suggests Papoose Canyon lavas are not derived from a lithospheric source. Gao et al. (2017) concluded that Papoose Canyon lavas equilibrated in mid-crustal magma chambers while experiencing assimilation of continental crust and undergoing multiple episodes of recharge from primitive basaltic melts. However, the higher average pressures reported in this study suggest Moho depth for the xenoliths. A possible explanation is the difference in samples between the two studies. While Gao et al. (2017) included some xenoliths in the sample set the majority of the focus for thermobarometery was on phenocrysts which could have equilibrated in a different environment than the xenoliths (e.g. Mid-crustal magma chambers). Nonetheless, this interpretation does not discount the possibility of crustal assimilation and leaves open the possibility of assimilation of the lower crust.

5.6.2 HSE fractionation and $^{187}Os/^{188}Os$ composition

Without the presence of metal, the HSE behave as highly chalcophile elements meaning they will be incorporated into sulfide phases in the lithosphere (Luguet & Reisberg, 2016). During partial melting HSE compatibility varies Re < Pd < Pt << Ru < Ir ≤ Os (Becker et al., 2006; Pearson et al., 2004), resulting in substantial fractionation particularly at lower degrees of melting (Day, 2013; Rehkamper et al., 1999). Examples of variable compatibility have been documented in comparisons of HSE fractionation between MORB, OIB, and komatiites where MORB and OIB tend to be IPGE poor and komatiites show a smaller degree of PPGE depletion relative IPGE (Day, 2013; Rehkamper et al., 1999). Low to moderate degrees of partial melt, such as OIB and MORB, will produce lavas that have low IPGE abundances relative to PPGE and high degrees of partial melt like komatiites will have more uniform PPGE to IPGE ratios. Likewise, Ireland et al. (2009) showed that the dominant control for HSE abundances, particularly the IPGE, in Hawaiian picrites is the modal abundance of early crystalizing phases like olivine and Cr-spinel. These systematic observations suggest the most significant controls on HSE abundances in mantle-melts are the degree of partial melt and mantle minerology followed by fractional crystallization from the parental melt.

Papoose Canyon cumulate xenoliths have depleted primitive mantle normalized HSE patterns that trend toward higher degrees of depletion with increasing HSE compatibility which is illustrated by the down trending patterns shown in **Figure 5.6a & b**. This pattern of fractionation is typical of low degrees of partial melting and has been widely observed in OIB and MORB suites (Day, 2013; Gannoun et al., 2016). Lavas from this study and previous BPVF work have trace element ratios (La/Yb versus Dy/Yb) consistent ~1 to 3% partial melt based on polybaric melt models. Peridotites from Oak Creek, interpreted by Lee (2002) as mantle xenoliths with shallow

equilibration depths, have primitive mantle normalized HSE patterns near unity. These samples are slightly depleted in Re and Pd versus Pt, Ru, Ir, and Os which suggests the retention of IPGE in the Owens Valley lithosphere (**Figure 5.6a & b**). The HSE presented here are broadly consistent with low degree partial melting and to a first order are complementary to regional mantle peridotite HSE patterns, showing relative enrichments in PPGE (Re, ±Pd, ±Pt) and depletions in IPGE (Ru, ±Ir, Os) (**Figure 5.6a & b**). Average $(Re/Os)_{PM}$ for the Papoose Canyon peridotites is 52 and pyroxenites is 251 which is not as extreme as other low degree melts such as OIB which originate deeper in the mantle. This raises the question of whether the low HSE composition of Papoose Canyon xenoliths are related to partial melting, crustal contamination, or are a source feature.

There are some noteworthy HSE fractionation features of theses samples that may help delineate the source of Papoose Canyon melting. Of the sample set three peridotites (PC1501a, PC1601g, -i) and two pyroxenites (PC1501c, -h) have highly fractionated relative HSE patterns. These five samples have highly variable absolute and relative abundances of Pd, Pt, and Ir. Osmium and Ir have similar partition coefficients and normally show very similar fractionation behavior during partial melting (Barnes et al., 1985), thus the expectation is Os/Ir ratios should approximate unity. Here, the Os/Ir ratios of both cumulate peridotites and pyroxenites show a high degree of variability (0.02 – 5.2) with only four peridotite samples approaching unity. As well, Ir anomalies ($Ir/Ir^* = (Ir/(Ru*Os)^{0.5})$) for peridotites are typically negative with the exception of two samples. All but one pyroxenite are strongly positive with five sample extending to extreme values >10. Correlations of Ir anomalies and Os/Ir ratios with olivine fractionation indicators such as Mg-number, MgO, and Ni are poor but decidedly trend down with the greatest degree of variability apparent in the pyroxenite subset. This suggests that the broader control on Os concentration is

olivine abundances however, the poor correlations may be attributed to a high degree of variability within the source.

Another key feature of HSE fractionation in this sample set is the positive Ru anomalies ($Ru/Ru^* = Ru/(Pt*Ir)^{0.5}$). Nine of the eleven peridotite samples have strongly positive Ru anomalies from 1.5 to 7.0. Only one of the seven pyroxenites (PC1601c) and transitional sample has a strongly positive Ru anomaly, PC1601b is near unity while the remainder is strongly negative. Five of these nine samples (four peridotites and one pyroxenite) have Cu and/or Cr above the average and median Cu and Cr values of the set for their respective species and are among the most magnesian particularly in the case of peridotites. This implies that the high Ru anomalies observed in these samples are the result of the accumulation of Cr-spinel, a phase which preferentially fractionates Ru, as opposed to a primary source or partial melting feature.

The third and final HSE fractionation characteristic for discussion are the generally high Pd abundances, particularly in pattern 1 peridotites, and variably fractionated Pd/Pt and Pd/Ir ratios. Platinum is considerably more compatible in sulfide than Pd (Mungall & Brenan, 2014), thus sulfide fractionation should not produce excessively low Pd/Pt ratios and any systematic style of sulfide fractionation should not result in the high variability observed here. Ratios of Pd/Pt in these cumulates vary considerably from 0.05 to 36.0 in the most extreme cases, and three peridotites PC1501d, -e, -f, and two pyroxenites PC1501c, and -h have $Pd/Pt < 1$. The low Pd and subsequent low Pd/Pt ratios for these samples are more likely reflective of source composition than sulfide fractionation. Chromium and Mg-number show good negative correlations with Pd/Pt ($r^2 = 0.64$ and 0.59, respectively) and Pd and Pt concentrations show similar correlations albeit with more scatter. This suggests that neither olivine nor Cr-spinel are significant factors for Pd/Pt fractionation. A weak positive correlation is observed between Pd/Pt and CaO which suggest

clinopyroxene may be a minor factor for PPGE fractionation. Primitive mantle normalized abundances of Pt in peridotite samples 1501a, 1601g, and -i are strongly depleted (**Figure 6a**). These samples correspond to some of the lowest Cu concentrations in the sample set. Likewise, pyroxenite samples 1501c and -h show strong relative Pt enrichments (**Figure 5.6b**) that correspond to high Cu concentrations. Overall, Cu and Pt have a good positive correlation (r^2 = 0.62), thus these relationships suggest that Cu-sulfide phase abundance is a dominant factor controlling Pt abundances for these samples. However, this does not carry over to Pd and the correlation with Cu does not do a great deal to explain the highly variable Pd/Pt fractionation or the low Pd abundances. Samples PC1501e, -g, and -h, and PC1601d, and -h have considerably low Pd/Ir ratios as well. This is noteworthy because the more incompatible PPGE, Pd, is expected to be more concentrated in melts than the more compatible IPGE Ir, which should remain in the residuum. However, this may be explained through the loss of Pd rich sulfide phases during the subduction process (Dale et al., 2009). Therefore, a reasonable conclusion is while Cu-sulfide phase abundance leverages absolute and relative PPGE abundances, the variably depleted nature is likely inherited from the mantle source. The HSE data presented here suggests the Papoose Canyon cumulates sample a subduction modified source. The high MgO and modest SiO_2 composition of the alkalic basalts are not indicative of melting of an oceanic slab as this would produce the opposite effect. Instead, it is more likely that metasomatizing melts reacted with the peridotite mantle to form small volumes of pyroxenite, similar to the binary source proposed by Blondes et al. (2008). Small volumes of highly fusible material could explain the variability observed in the inter-HSE ratios.

Another explanation for the variable and in some cases extreme fractionation observed in these samples is sulfur saturation which can cause significant fractionation of HSE. For OIB S-saturation

occurs at ~8 wt.% MgO and ≧8 wt.% MgO for MORB (Day, 2013). Host lavas from this study and others are consistently >9 wt.% MgO (Blondes et al., 2008; Gao et al., 2017; Gazel et al., 2012), and adjacent Jalopy cone lavas investigated by Gazel et al. (2012) show S content of ~5000 ppm, which both are strongly indicative of S-saturation. High MgO in the cumulate sample presented here are certainly a function of bulk minerology however, the decreasing Cu content versus increasing MgO provides supporting evidence for S-saturation in the cumulate samples. Sulfur saturation in basaltic melts will effectively fractionate IPGE from Re + PPGE particularly Os. Similar HSE fractionation patterns resulting from S-saturation were observed in Columbia River Basalt Group lavas, a continental flood basalt that erupted in a back-arc environment of the Cascadia subduction zone (Day et al., 2021). Ultimately, reducing the Os concentration of a melt makes the $^{187}Os/^{188}Os$ composition more susceptible to crustal contamination, a hypothesis which has been proposed for the Papoose Canyon by in previous studies (Blondes et al., 2008; Gao et al., 2017).

5.6.3 Crustal Contamination of Lavas and Cumulate Xenoliths

Prior work has identified a range of source and equilibration depths for the BPVF and Coso Volcanic Field to the south (**Figure 5.1a**). Temporal, geochemical, and isotopic variations, specifically in the Papoose Canyon sequence, suggest binary mixing of isotopically enriched and depleted end-members such as peridotite and pyroxenite (Blondes et al., 2008). Spinel facies mantle xenoliths from the Oak Creek location in the BPVF have Ca in orthopyroxene temperatures (1000° - 1100° C) that suggest melt extraction and equilibration in the shallow lithosphere (~35 km) (Beard & Glazner, 1995; Lee et al., 2006). In contrast, crustal assimilation and post eruptive recharge of a mid-crustal magma chamber based on clinopyroxene thermobarometery, trace-

element systematics, and Sr-Nd-Pb-Os isotope systematics was proposed by Gao et al. (2017) to explain the temporal isotopic and incompatible element variation of the Papoose sequence. Cumulate xenoliths from this study have an order of magnitude larger/smaller variation in incompatible element composition which exceeds the variation observed in the previously published field of BPVF basalts (**Figure 5.3a – d**) (Blondes et al., 2008; Gao et al., 2017; Gazel et al., 2012). To a first order this supports the hypothesis of multiple melt sources, but it also cannot eliminate the possibility of crustal assimilation having a significant effect on incompatible element compositions.

The relatively high MgO, low SiO_2 content, and abundance of olivine phenocrysts in BPVF basalts have supported initial interpretations that these basalts represent generally unaltered primitive melts from the mantle (Blondes et al., 2008; Gazel et al., 2012; Ormerod et al., 1991). However, later work demonstrated the distinct possibility that assimilation of crustal material has had a significant effect on BPVF basalts (e.g., LILE/HFSE ratios, HFSE versus $^{87}Sr/^{86}Sr$, $^{143}Nd/^{144}Nd$, $^{206}Pb/^{204}Pb$) (Gao et al., 2017). Cumulate xenoliths from this study have high LILE/HFSE ratios (La/Nb = 2.1 to 10.9) as would be expected from the incorporation of HFSE depleted continental crust or subduction-modified mantle material. The highly depleted HFSE reported here result have exceptionally high La/Nb ratios compared to average continental crust (La/Nb ~2.5) (McDonough & Sun, 1995). Correlations of LILE versus MgO (e.g., Ce/Pb) decrease with increasing MgO (**Figure 5.4f**) and generally fall below the mantle-derived melt value (Ce/Pb = 25 ±5) which is more typical of subduction arc magmas (Hofmann, 1988). In addition, these samples show linear trends in major and trace element systematics which is indicative of two-component mixing, as opposed to asymptotic relationships which is typical of fractional crystallization processes. Papoose Canyon clinopyroxene REE (La versus Sm) have a positive

linear correlation that is coincident with clinopyroxenes from (Gao et al., 2017). However, some major element correlations (Al_2O_3, TiO_2, & Fe_2O_3 vs. MgO) do not show linear trends and are instead suggestive of fractional crystallization processes (**Figure 5.4a, c, d**), as are linear trends between MgO, Mg-number, and compatible elements such as Ni (**Figure 5.4e**). These relationships are particularly robust in the older (>500 ka) Papoose Canyon and Oak Creek eruptions in the BPVF (Gazel et al., 2012).

To gain further insight into the effects of crustal contamination versus a subduction-modified component the trace element composition of the Papoose Canyon parent melt was modeled based on clinopyroxene compositions using the partition coefficients from McKenzie and O'Nions (1991) (**Figure 5.3f**). The modeled compositions show notable enrichments in LREE relative to Papoose Canyon and BPVF lavas which suggests crustal contamination from the parent magma. However, negative HFSE and Ti anomalies in both the parent melt and clinopyroxene point to a subduction-modified component. Supporting evidence for this is apparent in HFSE and LILE ratios for the parent melt. Here again, high La/Nb (8.1 – 16.3) indicate highly depleted HFSE and low Ce/Pb (0.38 – 0.14) shows the removal of high LILE fluids from the initial source.

Osmium isotopic ratios have been shown to be highly sensitive to assimilation processes when Os concentration is below 0.05 ng/g (e.g.: Day, 2013; Reisberg et al., 1993; Widom et al., 1999). Osmium concentrations for cumulate xenoliths from this study and others (Blondes et al., 2008; Gao et al., 2017) have unusually low Os concentrations and highly radiogenic $^{187}Os/^{188}Os$ (Avg = 0.1849 ±0.06, 1σ). The $^{187}Os/^{188}Os$ observed here are considerably higher than most mantle-derived magmas (Avg ≤ 0.15, e.g.: Hauri et al. (1996), Lassiter and Hauri (1998), Day (2013)) and are decoupled from lithophile isotopic systems (Sr-Nd-Pb; (Blondes et al., 2008; Gao et al., 2017). The peridotite samples are the least radiogenic ($\gamma Os_i = -4 - 22$) of the samples and

Os isotope systematics show no correlation with $^{187}Re/^{188}Os$ so in situ decay of Re can be discounted as a contributing factor to the radiogenic Os. However, pyroxenite samples form two discernable trends representing variable addition of Re and the ingrowth of ^{187}Os over time (**Figure 5.7**) and are considerably more radiogenic ($\gamma Os_i = 2.4 - 209$) with a much higher degree of variability than the peridotites. Under partial melting conditions Re is incompatible with partitioning behavior similar to ITE, thus continental crust tends to have high Re/Os and $^{187}Os/^{188}Os$ (Rehkamper et al., 1999). Ratios of Re/Os are extremely variable in this sample set with cumulate peridotites having generally lower Re/Os (Avg Re/Os = 52 ±134, 1σ) than cumulate pyroxenites (Avg Re/Os = 250 ±149, 1σ). A plausible explanation is because the IPGE are primarily hosted by sulfide inclusions in olivine and Re and the PPGE are hosted by interstitial sulfides which are more susceptible to melt and metasomatic reaction (Luguet et al., 2007). However, Re/Os, Pd/Ir, or Pt/Ir ratios show no statistically significant correlation with LILE or HFSE ratios that may suggest addition of a crustal component evident in Os isotopes or HSE. Additionally, the abundance of HSE in continental crust is so small that the portion of continental crust required to perturb the HSE abundances observed here would have a significant dilutionary effect on compatible major element systematics, such as MgO. Likewise, significant enrichments would be expected in incompatible major elements, whereas here lavas from the BPVF are compatible rich and incompatible poor to the point that they are generally considered primitive in nature. These interpretations are not meant to suggest that crustal contamination has not occurred, simply an argument to show that crustal contamination has not leveraged PGE abundances. Another possibility is the addition of a subducted slab component and/or incorporation of mafic lower crust. Due to the addition of continental sediment and seawater oceanic crust has high Re/Os which results in highly radiogenic Os with $^{187}Os/^{188}Os > 1$. Fluids derived from a remnant slab,

such as the Isabella Anomaly (Dougherty et al., 2021), could be a potential source of radiogenic Os in the Papoose Canyon cumulates. Likewise, mafic lower crust has similarly high Re/Os and melts ponding and equilibrating at the Moho could potentially assimilate mafic material from this boundary.

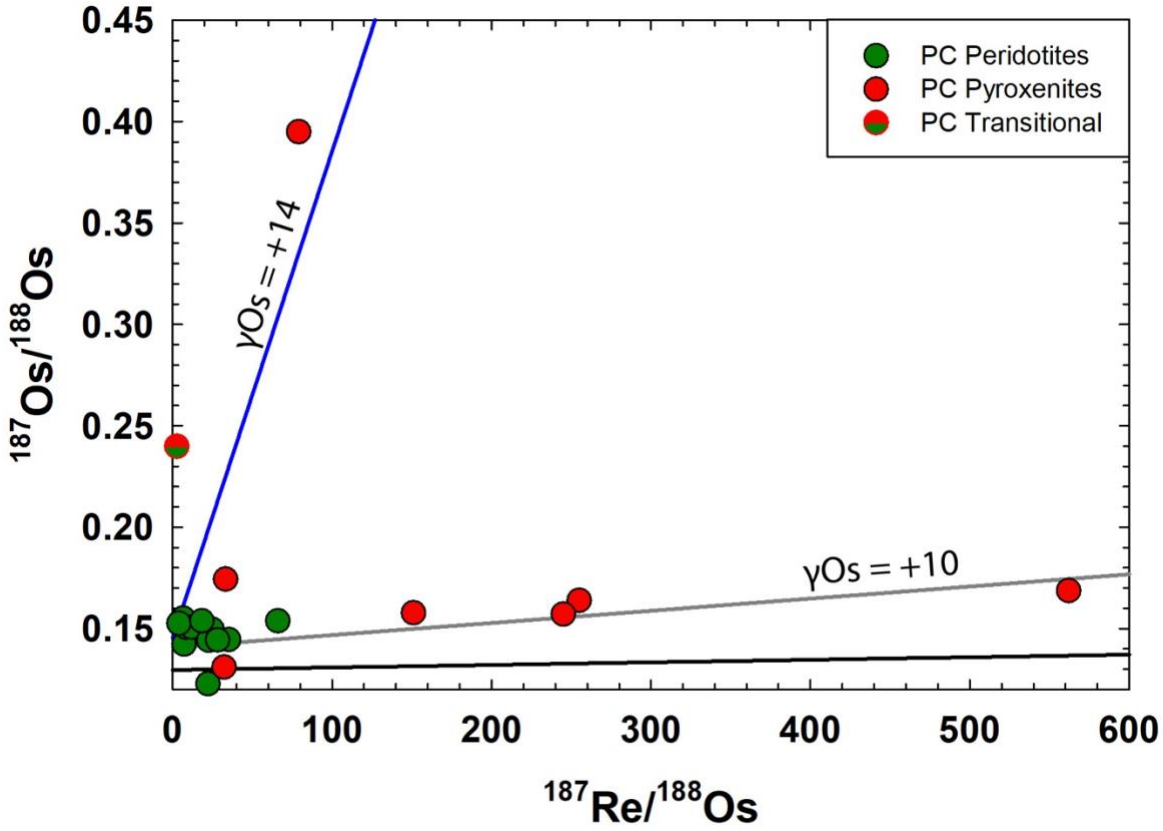

Figure 5.7 $^{187}Os/^{188}Os$ versus $^{187}Re/^{188}Os$ for Papoose Canyon peridotites and pyroxenites shown in terms of γOs (gray and blue lines). The black line shows an isochron with primitive mantle composition at 761 ka.

Previous studies have reported radiogenic $^{87}Sr/^{86}Sr$ and low $^{143}Nd/^{144}Nd$ for Papoose Canyon basalts and ultramafic xenoliths (Blondes et al., 2008; Gao et al., 2017), and Gao et al. (2017) also notes that these $^{87}Sr/^{86}Sr$ correlates well with 1/[Sr]. These observations, in addition to isotopically radiogenic, low Os, are indicative of assimilation of crustal material. The effect of

crustal assimilation on HSE composition and/or fraction is not as well constrained. However, incorporation of crustal material can add sulfur to the melt from the country rock. This process has been demonstrated in continental flood basalts (e.g., Day, 2013; Keays & Lightfoot, 2007) and crustal contamination of Hawaiian picrites was shown to dilute HSE abundances (Ireland et al., 2009). To further examine the effects crustal assimilation has on $^{187}Os/^{188}Os$ compositions and HSE fractionation a dynamic mixing model is used combining a parent melt with non-radiogenic Os composition and modestly fractionated PPGE/IPGE (Pt/Ir in this case) with a highly radiogenic, low Os and highly fractionated PPGE/IPGE crustal contaminant (**Figure 5.8**). Mixing models such as these can be greatly complicated due to the fact that crustal assimilation is intimately associated with fractional crystallization processes with regard to HSE (e.g., Ireland et al., 2009). Additionally, any mixing model is highly leveraged by the selected end-member compositions which in natural systems can have high degrees of variability. For these reasons a dynamic model using a parent melt with variable Os concentrations was used (0.5, 0.01, 0.005, 0.001 ng/g Os).These results show that only a small amount of crustal input is required to replicate the range of observed Os isotopic compositions and PPGE/IPGE fractionation, such that major- and trace-element abundances would be minimally affected. For most sample ~1 to 4.5% crustal addition can account for Pt/Ir fractionation with up to ~9% in the most extreme case. For the most radiogenic pyroxenite samples with low Os concentration as little as 2% crustal addition is required to produce observed $^{187}Os/^{188}Os$ values.

The sum of the evidence presented here and in previous work suggests that crustal contamination has likely had an effect on lava compositions in the Papoose Canyon and throughout the BPVF. The felsic composition of Crater Mountain in the northern BPVF provides evidence that magma differentiation occurs here, and like the Coso Volcanic Field to the south,

differentiation likely occurs in mid-crustal magma chambers (Mordick & Glazner, 2006). Olivine and clinopyroxene phenocrysts show a range of compositions from primitive to evolved, which suggests that BPVF basalts host some combination of phenocrysts and antecrysts. Nevertheless, major and trace-element, HSE, and $^{187}Os/^{188}Os$ systematics for some cumulate xenoliths, particularly the least radiogenic peridotites, presented in this study suggest a possible source characteristic that may be preserved. The high variability in radiogenic Os observed in the pyroxenites, best expressed as the range in γOs_i from 2.4 to 209, is strong evidence for crustal addition, as it is very unlikely that such a broad range could be a source signature. The cause of fractionated HSE patterns are more difficult to isolate however, S-saturation from crustal assimilation is a distinct possibility.

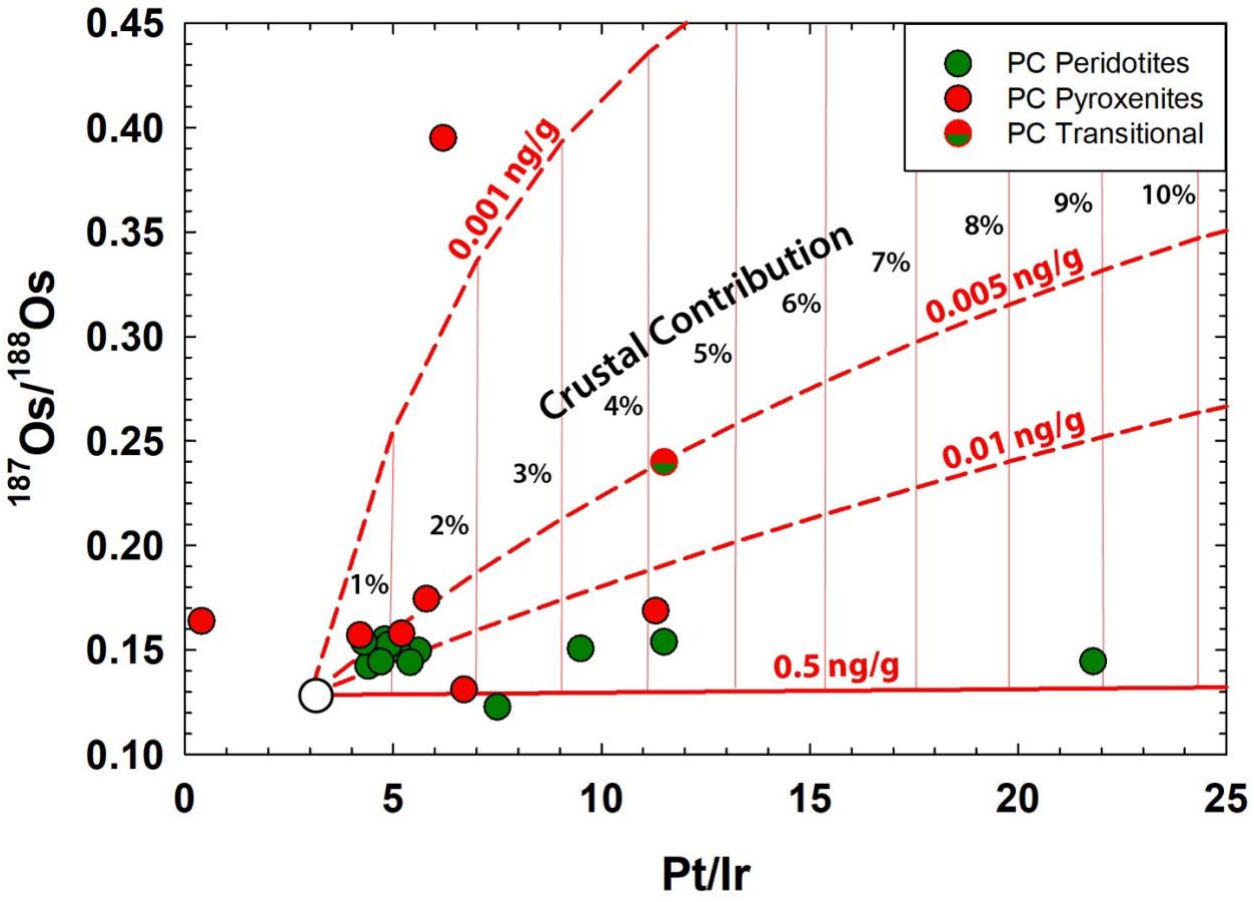

Figure 5.8 Modification of $^{187}Os/^{188}Os$ composition and HSE fractionation of Papoose Canyon cumulates by crustal contamination as a function of variable Os concentrations in a parent melt.

5.6.4 Effects of fO_2 on HSE Abundances

Papoose Canyon cumulate peridotites (PC1501b, -d, and -e) have calculated fO_2 that are strongly oxidized, consistent with previous BPVF melt inclusions from Jalopy and Quarry cones (Gazel et al., 2012; Kelley & Cottrell, 2012). The tectonic setting of the Owens Valley and broader Eastern Sierra Nevada region prior to the onset of dextral shearing was the Ancestral Cascades back-arc to Farallon plate subduction (Atwater, 1970; Nicholson et al., 1994). The implication of a previous subduction environment is that the underlying mantle has experienced metasomatism

and may preserve evidence of this from water entrained in the mantle from the subducting slab. Gazel et al. (2012) provided evidence to support this showing BPVF lavas contained > 1.5 wt.% H_2O and, based on this figure, calculated a mantle source containing 250 – 1900 μg/g H_2O, which overlaps back-arc basin values. Alternatively, sulfur has been suggested as an oxidizing agent in arc environments where Fe^{2+} is oxidized by S^{6+} (Bénard et al., 2018). The strongly oxidized results reported here (PC1501b = 2.78 ±1.2 ΔFMQ, PC1501d = 2.84 ±0.1 ΔFMQ, PC1501e = 2.24 ±0.6 ΔFMQ) exceed the highly oxidized Canary Islands (Nicklas et al., 2022) and are more similar to the most oxidized arc melt inclusions reported by Kelley and Cottrell (2009). High fO_2 has a significant effect on the HSE budget of melts, and this may be apparent in the low HSE abundances shown in these samples. At high fO_2 mantle sulfides are unstable and transition to sulfate where HSE are incompatible. This would also produce the HFSE anomalies noted in the previous section. Therefore, later BPVF related melting would then source an already HSE depleted mantle. An HSE stripped source may also explain why HSE show no systematic relationship with partial melt indicators such as MgO, which is typical for HSE in other volcanic systems for example Hawai'i, the Canary Islands, and the Azores (Day et al., 2010; Ireland et al., 2009; Waters et al., 2020). A variably scavenged and depleted mantle wedge source may also explain the high degree of variability observed in inter-HSE ratios.

Trace-element systematics presented here and trace-element and isotopic systematics for lavas and clinopyroxenes from Gao et al. (2017) have shown evidence for crustal contamination and assimilation. This leaves open the possibility that high fO_2 is not a source characteristic of an oxidized mantle wedge but is, in fact, the result of assimilation of continental crust. The most abundant redox sensitive element in mantle-derived melts is Fe. The Fe^{3+}/Fe^{2+} ratio, thus the overall Fe abundance control how fO_2 is affected by assimilation and contamination. Compared to

basaltic liquids, continental crust is Fe poor so it is expected that even moderate to significant assimilation of continental crust would have a negligible effect on fO_2 (Grocke et al., 2016). Thus, it is unlikely that the high fO_2 and subsequent effects on HSE are a product of crustal contamination and instead are more likely a feature of the BPVF mantle source.

5.6.5 Drivers of Volcanism in the Owens Valley

New data presented here and analysis of previous studies from the BPVF and Coso volcanic field provide evidence for an intact, thin lithosphere, and subduction metasomatized mantle beneath the Owens Valley. Beginning in the southern Owens Valley, the crust beneath the Coso volcanic field was determined to be ~30 km thick using P-wave arrivals from the 2019 Ridgecrest earthquakes (Wang et al., 2022). Near the BPVF, ~150 km north, Frassetto et al. (2011) determined a crustal thickness of ~35 – 40 km with receiver functions. This implies a relatively uniform crustal thickness throughout much of the Owens Valley, given a possible slight gradual thickening to the north. The lithosphere asthenosphere boundary (LAB) below the BPVF is particularly shallow, ~55 – 60 km determined by the maximum gradient in shear wave velocity (Rau & Forsyth, 2011). Frassetto et al. (2011) also observed a negative Ps conversion at ~55 km. Here there is some disagreement with melt model calculations from BPVF basalts where Wang et al. (2002) interprets the LAB to be ~10 – 15 km deeper albeit with some overlap in both estimates. This could be attributed to a time disparity whereby melting occurred at a deep LAB prior to lithospheric thinning, thus older basalts record deeper melting (Gazel et al., 2012). Arriving at an estimate for the LAB for the Coso volcanic field is less straight forward due to the presence of a large crustal magma chamber. A rough estimate is provided by a low surface wave velocity anomaly observed here that corresponds to a depth of 60 – 90 km (Jiang et al., 2018). However,

based on FeO and Na_2O_3 contents of basalts melting was constrained to ~60 km in this region and assuming this represents a rheological boundary effectively capping the melt, this is a reasonable estimate for the LAB (Mordick & Glazner, 2006; Wang et al., 2002).

Collectively, these observations depict an unusually thin lithosphere for a continental setting (**Figure 5.9**). From the BPVF to the Coso volcanic field to the south the lithospheric thickness is relatively uniform with a potentially gradual thickening toward the Coso volcanics. Basaltic volcanism from both locations, discussed in the previous sections, suggest a heterogeneous, metasomatized mantle underling the thin lithosphere, which is likely a carryover result of subduction of the Farallon slab, although metasomatic fluid addition may be an ongoing process from the Isabella anomaly (subducted Monterey microplate) (Gazel et al., 2012). It should be noted however that the eastern extent and depth of the Isabella anomaly is not well constrained (e.g.: Jiang et al., 2018). In the same Ridgecrest P-wave arrival study Wang et al. (2022) interpreted low Vp anomalies from ~7 – 20 km in the mid to lower crust as a large magma chamber suppling the Coso volcanic field. This is consistent with the clinopyroxene equilibration depth reported by Mordick and Glazner (2006). This magma chamber has a prominent elongated N-S orientation that is likely controlled by the extensional releasing bend between the northwest striking Airport Lake Fault and Owens Valley Fault (Wang et al., 2022). Magma chambers in the BPVF are not as well defined but some inferences can be made based on thermobarometery. The two-pyroxene results from this study provide a total equilibration range of 25 – 45 km with an average of 32 km. Gao et al. (2017) and Gazel et al. (2012) provided overlapping ranges of ~20 – 36 km based on olivine and clinopyroxene phenocrysts, which led to a mid to lower crustal sill model for magma storage. Together these results suggest a network of magma chambers feeding one or more volcanos beginning at the Moho and propagating through the crust. Many of the BPVF volcanos are oriented

along faults that are either splays of or related to the Owens Valley Fault. **Figure 5.1b** shows the Papoose Canyon, Quarry Cone, and Jalopy Cone along the southern section of the White Mountain Fault and Red Mountain and Fish Creek along splays of the Owens Valley Fault. This orientation suggests, at least to a first order, that like the Coso magma chamber BPVF magma chambers may be orienting in the direction of maximum principal stress. The timing of volcanism makes a broadly progressive trend in pulses beginning from south at ~4 Ma in the Coso volcanic field and moving north to the BPVF by ~1.3 Ma. The unusually thin lithosphere, proposed structure, and timing suggest that the dominant control on volcanism in this region is extensional beta factor.

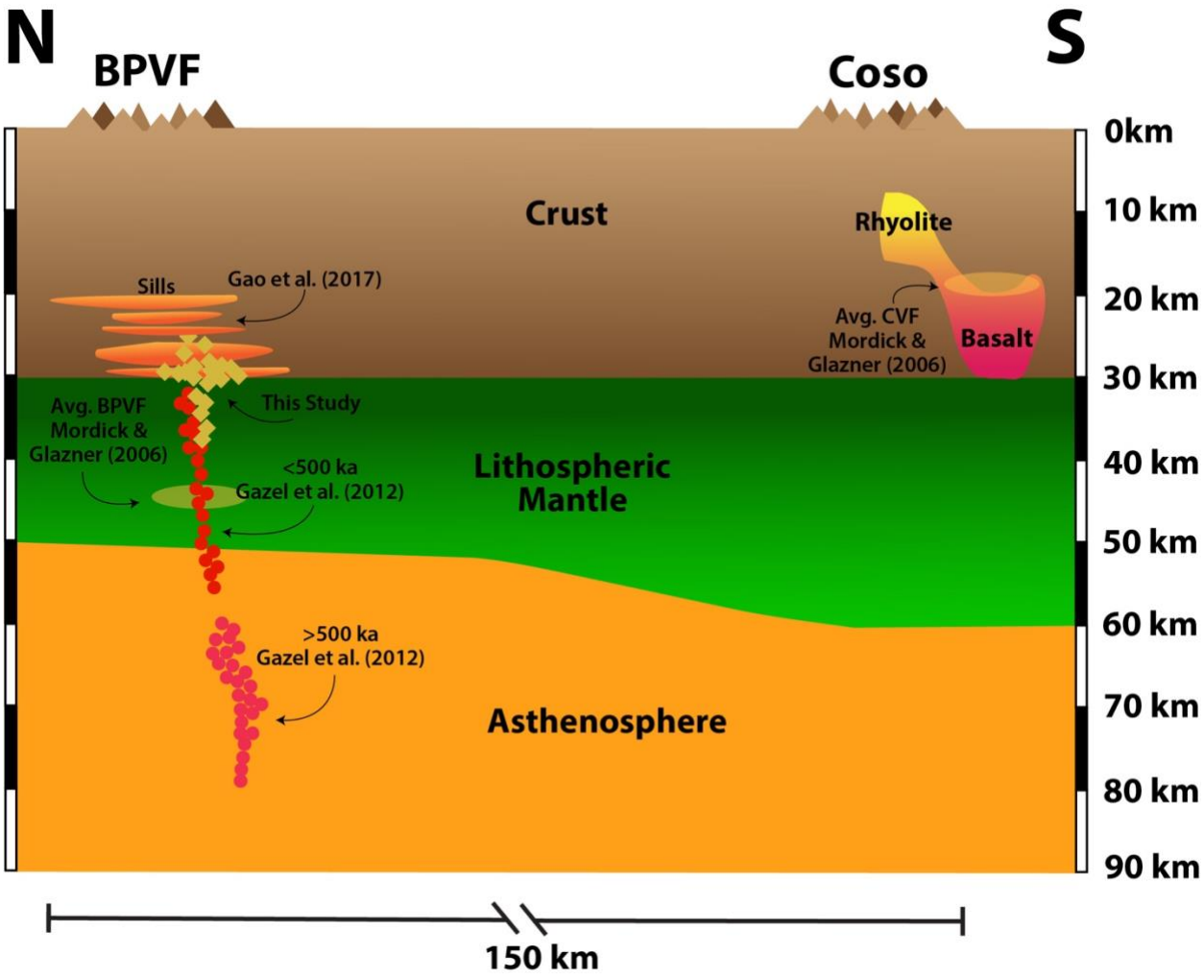

Figure 5.9 Conceptual model of the Owens Valley lithosphere. Moho, LAB, and magma chamber depth estimations are based on thermobarometery models from this study, Gao et al. (2017), Gazel et al. (2012) (BPVF), Mordick and Glazner (2006) (Coso) and seismic studies from Wang et al. (2022), Frassetto et al. (2011), Rau and Forsyth (2011) (details provided in text). The Coso magma chamber depicted in this figure is a simplification from Figure 12 in Wang et al. (2022).

5.5.6 Comparison to the East African Rift

The Sierra Nevada-Walker Lane region, which includes the Owens Valley, is considered by some authors to be the northern continuation of the Gulf of California rift system (e.g.: Busby, 2011; Faulds et al., 2008; Jayko & Bursik, 2011). This hypothesis proposes that northern

propagation of continental rifting has roughly followed the late northward transgression of the Mendocino triple junction, becoming a more coherent plate margin scale transtensional process ~12 Ma, concurrent with Gulf of California rifting (Busby, 2013). The Sierra Frontal Fault System, of which the Owens Valley Fault is a component, accommodates NW-SE movement between the North American plate and the Sierra Nevada microplate (Unruh et al., 2003) as well as the vertical component of Sierra Nevada uplift (Unruh, 1991). This contrasts with the predominantly ~W-E movement of the Basin and Range province and provides support for the continental rifting hypothesis. Structural separation and westward movement of the Sierra Nevada microplate relative the Colorado Plateau at ~3.5 Ma caused basin-forming deformation that resulted the linear valleys and dextral faults that define the Walker Lane (Stevens et al., 2013).

The East African Rift (EAR) is the southern are of an extensional triple junction that includes the Red Sea to the northwest and the Gulf of Aden to the east. This triple junction formed in response to the breakup of the Afro-Arabian shield beginning ~35 Ma which initially formed the Gulf of Aden (Watchorn et al., 1998) and progressed to form the Red Sea at ~28 Ma (Wolfenden et al., 2004). The earliest documented extension in the EAR began ~25 Ma in the Turkana region (Hendrie et al., 1994) and plate kinematic models suggest the three arms of the triple junction had joined by ~11 Ma (Wolfenden et al., 2004). Initiation of rifting was driven by the closing of the Neotethys, but the Afar plume has played a role as well as made evident in both geophysical and geochemical observations. The EAR is an example of the transition from a stable continental shield to a passive margin while the Owens Valley is a transition from an active convergent margin to passive divergence. The distinction in tectonic environment has inherent implications for regional lithospheric compositions however, similarities exist that may suggest some commonality in continental rift systems.

In common with Owens Valley lavas, EAR lavas show evidence of crustal assimilation. Here, crustal assimilation is most pronounced in the southern Kenya Rift of the EAR. This region has experienced the least degree of extension relative the broader EAR, thus has a thicker lithosphere and crust resulting in more residence time for melts (Furman, 2007). Basalts from this southern region of the EAR show enrichments in LILE and fluid mobile elements, typical of crustal inputs. Both the southern Kenya Rift and Western Rift are characterized by low Os and radiogenic $^{187}Os/^{188}Os$ (Nelson et al., 2012) which suggests minor contributions of continental crust could push Os isotopic ratios toward radiogenic values for more silica-saturated samples. Higher volumes of melt production in the EAR generally correspond to thinner lithosphere and a lack of crustal assimilation (Furman, 2007; Furman et al., 2016). Picrites are commonly reported in these areas nearer the triple junction, such as Northwest Kenya and Turkana (Nelson et al., 2012). This contrasts with BPVF basalts that have < 10% MgO despite uniformly thin lithosphere (**Figure 5.8**), but this is likely a source characteristic related to the Afar plume. In fact, unlike EAR lithospheric thickness of the Owens Valley has no control over the observed degree of crustal contamination.

Lithospheric thinning is a common feature to the most extended regions of the EAR, Ethiopian plateau, and the Owens Valley however mechanisms of lithospheric thinning differ. Beneath the Main Ethiopian Rift maximum shear wave velocities (~4.3 km/s) suggest a lithospheric thickness of 50 km (Dugda et al., 2007) similar to the Owens Valley. The adjacent the Ethiopian plateau, a topographic high ~2500m ASL has a similarly thin lithosphere estimated ~70 – 80 km (Dugda et al., 2007). The unusually thin lithosphere beneath the Owens Valley and EAR has been predominantly explained by the foundering slab or lithospheric drip hypothesis (Boyd et al., 2004; Ducea & Saleeby, 1998; Dugda et al., 2007; Jones et al., 2004; Jones et al., 1994; Lee et

al., 2000), although there is some debate regarding the Owens Valley. Here, metasomatically altered SCLM becomes gravitationally unstable and delaminates into the less dense asthenosphere. In the case of the Owens Valley this process is generally attributed to the foundering of the subducted Farallon slab either through delamination (e.g.: Ducea & Saleeby, 1998), or from a progressive NE – SW slab roll back (e.g.: Dickinson, 2006). In the case of EAR a more complex process is evoked whereby interaction between a rheologically weak, metasomatized cratonic root and the Afar plume accelerates the process of lithosphere erosion causing large scale "drips" (Furman et al., 2016). Despite these differences in the mechanisms of lithospheric thinning, similarities can be observed in the effect on the mantle. The EAR for example, during lithospheric drip, if the descending SCLM falls slowly it will conductively heat in the asthenosphere and only produce melting in the presence of wet peridotite. If it descends quickly there is no conductive heating, but the pressure increase causes devolatilization that can induce flux melting of the surrounding mantle (Elkins-Tanton, 2007). This behavior is similar to a subducting slab resulting in a fluid metasomatized mantle similar to documented observations from the Owens Valley from this study and others (Gazel et al., 2012).

5.6 Conclusions

The Papoose Canyon clinopyroxenes and orthopyroxenes record equilibration pressures of 0.85 ±0.38 GPa at an average temperature of 1081° C ±58°. This corresponds to a depth of ~25 – 39 km which is interpreted to encompass the Moho based on receiver function analysis (Frassetto et al., 2011). These results broadly correspond to other studies and thermobarometery models for the BPVF but differ for the Papoose Canyon specifically. The disparity for the Papoose Canyon may

represent the initial magma storage chamber prior to transit, storage, and recharge through a more complex mid-crustal magma system.

Trace element systematics show evidence for crustal contamination, particularly in the case of LILE. Additionally, low concentration Os and highly radiogenic $^{187}Os/^{188}Os$ is usually an indicator of contamination and in this case cannot be entirely ruled out as there is sufficient evidence to suggest $^{187}Os/^{188}Os$ has been affected by crustal assimilation. However, there is still sufficient evidence from HFSE and HSE to suggest source signature information is still intact. Here, HFSE anomalies, variably fractionated HSE, and low absolute and relative Pd are indicative of a subduction modified mantle source. New HSE data from the Papoose Canyon presented here can delineate between source characteristics and post emplacement contamination. Absolute and relative HSE abundances have features that are consistent with both source characteristics and mineral accumulation. Papoose Canyon cumulate xenoliths have $fO_2 > +2$ ΔFMQ which is consistent with a back-arc environment. This characteristic of the mantle source that has likely had a significant impact on absolute and relative HSE abundances and is not the result of contamination from continental crust.

Geophysical and thermobarometery models show the Owens Valley lithosphere is ~50 – 60 km thick. Shear wave velocities and clinopyroxene and olivine crystallization pressures suggest volcanism in the BPVF and Coso volcanic field are fed from magma chambers from the Moho to mid-crustal depths. These magma chambers appear to in geographical orientation with mapped faults suggesting that magma transit follows the direction of maximum principal strain to the north. The Walker Lane and Owens Valley is the northern propagation of the Gulf of California rift system, in a similar fashion as the EAR is the southern propagation of the Red Sea – Gulf of Aden rift system. Both propagating rift systems have thinning continental lithosphere albeit from

different mechanisms. Fluid metasomatized mantle is a common source feature of volcanics for both systems and based on regional differences in the EAR, degrees of crustal contamination may be largely dependent on lithospheric thickness.

5.7 Acknowledgments

Chapter 5 in part is currently being prepared for submission for publication of the material. Oller, Brian; Day, James M.D; Driscoll, Neal W. The dissertation author was the primary researcher and author of this material.

CHAPTER 6 CONCLUSIONS

This dissertation has presented new geochemical and Os-isotopic data to examine questions of mantle evolution, mixing of mantle source domains in two ocean island chains, and the magma source of an emerging continental rift system.

Chapter 2 establishes through HSE and Re-Os isotope systematics that spinel lherzolites dredged from the Ferrel Seamount sample an abandoned section of the Pacific-Cocos spreading ridge. This section of lithosphere experienced at least one ancient melt depletion event followed by at least two episodes of melt refertilization. A tectonic process termed "ridge jump" isolated this fragment of oceanic lithosphere from subduction when rifting transitioned east to the Mexican continent and formed the Gulf of California. Once isolated and preserved from subduction this fragment began experiencing ongoing low degree alkali melt refertilization that imparts incompatible major and trace element signatures similar to non-cratonic CLM observed in the western United States. These observations provide the basis for a new model explaining the evolution of oceanic lithosphere to non-cratonic CLM whereby an oceanic microplate is welded to the continental margin during "ridge jump." This differs from existing models that involve stacking, rafting, or imbrication in an active continental-oceanic subduction zone.

Chapter 3 examines the isotopically distinct Loa and Kea trends from the perspective of absolute and relative HSE abundances and $^{187}Os/^{188}Os$ and evaluates the potential for magma mixing between these two trends based on recently published geophysical evidence and new $^{187}Os/^{188}Os$ presented here. The new data shown in this this chapter suggests magma from Mauna Loa could have direct interaction with Kilauea magma either through a shared crustal magma chamber or through a plumbing system connecting the two chambers. Evidence is also shown suggesting Hualālai may incorporate 10 to 20% of a Mauna Kea component and edifice

contamination may be prevalent in both trends. Despite the evidence for mixing between the Loa and Kea trends and potential for contamination from the volcanic edifices the distinct Os isotopic signature unique to each trend is nonetheless preserved.

Chapter 4 is an analysis of Canary Islands mantle and ultramafic xenoliths and lavas. Spinel facies lherzolites and harzburgites studied in this chapter show up to 18% melt removal and evidence of low degree melt refertilization comes from HFSE fractionation and LREE enrichments. These samples also show non-radiogenic $^{187}Os/^{188}Os$ with corresponding ancient T_{RD} model ages which are indicative of Atlantic lithosphere, which shows clear evidence of hotspot modification. Highly siderophile element compositions of Canary lavas can be explained by ~11% fractionation of olivine, Cr-spinel, and sulfide from parental melt estimates. These compositions suggest many of the island likely originate from unique parental source melts with eastern islands sampling an EM2 endmember and the western islands sampling a HIMU endmember. Applying mixing models to explain $^{187}Os/^{188}Os$ for Canary lavas indicates ~3% assimilation of lithospheric material and the effects of crustal contamination appear to be negligible.

Chapter 5 discusses the magma source and the degree and effects of crustal contamination of the Papoose Canyon volcanic sequence, part of the Pleistocene Big Pine Volcanic Field in the Owens Valley, California, USA. Clinopyroxenes and orthopyroxenes record equilibration pressures that correspond to a depth of ~25 to 39 km, a range which spans the mid crust to the Moho. Incompatible trace element systematics, low Os, and highly radiogenic $^{187}Os/^{188}Os$ are indicative of crustal contamination and this is supported by magma equilibration and storage at lower to mid crustal depths. Yet, there is still sufficient evidence provided from absolute and relative HSE abundances the information about the source composition remains intact. Papoose Canyon olivines are highly oxidized (+2 ΔFMQ) which is consistent with other back-arc basins

and consistent with the subduction history of the Owens Valley during the Mesozoic. Comparisons between the Owens Valley and the East African Rift suggest that the degree of crustal contamination in both continental rift systems is largely a function of lithospheric thickness, and a fluid metasomatized mantle is a common source feature of both systems.

REFERENCES

Abouchami, W., Hofmann, A., Galer, S., Frey, F., Eisele, J., & Feigenson, M. (2005). Lead isotopes reveal bilateral asymmetry and vertical continuity in the Hawaiian mantle plume. *Nature*, *434*(7035), 851-856. https://doi.org/https://doi.org/10.1038/nature03402

Abratis, M., Schmincke, H.-U., & Hansteen, T. (2002). Composition and evolution of submarine volcanic rocks from the central and western Canary Islands. *International Journal of Earth Sciences*, *91*, 562-582. https://doi.org/https://doi.org/10.1007/s00531-002-0286-7

Alard, O., Griffin, W. L., Lorand, J. P., Jackson, S. E., & O'Reilly, S. Y. (2000). Non-chondritic distribution of the highly siderophile elements in mantle sulphides. *Nature*, *407*(6806), 891-894. https://doi.org/10.1038/35038049

Albarède, F. (1995). *Introduction to Geochemical Modeling*. Cambridge: Cambridge University Press. doi:10.1017/CBO9780511622960

Anderson, A. (1976). Magma mixing: petrological process and volcanological tool. *Journal of volcanology and geothermal research*, *1*(1), 3-33. https://doi.org/https://doi.org/10.1016/0377-0273(76)90016-0

Aparicio, A., Tassinari, C. C., García, R., & Araña, V. (2010). Sr and Nd isotope composition of the metamorphic, sedimentary and ultramafic xenoliths of Lanzarote (Canary Islands): Implications for magma sources. *Journal of volcanology and geothermal research*, *189*(1-2), 143-150. https://doi.org/https://doi.org/10.1016/j.jvolgeores.2009.10.017

Armytage, R. M. G., Brandon, A. D., Peslier, A. H., & Lapen, T. J. (2014). Osmium isotope evidence for Early to Middle Proterozoic mantle lithosphere stabilization and concomitant production of juvenile crust in Dish Hill, CA peridotite xenoliths. *Geochimica et Cosmochimica Acta*, *137*, 113–133. http://doi.org/10.1016/j.gca.2014.04.017

Artemieva, I. M. (2009). The continental lithosphere: Reconciling thermal, seismic, and petrologic data. *Lithos*, *109*(1-2), 23–46. http://doi.org/10.1016/j.lithos.2008.09.015

Aulinas, M., Gimeno, D., Fernandez-Turiel, J., Font, L., Perez-Torrado, F. J., Rodriguez-Gonzalez, A., & Nowell, G. (2010). Small-scale mantle heterogeneity on the source of the Gran Canaria (Canary Islands) Pliocene–Quaternary magmas. *Lithos*, *119*(3-4), 377-392. https://doi.org/https://doi.org/10.1016/j.lithos.2010.07.016

Atwater, T. (1970). Implications of Plate Tectonics for the Cenozoic Tectonic Evolution of Western North America. *Geological Society of America Bulletin*, *81*(12), 3513. http://doi.org/10.1130/0016-7606(1970)81[3513:IOPTFT]2.0.CO;2

Baker, J. A., & Jensen, K. K. (2004). Coupled 186Os–187Os enrichments in the Earth's mantle–core–mantle interaction or recycling of ferromanganese crusts and nodules? *Earth and Planetary Science Letters*, *220*(3-4), 277-286. https://doi.org/https://doi.org/10.1016/S0012-821X(04)00059-7

Ballhaus, C., Bockrath, C., Wohlgemuth-Ueberwasser, C., Laurenz, V., & Berndt, J. (2006). Fractionation of the noble metals by physical processes. *Contributions to Mineralogy and Petrology*, *152*(6), 667-684. https://doi.org/10.1007/s00410-006-0126-z

Barnes, S.-J., Naldrett, A., & Gorton, M. (1985). The origin of the fractionation of platinum-group elements in terrestrial magmas. *Chemical Geology*, *53*(3-4), 303-323. https://doi.org/https://doi.org/10.1016/0009-2541(85)90076-2

Batiza, R. (1977). Petrology and chemistry of Guadalupe Island: An alkalic seamount on a fossil ridge crest. *Geology*, *5*, 760–764.

Beard, B. L., & Glazner, A. F. (1995). Trace element and Sr and Nd isotopic composition of mantle xenoliths from the Big Pine volcanic field, California. *Journal of Geophysical Research: Solid Earth*, *100*(B3), 4169-4179. https://doi.org/https://doi.org/10.1029/94JB02883

Becker, H., Horan, M., Walker, R., Gao, S., Lorand, J.-P., & Rudnick, R. (2006). Highly siderophile element composition of the Earth's primitive upper mantle: constraints from new data on peridotite massifs and xenoliths. *Geochimica et Cosmochimica Acta*, *70*(17), 4528-4550. https://doi.org/https://doi.org/10.1016/j.gca.2006.06.004

Bénard, A., Klimm, K., Woodland, A. B., Arculus, R. J., Wilke, M., Botcharnikov, R. E., Shimizu, N., Nebel, O., Rivard, C., & Ionov, D. A. (2018). Oxidising agents in sub-arc mantle melts link slab devolatilisation and arc magmas. *Nature communications*, *9*(1). https://doi.org/10.1038/s41467-018-05804-2

Bennett, V., Esat, T., & Norman, M. (1996). Two mantle-plume components in Hawaiian picrites inferred from correlated Os–Pb isotopes. *Nature*, *381*(6579), 221-224.

Bierman, P., Gillespie, A., Whipple, K., & Clark, D. (1991). Quaternary geomorphology and geochronology of Owens Valley, California: Geological Society of America field trip. Geological excursions in southern California and Mexico: guidebook for the 1991 annual meeting. Geological Society of America, San Diego

Birck, J. L., Barman, M. R., & Campas, F. (1997). Re-Os isotopic measurements at the femtomole level in natural samples. *Geostandards newsletter, 21(1)*, 19-27.

Bizimis, M., Griselin, M., Lassiter, J. C., Salters, V. J., & Sen, G. (2007). Ancient recycled mantle lithosphere in the Hawaiian plume: osmium–hafnium isotopic evidence from

peridotite mantle xenoliths. *Earth and Planetary Science Letters*, *257*(1-2), 259-273. https://doi.org/https://doi.org/10.1016/j.epsl.2007.02.036

Blondes, M. S., Brandon, M. T., Reiners, P. W., Page, F. Z., & Kita, N. T. (2012). Generation of forsteritic olivine (Fo99· 8) by subsolidus oxidation in basaltic flows. *Journal of Petrology*, *53*(5), 971-984. https://doi.org/https://doi.org/10.1093/petrology/egs006

Blondes, M. S., Reiners, P. W., Ducea, M. N., Singer, B. S., & Chesley, J. (2008). Temporal–compositional trends over short and long time-scales in basalts of the Big Pine Volcanic Field, California. *Earth and Planetary Science Letters*, *269*(1-2), 140-154. https://doi.org/https://doi.org/10.1016/j.epsl.2008.02.012

Blusztajn, J. S., Hart, S. R., Ravizza, G., & Dick, H. J. B. (2000). Platinum-group elements and Os isotopic characteristics of the lower oceanic crust. *Chemical Geology*, *168*(1-2), 113-122.

Boyd, F. R. (1989). Compositional distinction between oceanic and cratonic lithosphere. *Earth and Planetary Science Letters*, *96*(1-2), 15–26. http://doi.org/10.1016/0012821X(89)90120-9

Boyd, F. R., & Mertzman, S. A. (1987). Composition and structure of the Kaapvaal lithosphere, southern Africa. *Magmatic Processes: Physicochemical Principles, The Geochemical Society, Special Publication No. I*, 3-12.

Boyd, O. S., Jones, C. H., & Sheehan, A. F. (2004). Foundering lithosphere imaged beneath the southern Sierra Nevada, California, USA. *Science*, *305*(5684), 660-662. https://doi.org/DOI: 10.1126/science.1099181

Brey, G. P., & Köhler, T. (1990). Geothermobarometry in Four-phase Lherzolites II. New Thermobarometers, and Practical Assessment of Existing Thermobarometers. Journal of Petrology, 31(6), 1353–1378

Brandon, A. D., Snow, J. E., Walker, R. J., Morgan, J. W., & Mock, T. D. (2000). 190Pt–186Os and 187Re–187Os systematics of abyssal peridotites. *Earth and Planetary Science Letters*, *177*(3-4), 319-335. https://doi.org/https://doi.org/10.1016/S0012-821X(00)00044-3

Brandon, A. D., Norman, M. D., Walker, R. J., & Morgan, J. W. (1999). ^{186}Os ^{187}Os systematics of Hawaiian picrites. *Earth and Planetary Science Letters*, *174*, 25-42.

Brandon, A. D., Walker, R. J., Morgan, J. W., Norman, M. D., & Prichard, H. M. (1998). Coupled 186Os and 187Os Evidence for Core-Mantle Interaction. *Science, 280*.

Bryce, J. G., DePaolo, D. J., & Lassiter, J. C. (2005). Geochemical structure of the Hawaiian plume: Sr, Nd, and Os isotopes in the 2.8 km HSDP-2 section of Mauna Kea volcano. *Geochemistry, Geophysics, Geosystems*, *6*(9).

Burton, K. W., Bourdon, B., Birck, J.-L., Allègre, C. J., & Hein, J. R. (1999). Osmium isotope variations in the oceans recorded by FeMn crusts. *Earth and Planetary Science Letters*, *171*(1), 185-197. https://doi.org/https://doi.org/10.1016/S0012-821X(99)00139-9

Busby, C. J. (2013). Birth of a plate boundary at ca. 12 Ma in the Ancestral Cascades arc, Walker Lane belt of California and Nevada. *Geosphere*, *9*(5), 1147-1160. https://doi.org/https://doi.org/10.1130/GES00928.1

Busby, C. J. (2011). Extensional and transtensional continental arc basins: Case studies from the southwestern United States. *Tectonics of sedimentary basins: Recent advances*, 382-404. https://doi.org/https://doi.org/10.1002/9781444347166.ch19

Byerly, B. L., & Lassiter, J. C. (2012). Evidence from mantle xenoliths for lithosphere removal beneath the central Rio Grande Rift. *Earth and Planetary Science Letters*, *355-356*, 82–93. http://doi.org/10.1016/j.epsl.2012.08.034

Canil, D., & Wei, K. (1992). Constraints on the origin of mantle-derived low Ca garnets. *Contributions to Mineralogy and Petrology*, *109*(4), 421–430. http://doi.org/10.1007/BF00306546

Canil, D. (2004). Mildly incompatible elements in peridotites and the origins of mantle lithosphere. *Lithos*, *77*(1-4), 375–393. http://doi.org/10.1016/j.lithos.2004.04.014

Carlson, R. W., Pearson, D. G., & James, D. E. (2005). Physical, chemical, and chronological characteristics of continental mantle. *Reviews of Geophysics*, *43*(1). https://doi.org/10.1029/2004rg000156

Carlson, R. W., Lugmair, G. W., & Macdougall, J. D. (1981). Crustal influence in the generation of continental flood basalts. *Nature*, *289*(5794), 160-162. https://doi.org/10.1038/289160a0

Carracedo, J. C., Badiola, E. R., Guillou, H., de La Nuez, J., & Torrado, F. P. (2001). Geology and volcanology of la Palma and el Hierro, western Canaries. *Estudios Geologicos-Madrid*, *57*, 175-273. https://doi.org/hal-03323419

Carracedo, J. C., Day, S., Guillou, H., Badiola, E. R., Cañas, J. A., & Torrado, F. P. (1998). Hotspot volcanism close to a passive continental margin: the Canary Islands. *Geological magazine*, *135*(5), 591-604. https://doi.org/https://doi.org/10.1017/S0016756898001447

Carracedo, J. C., Torrado, F. J. P., Ancochea, E., Meco, J., Hernán, F., Cubas, C. R., Casillas, R., Badiola, E. R., & Ahijado, A. (2002). Cenozoic volcanism II: the Canary islands. https://doi.org/https://doi.org/10.1144/GOSPP.18

Castillo, P. R. (2015). The recycling of marine carbonates and sources of HIMU and FOZO ocean island basalts. *Lithos*, *216*, 254-263.

Castillo, P. R., Clague, D. A., Davis, A. S., & Lonsdale, P. F. (2010). Petrogenesis of Davidson Seamount lavas and its implications for fossil spreading center and intraplate magmatism in the eastern Pacific. *Geochemistry*, *11*(2), http://doi.org/10.1029/2009GC002992

Chauvel, C., Maury, R. C., Blais, S., Lewin, E., Guillou, H., Guille, G., Rossi, P., & Gutscher, M.-A. (2012). The size of plume heterogeneities constrained by Marquesas isotopic stripes. *Geochemistry, Geophysics, Geosystems*, *13*(7), https://doi.org/10.1029/2012gc004123

Clague, D. A., & Dalrymple, G. B. (1987). The Hawaiian-emperor volcanic chain. *US Geol. Surv. Prof. Pap*, *1350*, 5-54.

Cousens, B. L., Spera, F. J., & Dobson, P. F. (1993). Post-eruptive alteration of silicic ignimbrites and lavas, Gran Canaria, Canary Islands: Strontium, neodymium, lead, and oxygen isotopic evidence. *Geochimica et Cosmochimica Acta*, *57*(3), 631-640. https://doi.org/https://doi.org/10.1016/0016-7037(93)90374-6

Cousens, B. L., Spera, F. J., & Tilton, G. R. (1990). Isotopic patterns in silicic ignimbrites and lava flows of the Mogan and lower Fataga Formations, Gran Canaria, Canary Islands: temporal changes in mantle source composition. *Earth and Planetary Science Letters*, *96*(3-4), 319-335. https://doi.org/https://doi.org/10.1016/0012-821X(90)90010-U

Cox, K. G. (1980). A Model for Flood Basalt Vulcanism. *Journal of Petrology*, *21*(4), 629-650. https://doi.org/10.1093/petrology/21.4.629

Creaser, R. A., Papanastassiou, D. A., & Wasserburg, G. J. (1991). Negative thermal ion mass spectrometry of osmium, rhenium and iridium. *Geochimica Et Cosmochimica Acta*, *55(1)*, 397-401

Davis, A. S., Clague, D. A., Bohrson, W. A., Dalrymple, G. B., & Greene, H. G. (2002). Seamounts at the continental margin of California: A different kind of oceanic intraplate volcanism. *GSA Bulletin*, *114*(3), 316–333.

Day, J. M. D., Troll, V. R., Aulinas, M., Deegan, F. M., Geiger, H., Carracedo, J. C., Pinto, G. G., & Perez-Torrado, F. J. (2022). Mantle source characteristics and magmatic processes during the 2021 La Palma eruption. *Earth and Planetary Science Letters*, *597*. https://doi.org/10.1016/j.epsl.2022.117793

Day, J. M. D., Walker, R. J., & Warren, J. M. (2017). ^{186}Os–^{187}Os and highly siderophile element abundance systematics of the mantle revealed by abyssal peridotites and Os-rich alloys. *Geochimica et Cosmochimica Acta*, *200*, 232–254. http://doi.org/10.1016/j.gca.2016.12.013

Day, J. M. (2016). Evidence against an ancient non-chondritic mantle source for North Atlantic Igneous Province lavas. *Chemical Geology*, *440*, 91-100.

https://doi.org/https://doi.org/10.1016/j.chemgeo.2016.07.002

Day, J. M. D., Waters, C. L., Schaefer, B. F., Walker, R. J., & Turner, S. (2016). Use of Hydrofluoric Acid Desilicification in the Determination of Highly Siderophile Element Abundances and Re-Pt-Os Isotope Systematics in Mafic-Ultramafic Rocks. Geostandards and Geoanalytical Research, 40, 49–65.

Day, J. M. D., Peters, B. J., & Janney, P. E. (2014). Oxygen isotope systematics of South African olivine melilitites and implications for HIMU mantle reservoirs. Lithos, 202-203, 76–84.

Day, J. M. D. (2013). Hotspot volcanism and highly siderophile elements. *Chemical Geology*, *341*, 50-74. https://doi.org/10.1016/j.chemgeo.2012.12.010

Day, J. M. D., Pearson, D. G., Macpherson, C. G., Lowry, D., & Carracedo, J. C. (2010). Evidence for distinct proportions of subducted oceanic crust and lithosphere in HIMU-type mantle beneath El Hierro and La Palma, Canary Islands. *Geochimica et Cosmochimica Acta*, *74*(22), 6565-6589. https://doi.org/10.1016/j.gca.2010.08.021

Day, J. M. D., Pearson, D. G., Macpherson, C. G., Lowry, D., & Carracedo, J.-C. (2009). Pyroxenite-rich mantle formed by recycled oceanic lithosphere: Oxygen-osmium isotope evidence from Canary Island lavas. *Geology*, *37*(6), 555-558. https://doi.org/10.1130/g25613a.1

Day, J., Walker, R., Hilton, D., Carracedo, J.-C., & Hanski, E. (2008). Constraining deep mantle contributions to Canary Island lavas. *Geochimica et Cosmochimica Acta*. https://doi.org/10.1016/j.gca.2008.05.007

Deegan, F. M., Troll, V. R., Barker, A., Harris, C., Chadwick, J., Carracedo, J. C., & Delcamp, A. (2012). Crustal versus source processes recorded in dykes from the Northeast volcanic rift zone of Tenerife, Canary Islands. *Chemical Geology*, *334*, 324-344. https://doi.org/https://doi.org/10.1016/j.chemgeo.2012.10.013

Demény, A., Vennemann, T., Hegner, E., Ahijado, A., Casillas, R., Nagy, G., Homonnay, Z., Gutierrez, M., & Szabó, C. (2004). H, O, Sr, Nd, and Pb isotopic evidence for recycled oceanic crust in the Transitional Volcanic Group of Fuerteventura, Canary Islands, Spain. *Chemical Geology*, *205*(1-2), 37-54.

D'Errico, M. E., Warren, J. M., & Godard, M. (2016). Evidence for chemically heterogeneous Arctic mantle beneath the Gakkel Ridge. *Geochimica et Cosmochimica Acta*, *174*, 291–312. http://doi.org/10.1016/j.gca.2015.11.017

Dickinson, W. R. (2006). Geotectonic evolution of the Great Basin. *Geosphere*, *2*(7), 353. https://doi.org/10.1130/ges00054.1

Dougherty, S. L., Jiang, C., Clayton, R. W., Schmandt, B., & Hansen, S. M. (2021). Seismic evidence for a fossil slab origin for the Isabella anomaly. *Geophysical Journal International*, *224*(2), 1188-1196. https://doi.org/https://doi.org/10.1093/gji/ggaa472

Ducea, M., & Saleeby, J. (1998). A case for delamination of the deep batholithic crust beneath the Sierra Nevada, California. *International Geology Review*, *40*(1), 78-93. https://doi.org/https://doi.org/10.1080/00206819809465199

Ducea, M. N., & Saleeby, J. B. (1996). Buoyancy sources for a large, unrooted mountain range, the Sierra Nevada, California: Evidence from xenolith thermobarometry. *Journal of Geophysical Research: Solid Earth*, *101*(B4), 8229-8244. https://doi.org/10.1029/95jb03452

Dugda, M. T., Nyblade, A. A., & Julia, J. (2007). Thin Lithosphere Beneath the Ethiopian Plateau Revealed by a Joint Inversion of Rayleigh Wave Group Velocities and Receiver Functions. *Journal of Geophysical Research: Solid Earth*, *112*(B8). https://doi.org/10.1029/2006jb004918

Elkins-Tanton, L. T. (2007). Continental magmatism, volatile recycling, and a heterogeneous mantle caused by lithospheric gravitational instabilities. *Journal of Geophysical Research: Solid Earth*, *112*(B3). https://doi.org/10.1029/2005jb004072

Faulds, J. E., Henry, C. D., Spencer, J., & Titley, S. (2008). Tectonic influences on the spatial and temporal evolution of the Walker Lane: An incipient transform fault along the evolving Pacific–North American plate boundary. *Ores and orogenesis: Circum-Pacific tectonics, geologic evolution, and ore deposits: Arizona Geological Society Digest*, *22*, 437-470.

Fodor, R. V., & Vandermeyden, H. J. (1988). Petrology of gabbroic xenoliths from Mauna Kea Volcano, Hawai'i. *Journal of Geophysical Research: Solid Earth*, *93*(B5), 4435-4452. https://doi.org/10.1029/JB093iB05p04435

Foley, S. F., Prelevic, D., Rehfeldt, T., & Jacob, D. E. (2013). Minor and trace elements in olivines as probes into early igneous and mantle melting processes. *Earth and Planetary Science Letters*, *363*, 181-191. https://doi.org/https://doi.org/10.1016/j.epsl.2012.11.025

Frassetto, A. M., Zandt, G., Gilbert, H., Owens, T. J., & Jones, C. H. (2011). Structure of the Sierra Nevada from receiver functions and implications for lithospheric foundering. *Geosphere*, *7*(4), 898-921. https://doi.org/10.1130/ges00570.1

French, S. W., & Romanowicz, B. (2015). Broad plumes rooted at the base of the Earth's mantle beneath major hotspots. *Nature*, *525*(7567), 95-99. https://doi.org/10.1038/nature14876

Frey, F. A., Huang, S., Xu, G., & Jochum, K. P. (2016). The geochemical components that distinguish Loa- and Kea-trend Hawaiian shield lavas. *Geochimica et Cosmochimica Acta*, *185*, 160-181. https://doi.org/10.1016/j.gca.2016.04.010

Frey, F. A., & Prinz, M. (1978). Ultramafic inclusions from San Carlos, Arizona: petrologic and geochemical data bearing on their petrogenesis. *Earth and Planetary Science Letters, 38(1),* 129-176

Frey, F. A., & Green, D. H. (1974). The minerology, geochemistry and origin of lherzolite inclusions in Victorian bassanites. *Geochimica et Cosmochimica Acta, 38(7),* 1023-1059

Fleet, M. E., Crocket, J. H., Liu, M., & Stone, W. E. (1999). Laboratory partitioning of platinum-group elements (PGE) and gold with application to magmatic sulfide–PGE deposits. *Lithos*, *47*(1-2), 127–142. http://doi.org/10.1016/S0024-4937(99)00011-0

Furman, T., Nelson, W. R., & Elkins-Tanton, L. T. (2016). Evolution of the East African rift: Drip magmatism, lithospheric thinning and mafic volcanism. *Geochimica et Cosmochimica Acta*, *185*, 418-434.

Furman, T. (2007). Geochemistry of East African Rift basalts: an overview. *Journal of African Earth Sciences*, *48*(2-3), 147-160. https://doi.org/https://doi.org/10.1016/j.jafrearsci.2006.06.009

Gaffney, A. M. (2002). Environments of Crystallization and Compositional Diversity of Mauna Loa Xenoliths. *Journal of Petrology*, *43*(6), 963-980. https://doi.org/https://doi.org/10.1093/petrology/43.6.963

Galer, S., & O'Nions, R. K. (1989). Chemical and isotopic studies of ultramafic inclusions from the San Carlos Volcanic Field, Arizona: a bearing on their petrogenesis. *Journal of Petrology*, *30*(4), 1033–1064. http://doi.org/10.1093/petrology/30.4.1033

Gannoun, A., Burton, K. W., Day, J. M. D., Harvey, J., Schiano, P., & Parkinson, I. (2016). Highly Siderophile Element and Os Isotope Systematics of Volcanic Rocks at Divergent and Convergent Plate Boundaries and in Intraplate Settings. *Reviews in Mineralogy and Geochemistry*, *81*(1), 651-724. https://doi.org/10.2138/rmg.2016.81.11

Gao, R., Lassiter, J. C., Clague, D. A., & Bohrson, W. A. (2022). Evolution of Hawaiian Volcano Magmatic Plumbing System and Implications for Melt/Edifice and Melt/Lithosphere Interaction: Constraints from Hualālai Xenoliths. *Journal of Petrology*, *63*(9). https://doi.org/10.1093/petrology/egac091

Gao, R., Lassiter, J. C., & Ramirez, G. (2017). Origin of temporal compositional trends in monogenetic vent eruptions: Insights from the crystal cargo in the Papoose Canyon sequence, Big Pine Volcanic Field, CA. *Earth and Planetary Science Letters*, *457*, 227-237. https://doi.org/https://doi.org/10.1016/j.epsl.2016.10.013

Gao, R., Lassiter, J. C., Barnes, J. D., Clague, D. A., & Bohrson, W. A. (2016). Geochemical investigation of Gabbroic Xenoliths from Hualalai Volcano: Implications for lower oceanic crust accretion and Hualalai Volcano magma storage system. *Earth and*

Planetary Science Letters, *442*, 162-172. https://doi.org/10.1016/j.epsl.2016.02.043

Gazel, E., Plank, T. A., Forsyth, D. W., Bendersky, C., Lee, C.-T. A., & Hauri, E. H. (2012). Lithosphere versus asthenosphere mantle sources at the Big Pine Volcanic Field, California. *Geochemistry, Geophysics, Geosystems*. https://doi.org/https://doi.org/10.7916/D8VX0S86

Gillespie, A. R., Huneke, J. C., & Wasserburg, G. J. (1984). Eruption age of a ~100,000-year-old basalt from ^{40}Ar-^{39}Ar analysis of partially degassed xenoliths. *Journal of Geophysical Research: Solid Earth*, *89*(B2), 1033-1048. https://doi.org/10.1029/jb089ib02p01033

Griffin, W. L., OReilly, S. Y., Ryan, C. G., Gaul, O., & Ionov, D. A. (1998). Secular variation in the composition of subcontinental lithospheric mantle: Geophysical and geodynamic implications. *Geodynamics*, 1–26.

Grocke, S. B., Cottrell, E., de Silva, S., & Kelley, K. A. (2016). The role of crustal and eruptive processes versus source variations in controlling the oxidation state of iron in Central Andean magmas. *Earth and Planetary Science Letters*, *440*, 92-104. https://doi.org/https://doi.org/10.1016/j.epsl.2016.01.026

Gurenko, A., Hoernle, K., Hauff, F., Schmincke, H.-U., Han, D., Miura, Y., & Kaneoka, I. (2006). Major, trace element and Nd–Sr–Pb–O–He–Ar isotope signatures of shield stage lavas from the central and western Canary Islands: insights into mantle and crustal processes. *Chemical Geology*, *233*(1-2), 75-112. https://doi.org/https://doi.org/10.1016/j.chemgeo.2006.02.016

Halliday, A. N., Lee, D.-C., Tommasini, S., Davies, G. R., Paslick, C. R., Fitton, J. G., & James, D. E. (1995). Incompatible trace elements in OIB and MORB and source enrichment in the sub-oceanic mantle. *Earth and Planetary Science Letters*, *133*(3-4), 379-395. https://doi.org/https://doi.org/10.1016/0012-821X(95)00097-V

Harpp, K. S., & Weis, D. (2020). Insights into the origins and compositions of mantle plumes: A comparison of Galápagos and Hawai'i. *Geochemistry, Geophysics, Geosystems*, *21*(9), e2019GC008887. https://doi.org/ https://doi.org/10.1029/2019GC008887

Hart, S. R., & Dunn, T. (1993). Experimental cpx/melt partitioning of 24 trace elements. *Contributions to Mineralogy and Petrology*, *113*(1), 1-8. https://doi.org/https://doi.org/10.1007/BF00320827

Harvey, J., Gannoun, A., Burton, K. W., Rogers, N. W., Alard, O., & Parkinson, I. J. (2006). Ancient melt extraction from the oceanic upper mantle revealed by Re–Os isotopes in abyssal peridotites from the Mid-Atlantic ridge. *Earth and Planetary Science Letters*, *244*(3-4), 606-621. https://doi.org/https://doi.org/10.1016/j.epsl.2006.02.031

Harvey, J., Yoshikawa, M., Hammond, S. J., & Burton, K. W. (2012). Deciphering the trace element characteristics in Kilbourne Hole peridotite xenoliths: melt–rock interaction and

metasomatism beneath the Rio Grande Rift, SW USA. *Journal of Petrology*, *53*(8), 1709-1742. https://doi.org/https://doi.org/10.1093/petrology/egs030

Hauri, E. H., Lassiter, J. C., & DePaolo, D. J. (1996). Osmium isotope systematics of drilled lavas from Mauna Loa, Hawai'i. *Journal of Geophysical Research: Solid Earth*, *101*(B5), 11793-11806.

Helffrich, G. R., & Wood, B. J. (2001). The Earth's mantle. *Nature*, *412*(6846), 501-507. https://doi.org/10.1038/35087500

Hellebrand, E., Snow, J. E., Hoppe, P., & Hofmann, A. W. (2002). Garnet-field melting and late-stage refertilization in 'residual'abyssal peridotites from the Central Indian Ridge. *Journal of Petrology*, *43*(12), 2305-2338. https://doi.org/https://doi.org/10.1093/petrology/43.12.2305

Hellebrand, E., Snow, J. E., Dick, H. J. B., & Hofmann, A. W. (2001). Coupled major and trace elements as indicators of the extent of melting in mid-ocean-ridge peridotites. *Nature*, *410*(6829), 677–681. http://doi.org/10.1038/35070546

Hendrie, D., Kusznir, N., Morley, C., & Ebinger, C. (1994). Cenozoic extension in northern Kenya: a quantitative model of rift basin development in the Turkana region. *Tectonophysics*, *236*(1-4), 409-438. https://doi.org/https://doi.org/10.1016/0040-1951(94)90187-2

Herzberg, C., & Rudnick, R. (2012). Formation of cratonic lithosphere: An integrated thermal and petrological model. *Lithos*, *149*, 4-15. https://doi.org/https://doi.org/10.1016/j.lithos.2012.01.010

Herzberg, C. (2004). Geodynamic Information in Peridotite Petrology. *Journal of Petrology*, *45*(12), 2507–2530. http://doi.org/10.1093/petrology/egh039

Hilton, D., Macpherson, C., & Elliott, T. (2000). Helium isotope ratios in mafic phenocrysts and geothermal fluids from La Palma, the Canary Islands (Spain): implications for HIMU mantle sources. *Geochimica et Cosmochimica Acta*, *64*(12), 2119-2132. https://doi.org/https://doi.org/10.1016/S0016-7037(00)00358-6

Hoernle, K. (1998). Geochemistry of Jurassic oceanic crust beneath Gran Canaria (Canary Islands): implications for crustal recycling and assimilation. *Journal of Petrology*, *39*(5), 859-880. https://doi.org/https://doi.org/10.1093/petroj/39.5.859

Hoernle, K., & Schmincke, H.-U. (1993). The role of partial melting in the 15-Ma geochemical evolution of Gran Canaria: a blob model for the Canary hotspot. *Journal of Petrology*, *34*(3), 599-626. https://doi.org/https://doi.org/10.1093/petrology/34.3.599

Hoernle, K., & Tilton, G. (1991). Sr-Nd-Pb isotope data for Fuerteventura (Canary Islands) basal complex and subaerial volcanics: applications to magma genesis and evolution.

Schweizerische Mineralogische und Petrographische Mitteilungen, *71*, 5-21. https://doi.org/10.5169/seals-54342

Hoernle, K., Tilton, G., & Schmincke, H.-U. (1991). SrNdPb isotopic evolution of Gran Canaria: evidence for shallow enriched mantle beneath the Canary Islands. *Earth and Planetary Science Letters*, *106*(1-4), 44-63. https://doi.org/https://doi.org/10.1016/0012-821X(91)90062-M

Hofmann, A. W. (1997). Mantle Geochemistry: The Message from Oceanic Volcanism. *Nature*, *385*, 219-229.

Hofmann, A. W. (1988). Chemical differentiation of the Earth: the relationship between mantle, continental crust, and oceanic crust. *Earth and Planetary Science Letters*, *90*(3), 297-314. https://doi.org/https://doi.org/10.1016/0012-821X(88)90132-X

Hoggard, M. J., Parnell-Turner, R., & White, N. (2020). Hotspots and mantle plumes revisited: Towards reconciling the mantle heat transfer discrepancy. *Earth and Planetary Science Letters*, *542*, 116317. https://doi.org/10.1016/j.epsl.2020.116317.

Huang, S., Hall, P. S., & Jackson, M. G. (2011). Geochemical zoning of volcanic chains associated with Pacific hotspots. *Nature Geoscience*, *4*(12), 874-878. https://doi.org/10.1038/ngeo1263

Ireland, T. J., Walker, R. J., & Brandon, A. D. (2011). 186Os–187Os systematics of Hawaiian picrites revisited: New insights into Os isotopic variations in ocean island basalts. *Geochimica et Cosmochimica Acta*, *75*(16), 4456-4475. https://doi.org/10.1016/j.gca.2011.05.015

Ireland, T. J., Walker, R. J., & Garcia, M. O. (2009). Highly siderophile element and 187Os isotope systematics of Hawaiian picrites: Implications for parental melt composition and source heterogeneity. *Chemical Geology*, *260*(1-2), 112-128. https://doi.org/10.1016/j.chemgeo.2008.12.009

Jackson, M.G., Shirey, S.B., Hauri, E.H., Kurz, M.D., Rizo, H. (2016). Peridotite xenoliths from the Polynesian Austral and Samoa hotspots: Implications for the destruction of ancient ^{187}Os and ^{142}Nd isotopic domains and the preservation of Hadean 129Xe in the modern convecting mantle. *Geochimica et Cosmochimica Acta*, *185*, 21-43.

Jackson, M. G., Hart, S. R., Konter, J. G., Kurz, M. D., Blusztajn, J., & Farley, K. A. (2014). Helium and lead isotopes reveal the geochemical geometry of the Samoan plume. *Nature*, *514*(7522), 355-358. https://doi.org/10.1038/nature13794

Jackson, M. G., Weis, D., & Huang, S. (2012). Major element variations in Hawaiian shield lavas: Source features and perspectives from global ocean island basalt (OIB) systematics. *Geochemistry, Geophysics, Geosystems*, *13*(9). https://doi.org/10.1029/2012gc004268

Jackson, M. G., & Dasgupta, R. (2008). Compositions of HIMU, EM1, and EM2 from global trends between radiogenic isotopes and major elements in ocean island basalts. *Earth and Planetary Science Letters*, *276*(1-2), 175-186. https://doi.org/https://doi.org/10.1016/j.epsl.2008.09.023

Jagoutz, E., Palme, H., Baddenhausen, H., Blum, K., Cendales, M., Dreibus, G., et al. (1979). The Abundance of Major, Minor and Trace Elements in the Earth's Mantle as Derived from Primitive Ultramafic Nodules. *Proceedings of Lunar and Planetary Science Conference*, 2031–2050.

Jagoutz, E. (1988). Nd and Sr systematics in an eclogite xenolith from Tanzania: Evidence for frozen mineral equilibria in the continental lithosphere. *Geochimica et Cosmochimica Acta*, *52*(5), 1285–1293. http://doi.org/10.1016/0016-7037(88)90282-7

Jayko, A. S., & Bursik, M. (2011). Active transtensional intracontinental basins: Walker Lane in the western Great Basin. *Tectonics of sedimentary basins: Recent advances*, 226-248. https://doi.org/https://doi.org/10.1002/9781444347166.ch11

Jiang, C., Schmandt, B., Hansen, S. M., Dougherty, S. L., Clayton, R. W., Farrell, J., & Lin, F.-C. (2018). Rayleigh and S wave tomography constraints on subduction termination and lithospheric foundering in central California. *Earth and Planetary Science Letters*, *488*, 14-26. https://doi.org/https://doi.org/10.1016/j.epsl.2018.02.009

Jochum, K. P., Nohl, U., Herwig, K., Lammel, E., Stoll, B., & Hofmann, A. W. (2005). GeoReM: a new geochemical database for reference materials and isotopic standards. *Geostandards and Geoanalytical Research*, *29*(3), 333-338.

Jochum, K., Seufert, H., Spettel, B., & Palme, H. (1986). The solar-system abundances of Nb, Ta, and Y, and the relative abundances of refractory lithophile elements in differentiated planetary bodies. *Geochimica et Cosmochimica Acta*, *50*(6), 1173-1183. https://doi.org/https://doi.org/10.1016/0016-7037(86)90400-X

Johansen, T.-S., Hauff, F., Hoernle, K., Klugel, A., & Kokfelt, T. F. (2005). Basanite to phonolite differentiation within 1550–1750 yr: U-Th-Ra isotopic evidence from the AD 1585 eruption on La Palma, Canary Islands. *Geology*, *33*(11), 897-900.

Johnson, K. T. M., Dick, H. J. B., and Shimizu, N. (1990), Melting in the oceanic upper mantle: An ion microprobe study of diopsides in abyssal peridotites, J. Geophys. Res., 95(B3), 2661– 2678, doi:10.1029/JB095iB03p02661.

Jones, C. H., Farmer, G. L., & Unruh, J. (2004). Tectonics of Pliocene removal of lithosphere of the Sierra Nevada, California. *Geological Society of America Bulletin*, *116*(11-12), 1408-1422. https://doi.org/10.1130/b25397.1

Jones, C. H., Kanamori, H., & Roecker, S. W. (1994). Missing roots and mantle "drips": Regional P_n and teleseismic arrival times in the southern Sierra Nevada and vicinity, California. *Journal of Geophysical Research: Solid Earth, 99*(B3), 4567-4601. https://doi.org/10.1029/93jb01232

Jones, T. D., Davies, D. R., Campbell, I. H., Iaffaldano, G., Yaxley, G., Kramer, S. C., & Wilson, C. R. (2017). The concurrent emergence and causes of double volcanic hotspot tracks on the Pacific plate. *Nature, 545*(7655), 472-476. https://doi.org/10.1038/nature22054

Keays, R. R., & Lightfoot, P. C. (2007). Siderophile and chalcophile metal variations in Tertiary picrites and basalts from West Greenland with implications for the sulphide saturation history of continental flood basalt magmas. *Mineralium Deposita, 42*(4), 319-336. https://doi.org/10.1007/s00126-006-0112-4

Kelley, K. A., & Cottrell, E. (2012). The influence of magmatic differentiation on the oxidation state of Fe in a basaltic arc magma. *Earth and Planetary Science Letters, 329*, 109-121. https://doi.org/https://doi.org/10.1016/j.epsl.2012.02.010

Kelley, K. A., & Cottrell, E. (2009). Water and the oxidation state of subduction zone magmas. *Science, 325*(5940), 605-607. https://doi.org/DOI: 10.1126/science.1174156

Lassiter, J. C., Anderson, D. W., Villanueva-Lascurain, D., Marshall, E. W., & Barnes, J. D. (2022). Xenolith Constraints on "Self-Assimilation" and the Origin of Low $\delta^{18}O$ Values in Mauna Kea Basalts. In *Isotopic Constraints on Earth System Processes* (pp. 133-166). https://doi.org/10.1002/9781119595007.ch6

Lassiter, J. C., Byerly, B. L., Snow, J. E., & Hellebrand, E. (2014). Constraints from Os-isotope variations on the origin of Lena Trough abyssal peridotites and implications for the composition and evolution of the depleted upper mantle. *Earth and Planetary Science Letters*, *403*(C), 178–187. http://doi.org/10.1016/j.epsl.2014.05.033

Lassiter, J. (2003). Rhenium volatility in subaerial lavas: constraints from subaerial and submarine portions of the HSDP-2 Mauna Kea drillcore. *Earth and Planetary Science Letters*, *214*(1-2), 311-325. https://doi.org/https://doi.org/10.1016/S0012-821X(03)00385-6

Lassiter, J., Hauri, E., Reiners, P., & Garcia, M. (2000). Generation of Hawaiian post-erosional lavas by melting of a mixed lherzolite/pyroxenite source. *Earth and Planetary Science Letters*, *178*(3-4), 269-284. https://doi.org/https://doi.org/10.1016/S0012-821X(00)00084-4

Lassiter, J., & Hauri, E. (1998). Osmium-isotope variations in Hawaiian lavas: evidence for recycled oceanic lithosphere in the Hawaiian plume. *Earth and Planetary Science Letters*, *164*(3-4), 483-496.

Le Bas, M. J., Maitre, R. W., Streckeisen, A., Zanettin, B., & Rocks, I. S. o. t. S. o. I. (1986). A Chemical Classification of Volcanic Rocks Based on the Total Alkali-Silica Diagram. *Journal of Petrology*, *27*(3), 745-750. https://doi.org/10.1093/petrology/27.3.745

Lee, C. T. A., Luffi, P., & Chin, E. J. (2011). Building and Destroying Continental Mantle. *Annual Review of Earth and Planetary Sciences*, *39*(1), 59–90. http://doi.org/10.1146/annurev-earth-040610-133505

Lee, C.-T. A. (2006). Geochemical/petrologic constraints on the origin of cratonic mantle. *Geophysical Monograph-American Geophysical Union*, *164*, *89*

Lee, C.-T. A. (2002). Platinum-group element geochemistry of peridotite xenoliths from the Sierra Nevada and the Basin and Range, California. *Geochimica et Cosmochimica Acta*, *66*(22), 3987-4005. https://doi.org/https://doi.org/10.1016/S0016-7037(02)00960-2

Lee, C. T., Rudnick, R. L., & Brimhall Jr, G. H. (2001). Deep lithospheric dynamics beneath the Sierra Nevada during the Mesozoic and Cenozoic as inferred from xenolith petrology. *Geochemistry, Geophysics, Geosystems*, *2*(12). https://doi.org/https://doi.org/10.1029/2001GC000152

Lee, C.-T., Yin, Q., Rudnick, R. L., Chesley, J. T., & Jacobsen, S. B. (2000). Osmium isotopic evidence for Mesozoic removal of lithospheric mantle beneath the Sierra Nevada, California. *Science*, *289*(5486), 1912-1916. https://doi.org/DOI: 10.1126/science.289.5486.1912

Lipman, P., & Coombs, M. (2006). North Kona slump: Submarine flank failure during the early tholeiitic shield stage of Hualalai Volcano. *Journal of volcanology and geothermal research*, *151*(1-3), 189-216.

Liu, C.-Z., Snow, J. E., Brügmann, G., Hellebrand, E., & Hofmann, A. W. (2009). Non-chondritic HSE budget in Earth's upper mantle evidenced by abyssal peridotites from Gakkel ridge (Arctic Ocean). *Earth and Planetary Science Letters*, *283*(1-4), 122–132. http://doi.org/10.1016/j.epsl.2009.04.002

Lonsdale, P. (1991). Structural Patterns of the Pacific Floor Offshore of Peninsular California. *AAPG Memoir*, *47*, 87–125.

Luffi, P., Saleeby, J. B., Lee, C. T. A., & Ducea, M. N. (2009). Lithospheric mantle duplex beneath the central Mojave Desert revealed by xenoliths from Dish Hill, California. *Journal of Geophysical Research: Solid Earth*, *114*(B3), 375. http://doi.org/10.1029/2008JB005906

Luguet, A., & Pearson, G. (2019). Dating mantle peridotites using Re-Os isotopes: The complex message from whole rocks, base metal sulfides, and platinum group minerals. *American Minerologist: Journal of Earth and Planetary Materials 104(2),* 165-189.

Luguet, A., & Reisberg, L. (2016). Highly Siderophile Element and 187Os Signatures in Non-cratonic Basalt-hosted Peridotite Xenoliths: Unravelling the Origin and Evolution of the Post-Archean Lithospheric Mantle. *Reviews in Mineralogy and Geochemistry*, *81*(1), 305–367. http://doi.org/10.2138/rmg.2016.81.06

Luguet, A., Shirey, S. B., Lorand, J.-P., Horan, M. F., & Carlson, R. W. (2007). Residual platinum-group minerals from highly depleted harzburgites of the Lherz massif (France) and their role in HSE fractionation of the mantle. *Geochimica et Cosmochimica Acta*, *71*(12), 3082-3097. https://doi.org/10.1016/j.gca.2007.04.011

Luguet, A., Lorand, J.-P., & Seyler, M. (2003). Sulfide petrology and highly siderophile element geochemistry of abyssal peridotites: a coupled study of samples from the Kane Fracture Zone (45°W 23°20N, MARK area, Atlantic Ocean). *Geochimica Et Cosmochimica Acta*, *67*(8), 1553–1570. http://doi.org/10.1016/S0016-7037(02)01133-X

Luguet, A., Alard, O., Lorand, J. P., Pearson, N. J., Ryan, C., & O'Reilly, S. Y. (2001). Laser-ablation microprobe (LAM)-ICPMS unravels the highly siderophile element geochemistry of the oceanic mantle. *Earth and Planetary Science Letters*, *189*(3-4), 285–294. http://doi.org/10.1016/S0012-821X(01)00357-0

Luhr, J. F., Nelson, S. A., Allan, J. F., & Carmichael, I. S. E. (1985). Active rifting in southwestern Mexico: Manifestations of an incipient eastward spreading-ridge jump. *Geology*, *13*(1), 54–57. http://doi.org/10.1130/0091-7613(1985)13<54:ARISMM>2.0.CO;2

Mann, U., Frost, D. J., Rubie, D. C., Becker, H., & Audétat, A. (2012). Partitioning of Ru, Rh, Pd, Re, Ir and Pt between liquid metal and silicate at high pressures and high temperatures-Implications for the origin of highly siderophile element concentrations in the Earth's mantle. *Geochimica et Cosmochimica Acta*, *84*, 593-613. https://doi.org/https://doi.org/10.1016/j.gca.2012.01.026

Mallick, S., Dick, H. J., Sachi-Kocher, A., & Salters, V. J. (2014). Isotope and trace element insights into heterogeneity of subridge mantle. *Geochemistry, Geophysics, Geosystems*, *15*(6), 2438-2453.

Marcantonio, F., Zindler, A., Elliott, T., & Staudigel, H. (1995). 0s isotope systematics of La Palma, Canary Islands: Evidence for recycled crust in the mantle source of HIMU ocean islands. *Earth and Planetary Science Letters*, *133*, 397-410. https://doi.org/https://doi.org/10.1016/0012-821X(95)00092-Q

Matusiak-Małek, M., Puziewicz, J., Ntaflos, T., Grégoire, M., Kukuła, A., & Wojtulek, P. M. (2017). Origin and evolution of rare amphibole-bearing mantle peridotites from Wilcza Góra (SW Poland), Central Europe. *Lithos*, *286-287*(C), 302–323. http://doi.org/10.1016/j.lithos.2017.06.017

McDonough, W. F., & Sun, S.-S. (1995). The composition of the Earth. *Chemical Geology*, *120*(3-4), 223-253. https://doi.org/https://doi.org/10.1016/0009-2541(94)00140-4

McKenzie, D., & O'Nions, R. (1991). Partial melt distributions from inversion of rare earth element concentrations. *Journal of Petrology*, *32*(5), 1021-1091. https://doi.org/https://doi.org/10.1093/petrology/32.5.1021

Meisel, T., Walker, R. J., Irving, A. J., & Lorand, J.-P. (2001). Osmium isotopic compositions of mantle xenoliths: A global perspective. *Geochimica et Cosmochimica Acta*, *65*(8), 1311–1323. https://doi.org/https://doi.org/10.1016/S0016-7037(00)00566-4

Michaud, F., Royer, J. Y., Bourgois, J., Dyment, J., Calmus, T., Bandy, W., et al. (2006). Oceanic-ridge subduction vs. slab break off: Plate tectonic evolution along the Baja California Sur continental margin since 15 Ma. *Geology*, *34*(1), 13. http://doi.org/10.1130/g22050.1

Montelli, R., Nolet, G., Dahlen, F. A., & Masters, G. (2006). A catalogue of deep mantle plumes: New results from finite-frequency tomography. *Geochemistry, Geophysics, Geosystems*, *7*(11), n/a-n/a. https://doi.org/10.1029/2006gc001248

Mordick, B. E., & Glazner, A. F. (2006). Clinopyroxene thermobarometry of basalts from the Coso and Big Pine volcanic fields, California. *Contributions to Mineralogy and Petrology*, *152*(1), 111-124. https://doi.org/10.1007/s00410-006-0097-0

Morgan, W. J. (1971). Convection Plumes in the Lower Mantle. *Nature*, *230*(5288), 42-43. https://doi.org/10.1038/230042a0

Müller, R. D., Sdrolias, M., Gaina, C., & Roest, W. R. (2008). Age, spreading rates, and spreading asymmetry of the world's ocean crust. *Geochemistry*, *9*(4), n/a–n/a. http://doi.org/10.1029/2007GC001743

Mungall, J. E., & Brenan, J. M. (2014). Partitioning of platinum-group elements and Au between sulfide liquid and basalt and the origins of mantle-crust fractionation of the chalcophile elements. *Geochimica et Cosmochimica Acta*, *125*, 265-289. https://doi.org/https://doi.org/10.1016/j.gca.2013.10.002

Nelson, W. R., Furman, T., van Keken, P. E., Shirey, S. B., & Hanan, B. B. (2012). OsHf isotopic insight into mantle plume dynamics beneath the East African Rift System. *Chemical Geology*, *320*, 66-79. https://doi.org/https://doi.org/10.1016/j.chemgeo.2012.05.020

Nicholson, C., Sorlien, C. C., Atwater, T., Crowell, J. C., & Luyendyk, B. P. (1994). Microplate capture, rotation of the western Transverse Ranges, and initiation of the San Andreas transform as a low-angle fault system. *Geology*, *22*(6), 491-495. https://doi.org/https://doi.org/10.1130/0091-7613(1994)022<0491:MCROTW>2.3.CO;2

Nicklas, R. W., Day, J. M., Jones, T. D., & Castillo, P. R. (2022). Evidence for a primitive deep mantle component in the source of Marquesas Islands Lavas from Os isotope and highly siderophile element abundance systematics. *Geochimica et Cosmochimica Acta, 329*, 51-69. https://doi.org/https://doi.org/10.1016/j.gca.2022.05.012

Nicklas, R. W., Hahn, R. K., Willhite, L. N., Jackson, M. G., Zanon, V., Arevalo Jr, R., & Day, J. M. (2022). Oxidized mantle sources of HIMU-and EM-type Ocean Island Basalts. *Chemical Geology, 602*, 120901.

Nisbet, E. G., Cheadle, M. J., Arndt, N. T., & Bickle, M. J. (1993). Constraining the potential temperature of the Archaean mantle: A review of the evidence from komatiites. *Lithos, 30*(3-4), 291–307. http://doi.org/10.1016/0024-4937(93)90042-B

Niu, Y., & O'Hara, M. J. (2003). Origin of ocean island basalts: A new perspective from petrology, geochemistry, and mineral physics considerations. *Journal of Geophysical Research: Solid Earth, 108*(B4), 63. http://doi.org/10.1029/2002JB002048

Niu, Y. (2004). Bulk-rock Major and Trace Element Compositions of Abyssal Peridotites: Implications for Mantle Melting, Melt Extraction and Post-melting Processes Beneath Mid-Ocean Ridges. *Journal of Petrology, 45*(12), 2423–2458. http://doi.org/10.1093/petrology/egh068

Nixon, G. T. (1982). The relationship between Quaternary volcanism in central Mexico and the seismicity and structure of subducted ocean lithosphere. *Geological Society of America Bulletin, 93*(6), 514–523. http://doi.org/10.1130/0016-7606(1982)93<514:TRBQVI>2.0.CO;2

Nixon, P. N. (1987). Mantle xenolith perspectives. *Mantle Xenoliths, 96*(3), 741–756.

Norman, M. D., & Garcia, M. O. (1999). Primitive magmas and source characteristics of the Hawaiian plume: petrology and geochemistry of shield picrites. *Earth and Planetary Science Letters, 168*(1-2), 27-44. https://doi.org/https://doi.org/10.1016/S0012-821X(99)00043-6

O'Connor, J. M., Stoffers, P., & Wijbrans, J. R. (2001). En echelon volcanic elongate ridges connecting intraplate Foundation Chain volcanism to the Pacifc-Antarctic spreading center. *Earth and Planetary Science Letters, 192*, 633-648.

Oller, B., Day, J. M. D., Driscoll, N. W., & Lonsdale, P. F. (2022). Generation of Continental Lithospheric Mantle by Tectonic Isolation of Oceanic Plate. *Geochemistry, Geophysics, Geosystems, 23*(11). https://doi.org/10.1029/2022gc010353

Ovchinnikova, G. V., Belyatsky, B., Vasil'eva, I. M., Levskii, L., Grachev, A. F., Araña, V., & Mitjavila, J. (1995). Sr-Nd-Pb Isotope Characterics of the Mantle Sources of Basalts from the Canary Islands. *Petrology, 3*, 172-182.

Oversby, V. M., Lancelot, J., & Gast, P. (1971). Isotopic composition of lead in volcanic rocks from Tenerife, Canary Islands. *Journal of Geophysical Research*, *76*(14), 3402-3413. https://doi.org/https://doi.org/10.1029/JB076i014p03402

Payne, J. A., Jackson, M. G., & Hall, P. S. (2013). Parallel volcano trends and geochemical asymmetry of the Society Islands hotspot track. *Geology*, *41*(1), 19-22. https://doi.org/10.1130/g33273.1

Paquet, M., Day, J.M.D., Brown, D.B. & Waters, C.L. (2022). Effective global mixing of the highly siderophile elements into Earth's mantle inferred from oceanic abyssal peridotites. *Geochimica et Cosmochimica Acta*, 316, 347-362.

Paquet, M., Day, J. M., & Castillo, P. R. (2019). Osmium isotope evidence for a heterogeneous 3He/4He mantle plume beneath the Juan Fernandez Islands. *Geochimica et Cosmochimica Acta*, *261*, 1-19. https://doi.org/https://doi.org/10.1016/j.gca.2019.06.039

Peach, C., Mathez, E. A., Keays, R. R., & Reeves, S. (1994). Experimentally determined sulfide melt-silicate melt partition coefficients for iridium and palladium. *Chemical Geology*, *117*(1-4), 361-377. https://doi.org/https://doi.org/10.1016/0009-2541(94)90138-4

Peach, C., Mathez, E., & Keays, R. (1990). Sulfide melt-silicate melt distribution coefficients for noble metals and other chalcophile elements as deduced from MORB: Implications for partial melting. *Geochimica et Cosmochimica Acta*, *54*(12), 3379-3389. https://doi.org/https://doi.org/10.1016/0016-7037(90)90292-S

Pearce, J. A., & Parkinson, I. J. (1993). Trace element models for mantle melting: application to volcanic arc petrogenesis. *Geological Society, London, Special Publications*, *76*(1), 373–403. http://doi.org/10.1144/GSL.SP.1993.076.01.19

Pearson, D. G., Carlson, R. W., Shirey, S. B., Boyd, F. R., & Nixon, P. H. (1995). Stabilization of Archaean lithospheric mantle: A ReOs isotope study of peridotite xenoliths from the Kaapvaal craton. *Earth and Planetary Science Letters*, *134*(3-4), 341–357. http://doi.org/10.1016/0012-821X(95)00125-V

Pearson, D. G., Canil, D., & Shirey, S. B. (2004). Mantle Samples Included in Volcanic Rocks: xenoliths and diamonds. *Treatise on geochemistry*, *2*, *568*.

Pearson, D. G., Irvine, G. J., Ionov, D. A., Boyd, F. R., & Dreibus, G. E. (2004). Re–Os isotope systematics and platinum group element fractionation during mantle melt extraction: a study of massif and xenolith peridotite suites. *Chemical Geology*, *208*(1-4), 29-59. https://doi.org/10.1016/j.chemgeo.2004.04.005

Pearson, D. G., & Wittig, N. (2008). Formation of Archaean continental lithosphere and its diamonds: the root of the problem. Journal of the Geological Society, 165(5), 895–914. http://doi.org/10.1144/0016-76492008-003

Pearson, D. G., Scott, J. M., Liu, J., Schaeffer, A., Wang, L. H., van Hunen, J., Szilas, K., Chacko, T., Kelemem, P. B. (2021). Deep continental roots and cratons. *Nature, 596*(7871), 199-210.

Peslier, A. H., Reisberg, L., Ludden, J., & Francis, D. (2000). Os isotopic systematics in mantle xenoliths; age constraints on the Canadian Cordillera lithosphere. *Chemical Geology, 166*, 85–101.

Peters, B. J., Day, J. M., & Taylor, L. A. (2016). Early mantle heterogeneities in the Réunion hotspot source inferred from highly siderophile elements in cumulate xenoliths. *Earth and Planetary Science Letters*, *448*, 150-160. https://doi.org/https://doi.org/10.1016/j.epsl.2016.05.015

Peucker-Ehrenbrink, B., Hanghoj, K., Atwood, T., & Kelemen, P. B. (2012). Rhenium-osmium isotope systematics and platinum group element concentrations in oceanic crust. *Geology, 40*(3), 199-202. https://doi.org/10.1130/g32431.1

Peucker-Ehrenbrink, B., Bach, W., Hart, S. R., Blusztajn, J. S., & Abbruzzese, T. (2003). Rhenium-osmium isotope systematics and platinum group element concentrations in oceanic crust from DSDP/ODP Sites 504 and 417/418. *Geochemistry, Geophysics, Geosystems*, *4*(7). https://doi.org/10.1029/2002gc000414

Peucker-Ehrenbrink, B., & Jahn, B. M. (2001). Rhenium-osmium isotope systematics and platinum group element concentrations: Loess and the upper continental crust. *Geochemistry, Geophysics, Geosystems*, *2*(10), n/a-n/a. https://doi.org/10.1029/2001gc000172

Pfänder, J. A., Münker, C., Stracke, A., & Mezger, K. (2007). Nb/Ta and Zr/Hf in ocean island basalts — Implications for crust–mantle differentiation and the fate of Niobium. *Earth and Planetary Science Letters*, *254*(1-2), 158–172. http://doi.org/10.1016/j.epsl.2006.11.027

Pilet, S., Baker, M. B., & Stolper, E. M. (2008). Metasomatized lithosphere and the origin of alkaline lavas. *Science*, *320*(5878), 916-919. https://doi.org/DOI: 10.1126/science.1156563

Pitcher, L., Helz, R. T., Walker, R. J., & Piccoli, P. (2009). Fractionation of the platinum-group elments and Re during crystallization of basalt in Kilauea Iki Lava Lake, Hawai'i. *Chemical Geology*, *260*(3-4), 196-210. https://doi.org/10.1016/j.chemgeo.2008.12.022

Prægel, N.-O., & Holm, P. M. (2006). Lithospheric contributions to high-MgO basanites from the Cumbre Vieja Volcano, La Palma, Canary Islands and evidence for temporal variation in plume influence. *Journal of volcanology and geothermal research, 149*(3-4), 213-239. https://doi.org/https://doi.org/10.1016/j.jvolgeores.2005.07.019

Putirka, K. D. (2017). Down the crater: where magmas are stored and why they erupt. *Elements, 13*(1), 11-16. https://doi.org/https://doi.org/10.2113/gselements.13.1.11

Putirka, K., Johnson, M., Kinzler, R., Longhi, J., & Walker, D. (1996). Thermobarometry of mafic igneous rocks based on clinopyroxene-liquid equilibria, 0-30 kbar. *Contributions to Mineralogy and Petrology, 123*(1), 92-108. https://doi.org/10.1007/s004100050145

Rau, C. J., & Forsyth, D. W. (2011). Melt in the mantle beneath the amagmatic zone, southern Nevada. *Geology, 39*(10), 975-978. https://doi.org/10.1130/g32179.1

Rehkamper, M., Halliday, A. N., Fitton, J. G., Lee, D.-C., Wieneke, M., & Arndt, N. T. (1999). Ir, Ru, Pt, and Pd in basalts and komatiites: New constraints for the geochemical behavior of the platinum-group elements in the mantle. *Geochimica et Cosmochimica Acta, 63*(22), 3915-3934. https://doi.org/https://doi.org/10.1016/S0016-7037(99)00219-7

Reiners, P. W. (2002). Temporal-compositional trends in intraplate basalt eruptions: Implications for mantle heterogeneity and melting processes. *Geochemistry, Geophysics, Geosystems, 3*(2), 1-30. https://doi.org/https://doi.org/10.1029/2001GC000250

Reisberg, L., Zindler, A., Marcantonio, F., White, W., Wyman, D., & Weaver, B. (1993). Os isotope systematics in ocean island basalts. *Earth and Planetary Science Letters, 120*(3-4), 149-167. https://doi.org/https://doi.org/10.1016/0012-821X(93)90236-3

Robinson, J. E., & Eakins, B. W. (2006). Calculated volumes of individual shield volcanoes at the young end of the Hawaiian Ridge. *Journal of volcanology and geothermal research, 151*(1-3), 309-317. https://doi.org/https://doi.org/10.1016/j.jvolgeores.2005.07.033

Rudnick, R. L., & Walker, R. J. (2009). Interpreting ages from Re–Os isotopes in peridotites. *Lithos, 112*, 1083-1095. https://doi.org/https://doi.org/10.1016/j.lithos.2009.04.042

Rudnick, R. L., & Lee, C.-T. (2002). Osmium isotope constraints on tectonic evolution of the lithosphere in the southwestern United States. *International Geology Review, 44*(6), 501-511. https://doi.org/https://doi.org/10.2747/0020-6814.44.6.501

Rudnick, R. L., McDonough, W. F., & Chappell, B. W. (1993). Carbonatite metasomatism in the northern Tanzanian mantle: Petrographic and geochemical characteristics. *Earth and Planetary Science Letters, 114*(4), 463–475. http://doi.org/10.1016/0012-821X(93)90076-L

Samson, S. D., & Patchett, P. J. (1991). The Canadian Cordillera as a modern analogue of Proterozoic crustal growth. *Australian Journal of Earth Sciences, 38*(5), 595–611. http://doi.org/10.1080/08120099108727994

Schulze, D. J. (1986). Calcium anomalies in the mantle and a subducted metaserpentinite origin for diamonds. *Nature, 319*(6053), 483–485. http://doi.org/10.1038/319483a0

Shen, W., Ritzwoller, M. H., & Schulte‐Pelkum, V. (2013). A 3‐D model of the crust and uppermost mantle beneath the Central and Western US by joint inversion of receiver functions and surface wave dispersion. *Journal of Geophysical Research: Solid Earth*, *118*(1), 262-276. https://doi.org/10.1029/2012jb009602

Shirey, S. B., & Richardson, S. H. (2011). Start of the Wilson cycle at 3 Ga shown by diamonds from subcontinental mantle. *Science*, *333*(6041), 434-436.

Shirey, S. B., & Walker, R. J. (1998). The Re-Os isotope system in cosmochemistry and high-temperature geochemistry. *Annual Review of Earth and Planetary Sciences*, *26*(1), 423-500.

Simon, N. S. C., Neumann, E.-R., Bonadiman, C., Coltorti, M., Delpech, G., Grégoire, M., & Widom, E. (2008). Ultra-refractory Domains in the Oceanic Mantle Lithosphere Sampled as Mantle Xenoliths at Ocean Islands. *Journal of Petrology*, *49*(6), 1223–1251. http://doi.org/10.1093/petrology/egn023

Sjoblom, M. P., Dorais, M. J., Christiansen, E. H., & Fodor, R. V. (2023). Mafic to ultramafic xenoliths from Mauna Kea, Hawai'i: clues to magma evolution from trace element compositions of clinopyroxene. *Contributions to Mineralogy and Petrology*, *178*(3). https://doi.org/10.1007/s00410-023-02001-3

Sleep, N. H. (1990). Hotspots and mantle plumes: Some phenomenology. *Journal of Geophysical Research: Solid Earth*, *95*(B5), 6715-https://doi.org/10.1029/JB095iB05p06715

Snortum, E., Day, J.M.D., Jackson, M.G. (2019) Pacific Lithosphere Evolution Inferred from Aitutaki Mantle Xenoliths, *Journal of Petrology*, Volume 60, Issue 9, Pages 1753–1772, https://doi.org/10.1093/petrology/egz047

Snortum, E., Day, J.M.D. (2020) Forearc origin for Coast Range Ophiolites inferred from osmium isotopes and highly siderophile elements, Chemical Geology, Volume 550, 2020, 119723, ISSN 0009-2541, https://doi.org/10.1016/j.chemgeo.2020.119723.

Snow, J. E., & Reisberg, L. (1995). Os isotopic systematics of the MORB mantle: results from altered abyssal peridotites. Earth and Planetary Science Letters, 133(3-4), 411–421

Snow, J.E., Schmidt., G. (1998) Constraints on Earth accretion deduced from noble metals in the oceanic mantle. Nature 391, 166-169.

Stern, R. J. (2002). Subduction zones. *Reviews of Geophysics*, *40*(4), 293–3–38. http://doi.org/10.1029/2001RG000108

Stevens, C. H., Stone, P., & Blakely, R. J. (2013). Structural evolution of the east Sierra Valley system (Owens Valley and vicinity), California: a geologic and geophysical synthesis. *Geosciences*, *3*(2), 176-215. https://doi.org/https://doi.org/10.3390/geosciences3020176

Stracke, A. (2012). Earth's heterogeneous mantle: A product of convection-driven interaction between crust and mantle. *Chemical Geology*, *330*, 274-299. https://doi.org/https://doi.org/10.1016/j.chemgeo.2012.08.007

Straume, E. O., Gaina, C., Medvedev, S., Hochmuth, K., Gohl, K., Whittaker, J. M., Abdul Fattah, R., Doornenbal, J. C., & Hopper, J. R. (2019). GlobSed: Updated Total Sediment Thickness in the World's Oceans. *Geochemistry, Geophysics, Geosystems*, *20*(4), 1756-1772. https://doi.org/10.1029/2018gc008115

Sun, S.-S. (1980). Lead isotopic study of young volcanic rocks from mid-ocean ridges, ocean islands and island arcs. *Philosophical Transactions of the Royal Society of London. Series A, Mathematical and Physical Sciences*, *297*(1431), 409-445. https://doi.org/https://doi.org/10.1098/rsta.1980.0224

Tanaka, R., Makishima, A., & Nakamura, E. (2008). Hawaiian double volcanic chain triggered by an episodic involvement of recycled material: Constraints from temporal Sr–Nd–Hf–Pb isotopic trend of the Loa-type volcanoes. *Earth and Planetary Science Letters*, *265*(3-4), 450-465. https://doi.org/10.1016/j.epsl.2007.10.035

Tatsumi, Y., Oguri, K., & Shimoda, G. (1999). The Behaviour of Platinum-Group Elements During Magmatic Differentiation in Hawaiian Tholeiites. *Geochemical Journal*, *33*, 237-247. https://doi.org/10.2343/geochemj.33.237

Thirlwall, M., Jenkins, C., Vroon, P., & Mattey, D. (1997). Crustal interaction during construction of ocean islands: Pb Sr Nd O isotope geochemistry of the shield basalts of Gran Canaria, Canary Islands. *Chemical Geology*, *135*(3-4), 233-262. https://doi.org/https://doi.org/10.1016/S0009-2541(96)00118-0

Thomas, L., Hawkesworth, C., Van Calsteren, P., Turner, S., & Rogers, N. (1999). Melt generation beneath ocean islands: A U-Th-Ra isotope study from Lanzarote in the Canary Islands. *Geochimica et Cosmochimica Acta*, *63*(23-24), 4081-4099. https://doi.org/https://doi.org/10.1016/S0016-7037(99)00310-5

Turner, J. S., & Campbell, I. H. (1986). Convection and mixing in magma chambers. *Earth-Science Reviews*, *23*(4), 255-352. https://doi.org/https://doi.org/10.1016/0012-8252(86)90015-2

Turner, S., Hoernle, K., Hauff, F., Johansen, T., Klügel, A., Kokfelt, T., & Lundstrom, C. (2015). 238 U–230 Th–226 Ra disequilibria constraints on the magmatic evolution of the Cumbre Vieja volcanics on La Palma, Canary Islands. *Journal of Petrology*, *56*(10), 1999-2024. https://doi.org/https://doi.org/10.1093/petrology/egv061

Unruh, J., Humphrey, J., & Barron, A. (2003). Transtensional model for the Sierra Nevada frontal fault system, eastern California. *Geology*, *31*(4), 327-330. https://doi.org/https://doi.org/10.1130/0091-7613(2003)031<0327:TMFTSN>2.0.CO;2

Unruh, J. R. (1991). The uplift of the Sierra Nevada and implications for late Cenozoic epeirogeny in the western Cordillera. *Geological Society of America Bulletin*, *103*(11), 1395-1404. https://doi.org/https://doi.org/10.1130/0016-7606(1991)103<1395:TUOTSN>2.3.CO;2

van den Broek, J. M., & Gaina, C. (2020). Microcontinents and continental fragments associated with subduction systems. *Tectonics*, *39*, e2020TC006063. https://doi.org/10.1029/2020TC006063

Volkening, J., Walczyk, T., & Heumann, K. G. (1991). Osmium isotope ratio determinations by negative thermal ionization mass spectrometry. *International Journal of Mass Spectrometry and Ion Processes*, *105(2)*, 147-159.

Walker, R. J., Morgan, J. W., Beary, E. S., Smoliar, M. I., Czamanske, G. K., & Horan, M. F. (1997). Applications of the $^{190}Pt/^{186}Os$ isotope system to geochemistry and cosmochemistry. *Geochimica et Cosmochimica Acta*, *61*(22), 4799-4807. https://doi.org/https://doi.org/10.1016/S0016-7037(97)00270-6

Walker, R., Carlson, R., Shirey, S., & Boyd, F. (1989). Os, Sr, Nd, and Pb isotope systematics of southern African peridotite xenoliths: implications for the chemical evolution of subcontinental mantle. *Geochimica et Cosmochimica Acta*, *53*(7), 1583-1595.

Wang, D., Wu, S., Li, T., Tong, P., & Gao, Y. (2022). Elongated Magma Plumbing System Beneath the Coso Volcanic Field, California, Constrained by Seismic Reflection Tomography. *Journal of Geophysical Research: Solid Earth*, *127*(6). https://doi.org/10.1029/2021jb023582

Wang, J., Xiong, X., Takahashi, E., Zhang, L., Li, L., & Liu, X. (2019). Oxidation State of Arc Mantle Revealed by Partitioning of V, Sc, and Ti Between Mantle Minerals and Basaltic Melts. *Journal of Geophysical Research: Solid Earth*, *124*(5), 4617-4638. https://doi.org/10.1029/2018jb016731

Wang, K., Plank, T., Walker, J. D., & Smith, E. I. (2002). A mantle melting profile across the Basin and Range, SW USA. *Journal of Geophysical Research: Solid Earth*, *107*(B1), ECV 5-1-ECV 5-21. https://doi.org/https://doi.org/10.1029/2001JB000209

Warren, J. M. (2016). Global variations in abyssal peridotite compositions. *Lithos*, *248-251*(C), 193–219. http://doi.org/10.1016/j.lithos.2015.12.023

Watchorn, F., Nichols, G., & Bosence, D. (1998). Rift-related sedimentation and stratigraphy, southern Yemen (Gulf of Aden). In *Sedimentation and Tectonics in Rift Basins Red Sea:-Gulf of Aden* (pp. 165-189). Springer. https://doi.org/https://doi.org/10.1007/978-94-011-4930-3_11

Waters, C. L., Day, J. M. D., Watanabe, S., Sayit, K., Zanon, V., Olson, K. M., Hanan, B. B., & Widom, E. (2020). Sulfide mantle source heterogeneity recorded in basaltic lavas from the Azores. *Geochimica et Cosmochimica Acta*, *268*, 422-445. https://doi.org/10.1016/j.gca.2019.10.012

Weis, D., Garcia, M. O., Rhodes, J. M., Jellinek, M., & Scoates, J. S. (2011). Role of the deep mantle in generating the compositional asymmetry of the Hawaiian mantle plume. *Nature Geoscience*, *4*(12), 831-838. https://doi.org/10.1038/ngeo1328

Wessel, P., Luis, J. F., Uieda, L., Scharroo, R., Wobbe, F., Smith, W. H. F., & Tian, D. (2019). The Generic Mapping Tools Version 6. *Geochemistry, Geophysics, Geosystems*, *20*(11), 5556-5564. https://doi.org/10.1029/2019gc008515

Wessel, P., Smith, W. H. F., Scharroo, R., Luis, J. and Wobbe, F. (2013), Generic Mapping Tools: Improved Version Released, *Eos Trans. AGU*, 94(45), 409.

Weyer, S., Münker, C., & Mezger, K. (2003). Nb/Ta, Zr/Hf and REE in the depleted mantle: implications for the differentiation history of the crust–mantle system. *Earth and Planetary Science Letters*, *205*(3-4), 309–324. http://doi.org/10.1016/S0012-821X(02)01059-2

Weyer, S., Münker, C., Rehkämper, M., & Mezger, K. (2002). Determination of ultra-low Nb, Ta, Zr and Hf concentrations and the chondritic Zr/Hf and Nb/Ta ratios by isotope dilution analyses with multiple collector ICP-MS. *Chemical Geology*, *187*(3-4), 295-313. https://doi.org/https://doi.org/10.1016/S0009-2541(02)00129-8

Widom, E., Hoernle, K. A., Shirey, S. B., & Schmnincke, H.-U. (1999). Os Isotope Systematics in the Canary Islands and Madeira: Lithospheric Contamination and Mantle Plume Signatures. *Journal of Petrology*, *40*(2), 279-296. https://doi.org/https://doi.org/10.1093/petroj/40.2.279

Wieser, P., Petrelli, M., Lubbers, J., Wieser, E., Ozaydin, S., Kent, A., & Till, C. (2022). Thermobar: An open-source Python3 tool for thermobarometry and hygrometry. *Volcanica*, *5*(2), 349-384. https://doi.org/10.30909/vol.05.02.349384

Wieser, P. E., Edmonds, M., Maclennan, J., Jenner, F. E., & Kunz, B. E. (2019). Crystal scavenging from mush piles recorded by melt inclusions. *Nature communications*, *10*(1), 5797. https://doi.org/https://doi.org/10.1038/s41467-019-13518-2

Wiesmaier, S., Deegan, F. M., Troll, V. R., Carracedo, J. C., Chadwick, J. P., & Chew, D. M. (2011). Magma mixing in the 1100 AD Montaña Reventada composite lava flow, Tenerife, Canary Islands: interaction between rift zone and central volcano plumbing systems. *Contributions to Mineralogy and Petrology*, *162*, 651-669. https://doi.org/https://doi.org/10.1007/s00410-010-0596-x

Wilding, J. D., Zhu, W., Ross, Z. E., & Jackson, J. M. (2023). The magmatic web beneath Hawai‘i. *Science*, *379*(6631), 462-468. https://doi.org/DOI: 10.1126/science.ade5755

Williamson, N. M. B., Weis, D., Scoates, J. S., Pelletier, H., & Garcia, M. O. (2019). Tracking the Geochemical Transition Between the Kea-Dominated Northwest Hawaiian Ridge and the Bilateral Loa-Kea Trends of the Hawaiian Islands. *Geochemistry, Geophysics, Geosystems*, *20*(9), 4354-4369. https://doi.org/10.1029/2019gc008451

Winterbourne, J., Crosby, A., & White, N. (2009). Depth, age and dynamic topography of oceanic lithosphere beneath heavily sedimented Atlantic margins. *Earth and Planetary Science Letters*, *287*(1-2), 137-151. https://doi.org/https://doi.org/10.1016/j.epsl.2009.08.019

Wolfenden, E., Ebinger, C., Yirgu, G., Deino, A., & Ayalew, D. (2004). Evolution of the northern Main Ethiopian rift: birth of a triple junction. *Earth and Planetary Science Letters*, *224*(1-2), 213-228. https://doi.org/https://doi.org/10.1016/j.epsl.2004.04.022

Woodland, S. J., Pearson, D. G., & Thirlwall, M. F. (2002). A Platinum Group Element and Re–Os Isotope Investigation of Siderophile Element Recycling in Subduction Zones: Comparison of Grenada, Lesser Antilles Arc, and the Izu–Bonin Arc. *Journal of Petrology*, *43*(1), 171-198. https://doi.org/10.1093/petrology/43.1.171

Workman, R. K., & Hart, S. R. (2005). Major and trace element composition of the depleted MORB mantle (DMM). *Earth and Planetary Science Letters*, *231*(1-2), 53–72. http://doi.org/10.1016/j.epsl.2004.12.005

Yang, J., Wang, C., Zhang, J., & Jin, Z. (2023). Genesis of Hawaiian lavas by crystallization of picritic magma in the deep mantle. *Nat Commun*, *14*(1), 1382. https://doi.org/10.1038/s41467-023-37072-0

Yang, H.-J., Frey, F., & Clague, D. (2003). Constraints on the source components of lavas forming the Hawaiian North Arch and Honolulu Volcanics. *Journal of Petrology*, *44*(4), 603-627. https://doi.org/https://doi.org/10.1093/petrology/44.4.603

Zhang, Z., & Hirschmann, M. M. (2016). Experimental constraints on mantle sulfide melting up to 8 GPa. *American Mineralogist*, *101*(1), 181-192. https://doi.org/https://doi.org/10.2138/am-2016-5308

Zhou, M.-F., Robinson, P. T., Malpas, J., & Li, Z. (1996). Podiform Chromitites in the Luobusa Ophiolite (Southern Tibet): Implications for Melt-Rock Interaction and Chromite Segregation in the Upper Mantle. Journal of Petrology, 37(1), 3–21.

Zindler, A., & Hart, S. (1986). Chemical geodynamics. *Annual Review of Earth and Planetary Sciences*, *14*(1), 493-571. https://doi.org/10.1146/annurev.earth.14.1.493